

Advances in the Soil-Structure Interaction Analysis -- from Surface Footings to Thermoactive Deep Foundations

Présentée le 9 mars 2021

Faculté de l'environnement naturel, architectural et construit
Laboratoire de mécanique des sols - Chaire gaz naturel Petrosvibri
Programme doctoral en mécanique

pour l'obtention du grade de Docteur ès Sciences

par

Cristiano GARBELLINI

Acceptée sur proposition du jury

Prof. D. Lignos, président du jury
Prof. L. Laloui, directeur de thèse
Prof. P. J. Bourne-Webb, rapporteur
Prof. D. Adam, rapporteur
Dr M. Fernández Ruiz, rapporteur

A mia madre, per essere un esempio di intraprendenza
A mio padre, per essere un esempio di umiltà
A mio fratello e mia sorella, per essere dei punti di riferimento
A Martina, per essere la mia compagna di vita

Abstract

Mutual interactions between soil and foundation play a fundamental role in the overall behaviour of constructions. Therefore, it is not surprising that soil-structure interaction has been the subject of numerous research works. This doctoral thesis is a theoretical contribution in this field.

Despite the available knowledge, the fact that specific studies on the behaviour of foundation structural elements and soil masses progressed independently constrained the understanding of the governing mechanisms, especially close to failure. This constitutes a serious limitation to the development of a consistent performance-based design strategy.

The first part of this dissertation presents an attempt in this direction. The limit state of surface footings subjected to centred and vertical loads is investigated considering simultaneously the structural failure and the soil bearing capacity. The relevance of the employed theoretical methods with respect to the real materials is critically reviewed. A simplified procedure for quantifying soil-structure interaction effects is presented. Despite the analysis deals with surface footings, the concepts can easily be extended to other conditions and geotechnical works.

The second part of the thesis focuses on the behaviour of thermoactive deep foundations. They are an innovative and environmentally friendly technology that couples the role of ground heat exchanger to that of structural support. An extensive numerical parametric analysis defines the main effects of the presence of a flexible raft cast directly on the ground. The potential benefits of considering reinforced concrete non-linear behaviour are discussed, and guidelines are provided for the performance-based design of energy piles.

Keywords: plasticity; limit analysis; bearing capacity; shear strength; energy piles; thermo-mechanical behaviour; group effects; finite elements; performance-based design.

Résumé

Les interactions entre sol et fondation jouent un rôle fondamental dans le comportement des structures. Par conséquent, il n'est pas surprenant que l'interaction sol-structure a fait l'objet de nombreux travaux de recherche. Cette thèse doctorale est une contribution théorique dans ce domaine.

Malgré les connaissances disponibles, le fait que des études spécifiques sur le comportement des éléments structuraux des fondations et du sol ont progressé de manière indépendante a limité la compréhension des mécanismes d'interaction, en particulier proche de la rupture. Cela constitue une limite sérieuse au développement d'une méthodologie de dimensionnement cohérente basée sur la performance.

La première partie de cette thèse fait un effort dans cette direction. L'état limite des semelles soumises à des charges centrées et verticales est étudié en considérant simultanément la rupture structurale et la capacité portante du sol. La pertinence des méthodes théoriques utilisées par rapport au matériaux réels fait l'objet d'un examen critique. Une procédure simplifiée pour quantifier les effets de l'interaction sol-structure est présentée. Bien que l'analyse porte sur les semelles superficielles, les concepts peuvent facilement être étendus à d'autres conditions et ouvrages géotechniques.

La deuxième partie de la thèse porte sur le comportement des fondations profondes thermoactives. Il s'agit d'une technologie innovante et durable qui associe le rôle d'échangeur de chaleur à celui de support structurel. Une analyse paramétrique numérique approfondie définit les principaux effets de la présence d'un radier flexible s'appuyant directement au sol. Les avantages potentiels de la prise en compte du comportement non-linéaire du béton armé sont discutés. Finalement, des lignes directrices sont fournies pour la conception des pieux énergétiques.

Mots clé : plasticité ; analyse limite ; capacité portante ; résistance à l'effort tranchant ; pieux énergétiques ; comportement thermo-mécanique ; effets de groupe ; éléments finis ; dimensionnement basé sur la performance.

Acknowledgments

This work has been supported by the Swiss National Science Foundation, project No. 174575, Division InterCo; and project No. 200021_175500, Division II.

This research was carried out at the Laboratory of Soil Mechanics (LMS) of the École Polytechnique Fédérale de Lausanne (EPFL) under the supervision of Prof. Lyesse Laloui. To him, I would like to express my sincere gratitude for giving me this opportunity. I am also grateful for the freedom and confidence he showed me in these four years. His valuable advices helped me keep my course.

I wish to thank Prof. Dimitrios Lignos for chairing my dissertation committee, and Prof. Peter Bourne-Webb, Prof. Dietmar Adam and Dr. Miguel Fernández Ruiz for reviewing my thesis.

The author is also indebted to Prof. Alessandro Rotta Loria for having been an essential guide in the early stages of this work. The fruitful entertained discussions inspired part of this study.

I would also like to express my appreciation to Prof. Aurelio Muttoni for sharing his profound knowledge of reinforced concrete.

I thank Dr. Jacopo Zannin, Matteo Bocco, Dr. Ginaluca Speranza, Angelica Tuttolomondo, José Bosch, Elena Ravera, and Prof. Melis Sutman for their valuable contributions and suggestions.

Finally, I would like to thank all the people who contributed in a way or another to this work and to my professional growth.

CRISTIANO GARBELLINI
LAUSANNE
AUGUST, 2020

Contents

Introduction	1
I Surface Footings	5
1 Limit State Analysis	7
1.1 Introduction	7
1.2 Stress-Strain Relationships	9
1.2.1 Common Yield Surfaces for Engenireeng Applications	10
1.2.2 Irreversibility Condition	11
1.2.3 Principle of Maximum Plastic Work	12
1.2.4 Drucker's Stability Postulate	12
1.2.5 Uniqueness of Solution	13
1.3 Limit Analysis for Associated Coaxial Materials	14
1.4 Limit Analysis for Non-Associated Materials	16
1.4.1 Non-Associated Coaxial Materials	16
1.4.2 Non-Associated Non-Coaxial Materials	20
1.4.3 Frictional Interfaces	21
1.5 Methods for Computing the Limit Load	22
1.6 Limit Analysis for Real Soils	23
1.7 Limit Analysis for Structures	25
1.7.1 Steel	25
1.7.2 Reinforced Concrete	25
1.8 Limit Analysis Considering Soil-Structure Interaction	28
1.9 Numerical Limit Analysis	28
1.10 Concluding remarks	29
2 Bearing Capacity of Surface Footings	31
2.1 Introduction	32
2.2 Plane Strain Problem	32
2.2.1 Weightless Mohr-Coulomb Material — $c-\phi$ soil	32
2.2.2 Ponderable Tresca Material — $c-\gamma$ soil	35
2.2.3 Ponderable Cohesionless Mohr-Coulomb Material — $\phi-\gamma$ soil	36
2.2.4 Ponderable Mohr-Coulomb Material — $c-\phi-\gamma$ soil	57

2.3	Three-Dimensional Problem	72
2.3.1	Weightless Mohr-Coulomb Material — $c-\phi$ soil	72
2.3.2	Ponderable Tresca Material — $c-\gamma$ soil	75
2.3.3	Ponderable Cohesionless Mohr-Coulomb Material — $\phi-\gamma$ soil	80
2.3.4	Ponderable Mohr-Coulomb Material — $c-\phi-\gamma$ soil	86
2.4	Real Soils	89
2.4.1	Presence of Water	89
2.4.2	Non-Associated Materials	90
2.4.3	Experimental Results	91
2.5	Concluding Remarks	95
3	Soil-Structure Interaction of Surface Footings	97
3.1	Introduction	98
3.2	Bearing Capacity of Soils	99
3.3	Contact Pressure	101
3.4	Shear Capacity of Concrete Members	102
3.5	Effects of Soil-Structure Interactions	104
3.5.1	Deep Beams	104
3.5.2	Short Span Beams	105
3.5.3	Slender Beams	106
3.5.4	Very Slender Beams	111
3.6	Concluding Remarks	126
II	Thermoactive Deep Foundations	127
4	Energy Piled Rafts	129
4.1	Introduction	130
4.2	Numerical Modelling	131
4.2.1	Parametric analysis	131
4.2.2	Mathematical Formulation	132
4.2.3	Finite Elements Model	135
4.3	Numerical Results	136
4.3.1	Typical Results of Raft Mean Displacements	136
4.3.2	Typical Results of Raft Differential Displacements	142
4.3.3	Typical Results of Thermal Stresses Induced in the Piles	144
4.4	Concluding Remarks	149
5	Thermal Stress Analysis of Energy Piles	153
5.1	Introduction	154
5.2	General Framework	155
5.3	Linear Elastic Thermal Stress Analysis of Bar Systems	156
5.3.1	Single Bar Systems	156
5.3.2	Capped Bars Systems	159

5.4	Material Models	162
5.4.1	Reinforced Concrete Tie Model	162
5.4.2	Load–Transfer Model for Soil–Pile Interface	165
5.4.3	Group Effects	165
5.5	Finite Elements Model	166
5.6	Performance of Single Energy Piles	167
5.7	Performance of Energy Piled Rafts	170
5.8	Concluding Remarks	172
6	The Role of Thermal Loads	179
6.1	Introduction	180
6.2	Performance-Based design of Energy Piles	182
6.2.1	Rationale	182
6.2.2	Design Case Studies and Material Parameters	183
6.2.3	Typical Design Problems	183
6.2.4	Design Method	185
6.2.5	Analysis Method	186
6.2.6	Verification Method	187
6.2.7	Combination of Actions at Ultimate Limit States	187
6.2.8	Partial Factors for Thermal Loads Applied to Energy Piles	187
6.3	Geotechnical ULS	189
6.3.1	Theoretical Considerations	189
6.3.2	Energy Pile Response for a Constant Applied Mechanical Load and Varying Pile Length	190
6.3.3	Energy Pile Response for Varying Applied Mechanical Loads and Constant Pile Length	191
6.3.4	Summary	192
6.4	Structural ULS	193
6.4.1	Theoretical Considerations	193
6.4.2	Energy Pile Response for a Constant Applied Mechanical Load and Varying Pile Length	194
6.4.3	Energy Pile Response for Varying Mechanical Loads and a Constant Pile Length	197
6.4.4	Summary	204
6.5	Concluding Remarks	207
	Conclusions and Perspectives	209
	A Hill Type Failure Mechanism	215
	B Shield and Drucker Type Failure Mechanism	219
	C 3D Tresca	223

D	3D Cohesionless Mohr-Coulomb	225
E	3D General Mohr-Coulomb	227
F	Modified Tension-Chord Model	229
	List of Symbols	233
	References	245
	Curriculum Vitæ	278

List of Figures

1.1	Traction t_i , and velocity jumps $[v]_i$, for coaxial and non-coaxial non-associated flow rules, [82]. Velocity jump vectors are located at A for coaxial associated and non-coaxial non-associated materials, and along the arc AC for coaxial non-associated materials. The particular case of de Josseling de Jong non-coaxial non-associated flow rule [73, 160] allows for two locations, A and D.	18
1.2	Multi-block failure mechanism.	19
1.3	Shear capacity of one way shear members without transverse reinforcement. Ratio between shear resistance V_R and plastic shear resistance V_{p1} (corresponding to the yielding of the flexural reinforcement and the crushing of concrete) as a function of the shear span ratio α . Depending on the slenderness of the member, shear capacity can be computed with stress fields (SF), modified stress fields (MSF), or critical shear crack theory (CSC). [107].	27
2.1	Failure mechanism for smooth (left) and rough (right) footings on a weightless Mohr-Coulomb soil.	33
2.2	Failure mechanism for smooth (left) and rough (right) footings on a Mohr-Coulomb soil.	36
2.3	Comparison of bearing capacity factor N_γ with respect to interface friction δ/ϕ for surface strip footings on cohesionless soils obtained by Chen [49] and Kumar [180].	52
2.4	Bearing capacity factor N_γ for perfectly rough surface footings on cohesionless soils. The grey region, named Computed values, defines the range of all values derived from a mechanical analysis (except Ritter results), whereas the green domain, named Estimated by curve fitting, defines the region of all analytical formulae derived by curve fitting.	57
2.5	Ratio $R_{N_\gamma} = N_\gamma(\delta/\phi)/N_\gamma(\delta/\phi = 1)$ versus shear strength angle ϕ . The filled areas define the range of values presented, namely those given by [49, 181, 183, 218, 229].	58
2.6	Ratio $R_{p_{f/c}} = \frac{p_f(\delta/\phi)}{c} / \frac{p_f(\delta/\phi=1)}{c}$ versus G according to the Hill and Prandtl type failure mechanisms computed by Chen [49].	63

2.7	Ratio between normalised bearing capacity p_f/c computed with the method of superposition of the exact bearing capacity factors and exact solution based on one consistent failure mechanism.	66
2.8	Exact normalised bearing capacity (points) and fitted model function 1 (grey surface).	69
2.9	Q-Q plot for model function 1.	69
2.10	Exact normalised bearing capacity (points) and fitted model function 2 (grey surface).	70
2.11	Q-Q plot for model function 2.	71
2.12	Upper bound of the bearing capacity factor N'_c for smooth rectangular footings resting on a Tresca material, [348].	77
3.1	Failure mechanism of smooth and rough strip footings resting on a dense and compact soil.	100
3.2	Qualitative contact pressure distribution under isolated surface strip footings. Solid lines represent the distribution at failure, whereas dashed lines correspond to a state prior to collapse.	102
3.3	Relative shear capacity versus shear span ratio. V_R is the shear resistance, V_{pl} denotes the shear force that causes the yielding of the flexural reinforcement and crushing of the concrete, a stands for the shear span, and d is the effective depth (maximum effective depth in a variable depth footing). The design method for each regime is indicated: SF stands for stress fields, MSF stands for modified stress fields, and CSC stands for critical shear crack theory.	103
3.4	Half of a slender footing with flexural reinforcement subjected to centred vertical load and uniform contact pressure. A strut-and-tie model (strut in dashed line and tie in solid line) shows the load transfer mechanisms. The critical shear crack is represented in grey. Adapted from [280].	104
3.5	Elastic-plastic stress field (left column) and k_c -value distribution (right column) at collapse for different contact pressure distributions.	106
3.6	Shear failure criteria based on the critical shear crack theory.	108
3.7	Shear capacity of the critical shear crack V_c over the shear capacity of the critical shear crack for uniform pressure distribution $V_{c,rect}$, according to the closed-form equation (3.15), as a function of the moment-to-shear slenderness ratio $\alpha_{cs,rect} = a_{cs,rect}/d$	110
3.8	Combined failure mechanism for plane strain conditions [281]. Velocity discontinuity lines within the soil are either a circular arc or a logarithmic spiral. The plastic hinge is shown with a grey circle in the middle of the footing.	112
3.9	Allowable stress field for combined failure in plane strain conditions [281].	113

3.10	Upper and lower bounds to the collapse load of a strip footing resting on a Tresca material. The normalised bearing capacity is plotted against the dimensionless resisting moment $\mu = M_R/(cB^2)$. The plateau corresponds to the well-known value $2 + \pi$	114
3.11	Upper and lower bounds to the collapse load of a strip footing resting on a cohesionless Mohr-Coulomb material. Left-hand side: upper bounds; right-hand side: upper and lower bounds. The normalised bearing capacity is plotted against the dimensionless resisting moment $\eta = M_R/(\gamma B^3)$. The values of the general shear failure (plateau) are taken from [218].	115
3.12	Upper and lower bounds to the collapse load of a strip footing resting on a general Mohr-Coulomb material, $\phi = 30^\circ$. First row: upper bounds; second row: black lines denote upper bounds whereas grey lines denote lower bounds.	117
3.13	Combined failure mechanism in three dimensions for a Tresca material.	119
3.14	Upper bounds to the collapse load for perfectly adherent rectangular footings with finite flexural resistance resting on a Tresca half-space.	120
3.15	Combined failure mechanism in three dimensions for a Mohr-Coulomb material.	121
3.16	Upper bounds to the collapse load for perfectly rough ($\delta = \phi$) rectangular footings with finite flexural resistance resting on a cohesionless Mohr-Coulomb half-space.	123
3.17	Upper bounds to the collapse load for perfectly rough ($\delta = \phi$) rectangular footings with finite flexural resistance resting on general Mohr-Coulomb half-spaces.	125
4.1	Schematic view of a typical piled raft configuration and definition of the normalised reference system.	132
4.2	Modification of raft-soil contact pressure (q) upon piles heating.	136
4.3	Zoom of the finite element model for the 5^2 configuration. (Source: [60]).	136
4.4	Raft to pile group displacement ratio R_r , pile group to single isolated pile displacement ratio R_s and raft to single isolated pile displacement ratio R with respect to dimensionless raft thickness t_r/d for the $n_p = 4^2$ configuration; both floating and end-bearing piles; $l/d = 25$; $s/d = 5$; $\nu_s = 0.3$; $X = 0, 1$ and 2 ; and $K = 10^2$ and 10^4	138
4.5	Raft to single isolated pile displacement ratio R with respect to pile normalised stiffness K for all floating pile configurations; $X = 0$; $l/d = 25$ and 50 ; $s/d = 5$; and $\nu_s = 0.3$	139
4.6	Raft to single isolated pile displacement ratio R as a function of the number of piles n_p for both floating and end-bearing piles; $l/d = 25$; $s/d = 5$; $\nu_s = 0.3$; $X = 0, 1$ and 2 ; and $K = 10^2$ and 10^4	141
4.7	Raft to single isolated pile displacement ratio R for floating piles; $n_p = 4^2$, $K = 3000$; $X = 0$; $t_r/d = 1$; $l/d = 10, 25, 50$ and 75 ; $\nu_s = 0.1, 0.3$ and 0.45 ; and $s/d = 3, 5$ and 8	142

4.8	Normalised raft differential displacement $\Delta w_{1;0.5}/\bar{w}_r$ and $\Delta w_{1;0}/\bar{w}_r$ with respect to t_r/d for $n_p = 4^2$; floating and end-bearing piles; $l/d = 25$; $\nu_s = 0.3$; $s/d = 5$; $X = 0, 1$ and 2 ; and $K = 10^2$ and 10^4	143
4.9	Raft uplift along normalised coordinate ξ for two configurations of floating piles, $n_p = 4^2$ (first two rows) and 5^2 (last two rows); $l/d = 25$; $\nu_s = 0.3$; $s/d = 5$; $X = 0, 1$ and 2 ; $K = 10^2$ and 10^4 ; and $t_r/d = 0.25, 0.5, 1, 2$ and 4	145
4.10	Distribution of normalised thermally induced axial stress in a central, external and corner floating pile in the 5^2 configuration; $l/d = 25$; $K = 10^2$; $\nu_s = 0.3$; $s/d = 5$; $X = 0, 1$ and 2 ; and $t_r/d = 0.25, 0.5, 1, 2$ and 4	146
4.11	Maximum normalised thermal stress in a central, external and corner floating pile with respect to normalised pile axial stiffness for the 4^2 configuration; $l/d = 25$; $\nu_s = 0.3$; $s/d = 5$; $X = 0$; $t_r/d = 1$; and $K = 10^2, 3 \cdot 10^3$ and 10^4	147
4.12	Evolution of the maximum normalised thermal stress with respect to the number of piles for a central pile; $\nu_s = 0.3$; $s/d = 5$; $t_r/d = 1$; $l/d = 25$ and 50 ; $K = 10^2$ and 10^4 ; and $X = 0, 1$ and 2	149
4.13	Change in maximum normalised thermal stress with respect to slenderness $l/d = 10, 25, 50$ and 75 ; Poisson's coefficient $\nu_s = 0.1, 0.3$ and 0.45 and spacing ratio $s/d = 3, 5$ and 8 for the 4^2 configuration; $K = 3 \times 10^3$; $t_r/d = 1$; and $X = 0$	150
5.1	Single bars with different boundary conditions: (a) free bar; (b) clamped bar; (c) bar partially restrained by head and base springs; (d) bar partially restrained by head, base, and shaft springs. Nodal displacements are indicated by x and spring stiffness by k	157
5.2	Bars partially restrained by a common rigid cap (second moment of area $I = \infty$) and with different boundary conditions: (a) system of two identical pinned bars; (b) system of n pinned bars; (c) system of n bars resting on base springs; (d) system of n bars partially restrained by base and shaft springs. Nodal displacements are indicated by x and spring stiffness by k	159
5.3	Constitutive models: (a) and (b) stress-strain diagrams for concrete and reinforcement; (c) bond shear-slip relationship.	163
5.4	Simple chord element and stress and strain profiles between two cracks. Adapted from [214].	164
5.5	Axial force versus reinforcement mean strain for a reinforced concrete tie according to the tension chord model. (Graph constructed from properties of Table 5.1).	165
5.6	Three-linear cyclic load-transfer constitutive model: (a) shaft reaction and (b) base reaction with tension cut-off.	166

5.7	Diagrams of strain induced by head force ε_{mec} , thermal imposed strain $\varepsilon_{\text{th,imp}}$, and sum of the two ε_{TOT} ; factor of imposed thermal strain η ; and dimensionless thermal force $N_{\text{th}}/N_{\text{blc}}$ for isolated pile; tension chord model (TC) and linear elastic pile (LE); traction force $F = 0.75N_y$ and then cooling $\Delta T = -22^\circ\text{C}$; both soil 1 and soil 2.	174
5.8	Diagrams of strain induced by head force ε_{mec} , thermal imposed strain $\varepsilon_{\text{th,imp}}$, and sum of the two ε_{TOT} ; factor of imposed thermal strain η ; and dimensionless thermal force $N_{\text{th}}/N_{\text{blc}}$ for isolated pile; tension chord model (TC) and linear elastic pile (LE); traction force $F = 1.1N_y$ and then cooling $\Delta T = -22^\circ\text{C}$; both soil 1 and soil 2.	175
5.9	Scheme of a steel frame with piled raft foundation, view of foundation with piles position, and zoom of piled raft with applied loads.	176
5.10	Diagrams of strain induced by cap force ε_{mec} , thermal imposed strain $\varepsilon_{\text{th,imp}}$, and sum of the two ε_{TOT} of a corner, an external, and the central pile for the piled raft foundation; traction force $F = 0.75N_y n_p$ and then uniform cooling of each pile $\Delta T = -22^\circ\text{C}$; soil 1.	177
5.11	Diagrams of factor of imposed thermal strain η , normalised mechanical force N_{mec}/\bar{F} , and dimensionless thermal force $N_{\text{th}}/N_{\text{blc}}$ of a corner (CO), an external (EX), and the central (IN) pile for the piled raft foundation; traction force $F = 0.75N_y n_p$ and then cooling of each pile $\Delta T = -22^\circ\text{C}$; soil 1.	178
6.1	Normalised axial loads for energy piles that are free at their head and subjected to heating, with a constant applied mechanical load and varying pile length.	195
6.2	Normalised axial loads for energy piles restrained at their head and subjected to heating, with a constant applied mechanical load and varying pile length.	196
6.3	Normalised axial loads for energy piles that are free at their head and subjected to cooling, with a constant applied mechanical load and varying pile length.	198
6.4	Normalised axial loads for energy piles restrained at their head and subjected to cooling, with a constant applied mechanical load and varying pile length.	199
6.5	Normalised axial loads for energy piles that are free at their head and subjected to heating, with a varying applied mechanical load and constant pile length.	200
6.6	Normalised axial loads for energy piles of $L/D = 50$ that are restrained at their head and subjected to heating, with a varying applied mechanical load and constant pile length.	201
6.7	Normalised axial loads for energy piles that are free at their head and subjected to cooling, with a varying applied mechanical load and constant pile length.	202

6.8	Normalised axial loads for energy piles of $L/D = 50$ that are restrained at their head and subjected to cooling, with a varying applied mechanical load and constant pile length.	203
6.9	Relationships between axial cross-sectional load and normalised axial displacement for energy piles made of reinforced concrete.	206
A.1	Kinematics of the Hill type failure mechanism.	218
B.1	Geometry and velocity field of the failure mechanism.	220
F.1	Simple chord element subjected to uniform axial load distribution, bond stress, steel axial stress, and steel axial strain distributions.	230

List of Tables

2.1	Exact bearing capacity factor ($N_c = p_f/c$) for footings on a weightless material, [298].	35
2.2	Bearing capacity factor ($N_\gamma = 2p_f/(\gamma B)$) for smooth footings obtained with the method of stress characteristics.	40
2.3	Bearing capacity factor ($N_\gamma = 2p_f/(\gamma B)$) for smooth footings obtained with the upper bound limit analysis.	42
2.4	Bearing capacity factor ($N_\gamma = 2p_f/(\gamma B)$) for smooth footings obtained with the lower bound limit analysis.	43
2.5	Exact bearing capacity factor ($N_\gamma = 2p_f/(\gamma B)$) for smooth footings, [217].	44
2.6	Bearing capacity factor ($N_\gamma = 2p_f/(\gamma B)$) for perfectly rough footings according to Terzaghi's failure mechanism.	45
2.7	Bearing capacity factor ($N_\gamma = 2p_f/(\gamma B)$) for perfectly rough footings obtained with the limit equilibrium method.	47
2.8	Bearing capacity factor ($N_\gamma = 2p_f/(\gamma B)$) for perfectly rough footings obtained with the method of characteristics.	51
2.9	Bearing capacity factor ($N_\gamma = 2p_f/(\gamma B)$) for perfectly rough footings obtained with the upper bound limit analysis.	55
2.10	Bearing capacity factor ($N_\gamma = 2p_f/(\gamma B)$) for perfectly rough footings obtained with the lower bound limit analysis.	56
2.11	Exact bearing capacity factor ($N_\gamma = 2p_f/(\gamma B)$) for perfectly rough footings, [218].	57
2.12	Normalised bearing capacity (p_f/c) for smooth footings, [169]. The results were read from graphical representation.	59
2.13	Normalised bearing capacity (p_f/c) for smooth footings. (i) [62]; (ii) [370].	60
2.14	Normalised bearing capacity (p_f/c) for smooth footings, [192].	60
2.15	Exact normalised bearing capacity (p_f/c) for smooth footings, [215].	60
2.16	Normalised bearing capacity (p_f/c) for smooth footings, [49].	61
2.17	Normalised bearing capacity (p_f/c) for perfectly rough footings, [192].	62
2.18	Normalised bearing capacity (p_f/c) for perfectly rough footings, [49].	63
2.19	Normalised bearing capacity (p_f/c) for perfectly rough ($\delta = \phi$) footings, [233].	64
2.20	Normalised bearing capacity (p_f/c) for perfectly rough footings, [130, 411].	65
2.21	Exact normalised bearing capacity (p_f/c) for perfectly rough footings, [217].	66

2.22	Chebyshev coefficients c_k for the model function 1.	68
2.23	Coefficients for the model function 2.	70
2.24	Bearing capacity factor ($N_c = p_f/c$) for circular smooth footings on a weightless Mohr-Coulomb material.	74
2.25	Bearing capacity factor ($N'_c = p_f/c$) for perfectly rough circular footings on a weightless Mohr-Coulomb material.	74
2.26	Shape factor ($s_c = N'_c/N_c$) for perfectly rough rectangular footings on a weightless Mohr-Coulomb material, [235].	75
2.27	Shape factor ($s_c = N'_c/N_c$) for perfectly rough rectangular footings on a weightless Mohr-Coulomb material, [412].	76
2.28	Bearing capacity factor ($N'_c = p_f/c$) for perfectly rough rectangular footings computed with the upper bound limit analysis, [235].	79
2.29	Bearing capacity factor ($N'_c = p_f/c$) for perfectly rough rectangular footings (L:lower, U:upper), [334].	79
2.30	Bearing capacity factor ($N'_c = p_f/c$) for perfectly rough rectangular footings (FE: finite element analyses, U: upper bound based on the Prandtl type failure mechanism derived from that of Shield and Drucker [348]), [119].	80
2.31	Bearing capacity factor ($N'_\gamma = 2p_f/(\gamma B)$) for smooth circular footings, and shape factor ($s_\gamma = N'_\gamma/N_\gamma$).	82
2.32	Bearing capacity factor ($N'_\gamma = 2p_f/(\gamma B)$) for perfectly rough circular footings, and shape factor ($s_\gamma = N'_\gamma/N_\gamma$).	84
2.33	Shape factor ($s_\gamma = N'_\gamma/N_\gamma$) for perfectly rough rectangular footings, [235]. It applies to the bearing capacity coefficient ($N_\gamma = 2p_f/(\gamma B)$) given in [233], approximate by (2.25).	85
2.34	Shape factor ($s_\gamma = N'_\gamma/N_\gamma$) for perfectly rough rectangular footings, [412]. It applies to the bearing capacity coefficient $N_\gamma = 2p_f/(\gamma B)$ given in [233], approximate by (2.25).	86
2.35	Shape factor ($s_\gamma = N'_\gamma/N_\gamma$) for perfectly rough rectangular footings, [202]. It applies to the exact bearing capacity coefficient N_γ given in [218], approximate by (2.15).	86
2.36	Normalised bearing capacity (p_f/c) for smooth circular footings [62], and shape factor ($s_{c\gamma}$) computed with respect to the exact solution.	87
2.37	Normalised bearing capacity (p_f/c) for perfectly rough circular footings, [103].	88
2.38	Normalised bearing capacity (p_f/c) for perfectly rough circular footings, [215], and shape factor ($s_{c\gamma}$) computed with respect to the exact solution for strip footings.	88
2.39	Normalised bearing capacity (p_f/c) for perfectly rough rectangular footings ($B/L = 0.5$), [235].	89
3.1	Expressions for the computation of $a_{cs} = M_{Ed}/V_{Ed}$. The value of ξ_{cs} is equal to $b/2 + d/2$ for the hyperbolic criterion and to d for the power law.	109

4.1	Material properties used in the finite element model. The word <i>variable</i> refers to those parameters that were varied to obtain specific values for the parametric analysis (see section 4.2.1).	133
5.1	Mechanical properties of concrete and reinforcement.	168
6.1	Material properties used for the analyses in this study.	184
6.2	Normalised vertical head displacements for energy piles of $D = 0.5$ m that are free at their head and subjected to cooling, with a constant applied mechanical load and varying pile length.	191
6.3	Normalised vertical head displacements for energy piles of $D = 1$ m that are free at their head and subjected to cooling, with a constant applied mechanical load and varying pile length.	191
6.4	Normalised vertical head displacements for energy piles of $D = 0.5$ m that are free at their head and subjected to cooling, with a varying applied mechanical load and constant pile length.	192
6.5	Normalised vertical head displacements for energy piles of $D = 1$ m that are free at their head and subjected to cooling, with a varying applied mechanical load and constant pile length.	192

What is new is the inter-relation of concepts, the capacity to create new types of calculation, and the unification of the bases for judgement.

Andrew N. Schofield and Charles P. Wroth,
Critical State Soil Mechanics

Introduction

Problem Statement

The analysis of soil-structure interacting systems dates back to the birth of soil mechanics itself, attributable to the early studies on fortifications carried out by French engineers in the 19th and 20th centuries [11, 61, 261, 283]. Since then, the behaviour of foundations has been the object of extensive theoretical and experimental research.

Conventional foundations play the role of structural support, reducing high concentrated stresses coming from the superstructure to admissible levels for the soil. Recently, the role of ground heat exchanger has been incorporated into foundation elements, leading to an innovative and environmentally friendly technology known as *energy foundations* or *thermoactive foundations*.

In this thesis, the behaviour of conventional surface footings and thermoactive deep foundations is considered. The former is the subject of the first part, whereas the latter of the second part. The *fil rouge* which links the two parts is the attempt to integrate the knowledge coming from the soil and structural mechanics under a unified framework, in order to investigate soil-structure interactions in a more rational, and possibly realistic, way.

The first part of the thesis is dedicated the limit state analysis of isolated surface footings subjected to centred and vertical load. The failure mechanism of a rigid footing resting on a dense soil is known as *general shear failure* [384] and is analogous to the indentation of a flat rigid punch or die into a mild-steel solid [134, 298]. Most of the available research on the bearing capacity of soils is based on the aforementioned hypothesis of rigid foundation [25, 49, 71, 118, 217, 232, 359, 384, 396]. Actual footings are reinforced concrete members without transverse reinforcement, and the governing failure modes are generally identified with the help of the Kani's diagram [163]. The latter is a function of the geometry of the structure and the boundary conditions [41, 252, 280, 409]. Therefore, it can be stated that the actual performance of footings is affected by

soil-structure interaction. Despite this fact, little effort has been made to quantify its significance [72, 281], or to develop a simplified yet consistent methodology to address similar problems.

The second part of the dissertation focuses on the thermo-mechanical behaviour of energy piles. The coupled role of structural support and geothermal heat exchanger led the design of piles to unprecedented challenges with respect to thermal loads [22, 187, 222, 315, 335]. Experimental research investigated the response of single energy piles [17, 18, 21, 168, 188, 189, 248, 377, 399, 402] and small groups of energy piles [81, 238, 322], and highlighted that measurable thermally induced mechanical effects are present. Subsequent theoretical research focused on the numerical reproduction of the measured data [81, 168, 190, 273, 317, 322, 379], and the extension of simplified analysis tools for conventional piles to address thermal loads [5, 154, 320, 321, 325]. A key aspect in the design is the structural effect of thermal loads. The available knowledge, and the resulting official design guidelines [46, 124, 350], do not adequately consider the displacement-based nature of such a load and the reinforced concrete ductility capacity. This led to the apparent inconsistency with respect to the design of reinforced concrete structural elements which undergo seasonal temperature variations of the same magnitude, for which in general only serviceability limit states are concerned. The impossibility to carry out full-scale parametric analyses, and the practical difficulties in performing laboratory testing limit the ability to define general trends. Therefore, the conceptual design process is somehow restricted by such a lack of theoretical knowledge. In this regard, the effect of a flexible raft cast directly on the ground on the overall behaviour of energy foundations was not investigated before, except for the two extreme cases of perfectly flexible and rigid cap.

Structure of the Thesis and Scientific Contributions

This doctoral dissertation is a compilation of two state-of-the-art chapters written in the form of journal articles, a submitted article, and three published articles. The document is completed by a general introduction and conclusion. It has not been found practical to maintain neither a uniform notation, nor a uniform sign convention throughout the thesis owing to the difference between soil and structural mechanics. The symbols used are clearly stated for each chapter and summarised at the end of the document (page 233).

Chapter 1 In order to investigate soil-structure interactions in surface footings at the ultimate limit state, this chapter presents a state-of-the-art of limit theorems ac-

cording to the theory of plasticity. First, the basic principles for the uniqueness of the solution are briefly discussed. Then, theorems for associated coaxial, non-associated coaxial and non-coaxial materials are introduced. Attention is devoted to the limit theorems for frictional interfaces and the assumption of perfect plasticity. Finally, the applicability to real soils and structures is critically examined.

Chapter 2 An attempt is made to categorise the available knowledge about the bearing capacity of rigid surface footings under centred and vertical load. The results are examined with the help of the limit theorems and discussed with respect to experimental data. Two new analytical expressions for the computation of the bearing capacity of rigid and perfectly rough surface footings resting on general soils are presented.

Chapter 3 In this chapter, corresponding to a journal article submitted for the special issue of Computers and Geotechnics dedicated to the memory of Prof. Gyan N. Pande, the knowledge gained in the first two chapters is exploited to address the first objective of the thesis. The foundation collapse load is evaluated considering simultaneously the soil bearing capacity and the structural governing failure modes.

Chapter 4 This chapter corresponds to the published journal article [114]. In order to assess the effect of a flexible raft cast directly on the ground and to draw general trends with respect to the number of energy piles, an extensive parametric numerical analysis, as often done previously to study conventional piled rafts [30, 54, 55, 59, 68, 74, 186, 193, 210, 272, 284, 308, 326, 382], was carried out. The results are presented graphically through dimensionless parameters.

Chapter 5 This chapter presents the published journal article [113], which addresses the last objective of the thesis. The first part introduces simple expressions and a few closed-form solutions which may be used to define bounds of possible thermally induced axial stresses. The second part investigates the performance of energy piles subjected to traction forces considering reinforced concrete post-cracking behaviour. For this purpose, a new finite element code was developed.

Chapter 6 This chapter, corresponding to the published journal article [316], proposes a performance-based design approach for energy piles. The outcomes of chapters 4 and 5, and those of the first two authors of the paper, are integrated in a single framework to provide useful design guidelines.

Part I

Surface Footings

*Essentially, all models are wrong, but some are useful.
However, the approximate nature of the model must
always be borne in mind.*

George E. P. Box, Empirical Model-Building and
Response Surfaces

1

Limit State Analysis: State-of-the-Art

GEOTECHNICAL PROBLEMS CAN be grouped under two categories: (i) serviceability limit state and (ii) ultimate limit state. The former deals with functionality, comfort and aspect, whereas the latter is concerned with safety. The theory of limit analysis addresses the direct determination of the collapse load, thereby assessing the degree of safety of an engineering application, without carrying out a step-by-step analysis. Despite several scientific contributions and surveys on the subject exist, soil masses and structures are usually treated separately. However, geotechnical applications are often concerned with problems of soil-structure interaction. In this contribution, the limit theorems of limit analysis are reviewed. Key aspects for soils, reinforced concrete members and interfaces are discussed. The suitability of limit analysis for soil-structure interaction problems is investigated. Finally, it is shown that extended limit theorems can be efficiently applied to get useful bounds to the actual collapse load of any soil-structure interacting system.

1.1 Introduction

In continuum mechanics, the mechanical state of solids is defined by elastic-plastic stress-strain relationships. The first part describes the reversible behaviour, whereas the second

part describes the irreversible behaviour.

Despite the theory of plasticity has its roots in the mechanics of soils [61, 304], the fundamental principles and first achievements were made in the mechanics of metals [134, 135, 147, 195, 240, 241, 297, 309, 328, 387]. Early attempts to transfer this knowledge to soil mechanics are due to Drucker, Prager, Shield and Jenike [86, 97, 159, 342, 343, 346]. The actual relevance of key features used for metals such as normality and perfect plasticity were critically reviewed by a number of authors [84, 87, 95, 136–138]. The critical state concept [313, 338] acted as a further input in the development of elastic-plastic theories for soils. To Drucker [88] and Chen [48] is due the first application of the theory of plasticity to reinforced concrete and concrete blocks, respectively.

When plastic strains spread over a sufficient region, a slight increase in the applied load is generally sufficient to produce plastic strains of a magnitude which would, in an actual structure, be regarded as amounting to *collapse* [146]. Such a mechanical state is termed *state of impending collapse*, or simply *limit state*. According to this definition, the load carrying capacity is the extreme loading that a body, or assemblage of bodies, can sustain without ceasing to be useful for the purpose for which it was conceived [96]. The corresponding load is termed *limit load*, *collapse load*, or *failure load*. *Limit analysis* is the branch of the theory of plasticity which deals with the determination of the *ultimate limit state* of solids.

Geotechnical limit state analysis was developed long before the theory of plasticity, mainly to solve lateral earth thrust problems [11, 36, 61, 283, 304, 306, 307]. It was then extended in a general fashion by Terzaghi [384]. Valuable contributions were given, among others, by [39, 49, 52, 86, 87, 97, 230, 232, 332, 366, 367]. A survey of geotechnical limit state design may be found in [227].

In structural engineering, limit state analysis and design was first introduced by Kazinczy [166] and Kist [167]. Developments in this field were made by a number of authors [4, 88, 90, 91, 96, 98, 125, 146, 147, 279, 291, 294, 310, 380, 390, 391].

In the subsequent decades, much effort has been put into laboratory testing, generalisation of stress-strain relationships [76, 194, 339], and the development of computational techniques [413].

Owing to the widespread of publications, a number of surveys has been proposed over the years in order to collect the fundamental principles and achievements. Among others, some key overviews focusing on metal plasticity may be found in [27, 51, 93, 117, 147, 162, 209, 219, 260, 290, 293, 295]; others concerned with geomaterials may be get from [49, 52, 53, 65, 339, 358, 407]; whereas those interested in structural concrete may be read in [44, 50, 106, 213, 253, 257, 266]. Despite this great effort, for engineers dealing

with soil-structure interaction problems, the key aspects remain separate. This might make hard the first contact with the theory of limit analysis, especially if a knowledge of the underlying assumptions is required. This paper aims at giving a concise survey on the fundamentals of the theory of plasticity, its extension to soils and structural concrete, and a few hints for problems of soil-structure interaction.

In the following, the Einstein summation convention is adopted and compression is taken as positive.

1.2 Stress-Strain Relationships

Elastic-plastic theories can be grouped under two categories [147, 290]: (i) total strain theories and (ii) incremental strain theories. Equations pertaining to the former were first developed by Nadai [259] and Hencky [135], who assumed that the total plastic strain is proportional to the deviatoric stress components. In general, these equations do not satisfy the continuity condition between elastic and plastic stress-strain equations [131], and can lead to a modification of plastic strains during unloading [147]. Therefore, they are not suited for a consistent mathematical description of elastic-plastic materials. On the other hand, incremental strain theories relate the increment of plastic strain (or strain rate) to the stress components. This great insight is due to de Saint-Venant [328], who associated the principal axes of the plastic strain increment (and not the total strain) to the principal axes of stresses. This coincidence is known as *coaxiality*.

Assuming purely incompressible plastic flow, the equations were developed for the Tresca yield criterion [387] and plane strains by de Saint-Venant [328], and for the general case by Lévy [195]. Later, they were reformulated by Mises [240] for the homonymous yield condition. The Saint-Venant-Lévy-Mises equations, which describe the behaviour of a rigid-perfectly plastic solid, may be expressed in the form

$$\begin{cases} \dot{\epsilon}_{ij} = \dot{\epsilon}_{ij}^p = \dot{\lambda} s_{ij} & \text{if } f(s_{ij}) = 0 \\ \dot{\epsilon}_{ij} = 0 & \text{if } f(s_{ij}) < 0 \end{cases} \quad (1.1)$$

where $\dot{\epsilon}_{ij}$ is the strain rate tensor, superscript p stands for plastic, $\dot{\lambda}$ is the plastic multiplier, s_{ij} is the deviation of the Cauchy's stress tensor σ_{ij} ($s_{ij} = \sigma_{ij} - \frac{1}{3}\sigma_{ij}\delta_{ij}$, with δ_{ij} denoting the Kronecker delta), and f is the yield function.

The first elastic-plastic constitutive law as we understand it today is probably the Prandtl-Reuss theory [297, 309], which was described by Truesdell as follows [388]

The Prandtl-Reuss theory may be described as postulating that in an incompressible

body subject to infinitesimal strain the stress is the sum of that given by the classical linear elasticity plus that given by the classical theory of viscous fluids, except that the viscosity instead of being a material constant is a certain function of the stress deviator—the nature of this function being specified by the yield condition, which for an isotropic material is a single scalar equation connecting the stress invariants.

Prandtl-Reuss equations write

$$\begin{cases} \dot{\varepsilon}_{ij} = \dot{\varepsilon}_{ij}^e + \dot{\varepsilon}_{ij}^p = \frac{1+\nu}{E} \dot{\sigma}_{ij} - \frac{\nu}{E} \dot{\sigma}_{ij} \delta_{ij} + \dot{\lambda} s_{ij} & \text{if } f(s_{ij}) = 0 \\ \dot{\varepsilon}_{ij} = \dot{\varepsilon}_{ij}^e = \frac{1+\nu}{E} \dot{\sigma}_{ij} - \frac{\nu}{E} \dot{\sigma}_{ij} \delta_{ij} & \text{if } f(s_{ij}) < 0 \end{cases} \quad (1.2)$$

where superscript e stands for elastic, $\dot{\sigma}_{ij}$ denotes the Cauchy's stress rate tensor, and E and ν are the Young's modulus and Poisson's coefficient, respectively. Given that these theories were developed in the context of metal plasticity, the adoption of a plastic strain rate parallel to the deviatoric stress is a straightforward consequence of the incompressibility condition and the invariance of the yield stress in shear upon confinement.

Mises [241] introduced the concept of *plastic potential* and suggested the following mathematical expression

$$\dot{\varepsilon}_{ij}^p = \dot{\lambda} \frac{\partial f(\sigma_{ij})}{\partial \sigma_{ij}} \quad (1.3)$$

According to (1.3), for any smooth yield surface the direction of $\dot{\varepsilon}_{ij}$ is uniquely defined by the stress state σ_{ij} and is normal to the yield surface. Mises flow rule is also known as *normality condition* or *associated flow rule*. On the other hand, if the yield function has vertices, the orientation of $\dot{\varepsilon}_{ij}$ at these locations is not defined and lies inside a cone constructed from the normals on each side of singularity [83, 86]. Koiter [172] and Prager [292] proposed a general form of the Mises flow rule for non-smooth yield surfaces. This law is a linear combination of the Mises flow rule for each function describing the load surface:

$$\dot{\varepsilon}_{ij} = \dot{\lambda}_k \frac{\partial f_k(\sigma_{ij})}{\partial \sigma_{ij}} \quad (1.4)$$

The aforementioned concepts constitute the basis of the theory of plasticity for associated coaxial materials, upon which the theorems of the limit analysis are founded.

1.2.1 Common Yield Surfaces for Engineering Applications

Two pressure independent and two pressure dependent yield criteria are generally employed in engineering applications. The former are the Tresca [387] and the Mises [240]

yield surfaces, whereas the latter are the Mohr-Coulomb (Coulomb law of friction [61] defined in the Mohr stress space [242]) and the Drucker-Prager [97] yield surfaces.

A generalised Mohr-Coulomb law may be written as [384]:

$$f = \sigma_I - \sigma_{III} - (\sigma_I + \sigma_{III}) \sin \phi - 2c \cos \phi = 0 \quad (1.5)$$

where c is the apparent cohesion, ϕ is the shear strength angle, and σ_I and σ_{III} are the major principal and minor principal normal stresses, respectively. The Drucker-Prager yield criterion writes

$$f = \alpha I_1 + \sqrt{J_2} - k = 0 \quad (1.6)$$

where α and k are positive material parameters, I_1 is the first invariant of the stress tensor:

$$I_1 = \frac{1}{3} \sigma_{ii},$$

and J_2 denotes the second invariant of the stress deviation:

$$J_2 = \frac{1}{2} s_{ij} s_{ij}$$

Note that the Mohr-Coulomb law reduces to the Tresca maximum shear stress criterion when $\phi = 0$, whereas the Drucker-Prager load function becomes equal to the Mises yield condition for $\alpha = 0$. In the three-dimensional space of principal stresses, Tresca yield surface is a right regular hexagon cylinder, Mises yield surface is a right circular cylinder, Mohr-Coulomb yield function is a right hexagon cone with apex in the tensile octant [343], and Drucker-Prager yield criterion is represented by a right circular cone with apex in the tensile octant. Each surface has its axis equally inclined to the coordinate axes.

1.2.2 Irreversibility Condition

The irreversibility condition is the direct consequence of the permanent character of plastic strains. It states that work done in producing plastic deformations cannot be regained [150, 293]. This means that the work of the stresses on the change of plastic strains is positive whenever a change of plastic strains occurs (zero only if $\dot{\varepsilon}_{ij}^p = 0$)

$$\sigma_{ij} \dot{\varepsilon}_{ij}^p \geq 0 \quad (1.7)$$

For a work-hardening or perfectly plastic material, if the yield surface is *convex*, associativity ensures the respect of this principle. Convexity is also a sufficient condition to avoid absurd transitions from loading to unloading processes, and vice versa [150].

1.2.3 Principle of Maximum Plastic Work

This principle was stated by Mises [241] as a variational principle, and Hill [141] demonstrated that it corresponds to a maximum. The principle is based on the assumption of Mises flow rule (normality condition), convexity of the yield surface, and negligible elastic strain rates. It states that among all admissible stress states σ_{ij}^* (which lie within or on the yield surface), the actual state σ_{ij} (the one on the yield surface producing plastic strains) maximises the plastic work done in a given plastic strain increment. Mathematically it writes

$$(\sigma_{ij} - \sigma_{ij}^*) \dot{\epsilon}_{ij}^p \geq 0 \quad (1.8)$$

Other than to rigid-plastic materials, at the instant of impending plastic flow this principle applies equally to elastic-perfectly plastic materials. This because any strain increment from that state is plastic only [96, 98].

1.2.4 Drucker's Stability Postulate

Drucker's stability postulate was advanced in order to derive normality and convexity for elastic-plastic materials from a more fundamental perspective [83, 92]. The postulate may be stated as follows [407]

Consider an element initially in some state of stress, to which by an external agency an additional set of stresses is slowly applied and slowly removed. Then, during the application of the added stresses and in a cycle of application and removal of the added stresses, the work done by the external agency is non-negative, zero only when purely elastic changes take place.

The postulate leads to the following relations

$$\begin{aligned} (\sigma_{ij} - \sigma_{ij}^*) \dot{\epsilon}_{ij}^p &\geq 0 \\ \dot{\sigma}_{ij} \dot{\epsilon}_{ij}^p &\geq 0 \end{aligned} \quad (1.9)$$

It is noteworthy that Drucker's stability postulate includes both the irreversibility condition and the principle of maximum plastic work. Convexity of the yield function and

normality are shown to be sufficient conditions to satisfy Drucker's postulate. (Bodies showing negative hardening, i.e. softening, are *unstable* in Drucker's sense.)

1.2.5 Uniqueness of Solution

The following concepts are all based either on the principle of maximum plastic work or on the Drucker's stability postulate. Therefore, convexity of the yield surface and normality are sufficient conditions for their validity.

Melan [224] and Greenberg [121] demonstrated that when an elastic-perfectly plastic material is subjected to known rates of body forces, surface tractions and velocities, the solution of stress rates is unique. Melan [225] and Prager [293] extended this theorem to work-hardening elastic plastic materials. The generalisation to singular yield surfaces is due to Koiter [172], both for work-hardening and perfectly plastic materials.

Strain rates are uniquely defined by stress rates in work-hardening materials. This conclusion may not be drawn for perfectly plastic solids, given that plastic strains can occur under constant stresses. However, the instantaneous mode of deformation may be defined by regarding the perfectly plastic material as a limiting case of a work-hardening material [142, 171].

The uniqueness of stress rates and strain rates ensures that a step-by-step analysis converges toward a unique solution. However, the aim of the limit analysis is precisely to avoid such a computation. Such a goal can be achieved by assuming a monotonic and proportional loading. Suppose that the system of load at collapse is defined by a unique *load multiplier* q . This means that for a given set of applied forces Q , the load configuration at collapse is given by

$$Q_c = Q_{\text{fix}} \cup qQ_{\text{var}} \quad (1.10)$$

where $Q_{\text{fix}} \subset Q$ is the subset of forces that are kept constant, whereas $Q_{\text{var}} = Q - Q_{\text{fix}}$ is the subset of forces that are increased until the limit state. Evidently $Q_{\text{fix}} \cap Q_{\text{var}} = \emptyset$.

A theorem due to Hill [146] states that in a rigid-plastic (perfectly plastic or strain-hardening) material, the state of stress is uniquely defined in a certain part of the plastic region under given boundary conditions. This zone constitutes either part of the plastic region or the entire plastic region and covers the whole material that can deform under the given boundary conditions. However, the instantaneous mode of deformation in the zone may not be uniquely defined. Hill [142] indicated that, when more than one mode is compatible with the boundary conditions, the physically possible mode is singled out by the compatibility between the stress rate distribution and the rate of hardening with the

given surface tractions rate (a limiting process is required in case of perfect plasticity). A method for isolating the domain which is occupied by the complete set of deformation modes was suggested by Bishop [13]. This remarkable achievement is of interest also for elastic-perfectly plastic materials, because when the loads are increased monotonically, they approach asymptotically the plastic-rigid yield point loads [146]. This meets exactly the domain of validity of the limit analysis defined by the unique load multiplier.

Note that problems of plane strain and axial symmetry are of particular interest because, as pointed out by Prager [293] and Hill [146], the fully plastic stress distribution is *statically determinate* if the boundary conditions involve only stresses and not displacements.

A more comprehensive discussion on uniqueness may be found in [89, 140, 142–145, 245]. In the following, convexity of the yield surface is implicitly assumed.

1.3 Limit Analysis for Associated Coaxial Materials

The theory of limit analysis aims at establishing rigorous techniques for bounding the limit load. Theorems for this purpose were derived by Hill [146] for work-hardening rigid-plastic and rigid-perfectly plastic associated materials, and by Drucker et al. for Prandtl-Reuss materials [96] and general elastic-perfectly plastic associated materials [98]. Hill defined as limit the load intensity at which deformation first occurs, whereas Drucker et al. defined it as the intensity at which deformation could first take place under constant load, state termed *incipient plastic flow*. Bounds for the limit load can be obtained through the following theorems:

Theorem 1 (Lower bound). *If a safe statically admissible state of stress, i.e. satisfying the equilibrium equations and stress boundary conditions and which nowhere violates the yield criterion, can be found at each stage of loading, collapse will not occur under the given loading schedule.*

Theorem 2 (Upper bound). *Collapse must occur if for any compatible flow pattern, considered as plastic only, the rate at which the external forces do work on the body equals or exceeds the rate of internal dissipation.*

Theorem 2 can be expressed mathematically as

$$\int_S t_i v_i \, dS + \int_V \gamma_i v_i \, dV \geq \int_V \sigma_{ij} \dot{\epsilon}_{ij}^p \, dV + \int_{[S]} t_i [v]_i \, d[S] \quad (1.11)$$

where the left hand side represents the rate of external work of surface tractions t_i over velocities v_i at boundary S , and body forces γ_i over velocities v_i in region V . The right hand side denotes the rate of work done by the stresses σ_{ij} over plastic strain rates $\dot{\epsilon}_{ij}^p$ and dissipated in region V , and tractions t_i over velocity jumps $[v]_i$ along the velocity discontinuity surface $[S]$. When the rate at which external forces do work equals the rate of internal dissipation, (1.11) is often termed *energy balance equation*. From theorems 1 and 2, the next corollary follows

Corollary 1 (Complete solution). *A statically admissible state of stress, together with one or more kinematically admissible modes of deformation, corresponds to the actual limit load (under the given assumptions). In fact, if Q_l and Q_u are lower and upper bounds, respectively, the exact collapse load Q_c satisfies*

$$Q_l \leq Q_c \leq Q_u$$

A fundamental assumption lies behind theorems 1 and 2, namely that geometry changes on equilibrium conditions are disregarded (small displacements and strains). Actually, the hypothesis of small deformations does not preclude the application of the limit analysis method to situations where equilibrium conditions are modified, provided that they are taken into account, i.e. the limit analysis theorems are applied on the modified geometry. Of course, each result pertains to a given configuration. This approach was suggested by Onat and Haythornthwaite [270], who satisfactorily applied the limit analysis method to a simple supported plate subjected to finite deflections considering membrane forces.

Proofs of the lower and upper bound theorems require normality and elastic strain rates to be zero. In a rigid-plastic material, the strain rates are evidently fully plastic. For an elastic-ideally plastic material, Drucker et al. [96, 98] showed that once the surface tractions have reached the intensity necessary for impending plastic flow, the incipient plastic flow takes place under constant stresses (due to the first hypothesis of small deformations, because generally stresses do not remain constant under finite strains, even if the hardening is zero). Under these circumstances, the elastic strain rates vanish.

The interpretation based on a linear elastic-perfectly plastic material is often preferred for its physical meaning. However, a rigid-plastic material is commonly assumed, because it simplifies the construction of admissible stress fields and failure mechanisms. The method of Bishop [12] for constructing a fully plastic stress field into the rigid region, and the method of Cox et al. [63] for constructing a stress field which is not fully plastic into

the rigid region (developed for weightless materials and extended to ponderable solids by Martin [217] and Smith [364]) are common techniques employed in soil mechanics problems. Owing to the fact that real materials exhibit at least a small elastic range, it might seem necessary to assume perfect plasticity. Nevertheless, such an assumption in soil mechanics could be as rude as imposing an indefinitely large elastic stiffness. Therefore, no matter which interpretation is preferred, the relevant condition for a reliable application of the limit analysis method is that, at the instant of incipient collapse, the elastic strain rates must be negligible compared to the plastic strain rates.

It is noteworthy that stress or velocity discontinuities are permissible and are generally convenient for computational purposes [97].

Interestingly, as remarked by Koiter [171] and Radenkovic [300], the postulate of maximum plastic work is a sufficient condition, but not necessary, for the proofs of the lower and upper bound theorems. Nevertheless, without further considerations, the limit theorems are strictly applicable only to coaxial materials with an associated flow rule.

1.4 Limit Analysis for Non-Associated Materials

1.4.1 Non-Associated Coaxial Materials

The first limit theorems for materials with non-associated flow rule are due to Radenkovic [299, 300]:

Theorem 3 (Lower bound for non-associated coaxial materials). *If there exists an equilibrium stress distribution σ_{ij} which satisfies the stress boundary conditions and is such that throughout the body $g(\sigma_{ij}) \leq 0$, where g is a convex function satisfying the normality condition and completely inscribed into the yield surface $f(\sigma_{ij}) = 0$, then the body will not collapse.**

Theorem 3 is actually an application of theorem 1 to the problem under consideration, but where the non-associated material has been replaced by a fictitious weaker material with associated flow rule. If the weaker material will not collapse, condition ensured by theorem 1, the stronger material will not collapse as well.

Theorem 4 (Upper bound for non-associated coaxial materials). *Assume two identical bodies made of two materials characterised by the same yield criterion. Assume also that one material follows an associated flow rule, whereas the other not. Then, the actual limit*

*This formulation is due to Palmer [276], who gave the same lower bound theorem as Radenkovic, probably independently, a few years later.

load for the associated material cannot be lower than the actual limit load for the non-associated material. It follows that an upper bound solution for the associated material is also an upper bound for the non-associated material.

Theorem 4 is also an application of theorem 1. Assume that the actual limit load for a non-associated material is known. Its corresponding state of stress will be admissible for an associated material with the same yield condition. Given that limit theorems have been proven true for associated materials, theorem 1 implies that this load is a lower bound to the collapse load for the material satisfying the normality condition. Hence, the collapse load of a non-associated material cannot be higher than the collapse load of the equivalent associated material. The other way around does not hold, because theorem 1 does not apply to non-associated flow rules. Moreover, this would lead to the conclusion that the flow rule would have no effect on the value of the limit load in any problem, which is obviously not the case. The same theorems were discussed also by Sacchi and Save [327] in a more general manner. It is clear that with theorems 3 and 4, the true limit load cannot be reached by a procedure of subsequent approximations, which would appear justified by the fact that uniqueness is not ensured. Nevertheless, these theorems allow to bracket the collapse load between two fixed bounds.

Further insight on the influence of non-associativity is due to Davis [65]. In a non-associated coaxial material obeying to the Mohr-Coulomb yield criterion, the unit rate of plastic work \dot{D}_V in a continuous deforming region V , is given by

$$\dot{D}_V = (\dot{\epsilon}_1 - \dot{\epsilon}_3) \left[\frac{\sigma_1 + \sigma_3}{2} (\sin \phi - \sin \psi) + c \cos \phi \right] \quad (1.12)$$

where $\dot{\epsilon}_1$, $\dot{\epsilon}_3$, σ_1 , and σ_3 are principal strain rates and stresses. It is found that in a statically determinate plane strain or axially symmetry problem, the velocity characteristics do not coincide with the stress characteristics. This implies that the state of stress at velocity discontinuities is given by a point in the Mohr's diagram which lies on the largest circle tangent to the Mohr-Coulomb line, $\tau = c + \sigma_n \tan \phi$, but not on the latter. Nevertheless, the shear stress τ^* and the normal stress σ_n^* acting at velocity discontinuity lines are related by the following similar relation (see also Figure 1.1)

$$\tau^* = c^* + \sigma_n^* \tan \phi^* \quad (1.13)$$

where

$$c^* = \eta c \quad (1.14a)$$

$$\tan \phi^* = \eta \tan \phi \quad (1.14b)$$

$$\eta = \frac{\cos \phi \cos \psi}{1 - \sin \phi \sin \psi} \quad (1.14c)$$

The rate of plastic work per unit length on a velocity discontinuity line, \dot{D}_L , is

$$\begin{aligned} \dot{D}_L &= [v]_t (\tau^* - \sigma_n^* \tan \psi) \\ &= [v]_t [c^* + \sigma_n^* (\tan \phi^* - \tan \psi)] \\ &= \frac{[v]_t}{1 - \sin \phi \sin \psi} \left[c \cos \phi \cos \psi + \frac{\sigma_n^*}{\cos \psi} (\sin \phi - \sin \psi) \right] \end{aligned} \quad (1.15)$$

where $[v]_t$ is the tangential velocity jump across the discontinuity. By means of equations (1.12) and (1.15), Davis pointed out that the rate of plastic work is independent on the stress distribution only when $\psi = \phi$ (in this case $c^* = c$ and $\phi^* = \phi$). Therefore, it would seem that the limit theorems 1 and 2 are not applicable when $\psi < \phi^\dagger$.

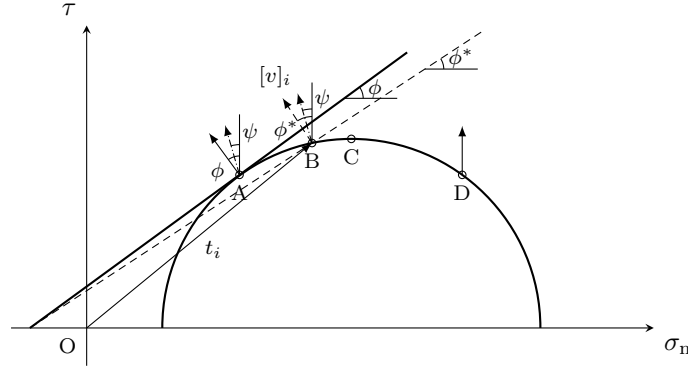


Figure 1.1 – Tractions t_i , and velocity jumps $[v]_i$, for coaxial and non-coaxial non-associated flow rules, [82]. Velocity jump vectors are located at A for coaxial associated and non-coaxial non-associated materials, and along the arc AC for coaxial non-associated materials. The particular case of de Josseling de Jong non-coaxial non-associated flow rule [73, 160] allows for two locations, A and D.

In the particular case of *translational failure mechanisms* (Figure 1.2), upper bound theorems for non-associated materials were given by Drescher and Detournay [82], both

[†]The case $\psi > \phi$ is unrealistic and can be disregarded [65].

for coaxial and non-coaxial behaviour. A translational failure mechanism is a rupture figure made of rigid bodies delimited by straight lines of constant velocity discontinuity. In such a situation, internal energy dissipation occurs only along these lines. On the latter, the state of stress is given by (1.13). Owing to the fact that a multi-block failure mechanism can be regarded as an assemblage of rigid bodies of infinite strength surrounded by plastic layers, and that plastic flow can occur only when (1.13) is satisfied on the latter, one may choose a fictitious dilatancy angle $\psi = \phi^*$ in the energy balance equation, so that the rate of internal work is independent of the state of stress. Because the plastic material is now associated, the energy balance equation can be used to obtain an upper bound to the collapse load. The fact that it constitutes an upper bound to the actual dilating behaviour is ensured by theorem 4 and the fact that $\psi < \phi^*$. The following upper bound theorem was formulated by Drescher and Detournay:

Theorem 5 (Upper bound for non-associated coaxial materials). *An upper bound to the actual collapse load of a non-associated coaxial material can be obtained from a translational failure mechanism and the energy balance equation, provided that the rate of internal work and the velocity field are taken as for the flow rule associated to the “modified” yield condition $f^*(\sigma_{ij})$. However, the failure mechanism must be admissible (also) for the non-associated flow rule; this is satisfied if the mechanism is statically determinate.*

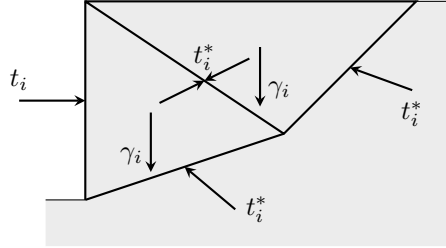


Figure 1.2 – Multi-block failure mechanism.

It is noteworthy that in statically determinate systems, and in absence of inertia forces, the principle of virtual velocities expresses static equilibrium, and that the energy balance equation is an application of such a principle. Therefore, the collapse load computed through the energy balance equation and through the equilibrium of forces must be the same, provided that the inclination of forces is derived from the relation between τ^* and σ_n^* at the velocity discontinuity lines. It follows from the above that the collapse load obtained with the limit equilibrium method and a multi-block rupture figure is a rigorous upper bound.

Given that the equilibrium of forces is made at the blocks level, it is not known whether the state of stress is admissible or not. It is important to note that it is not possible to use theorem 3 by selecting $g(\sigma_{ij}) = f^*(\sigma_{ij})$, because $g(\sigma_{ij})$ must satisfy the normality condition with respect to the *actual* plastic strain increment, which is evidently not the case because $\phi^* \neq \psi$. To see this, it suffices to consider the case of plastic distortion at constant volume, i.e. $\psi = 0$. In the Mohr's diagram $g(\sigma_{ij})$ must be a horizontal line, but (1.14) gives $\tan \phi^* = \sin \phi$, which is not horizontal, except for the trivial case $\phi = 0$.

It is noteworthy to consider the implications of the determination of soil shear strength properties in relation to the conventional shear box [65]. The imposed plane of failure must, for most of its surface, be a velocity discontinuity. Hence, the cohesion and shear strength angle obtained from the conventional interpretation of the test are c^* and ϕ^* .

1.4.2 Non-Associated Non-Coaxial Materials

Based on translational failure mechanisms, Drescher and Detournay [82] derived the following theorem:

Theorem 6 (Upper bound for non-associated non-coaxial materials). *For flow rules and non-coaxiality that lead to a velocity jump located on the Mohr-Coulomb line (point A in Figure 1.1), the dilatancy angle ψ has no effect on the limit load determined from a translational failure mechanism. Indeed, the angle ψ affects only the hodograph; the yield condition that governs the equilibrium of forces remains the same.*

Theorem 6 states that for any value of $\psi \in [0; \phi]$, the upper bound computed for a given geometry of the failure mechanism is the same. This is due to the fact that the state of stress at velocity discontinuities is always given by the Mohr-Coulomb line, $\tau = c + \sigma_n \tan \phi$. If the dilatancy angle has no effect, theorem 1 and corollary 1 are applicable and the solution is unique, because the limit load is the same as for $\psi = \phi$.

It is interesting to note that some continuous deforming zones, as radial shear regions, can be regarded as an infinite number of rigid blocks [49]. This makes the outcomes of Drescher and Detournay extremely powerful (see for instance the excellent correlation between limit analysis solutions of Michalowski and Shi [237], and finite element results of [123] for incompressible soils).

In case of non-associated materials the irreversibility condition must be checked [82]. However, for translational failure mechanisms, $0 \leq \psi \leq \phi$ ensures the respect of this condition.

Proof. Assume a translational failure mechanism, so that coaxial and non-coaxial flow rules can be represented in the Mohr diagram (Figure 1.1). Let $[v]_i$ be the vector of velocity jumps and t_i the vector of corresponding tractions. Given that $0 \leq \psi \leq \phi$, it follows from the geometrical construction that $0 < \angle([v]_i, t_i) \leq \pi/2$. Therefore, irrespective of coaxiality, the following relation holds for any possible value of ψ

$$t_i[v]_i \geq 0 \quad \square$$

The particular case of de Josseling de Jong flow rule [73, 160] (point D in Figure 1.1) was also discussed by Drescher and Detournay [82].

1.4.3 Frictional Interfaces

The limit theorems are valid for frictional interfaces if there is no slip or if the frictional forces are known [97], because they can be treated as surface tractions. The issue is that in general their distribution is not known. A useful set of limit theorems due to Drucker [85] may be summarised as follows

Theorem 7 (Lower bound for frictional interfaces). *The limit load for an assemblage of bodies with frictional interfaces is bounded below by the limit load for the same bodies with zero friction on the interfaces.*

Theorem 8 (Upper bound for frictional interfaces). *The limit load for an assemblage of bodies with frictional interfaces is bounded above by the limit load for no relative motion at the interfaces and also by the limit load for the same assemblage cemented at the interfaces by a cohesionless soil.*

A less conservative upper bound theorem for frictional interfaces were given later by the same author [87]:

Theorem 9 (Upper bound for frictional interfaces). *Failure should be assumed to occur if for a pattern of deformation the work done by the applied forces exceeds the allowable dissipation. The allowable dissipation is to be computed from any equilibrium distribution of normal stresses on the assumed surfaces of sliding.*

If theorems 7 and 8 give close solutions, or even the same result, the problem may be considered solved. If not, techniques are required to refine the bracketing of the limit load.

Mroz, Drescher, Collins, and Justo [56–58, 161, 246] showed that rigorous upper bound solutions can be obtained by adopting a velocity field which is constant along the

contact surface and inclined at the angle of friction δ to the normal to the interface. In the computation of the rate of work due to friction \dot{D}_δ , the velocity can be taken out of the integral because it is constant. Because the interface shear strength is fully mobilised, \dot{D}_δ can be expressed in terms of the resultant force acting on the interface $T_i = \int_L t_i dl$, where t_i is the vector of surface tractions acting on the interface, and the angle between it and the velocity jump at the interface, $\theta = \angle([v]_i, T_i)$

$$\dot{D}_\delta = \int_L [v]_i t_i dl = [v]_i \int_L t_i dl = [v]_i T_i = \|[v]_i\| \|T_i\| \cos \theta \quad (1.16)$$

where $\|\cdot\|$ is the 2-norm operator (note that with $\|\cdot\|$ the Einstein's summation convention does not apply). The direction of $[v]_i$ implies that either $\theta = 0$ or $\theta = \pi/2$. This is equivalent to replace the interface by an infinitely thin layer of associated coaxial material obeying to a cohesionless Mohr-Coulomb law with shear strength angle δ . This approach can actually be seen as an application of theorem 8 and the fact that limit theorems are applicable to inhomogeneous materials [86].

A different approach was employed by Chen [49], who computed the energy dissipation due to friction as the product between the frictional force $\|T_i\| \sin \delta$, and the tangential component of the relative velocity at the interface $[v]_t$, assumed constant. This is equivalent to model the interface as a layer of non-associated non-coaxial material with $\psi = 0$ and for which the yield stress is given by $\tau = \sigma_n \tan \delta$. Due to theorem 6, the same solution would be obtained by selecting $\psi = \delta$.

Therefore, for translational failure mechanisms the two methods of considering interfaces are equivalent [82]. It is interesting to note that the approach of Chen is a direct application of theorem 9. In fact, if the relative velocity is constant, \dot{D}_δ is independent of the normal stress distribution, but depends only on its resultant through the relation $\|T_i\| \sin \delta = N \tan \delta$, where $N = \int_L \sigma_n dl$ can be expressed in terms of the applied loads by equilibrium considerations.

1.5 Methods for Computing the Limit Load

The way of determining the collapse load is generally categorised in one of the three following methods:

1. Limit analysis method
2. Limit equilibrium method
3. Method of characteristics

The first method is nothing but the rigorous application of the limit theorems of the theory of plasticity. The second method is based on the assumption of a rigid-perfectly plastic material and expresses equilibrium between applied forces and resisting forces mobilised along failure surfaces. Obviously, it requires that the system is statically determined, otherwise further assumptions must be made. It was highlighted above that in case of translational failure mechanisms this approach yields rigorous upper bound solutions. The third method establishes a set of partial differential equations. These equations express either equilibrium and yield condition [174, 175], or the kinematics of the failure mechanism [342]. The former gives a network of stress characteristics defining the shear strength mobilisation. Given that the stress field obtained is generally not extended throughout the entire solid, the solution is not a rigorous lower bound. The latter gives the network of velocity characteristics and the application of equation (1.11) provides a rigorous upper bound. The system of equations is definite only in plane strain conditions. In axial symmetry conditions the set of equations is not always definite, e.g. the problem of indentation of a circular rigid punch requires the additional hypothesis of Haar and Karmán [126] concerning the intermediate principal stress σ_θ .

Under the light of the limit analysis, the second and the third method are actually techniques employed to obtain either a lower or an upper bound to the actual collapse load. It is noteworthy that when the method of characteristics is used, the geometry of the plastic region containing the deforming zone arises naturally and there are good chances that the solution is the correct one. For instance, the partial stress fields obtained by Sokolovskii [366, 367] for the bearing capacity of smooth surface footings, and the solution of Lundgren and Mortensen [201] for rough footings have been proven to be exact [217].

1.6 Limit Analysis for Real Soils

The theory of plasticity requires convexity and normality to be generally valid [83, 92, 95, 141, 293]. The first condition is not at issue given that it is observable also experimentally. The second condition is more delicate, because the predicted dilation is usually larger than what found in experiments. Besides the intrinsic simplification of the theory with respect to reality, the discrepancy is also due to the fundamental differences between plastic and frictional systems, and soils are frictional systems at a certain extent [95]. The lack of normality and frictional interfaces can be handled with the theorems for non-associated materials described previously.

It is customary to assume the concept of perfect plasticity arbitrarily valid. However, soils often undergo isotropic consolidation. An idealisation of soils as work-hardening

elastic-plastic bodies was proposed by Drucker [95]. Notwithstanding, a perfectly plastic state may be reached at collapse [87, 95], which depends on the loading path. Therefore, it is fundamental to understand what is the limit state under investigation, i.e. *general shear failure* or *excessive volumetric deformation*, and how it will be reached. The former is typical of dense soils, whereas the latter of loose materials [384]. Strength parameters should be determined based on the most probable loading path. It is noteworthy that real soils might exhibit post-peak softening, which means that failure surfaces may be characterised by different degrees of shear strength mobilisation. Ideal plasticity is a simple but effective way to tackle this issue.

Another approach would be to take advantage of the fact that soils tend to a *critical state* [338], which can be described by perfect plasticity. This was discussed by Jenike, Shield, and Mroz [158, 159, 246]. Basically, during plastic flow at constant volume, the state of the material will be close to the critical state line, which can be described by a cohesionless Mohr-Coulomb yield condition. Given that velocity vectors are not perpendicular to the critical state line, the flow rule is non-associated. Therefore, use has to be made of the theorems for non-associated materials. Useful bounds may also be determined through the following inequality [65]:

$$\underset{\substack{\phi=\phi_{cv} \\ \psi=0}}{Q_c^t} \leq Q_c^{r,cv} < Q_c^{r,p} \leq \underset{\substack{\phi=\phi_p \\ \psi=\psi_p}}{Q_c^t} \leq \underset{\phi=\phi_p}{Q_c^t} \quad (1.17)$$

where Q_c denotes the collapse load, and superscripts are as follows: t correct theoretical value for the ideal material, r actual value for the real soil, cv constant volume, and p peak.

Soil strength is strongly affected by the presence of water. When the soil is saturated and there is no water flow, or seepage forces can be neglected, undrained and drained situations must be distinguished. The former implies the utilisation of undrained strength parameters c_u and ϕ_u , and bulk density γ ; whereas the latter requires drained values c' and ϕ' , and submerged weight γ' . When steady seepage exists in the soil mass, a seepage analysis is required and limit analysis must be performed in terms of effective stresses. The limit theorems can also be applied to partially saturated soil masses. Suction may be conveniently considered as an increase of the apparent cohesion, i.e. a shift of the Mohr-Coulomb line, with the upper bound theorem, whereas it may be considered either as an increase of the isotropic stress tensor, i.e. a shift of the Mohr circle, or as an increase in apparent cohesion, when applying the lower bound theorem. When the soil mass is characterised by inhomogeneous water conditions, different shear strength properties

may be allocated to each region.

The limit analysis is apt to be of great use to deal with inhomogeneity of soil masses [86], anisotropy [49], and inability to take tensile stresses [86, 97].

Limitations on the validity of a simple idealisation are to be expected along with disagreement in detail with experimental, and even more with real, data [84]. Nevertheless, the limit state is a matter of definition and the corresponding yield surface should be determined by the most significant features of the problem to be solved. In a problem of ultimate limit state, the crucial information is the value of the collapse load, whereas the detailed knowledge on the local value of plastic strains is generally of little concern.

1.7 Limit Analysis for Structures

In soil engineering applications, the structural component is generally made of steel, reinforced concrete or a mix of the latter. Typical examples are walls, footings, rafts, piles and tunnel linings. It is noteworthy that, although the above discussion was based on continuum mechanics, all theorems and concepts are equally applicable to structural mechanics through generalised stresses and strains, i.e. axial force-axial displacement rate, bending moment-rotation rate [51, 72, 94, 291]. The main difference between structural elements and solids is that ductility capacity is not ensured by the material itself, but is strongly related to the connections between members, their slenderness, and loading conditions (instability problems, shear brittle failure).

1.7.1 Steel

Mild-steel does not deserve further details, given that the theory of plasticity was developed for this material. On the other hand, recent high strength steels might require further considerations owing to their reduced capacity of plastic deformation. The applicability of the limit theorems to steel structures is generally constrained by the ductility capacity of connections (i.e. welded connections) and potential instabilities. For this reason, connections and regions of load introduction are often equipped with stiffeners.

1.7.2 Reinforced Concrete

Reinforced concrete structures are probably the most common type of structures in geotechnical applications. Despite concrete by itself cannot be considered a plastic material, reinforced concrete members can sustain considerable plastic deformations if proper reinforcement is provided. It is commonly admitted that concrete takes compressive

stresses, whereas reinforcement takes tensile stresses [88, 106, 257]. The behaviour of concrete in compression is characterised by a post-peak softening, which increases with concrete compressive strength. This is managed by the adoption of perfect plasticity [88, 101, 257, 349]. Reinforcement is usually mild-steel. A lower bound theorem specific for reinforced concrete structures was given by Drucker [88]

Theorem 10 (Lower bound for reinforced concrete). *If an equilibrium distribution of stresses can be found in the concrete and the steel which is nowhere tensile in the concrete and is everywhere at or below yield, the structure will not collapse or will just be at the point of collapse.*

The application of theorem 10 with all the specific rules for concrete is known as the *theory of stress fields*. This theory has its roots in the works of Ritter [312] and Mörsch [243], when the theory of plasticity was still unknown, and gained maturity in the 1970s and 1980s at the institutes of technology in Zurich and Copenhagen [253]. At the same time, a complementary approach was under development in Germany, the *strut-and-tie method*. The latter is based on the equilibrium of forces, and basically consists in deriving a fictitious truss structure inside the concrete member which nowhere violates the yield limit and is in equilibrium with the external loads. These two approaches are complementary [253, 257].

Vecchio and Collins [394] showed that uniformly cracked concrete can efficiently be treated as a new material with its own stress-strain characteristics. The constitutive relation, and in particular the compressive strength, is mainly governed by the orientation of the cracks, their opening, and their penetration within the compressive stress field. To Schlaich [337] is due a general approach for the design of reinforced concrete members. According to this method, the structure is subdivided into regions where the Euler-Bernoulli hypothesis of plane sections is satisfied and regions where it is not (geometric discontinuities and introduction of concentrated loads). The former are treated with the classical beam theory, whereas the latter are analysed more in detail through the theory of stress fields or the strut-and-tie method.

In a similar fashion to Saint-Venant-Lévy-Mises and Prandtl-Reuss relationships, rigid plastic and elastic-plastic stress fields formulations were devised. Their advantages and drawbacks were discussed in [173].

If slender members are subjected to shear forces, a fundamental distinction must be made, namely members with and members without transverse reinforcement. For members pertaining to the latter category, the theory of plasticity cannot always be applied, because failure might occur by quick development of a critical crack [43, 256,

354, 393, 409]. A general theory able to handle one way shear and punching shear is the *critical shear crack theory* [42, 107, 251, 252, 280, 356]. This aspect is qualitatively depicted in Figure 1.3 for one way shear members without transverse reinforcement. The diagram shows that shear strength is mainly governed by the shear span ratio α ($\alpha = a/d$, where a is the shear span and d is the effective depth). This diagram shows that stress fields (SF), rigid-plastic or elastic-plastic, can be used to compute deep ($\alpha < \alpha_1$) and very slender ($\alpha > \alpha_3$) beams, because failure occurs by yielding of the flexural reinforcement and crushing of the concrete. In moderate deep beams ($\alpha_1 \leq \alpha \leq \alpha_2$) the presence of cracks reduce the concrete compressive strength, and thus the modified stress fields (MSF) theory must be adopted. Finally, for slender members the shear capacity is mainly governed by shear transfer actions across a critical shear crack (CSC). Analogous considerations can be drawn for punching shear [353]. This aspect is of paramount importance in geotechnical applications, because footings and rafts are generally designed without transverse reinforcement.

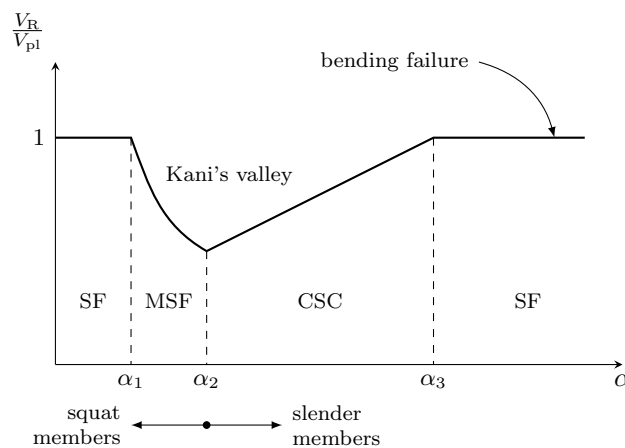


Figure 1.3 — Shear capacity of one way shear members without transverse reinforcement. Ratio between shear resistance V_R and plastic shear resistance V_{pl} (corresponding to the yielding of the flexural reinforcement and the crushing of concrete) as a function of the shear span ratio α . Depending on the slenderness of the member, shear capacity can be computed with stress fields (SF), modified stress fields (MSF), or critical shear crack theory (CSC). [107].

The design of new reinforced concrete structures is nowadays generally based on the method of stress fields.

1.8 Limit Analysis Considering Soil-Structure Interaction

The application of limit analysis considering soil-structure interaction means that the strength of both soil and structure is taken into account. Owing to the fact that these two components do not behave independently, the correct assessment of the collapse load must consider their mutual interaction. This means that an admissible stress field in the structure must be extended throughout the soil and vice versa, and combined failure mechanisms must be considered. Such solutions are not common due to the number of parameters involved. A few solutions were proposed for surface strip footings [72, 111, 281], and for cut-and-cover tunnels [33, 281].

These type of analyses are of particular interest if the collapse load of an existing structure is sought, because often a combined failure mechanism characterises the transition from a rupture figure involving only the soil mass and another affecting only the structure. Limit theorems for non-associated materials and frictional interfaces may be useful to take into account some aspects peculiar to soil-structure interacting systems.

1.9 Numerical Limit Analysis

Lysmer [205] introduced a technique for computing rigorous lower bounds based on the finite elements method and linear programming. Since then, a number of improvements have been proposed for the lower bound [16, 203, 207, 360], and for upper bound [16, 204, 208, 361, 362]. Other approaches, such as the discontinuity layout optimisation for the determination of the optimal failure mechanism have also gain popularity [365].

It is noteworthy to cite, among others, the following softwares for the limit analysis: OptumCE [271], a finite element software able to perform both lower and upper bound limit analyses of geotechnical applications, and reinforced concrete panels and slabs; LimitState [196], a discontinuity layout software for the upper bound limit analysis of soil masses and reinforced concrete slabs; and jconc [106], a finite element software for the automatic generation of elastic plastic stress fields within reinforced concrete members.

Jconc uses a classical displacement-based finite elements formulation. Therefore, the solution is not a rigorous lower bound, both because equilibrium is satisfied in average over the finite elements, and because the bi-linear behaviour of the reinforcement involves strain rates that are not fully plastic, which is a necessary condition for the proof of the lower bound theorem. Nevertheless, the solution can be extremely useful in real applications [254], where any theoretical hypothesis is actually never met.

1.10 Concluding remarks

The theorems of the limit analysis have been reviewed. The fundamental principles of the theory of plasticity have been presented and the conditions for uniqueness have been highlighted. Extended limit theorems for non-associated materials and frictional interfaces have been exposed and their usefulness for real soils has been remarked. Particular attention has been devoted to the assumption of perfect plasticity. Limit theorems for reinforced concrete and soil-structure interacting systems have also been discussed. Some of the main conclusions that can be drawn from this research are as follows:

- The limit theorems and the uniqueness of the solution can be proven generally true only for convex yield surfaces and associated coaxial materials.
- The collapse load of non-associated materials can be bounded between fixed limits corresponding to associated materials.
- In the case of translational failure mechanisms, an upper bound for non-associated materials can be computed with a fictitious modified yield condition.
- The definition of the yield criterion for soils might not be independent on the application under investigation (simplified criteria are path dependent).
- Extended limit theorems and translational failure mechanisms can be conveniently used to analyse soil-structure interacting systems.

It is the author opinion that a rigorous approach to the problem of limit loads is essential for a comprehensive understanding of the phenomenon. The derivation of the limit theorems by itself is the result of a rigorous mathematical treatment of the problem. However, it is also clear that a number of hypotheses and simplifications must be made for engineering applications, which lead inevitably to approximate results. The extent of such simplifications is strongly related to the problem under investigation.

Acknowledgements

The support of the Swiss National Science Foundation (project No. 174575, Division InterCo) is acknowledged.

In order to be useful, the knowledge of theory must be combined with a thorough knowledge of the physical properties of real soils and the difference between the behaviour of soils in the laboratory and in the field.

Karl Terzaghi, Theoretical Soil Mechanics

2

Bearing Capacity of Surface Footings under Centred and Vertical Load: State-of-the-Art

THE EVALUATION OF the bearing capacity of surface footings is a classical problem in applied soil mechanics and is of paramount importance in design practice. Therefore, many solutions have been advanced during the years. Despite the number of works dedicated to the subject, a comprehensive and direct comparison of the available solutions and the implications of their underlying assumptions are somehow missing. As a consequence, it is not clear whether new and more refined theoretical results are either needed or susceptible to provide real improvements for the design. In this study, an attempt is made to fill this gap. A collection of solutions categorised by footing type, soil constitutive model, and computation technique is presented. The underlying assumptions and the subsequent limitations are discussed. It is shown that advanced numerical techniques are of practical relevance only if key aspects pertaining to real soils such as flow rule, and influence of loading and strain conditions on shear strength parameters, that cannot be considered directly by simplified limit analyses, are taken into account.

2.1 Introduction

The analysis of collapse load is a key aspect in the design process of foundations. The theory of *general shear failure* for shallow footings on dense soils has been developed by Terzaghi [384] and Meyerhof [232], and generalised in the known form by Brinch Hansen [25]. In the case of surface footings, the resistance is given by the apparent cohesion and the mass of soil displaced that opposes to the indentation of the footing.

Over the years, many solutions have been proposed based on the *limit state* theories, i.e. limit equilibrium method, method of stress characteristics, and limit analysis method, or based on step-by-step analyses. Alongside, a number of reviews have been published [7, 23, 230, 231, 274, 341, 351, 397, 408]. Due to length restrictions, these surveys are generally limited to a few selected solutions. Moreover, the main underlying assumptions and their consequences on the results, and the connection with experimental data and real soils are not always clarified.

In this research, an effort is made to clarify the aforementioned aspects for surface footings subjected to a centred and vertical load. Most of the theoretical aspects and the main conclusions can, however, be extended to shallow footings under combined loads. The second and third sections are devoted to the theoretical derivation of bearing capacity coefficients for strip and finite length footings, respectively. Attention is given to the effect of footing roughness. Numerical values are presented in tabulated form, so that they can be easily used by other researchers. Analytical expressions are reported with their precision or range of applicability. Two new formulae for the bearing capacity of surface strip footings on general Mohr-Coulomb soils are derived. In the third section, the relevance of the theoretical solutions are critically analysed with respect to real soils, i.e. the presence of water, the flow rule, and the influence of strain conditions on the shear strength parameters. Finally, concluding remarks are summarised.

2.2 Plane Strain Problem

Rectangular footings with aspect ratio $L/B \geq 5$ can be analysed in the framework of plane strains.

2.2.1 Weightless Mohr-Coulomb Material — $c-\phi$ soil

To the author's knowledge, Prandtl [298] derived the first field of stress characteristics for the uniform indentation pressure p_f on a weightless rigid material defined by a perfectly plastic Mohr-Coulomb yield criterion (cohesion c and shear strength angle ϕ). His

solution (right of Figure 2.1) comprises a central wedge beneath the load in the Rankine plastic state, two lateral wedges in the Rankine plastic state, and two logarithmic spiral sectors with a family of straight stress characteristics radiating from the edge of the load and a family of logarithmic spiral stress characteristics. In terms of bearing capacity factor $N_c = p_f/c$, the solution writes

$$N_c = \cot \phi \left(e^{\pi \tan \phi} N_\phi - 1 \right) \quad (2.1)$$

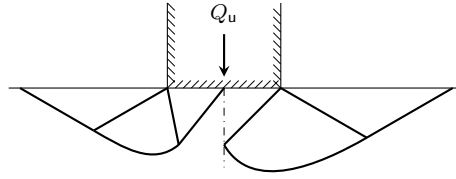


Figure 2.1 – Failure mechanism for smooth (left) and rough (right) footings on a weightless Mohr-Coulomb soil.

$N_\phi = \tan^2 \left(\frac{\pi}{4} + \frac{\phi}{2} \right)$ is the *flow value* [384]. When $\phi = 0$, the Mohr-Coulomb criterion reduces to the Tresca yield condition*, and the Prandtl solution is

$$N_c = \lim_{\phi \rightarrow 0^+} \cot \phi \left(e^{\pi \tan \phi} N_\phi - 1 \right) = 2 + \pi \quad (2.2)$$

The kinematic admissibility of Prandtl solution for Tresca materials was shown by Prager and Hodge [296].

Hencky [134] suggested an alternative partial plastic stress field for a Tresca material, which gives the same solution as (2.2). This solution involves two wedges beneath the base instead of one as proposed by Prandtl. Hill [148] showed that Hencky solution applies to the indentation of a flat rigid and smooth die, and that an admissible velocity field can be associated to the stress characteristics. This failure mechanism is known as Hill type failure mechanism.

Shield [342] extended the Hill mechanism to the case of a general weightless Mohr-Coulomb material ($\phi > 0$) and showed that an admissible velocity field can be associated to both the Prandtl and Hill type partial stress fields. The solution for this extended Hill failure mechanism is still given by equation (2.1). Actually, it is not surprising that Prandtl and Hill type solutions are the same for weightless materials. The rigid region outside the deforming zone can be stressed either elastically or plastically. Therefore, the

*Tresca yield criterion coincides with the Mises yield criterion in plane strains because $\sigma_{II} = 0.5(\sigma_I + \sigma_{III})$ for an incompressible plastic flow [195].

plastic stress field of the Hencky solution can be extended in order to recover the Prandtl plastic region. It can then be stated that there are two limiting deformation modes associated to a unique plastic stress field. In fact, a theorem due to Hill [146] states that in a rigid-plastic associated material, the state of stress is uniquely defined in a certain part of the plastic region under given boundary conditions. This zone forms part (or sometimes all) of the plastic region and covers the whole material that can deform under the given boundary conditions. However, the instantaneous mode of deformation may not be uniquely defined. The extension of the deforming region, which defines the volume of matter displaced, does not play a role because the moving material is weightless.

It is noteworthy that for a footing resting on a general weightless Mohr-Coulomb material, the contact pressure at failure is not constant, but increases from the edge to the centre of the footing. The value of p_f given by (2.1) corresponds to the average pressure. This was shown by Meyerhof [232], who derived the same bearing capacity factor by expressing the equilibrium of resultant forces acting on the central wedge[†].

Bishop [12] extended Prandtl and Hencky partial stress fields into the rigid body of a Tresca material, whereas Shield [345] extended Prandtl partial stress field in an admissible manner for $\phi < 75^\circ$. Given that an admissible velocity field can be associated to both solutions, it may be concluded that (2.1) is the exact solution for the maximum average indentation pressure on a weightless rigid-perfectly plastic associated Mohr-Coulomb material (provided that $\phi < 75^\circ$). Chen [49] explicitly showed the coincidence with upper bound solutions for both rupture figures. The exact values of N_c are summarised in Table 2.1.

It is noteworthy that the roughness of the footing does not have any influence on the bearing capacity. The proof requires the use of a set of theorems obtained by Drucker [85]. These show that the collapse load of an indenter is bounded from below by the limit load with zero friction at the interface, and from above by the limit load corresponding to the kinematic boundary condition of no relative slip at the interface. Given that Hill (frictionless interface) and Prandtl (no relative motion) complete solutions coincide, the solution is independent of interface friction.

Shield [343] obtained a rigorous lower bound to the uniform strip load, or average indentation pressure, through the superposition of simple homogeneous stress fields. The bearing capacity factor is

[†]Terzaghi [384] already suggested that Prandtl solution expresses the average contact pressure. The same was suggested by Shield [343, 347].

$$N_c = \frac{N_\phi^{\frac{3}{2}}}{2} \left(4 + \sin \phi + \sin^2 \phi + (1 + \sin \phi) \sqrt{4 + \sin^2 \phi} \right) + 2\sqrt{N_\phi} \quad (2.3)$$

The difference between (2.3) and the exact solution increases with increasing ϕ , $N_{c,\text{lower}}(\phi = 0) = 5.00$ and $N_{c,\text{lower}}(\phi = \pi/4) = 66.9$.

Table 2.1 – Exact bearing capacity factor ($N_c = p_f/c$) for footings on a weightless material, [298].

ϕ [deg]	0	5	10	15	20	25	30	35	40	45
N_c	5.14	6.49	8.34	11.0	14.8	20.7	30.1	46.1	75.3	134

2.2.2 Ponderable Tresca Material — c – γ soil

The earliest theoretical methods for the computation of the bearing capacity of surface strip footings on ponderable materials defined by the Tresca yield condition, as reported by Wilson [404], are the method of Hogentogler and Terzaghi [151] ($N_c = 4.0$), the circular-arc method of Fellenius [105] ($N_c = 5.52$) which assumes completely circular failure surfaces, the circle method of Krey [177] ($N_c = 6.05$) which supposes a combination of circular and planar failure surfaces, and the modified Krey's method ($N_c = 5.41$) which optimises the location of the critical failure surface. Ritter [311] was, to the author's knowledge, the first to compute the bearing capacity of shallow footings on general soils, i.e. considering the contribution of the soil self-weight, and assuming the overburden soil as a uniform pressure. For surface footings on a Tresca material, his solution writes

$$N_c = \lim_{\phi \rightarrow 0^+} \cot \phi (N_\phi^2 - 1) = 4 \quad (2.4)$$

Palmer [277] modified Prandtl's solution to take into account the soil self-weight, which contribution vanishes for $\phi = 0$ and N_c is given by (2.2). These techniques do not specify anything about the footing roughness.

Later Terzaghi [384], starting from his failure mechanism for perfectly rough strip footings on general soils, proposed the following relation

$$N_c = \lim_{\phi \rightarrow 0^+} \cot \phi \left(\frac{e^{(\frac{3}{2}\pi - \phi) \tan \phi}}{2 \cos^2(\frac{\pi}{4} + \frac{\phi}{2})} - 1 \right) = \frac{3}{2}\pi + 1 = 5.71 \quad (2.5)$$

For smooth footings he adopted the Prandtl failure mechanism.

All the above results, except the solutions of Palmer and Terzaghi for smooth interfaces, cannot be correct because Salençon [331] demonstrated that the bearing capacity of a Tresca material is independent of its self-weight. This can actually be inferred directly from the previous section and the application of the upper bound theorem of the limit analysis, which shows that the rate of work done by the weight is zero [49], both for the Prandtl and the Hill failure mechanisms. Therefore, given that the lower bound solution for the weightless soil is admissible for the ponderable soil [115], and that it coincides with the upper bound solution for the ponderable material, (2.2) is the exact solution and is independent of the soil self-weight, and also of the base roughness. The invariance of N_c with respect to footing roughness was suggested also by Meyerhof [232], and confirmed experimentally by Skempton [359].

2.2.3 Ponderable Cohesionless Mohr-Coulomb Material — ϕ - γ soil

The set of partial differential equations satisfying equilibrium and Mohr-Coulomb yield condition for a ponderable material were derived by Kötter [174]. The resolution is complicated, because the characteristics are allowed to be curved everywhere (Figure 2.2). No closed form solutions are known.

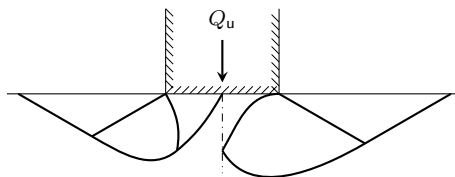


Figure 2.2 – Failure mechanism for smooth (left) and rough (right) footings on a Mohr-Coulomb soil.

Ritter [311] defined a failure mechanism made of a wedge below the footing in Rankine plastic state and a less well defined state outside this region made of curved rupture surfaces, which cut the ground level at an angle $\pi/4 - \phi/2$. He integrated the major principal stresses, computed with Kötter's equations, along a major principal plane which encompasses the base. Given that he did not consider properly the curvature of the slip lines and that they are not well defined everywhere, the direction of the major principal plane is probably wrong. Moreover, it is not clear whether the solution corresponds to the case of a smooth or a rough footing. Ritter wrote that the loading causes the soil to be laterally displaced. This statement in conjunction with the assumption that the base

is a principal plane, suggests that the interface should be considered smooth. On the other hand, the rupture surfaces starting at the footing edges are supposed to meet at the axis of symmetry, creating a wedge under the base which could also be interpreted with a downward movement, thus corresponding to a rough base. These aspects might explain the difference with respect to the exact solution (see below), and why there is not a unique trend. Tables 2.2 and 2.8 show that the values of N_γ provided by Ritter are higher than those for rough footings for $\phi \leq 15^\circ$, between smooth and rough for $20^\circ \leq \phi \leq 25^\circ$ and lower than those for smooth footings for $\phi \geq 30^\circ$. The formula derived by Ritter is

$$N_\gamma = \frac{2p_f}{\gamma B} = \frac{\sqrt{N_\phi}}{2} (N_\phi^2 - 1) \quad (2.6)$$

where γ is the soil self-weight, and B the breadth of the footing.

Smooth footing

Limit equilibrium method

Terzaghi [384] gave the first comprehensive description of the punching failure mechanism of footings. His approach for rough footings, based on the limit equilibrium method, is still one of the most used by practitioners. However, he did not furnish explicit results for smooth interfaces. He just said that the same procedure used for rough footings can be applied, but to a mechanism in which the trapped wedge makes an angle $\psi = \pi/4 + \phi/2$ with the base, instead of $\psi = \phi$. Meyerhof [229] pointed out that the bearing capacity calculated in this way is greater than that of a rough base, which seems reasonable because the extent of the failure mechanism is greater, and the factor N_γ is related to the mass of soil displaced. This outcome contradicts the limit theorems for frictional interfaces [85], according to which the limit load of an assemblage of bodies with frictional interfaces is bounded below by the limit load for the same bodies with zero friction, and the experimental evidences of Meyerhof [232], which showed that $N_{\gamma, \text{smooth}} \approx 0.5 N_{\gamma, \text{rough}}$ (relation proposed later by the same author [228], in which $N_{\gamma, \text{rough}}$ can be approximated by (2.15)). After the solution of Meyerhof [232] for perfectly rough footings, which assumes $\psi = \pi/4 + \phi/2$, several authors adopted the same geometry for the trapped wedge (see below), and obtained results comparable to those of Terzaghi for $\psi = \phi$. Therefore, the suggestion of Terzaghi cannot be correct for smooth footings.

Method of stress characteristics

Caquot and Kérisel [37] obtained values of the bearing capacity factor N_γ by assim-

lating the problem of bearing capacity to that of passive earth pressure, for which they derived the partial field of stress characteristics[‡] (Table 2.2). Other authors [15, 66, 120, 130, 133, 181, 191] (Table 2.2) adopted the procedure developed by Sokolovskii [366, 367] for the construction of the stress characteristics field, which matches that proposed earlier by Lundgren and Mortensen [201].

It is noteworthy that the values of N_γ given by Larkin [191] have somehow been multiplied by two [133]. It seems that he computed N_γ with the maximum, rather than the average, contact pressure. Therefore, the values reported in Table 2.2 are half of those given in [191]. A similar issue appears to the values attributed to Sokolovskii [366] reported by some authors [49, 211, 389]. These values are twice those reported by Grahm and Stuart [120], and Martin [216]. The latter, from whom the values in Table 2.2 attributed to Sokolovskii are taken, gave a probable explanation to this mistake.

Poulos [287] suggested the following expression to approximate the numerical results obtained by Davis and Booker [66]

$$N_\gamma = 0.0663e^{9.3\phi} \quad (2.7)$$

where ϕ is expressed in radians. Han et al. [130] proposed the following analytical formula

$$\begin{aligned} N_\gamma &= \beta N_{\gamma,\max} \\ \beta &= \sum_{i=0}^4 a_i \tan^i \phi \end{aligned} \quad (2.8)$$

$N_{\gamma,\max}$ is the bearing capacity factor computed with the geometry of the failure mechanism for a weightless soil. In case of smooth footings the geometry is given by the Hill type failure mechanism proposed by Shield [342], and the expression was given by Chen [49]

[‡]The writer is not aware whether the tabulated values of N_γ were already present in the first edition of the book published in 1949 [39].

$$N_{\gamma, \max} = \frac{\sqrt{N_\phi}}{4} \left(e^{\frac{3\pi}{2} \tan \phi} \sqrt{N_\phi} - 1 \right) + \frac{3 \sin \phi}{1 + 8 \sin^2 \phi} \left[\left(\sqrt{N_\phi} - \frac{\cot \phi}{3} \right) e^{\frac{3\pi}{2} \tan \phi} + \frac{\cot \phi}{3} \sqrt{N_\phi} + 1 \right] \quad (2.9)$$

The coefficients a_i are: $a_0 = 0.281$, $a_1 = 0.715$, $a_2 = -0.747$, $a_3 = 0.345$, and $a_4 = -0.0654$.

Limit analysis method

Bearing capacity factors obtained through the upper bound theorem of the limit analysis are summarised in Table 2.3. Chen [49] and Michalowski [233] assumed a Hill type failure mechanism. However, the latter did not consider the radial shear zone as a continuous deforming region, but subdivided it into triangular blocks where the base inclination was left as an optimisation parameter. In this way, the region is not constrained by a logarithmic spiral failure line. His solution can be estimated with

$$N_\gamma = e^{5.1 \tan \phi} \tan \phi \quad (2.10)$$

Kumar [180] bounded the radial shear zone by a logarithmic spiral, but he did not impose the focus at the footing edge. It is interesting to note that values of Michalowski [233] and Kumar [180] are very close, suggesting that the actual failure surface obtained by Michalowski is close to a logarithmic spiral.

Numerical upper bounds (Table 2.3) computed with the finite elements method were obtained using linear programming [184, 363, 389], non-linear programming [149], and second-order cone programming [208]. Lower bounds (Table 2.4) were obtained using linear programming [183, 363, 389], non-linear programming [149], and second-order cone programming [207]. Hjiat et al. [149] bracketed the exact solution very closely, and proposed the following analytical expression to approximate the average between lower and upper bounds

$$N_\gamma = \beta N_{\gamma, \text{rough}} \quad (2.11)$$

$$\beta = \sum_{i=0}^5 a_i \tan^i \phi$$

Table 2.2 – Bearing capacity factor ($N_\gamma = 2p_f/(\gamma B)$) for smooth footings obtained with the method of stress characteristics.

ϕ [deg]	Caquot and Kerisel (1956)	Sokolov. (1965) ^a	Larkin (1968)	Hansen and Chris. (1969) ^b	Davis and Booker (1971) ^{ab}	Graham and Stuart (1971)	Bolton and Lau (1993)	Kumar (2009)	Han et al. (2016)
5	–	0.09	–	–	–	–	0.09	0.087	0.085
10	0.336	0.28	–	–	0.30	–	0.29	0.282	0.281
15	0.776	0.70	–	0.7	0.67	–	0.71	0.699	0.699
20	1.66	1.58	–	1.6	1.5	–	1.60	1.58	1.58
25	3.48	3.46	–	3.5	3.2	–	3.51	3.46	3.46
30	7.39	7.65	7.85	7.5	8.1	7.6 ^b	7.10	7.64	7.65
35	16.4	17.6	–	18	18	17.4	17.8	17.5	17.6
40	39.3	43.3	43.5	44	43	42 ^b	44.0	43.1	43.2
45	105	–	–	120	100	–	120	117	118

^a Taken from [216].^b Read from graphical representation.

where $N_{\gamma, \text{rough}}$ is given by (2.26), and $a_0 = 0.9232$, $a_1 = -2.4101$, $a_2 = 6.4821$, $a_3 = -9.4059$, $a_4 = 6.991$ and $a_5 = -2.0675$. The coefficient β tends the value 0.5 as the friction angle approaches 45° .

Smith [364] and Martin [215, 217] extended the incomplete stress field obtained with the method of characteristics, thus obtaining rigorous lower bound solutions, for any value of footing roughness. Martin [215, 217] showed that the velocity characteristics, which coincide with the stress characteristics for an associated material, define an admissible deforming mode and provide upper bounds coincident with the lower bounds[§]. The exact results for smooth surface footings on cohesionless soils are given in Table 2.5.

It is noteworthy that all the solutions derived with the method of stress characteristics are in very close agreement with the exact solution. It may be concluded therefore that the differences are only due to numerical reasons.

[§]For smooth and perfectly rough shallow footings, the exact solution may be obtained through the free software ABC [215].

Table 2.3 – Bearing capacity factor ($N_\gamma = 2p_f/(\gamma B)$) for smooth footings obtained with the upper bound limit analysis.

ϕ [deg]	Chen (1975)	Sloan and Yu (1996) ^a	Mich. (1997)	Ukrit. et al. (2003)	Kumar (2004)	Hjiaj et al. (2005)	Makro. and Martin (2007)	Kumar and Kouzer (2007)
5	0.131	–	0.127	0.09	0.12 ^a	0.091	0.085	0.10
10	0.461	–	0.423	0.30	0.41 ^a	0.299	0.282	0.31
15	1.16	1.3	1.05	0.75	1.0	0.737	0.703	0.78
20	2.68	2.5	2.33	1.73	2.3 ^a	1.67	1.59	1.74
25	5.90	5.0	5.02	3.94	5.0 ^a	3.65	3.48	3.82
30	12.7	9.5	10.9	8.54	10.9	8.08	7.70	8.47
35	28.6	26.0	24.7	21.2	24.8	18.5	17.7	19.7
40	71.6	55.0	60.2	54.2	60.3	45.4	43.6	50.4
45	195	–	164	157	164	123	119	142

^a Read from graphical representation.

Table 2.4 – Bearing capacity factor ($N_\gamma = 2p_f/(\gamma B)$) for smooth footings obtained with the lower bound limit analysis.

ϕ [deg]	Sloan and Yu (1996) ^a	Ukritchon et al. (2003)	Hijiaj et al. (2005)	Makro. and Martin (2005)	Smith (2005)	Kumar and Khatri (2008)
5	–	0.08	0.086	0.084	–	0.08
10	–	0.27	0.283	0.280	–	0.27
15	0.5	0.68	0.701	0.697	0.70	0.67
20	1.5	1.52	1.58	1.58	1.58	1.51
25	3.0	3.33	3.45	3.45	3.46	3.31
30	7.0	7.18	7.62	7.63	7.65	7.26
35	17.0	15.7	17.5	17.5	17.6	16.5
40	37.5	38.5	42.8	43.0	43.2	39.9
45	–	94	116	117	118	105

^a Read from graphical representation.

Table 2.5 – Exact bearing capacity factor ($N_\gamma = 2p_t/(\gamma B)$) for smooth footings, [217].

ϕ [deg]	5	10	15	20	25	30	35	40	45
N_γ	0.084	0.281	0.699	1.58	3.46	7.65	17.6	43.2	118

Rough footing

For practical applications, the base of reinforced concrete footings can always be taken as perfectly rough, i.e. $\delta = \phi$ [232].

Limit equilibrium method

Table 2.7 summarises the values of the bearing capacity factor N_γ obtained with the limit equilibrium method. Palmer [277] proposed probably the first formula for the contribution of soil weight with a clear idea of an imposed trapped wedge beneath the base. This formula was called modified Prandtl formula and for cohesionless soils reduces to

$$N_\gamma = \sqrt{N_\phi} (e^{\pi \tan \phi} N_\phi - 1) \quad (2.12)$$

Terzaghi [384] assumed a Prandtl type failure mechanism with trapped wedge underneath the base of angle $\psi = \phi$. He then optimised the position of the focus of the logarithmic spiral curve, and obtained the following bearing capacity factor

$$N_\gamma = \frac{\tan \phi}{2} \left(\frac{K_{p\gamma}}{\cos^2 \phi} - 1 \right) \quad (2.13)$$

where $K_{p\gamma}$ is the coefficient of passive earth pressure. As noted by Bowles [23], Terzaghi never explained in detail how he obtained the $K_{p\gamma}$ used to compute the bearing capacity factor N_γ . He gave, however, a small scale curve of ϕ versus N_γ for $0^\circ \leq \phi \leq 39^\circ$ and three specific values at $\phi = 0^\circ$, 34° and 48° . Actually, Terzaghi just mentioned that $K_{p\gamma}$ can be computed graphically. Bowles, using a curve fitting method, provided values of N_γ for $0^\circ \leq \phi \leq 50^\circ$. Later, Kumbhojkar [185] presented explicit analytical expressions for calculating N_γ according to Terzaghi's mechanism. The differences with respect to the results presented by Terzaghi are presumably due to the inherent limitations of the graphical procedure. Also Dewaikar and Mohapatro [77] computed N_γ based on Terzaghi's mechanism, but employing Kötter's equations. In Table 2.6 all these values and the corresponding back-computed $K_{p\gamma}$ are given.

Some years later, Meyerhof published his bearing capacity theory [232], according to

Table 2.6 – Bearing capacity factor ($N_\gamma = 2p_f/(\gamma B)$) for perfectly rough footings according to Terzaghi’s failure mechanism.

ϕ [deg]	Terzaghi (1943) ^a		Kumbhojkar (1993)		Dewaikar and Mohapatro (2003)	
	N_γ	$K_{p\gamma}$	N_γ	$K_{p\gamma}$	N_γ	$K_{p\gamma}$
5	0.5	12.2	0.144	4.26	–	–
10	1.2	14.7	0.559	7.12	–	–
15	2.5	18.6	1.52	11.5	–	–
20	5.0	25.0	3.64	18.5	–	–
25	9.7	35.0	8.34	30.2	8.36	30.3
30	19.7	52.0	16.2	42.8	21.4	56.4
35	42.4	82.0	45.4	87.7	53.8	104
40	100	141	115	161	141	198
45	298	298	325	326	407	408

^a After [23].

which the failure mechanism is characterised by a trapped wedge of angle $\psi = \pi/4 + \phi/2$, two logarithmic spiral sectors and two Rankine plastic regions. In that paper the optimum values of N_γ were given graphically. However, they were tabulated in the proceedings of the second ICSMFE [226]. A few years later, Meyerhof [229] suggested to optimise the geometry of the elastic trapped wedge, which led to $\psi_{\text{opt}} \approx 1.2\phi$. Later, Terzaghi himself adopted this solution [385]. In that study, Meyerhof conducted the first theoretical analysis on the influence of footing roughness on the ultimate bearing capacity. Interface friction was taken into account assuming that the central elastic wedge increases from zero for a smooth base to the footing breadth for $\delta = \phi$. Considering that the bearing capacity of a smooth footing can be roughly taken as half of that of a perfectly rough footing, Meyerhof proposed the following expression

$$\begin{aligned}
 N_\gamma &= \left(n + \frac{1 - n^2}{2} \right) N_{\gamma, \text{rough}} \\
 n &= \frac{\tan \delta}{\tan \phi} \\
 B_{\text{wedge}} &= nB
 \end{aligned} \tag{2.14}$$

Later, Meyerhof [228] suggested to approximate the optimum bearing capacity ($\psi = \psi_{\text{opt}}$) with the following analytical expression

$$N_\gamma = (N_q - 1) \tan(1.4\phi) \tag{2.15}$$

A formula very close to (2.15) was given by Spangler and Handy [369] (taken from [23]):

$$N_\gamma = 1.1(N_q - 1) \tan(1.3\phi) \quad (2.16)$$

Janbu [156] applied the generalised procedure of slices to derive bearing capacity of shallow footings under centred vertical or inclined load. He assumed a failure mechanism given by the geometry of Prandtl's solution. The bearing capacity factor he obtained is

$$N_\gamma = \frac{N_h}{2}(N_q - 1) \quad (2.17)$$

where

$$N_h = \frac{e^{(\frac{\pi}{4} - \frac{\phi}{2}) \tan \phi}}{\cos(\frac{\pi}{4} + \frac{\phi}{2})}$$

Zhu et al. [410] used the method of triangular slices, which is within the limit equilibrium method, to compute the bearing capacity factor. In this method, the passive failure region is not bounded by a logarithmic spiral surface, but it is divided into a number of triangular slices and the critical base inclination of each slice is determined based on the principle of optimality. They considered three cases: (1) $\psi = \phi$, (2) $\psi = \pi/4 + \phi/2$, and (3) $\psi = \psi_{\text{opt}}$. The results of case 1 are lower than those of Terzaghi [384], whereas those of cases 2 and 3 are slightly higher compared to those of Meyerhof [229, 232]. They proposed the following analytical expressions

$$N_\gamma = \begin{cases} (2N_q + 1) \tan^{1.35} \phi & \text{case 1} \\ (2N_q + 1) \tan(1.07\phi) & \text{case 2} \\ (2N_q + 1) \tan^{1.45} \phi & \text{case 3} \end{cases} \quad (2.18)$$

Silvestri [352] proposed a limit equilibrium analysis based on a Prandtl type failure mechanism (Table 2.7). He considered the possibility of non-associated flow rules based on the outcomes of Davis [65], and Drescher and Detournay [82] (cf. section 2.4.2). Silvestri optimised the angle of the trapped wedge and that of the logarithmic spiral sector. He obtained $\psi_{\text{opt}} \approx 22^\circ + 0.8\phi$.

Method of stress characteristics

The results presented in this section are summarised in Table 2.8. A general procedure to construct the field of stress characteristics was given by Lundgren and Mortensen [201]. The partial stress field obtained involves a trapped non-plastic curved wedge beneath

Table 2.7 – Bearing capacity factor ($N_\gamma = 2pf/(\gamma B)$) for perfectly rough footings obtained with the limit equilibrium method.

ϕ [deg]	Ritter (1936)	Palmer (1938)	Terzaghi (1943) ^a	Meyerhof		Janbu (1957)	Zhu et al. (2001)			Silvestri (2003)
				(1951) ^b	(1955)		case 1	case 2	case 3	
5	0.229	0.620	0.5	0.05	–	0.448	0.139	0.385	0.107	–
10	0.606	1.75	1.2	0.6	–	1.29	0.552	1.12	0.453	–
15	1.23	3.83	2.5	1.8	1.1	2.88	1.49	2.54	1.31	–
20	2.26	7.71	5.0	4.8	2.8	5.88	3.50	5.31	3.37	–
25	3.98	15.2	9.7	10.7	6.9	11.7	7.87	10.9	7.86	9.15
30	6.93	30.1	19.7	22.9	16.0	23.5	17.7	22.9	17.6	19.5
35	12.1	62.0	42.4	58.4	40.0	48.9	41.0	50.2	40.2	43.8
40	21.6	136	100	116	90	108	102	119	97.9	107
45	39.8	323	298	305	256	259	279	313	264	293

^a After [23].^b Taken from [226].

the base, which extent increases with increasing interface friction angle δ . For surface footings on cohesionless materials, this wedge never spans over the entire base and a family of stress characteristics becomes tangential to the base. The solution of Lundgren and Mortensen pointed out that the existence of a trapped wedge arises “naturally” when constructing the network of slip lines complying with the symmetry conditions with respect to the footing centre line. As already mentioned, some authors imposed a predefined geometry of the trapped wedge, and then constructed the field of stress characteristics. This approach has two consequences. First, from a theoretical point of view, it leads necessarily to wrong solutions [217, 364], because the problem has been modified in a new one, i.e. a wedged indenter with interface friction angle $\delta = \phi$. Second, a theorem due to Drucker [85] states that the collapse load of a footing is bounded above by the limit load for no relative motion at the interface, thus higher bearing capacity factors have to be expected. In Table 2.8, it can be noticed that the assumption of a predefined triangular trapped wedge yields higher results.

Brinch Hansen [25] proposed the analytical expression (2.19) for the factor N_γ [¶] based on the idea that the actual factor should lie between a lower bound obtained through the procedure of Lundgren and Mortensen and an upper bound given by the values of Meyerhof [232]. The reason for this could be attributed to the erroneous statement made by Brinch Hansen that the rupture figure of Lundgren and Mortensen is not kinematically admissible, presumably motivated by the idea that the trapped wedge should spans over the entire base. However, Larkin [192] demonstrated that the mechanism is kinematically admissible and Martin [217] showed that the procedure of Lundgren and Mortensen leads to the exact solution.

$$N_\gamma = 1.8(N_q - 1) \tan \phi \quad (2.19)$$

Later, in a lecture given in Japan in 1968 (reprinted in [26]), Brinch Hansen proposed a revised formula intended to match the results obtained with the rupture figure of Lundgren and Mortensen, which is

$$N_\gamma = 1.5(N_q - 1) \tan \phi \quad (2.20)$$

Based on the rupture figure of Lundgren and Mortensen, Hansen and Christensen [133] gave the values of N_γ in graphical form for any value of interface roughness ($0 \leq \delta \leq \phi$).

[¶]This is actually a better approximation of a formula proposed by Brinch Hansen in 1955, which was based on the unique value of N_γ given by Lundgren and Mortensen [201]: $N_\gamma = N_q - 1$.

Bolton and Lau [15] adopted $\psi = \pi/4 + \phi/2$, whereas Graham and Stuart [120] used $\psi = \phi$. Caquot and K  risel applied their theory of lateral earth thrust against retaining walls adapted to the geometry of surface footings. They considered both the case with imposed trapped wedge defined by $\psi = \pi/4 + \phi/2$ [38], and the case with perfectly rough base [37]. Vesic [397] suggested a formula that approximates on the safe side the results of Caquot and K  risel [38] (not exceeding 10 % for $15^\circ < \phi < 45^\circ$ and not exceeding 5 % for $20^\circ < \phi < 40^\circ$)

$$N_\gamma = 2(N_q + 1) \tan \phi \quad (2.21)$$

Graham and Stuart [120], in addition to the case of an imposed trapped wedge, studied the cases of constant and variable δ at the soil-footing interface, from $\delta = 0$ at the centreline to $\delta = \phi$ at the corner. Their solution for perfectly rough bases appears erroneous, because the resulting trapped wedge is quite different from the solution of Lundgren and Mortensen and the resulting values of the bearing capacity factor are undoubtedly too high, $N_\gamma = 63.3$ for $\phi = 35^\circ$ compared to 34.5 of the exact solution [217].

Although a variation of δ along the base is probably a real phenomenon, with a higher value at the corner due to a lower level of confinement, the adoption of such a variable δ is questionable. First of all, a variation from 0 to ϕ seems unrealistic. Second, they justify its variation by some condition of stress distribution across the centreline of the footing (plane of symmetry). However, this means that the angle δ that they used is not the interface shear strength angle, but rather the mobilised shearing angle, which increases from zero at the footing centre to δ at the edge of the trapped wedge (see [181, 215, 364] for a detailed description). Therefore, the solution obtained with the method of characteristics is necessarily wrong, because the method is based on the combination of equilibrium equations and yield condition, and if the angle is not the interface shear strength angle, the equations are actually not describing the point of yield. Martin [217] also concluded that their solution is wrong.

Salen  on [333] obtained values of N_γ for perfectly rough footings with the method of characteristics that are in close agreement with the exact solution. Kumar [179] obtained slightly higher results. This could be explained by the fact that, when employing the method of characteristics, it is numerically convenient to consider the N_γ problem as a limiting case of the bearing capacity of shallow footings on cohesionless soils [15, 66, 120, 191, 215, 217]:

$$N_\gamma = \lim_{\frac{\gamma B}{q} \rightarrow \infty} \frac{2p_f}{\gamma B} \quad (2.22)$$

where q is the uniform overburden pressure. Martin [215, 217] showed that a $\gamma B/q$ ratio of 10^9 is large enough for a 4-digit precision. The results obtained by Kumar [179] have values of $\gamma B/q$ that range from 1.3 for $\phi = 5^\circ$ to 143 for $\phi = 50^\circ$. This explains also why the precision of his results increases with increasing ϕ (Table 2.8).

Solutions obtained by Davis and Booker [66] for perfectly rough bases were approximated by Poulos [287] with

$$N_\gamma = 0.1045e^{9.6\phi} \quad (2.23)$$

Kumar [181] obtained N_γ for any value of interface roughness. The latter results for $\delta = \phi$ are better compared to those obtained previously [179]. This could be attributed to the higher values of the parameter $\gamma B/q$, which was seen to vary between 10^2 and 10^5 , compared to 1.3 and 143 used earlier, and likely to an increased refinement of the finite difference mesh.

The values of the bearing capacity factor given by Han et al. [130] for $\delta = \phi$, obtained as explained previously, match the exact solution (Table 2.8). The proposed analytical expression takes the same form as (2.8), but now $N_{\gamma,\max} = N_{\gamma,\max,\text{rough}} = 2N_{\gamma,\max,\text{smooth}}$ ($N_{\gamma,\max,\text{smooth}}$ is given by (2.9)), $a_0 = 0.142$, $a_1 = 1.065$, $a_2 = -1.047$, $a_3 = 0.441$, and $a_4 = -0.0719$. The variation of the ratio $R_{N_\gamma} = N_{\gamma,\text{smooth}}/N_{\gamma,\text{rough}}$, which is very close to that obtained by Hjaiaj et al. [149] (see below), decreases with increasing ϕ , and for $\phi = 45^\circ$ is 0.5. It is noteworthy that $0.6 \geq R_{N_\gamma} \geq 0.5$ for $15^\circ \leq \phi \leq 45^\circ$.

Table 2.8 – Bearing capacity factor ($N_\gamma = 2p_f/(\gamma B)$) for perfectly rough footings obtained with the method of characteristics.

ϕ [deg]	Caquot and Kérisel (1953) ^a	Lundg. and Morten. (1953)	Caquot and Kérisel (1956)	Hansen and Chris. (1969) ^b	Davis and Booker (1971) ^b	Salen. and Matar (1982)	Bolton and Lau (1993) ^a	Kumar (2003)	Kumar (2009)	Han et al. (2016)
5	–	–	–	–	–	–	0.62	0.23	0.114	0.113
10	1.60	–	0.88	–	0.46	0.434	1.71	0.69	0.430	0.433
15	2.98	–	1.76	1.2	1.2	–	3.17	1.60	1.17	1.18
20	5.69	–	3.51	2.9	2.9	2.84	5.97	3.43	2.82	2.84
25	11.2	–	7.17	7.0	6.1	6.49	11.6	7.18	6.46	6.49
30	22.7	14.8	14.8	15.0	15.0	14.8	23.6	15.6	14.7	14.8
35	49.1	–	32.9	35.0	35.0	34.5	51.0	35.2	34.3	34.5
40	114	–	78.1	85.0	83.0	85.5	121	85.7	85.1	85.6
45	300	–	169	230	200	234	324	233	233	234

^a Imposed trapped wedge.^b Read from graphical representation.

Limit analysis method

Chen [49] obtained upper bounds for any value of δ based on the minimum between optimised Hill and Prandtl type failure mechanisms. Energy dissipation due to friction was computed as the product between the friction force and the tangential component of the relative velocity at the interface. For the case of optimum Prandtl type failure mechanism, he suggested $\psi_{\text{opt}} = 15^\circ + \phi$ within 5 % and proposed the following expression, which is within 6 % for $20^\circ \leq \phi \leq 40^\circ$ and within 8 % for $15^\circ \leq \phi \leq 45^\circ$

$$N_\gamma = 2(N_q + 1) \tan\left(\frac{\pi}{4} + \frac{\phi}{5}\right) \tan \phi \quad (2.24)$$

Kumar [180] idealised the interface as an infinitely thin layer of associated material defined by a cohesionless Mohr-Coulomb criterion with shear strength angle δ . Drescher and Detournay [82] showed that for translational failure mechanisms both approaches to consider interface friction are rigorous upper bounds and, moreover, are equivalent. The mechanisms used by Chen can be considered translational because he showed that the dissipation in the radial shear regions can be computed as the limit of an infinite number of rigid blocks. Figure 2.3 shows that in both approaches base friction has the same impact on the bearing capacity coefficient. The slight increase of the gap between the two solutions is attributable to a better optimisation of the geometry in the mechanism suggested by Kumar [180].

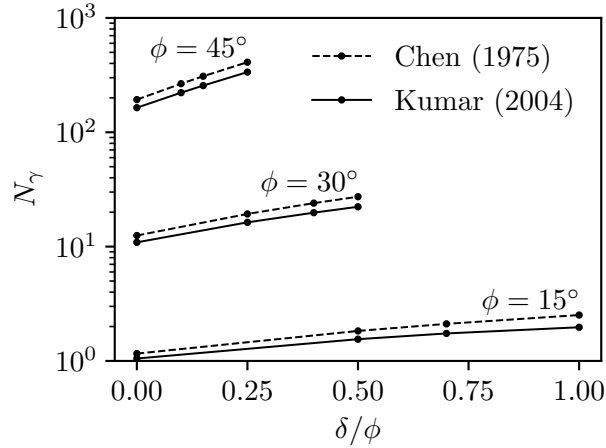


Figure 2.3 – Comparison of bearing capacity factor N_γ with respect to interface friction δ/ϕ for surface strip footings on cohesionless soils obtained by Chen [49] and Kumar [180].

Michalowski [233] obtained better upper bound solutions for perfectly rough footings assuming a multi-block Prandtl type failure mechanism, which does not constraints the radial shear zone to a logarithmic spiral curve. His results can be estimated with (2.25)

within 1 % for ϕ from 25° to 50° .

$$N_\gamma = e^{0.66+5.11 \tan \phi} \tan \phi \quad (2.25)$$

Michalowski gave also results for non-associated materials through relations (2.53) and (2.54). Soubra [368] adopted a multi-block failure mechanism close to that of Michalowski [233], except for the fact that the external triangles are not assumed isosceles *a priori*. However, the results are slightly higher with respect to those of Michalowski. The difference is probably due to the number of blocks adopted. Wang et al. [403] computed upper bounds for perfectly rough strip footings with a multi-block Prandtl type failure mechanism not only based on triangular blocks, but also quadrilateral. They obtained higher values compared to those of Michalowski [233].

It is noteworthy that according to Chen [49] and Kumar [180], the value of δ/ϕ needed to mobilize the full friction decreases continuously with increasing ϕ . On the other hand, the stress characteristics solution [181, 217, 364] showed that for a given value of ϕ , N_γ continuously increases with δ . For instance, for $\phi = 30^\circ$, according to Chen [49] and Kumar [180] the bearing capacity does not increase for $\delta \geq 0.5\phi$. This is actually due to the fact that for the assumed Prandtl type failure mechanism, the trapped wedge spans over the entire footing and is not a function of δ . Therefore, when this mechanism is governing over the Hill type failure mechanism, the bearing capacity is fixed. On the other hand, in the slip lines solution, the width and geometry of the trapped wedge depends upon δ .

Numerical upper bounds computed with the finite elements method were obtained for perfectly rough footings using linear programming [363, 389], non-linear programming [149], second-order cone programming [202, 208], and for any value of base roughness using linear programming [184]. Lower bounds for perfectly rough footings were obtained using linear programming [363, 389], non-linear programming [149], second-order cone programming [202, 207], and for any value of base roughness using linear programming [183]. The bracketing of the exact solution obtained by Hjjaj et al. [149] is quite close, and they proposed the following analytical expression to estimate the exact N_γ for perfectly rough footings, evaluated as the mean value between their lower and upper bounds

$$N_\gamma = e^{\frac{1}{6}(\pi+3\pi^2 \tan \phi)} \tan^{\frac{2}{3}\pi} \phi \quad (2.26)$$

The supposedly rigorous lower bounds of Hjjaj et al. for $\phi < 15^\circ$ lie slightly above

the exact values [218]. The difference is in the third digit, thus this could be due to numerical approximations and round off errors. It is interesting to note that the trapped wedge compute by Hjiat et al., both with the lower and upper bound, is bounded by a curved line which becomes tangential to the base, as obtained with the method of characteristics. The better upper bounds obtained by Hjiat et al. with respect to Kumar [184] for perfectly rough bases shown in Table 2.9 indicate the superiority of carrying out non-linear optimisation.

Assuming no relative slip, and eventually also the geometry of the trapped wedge, is theoretically not justified [217], if not by the need to obtain absolute upper bounds to any problem of indentation, which might be a useful information.

Martin demonstrated that the partial field of stress characteristics, for any value of base roughness, can be extended throughout the rigid body in an admissible manner and that the solutions coincide with the upper bounds obtained with the associated velocity characteristics [215, 217]. He gave results for the specific cases $\delta/\phi = 1/2, 2/3$ and 1 in tabulated form [218]. The same year, Smith [364] independently obtained rigorous lower bound solutions which match the exact values. He gave tabulated results for $\delta/\phi = 1/2$ and 1. Smith proposed the following formula for perfectly rough footings, which is within 1 % over the range 20° to 50° . The error reaches 3 % at 15° and 55° .

$$N_\gamma = 1.75 \left(e^{(0.75\pi + \phi) \tan \phi} N_\phi - 1 \right) \tan \phi \quad (2.27)$$

Salgado [202] proposed a simpler equation to fit the exact values obtained by Martin, which basically is just a little improvement of Meyerhof's equation (2.15):

$$N_\gamma = (N_q - 1) \tan(1.32\phi) \quad (2.28)$$

Loukidis and Salgado [199] performed classical incremental finite element analyses with the code SNAC, modelling the soil as a homogeneous isotropic linear elastic-perfectly plastic material. They investigated also the effect of the flow rule. For an associated material, they computed bearing capacity factors for $\phi = 30^\circ, 35^\circ, 40^\circ$ and 45° , and obtained $N_\gamma = 15.2, 35.5, 87.7$ and 240, which match very well the exact solution (Table 2.11). The fact that the results are constantly higher might be explained with the no-slip constraint imposed at the footing interface. They approximated the results with the expression

$$N_\gamma = (N_q - 1) \tan(1.34\phi) \quad (2.29)$$

Figure 2.4 shows that the range of proposed bearing capacity factors N_γ is quite wide,

Table 2.9 – Bearing capacity factor ($N_\gamma = 2p_f/(\gamma B)$) for perfectly rough footings obtained with the upper bound limit analysis.

ϕ [deg]	Chen (1975)	Sloan and Yu (1996) ^a	Micha. (1997)	Soubra (1998)	Wang et al. (2001)	Ukritch. et al. (2003)	Kumar (2004)	Hjiaj et al. (2005)	Makro. and Martin (2007)	Kumar and Kouzer (2007)	Lyamin et al (2007)
5	0.382	–	0.181	–	–	0.12	0.181	0.120	0.118	0.13	–
10	1.16	–	0.706	–	1.67	0.47	0.706	0.455	0.447	0.49	–
15	2.73	2.5	1.94	1.95	3.53	1.31	1.94	1.24	1.22	1.32	–
20	5.87	5.0	4.47	4.49	6.56	3.27	4.47	2.96	2.96	3.16	–
25	12.4	11.3	9.77	9.81	12.3	7.52	9.77	6.74	6.86	7.26	7.09
30	26.7	20.0	21.4	21.5	24.2	17.4	21.4	15.2	16.0	16.5	15.9
35	60.2	50.0	48.7	49.0	50.9	42.4	48.7	35.6	38.8	39.0	37.0
40	147	120	119	120	123	111	119	88.4	104	98.5	91.9
45	401	–	323	327	331	315	323	241	309	280	255

^a Read from graphical representation.

Table 2.10 – Bearing capacity factor ($N_\gamma = 2p_f/(\gamma B)$) for perfectly rough footings obtained with the lower bound limit analysis.

ϕ [deg]	Sloan and Yu (1996) ^a	Ukritchon et al. (2003)	Hjiaj et al. (2005)	Makro. and Martin (2005)	Smith (2005)	Lyamin et al. (2007)	Kumar and Khatri (2008)
5	–	0.11	0.115	0.112	–	–	0.11
10	–	0.41	0.434	0.427	–	–	0.40
15	1.0	1.13	1.18	1.17	1.18	–	1.09
20	2.5	2.67	2.82	2.81	2.84	–	2.65
25	6.3	5.95	6.43	6.45	6.49	6.44	6.02
30	12.5	13.2	14.6	14.7	14.8	14.6	13.7
35	32.5	29.3	34.0	34.2	34.5	33.8	31.9
40	63.8	69.9	83.3	84.7	85.6	82.3	77.9
45	–	165	225	231	234	222	205

^a Read from graphical representation.

and that the majority of them overestimate the exact solution. It is noteworthy that the solution provided by Meyerhof [229] with ψ_{opt} match very well the exact solution.

Table 2.11 – Exact bearing capacity factor ($N_\gamma = 2p_f/(\gamma B)$) for perfectly rough footings, [218].

ϕ [deg]	5	10	15	20	25	30	35	40	45
N_γ	0.113	0.433	1.18	2.84	6.49	14.8	34.5	85.6	234

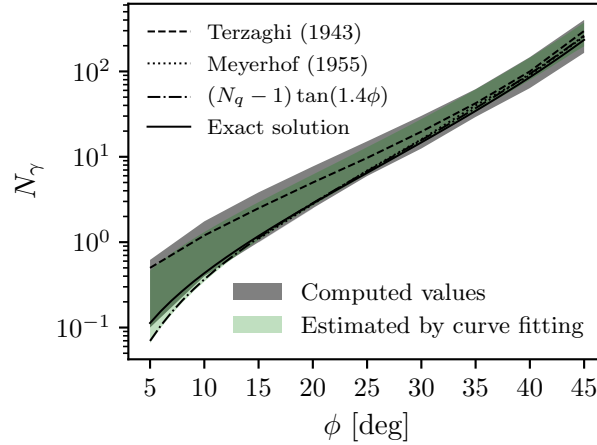


Figure 2.4 – Bearing capacity factor N_γ for perfectly rough surface footings on cohesionless soils. The grey region, named Computed values, defines the range of all values derived from a mechanical analysis (except Ritter results), whereas the green domain, named Estimated by curve fitting, defines the region of all analytical formulae derived by curve fitting.

Real footings are not perfectly rough, but it could be expected that $0.5 \leq \delta/\phi \leq 1$. The ratio R_{N_γ} between the bearing capacity factor for partly rough footings $N_\gamma(\delta/\phi < 1)$ and perfectly rough footings $N_\gamma(\delta/\phi = 1)$ is shown in Figure 2.5. According to the exact solution, the reduction of the bearing capacity does not exceeds 10 % for $\delta/\phi = 2/3$ and 20 % for $\delta/\phi = 1/2$. Solutions proposed by other authors, defined by the filled area in the figure, show a slightly higher variability. Therefore, the assertion of Meyerhof [232] that in practice the base can always be taken as perfectly rough is verified.

2.2.4 Ponderable Mohr-Coulomb Material — c – ϕ – γ soil

General soils in drained conditions are usually better characterised by a Mohr-Coulomb yield criterion with cohesion and shear strength angle. The optimum geometry of the failure mechanism is thus function of the shear strength angle, the cohesion, the footing width and the soil self-weight [384]. Introducing the dimensionless soil weight parameter $G = 0.5\gamma B/c$ [62], the normalised bearing capacity writes

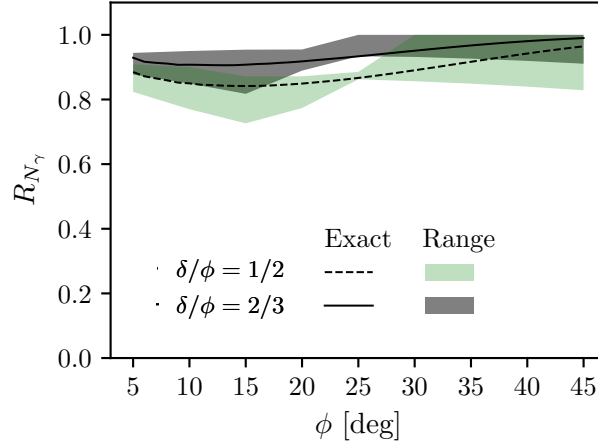


Figure 2.5 – Ratio $R_{N_\gamma} = N_\gamma(\delta/\phi)/N_\gamma(\delta/\phi = 1)$ versus shear strength angle ϕ . The filled areas define the range of values presented, namely those given by [49, 181, 183, 218, 229].

$$\frac{p_f}{c} = N_c + GN_\gamma \quad (2.30)$$

The nature of the problem is such that the self-weight cannot weaken the material against the indentation pressure. This means that $N_c(\gamma) + GN_\gamma(\gamma) \geq N_c(\gamma = 0)$, and therefore (2.1) is a lower bound to the average strip pressure on a general ponderable soil, regardless of base roughness.

Given that the bearing capacity factors N_c and N_γ depend upon the geometry of the failure mechanism, and that the latter is affected by ϕ and G , they cannot be expressed as a function of ϕ alone. However, Terzaghi [384] suggested to apply the principle of superposition on a predefined geometry of the failure mechanism, and to compute each component on the assumption that the surface of sliding corresponds to the conditions for that particular component, i.e. $N_c(\gamma = 0, \phi)$ and $N_\gamma(c = 0, \phi)$. The same was assumed by Meyerhof [232], but with a different geometry of the failure mechanism, and by many others. Later, Meyerhof [229] proposed to optimise the geometry of the failure mechanism for each component computed separately. This approach was adopted by Terzaghi himself [385], and is common in design practice. It is noteworthy that the bearing capacity factors are computed according to two different sliding surfaces.

The main advantages of the superposition method are that the bearing capacity coefficients can be expressed as a function of ϕ alone, and that the sum of the minima is lower than the consistent minimum. This because G affects N_γ more than N_c , and N_γ has its lowest value for $\lim_{G \rightarrow \infty} N_\gamma$, i.e. for a cohesionless soil [233, 384, 385] (cf. Figure 2.7).

From a theoretical perspective, however, it is interesting to know the solution cor-

responding to a consistent failure mechanism. This is the only possibility for a reliable comparisons between theory and experimental data^{||}. In the following, such coefficients are presented.

Smooth Footing

Solutions based on the method of stress characteristics generally adopt the approach of Sokolovskii [366, 367], where the soil is considered cohesionless but subjected to a hydrostatic pressure $c \cot \phi^{**}$. Charts covering a wide range of soil parameters based on this method were given by Ko and Scott [169] (Table 2.12). Cox [62] also obtained the partial stress field with the method of characteristics and provided values of the normalised bearing capacity p_f/c . The same year, Spencer [370] applied the perturbation method. The results of Cox and Spencer are reported in Table 2.13, where it can be seen that they match very well, although the values of Spencer are slightly higher for increasing ϕ . Considering that the values of Ko and Scott were read from graphical representation, it can be concluded that they are nearly the same as those provided by Cox.

Table 2.12 – Normalised bearing capacity (p_f/c) for smooth footings, [169]. The results were read from graphical representation.

ϕ [deg]	G			
	1	2	4	10
5	6.5	6.5	7.1	7.8
10	9.2	9.2	10.8	14.2
15	12.1	13.2	16.5	23.1
20	17.8	19.3	26.7	38.6
25	26.9	29.0	41.4	70.4
30	42.2	45.2	75.3	133
35	69.2	96.9	148	258
40	143	196	301	565
45	295	455	723	–

Larkin [192] provided upper bound solutions based on the velocity field derived with the method of characteristics, but only for $\phi = 40^\circ$ (Table 2.14). The results of Cox, and of Ko and Scott for the given precision, are almost identical to the upper bound solution

^{||}It should be said that such a comparison is complicated by the intrinsic difficulty to evaluate the appropriate physical properties and the fact that soil shear strength parameters are affected by the testing technique.

^{**}Note that this is not an application of the Caquot rule of equivalent states [36], because the hydrostatic stress $c \cot \phi$ is not simply added to the solution of a cohesionless soil, but enters in the formulation of the problem. For a comprehensive description on the applicability of the rule of corresponding states, see [234].

Table 2.13 – Normalised bearing capacity (p_f/c) for smooth footings. (i) [62]; (ii) [370].

ϕ [deg]	G					
	0.01	0.1		1		10
	(i)	(i)	(ii)	(i)	(ii)	(i)
0	5.14	5.14	5.14	5.14	5.14	5.14
10	8.35	8.42	8.42	9.02	9.07	13.6
20	14.9	15.2	15.2	17.9	18.3	37.8
30	30.3	31.6	31.7	42.9	45.3	127
40	76.1	83.0	83.5	139	157	574

given by Larkin. The differences are likely due to round off errors. Their solution is exact, because Martin [217] showed that the solution obtained with the method of stress characteristics is complete (cf. Table 2.15).

Table 2.14 – Normalised bearing capacity (p_f/c) for smooth footings, [192].

ϕ [deg]	G						
	0.1	0.2	0.4	1	2	4	10
40	83.3	90.4	104	139	193	293	573

Table 2.15 – Exact normalised bearing capacity (p_f/c) for smooth footings, [215].

ϕ [deg]	G							
	0.01	0.1	0.2	0.4	1	2	4	10
5	6.49	6.51	6.54	6.59	6.73	6.95	7.36	8.45
10	8.35	8.42	8.49	8.63	9.02	9.63	12.8	13.6
15	11.0	11.1	11.3	11.6	12.5	13.8	16.1	22.2
20	14.9	15.2	15.5	16.1	17.9	20.5	25.3	37.8
25	20.8	21.4	22.1	23.4	26.9	32.2	41.7	67.2
30	30.3	31.6	33.0	35.7	42.9	53.7	73.3	127
35	46.5	49.4	52.5	58.2	73.6	96.8	139	257
40	76.1	83.1	90.3	104	139	193	293	573
45	136	155	173	207	299	438	699	1447

Chen [49] gave upper bound solutions based on a Hill type failure mechanism. He provided graphical results and also the objective function of the normalised bearing capacity p_f/c . It is the writer opinion that the formula provided by Chen for the coefficient N_c is not correct. In fact, it is found that $\lim_{\phi \rightarrow 0^+} p_f/c \neq 2 + \pi$, which is known to be the exact solution ($\lim_{\phi \rightarrow 0^+} N_\gamma = 0$ and thus the error must be in N_c). Moreover, in a few cases, for small values of ϕ the bearing capacity is slightly higher than that computed

with a Prandtl type failure mechanism, which violates Drucker's frictional limit theorems [85]. In the following, the results attributed to Chen for the Hill type failure mechanism (Table 2.16) are based on a formulation of N_c derived by the author (Appendix A). The results of Chen for either $\phi \leq 20^\circ$ or $G \leq 0.2$ are in good agreement with the exact solutions.

Table 2.16 – Normalised bearing capacity (p_f/c) for smooth footings, [49].

ϕ [deg]	G							
	0.01	0.1	0.2	0.4	1	2	4	10
5	6.49	6.51	6.54	6.59	6.73	6.97	7.41	8.64
10	8.35	8.42	8.49	8.63	9.04	9.71	10.9	14.3
15	11.0	11.1	11.3	11.6	12.5	14.0	16.8	24.5
20	14.9	15.2	15.5	16.2	18.1	21.2	26.9	43.4
25	20.8	21.4	22.1	23.5	27.4	33.7	45.8	80.8
30	30.3	31.6	33.1	36.0	44.3	57.6	83.4	159
35	46.5	49.5	52.7	59.1	77.5	107	165	337
40	76.1	83.3	91.2	106	151	222	364	786
45	136	156	176	217	336	531	919	2078

Han et al. [130] adopted the formulation of the problem already employed by Zhu et al. [411], and then they solved it with the method of stress characteristics. This approach is based on that of Sokolovskii (cohesionless soil but subjected everywhere to a hydrostatic pressure $c \cot \phi$), and the assumption that N_c and N_q , where $N_q = e^{\pi \tan \phi} N_\phi$ is the bearing capacity factor due to the overburden pressure obtained by Reissner [305] for a weightless material, are not affected by the soil self-weight, so that the relation $N_c = (N_q - 1) \cot \phi$ holds. The ultimate mean pressure may then be written as

$$\bar{p}_f = \lambda N_q + \frac{1}{2} N_\gamma \quad (2.31)$$

where $\bar{p}_f = (p_f + c \cot \phi) / \gamma B$ is the normalised bearing capacity, and $\lambda = (q + c \cot \phi) / \gamma B$ is the surcharge ratio ($q = 0$ for surface footings and thus $\lambda = 0.5 \cot \phi / G$). According to (2.31), N_γ is affected by ϕ and λ , and thus by G . However, this approach cannot be considered consistent with one failure mechanism, given that N_c is assumed constant. Nevertheless, the approach can be justified by the fact that λ affects more N_γ than N_c or N_q , as mentioned above. Han et al. gave tabulated results as a function of ϕ and λ , and proposed the following analytical expression

$$N_\gamma = N_{\gamma, \min} + \frac{N_{\gamma, \max} - N_{\gamma, \min}}{1 + \left(\frac{A_0}{\lambda}\right)^p} \quad (2.32)$$

where $N_{\gamma,\min}$ is the factor for a cohesionless soil ($\lambda = 0$) and is given by (2.8), $N_{\gamma,\max}$ is the factor for a cohesionless soil computed assuming the failure mechanism of a weightless material and is given by (2.9), $p = 0.75$, and A_0 is

$$A_0 = \sum_{i=0}^3 \beta_i \tan^i \phi \quad (2.33)$$

with $\beta_i = 0.188, 0.102, 0.101$ and 0.222 .

Rough footing

Larkin [192] computed upper bounds for perfectly rough footings by associating the velocity characteristics to the stress characteristics derived by Lundgren and Mortensen [201], and equating the rate of internal energy dissipated by such velocity fields to the rate of external work done by the footing pressure (Table 2.17). He noticed that for $\phi = 40^\circ$, $G = 18.76$ is the upper limit for which the condition of no relative slip at the interface is met. Motivated by the idea that the trapped wedge should span over the entire base, he concluded that the correct stress and velocity characteristics were not known for $G > 18.76$. This conclusion is incorrect. The transition from a condition of no relative slip at the interface depends upon the geometry (plane strains or axial symmetry), the shear strength angle, and the dimensionless parameter $F = 2G \tan \phi$ [66, 215, 217, 364]. For instance, for $\phi = 30^\circ$, the threshold is $G = 9.509$.

Table 2.17 – Normalised bearing capacity (p_f/c) for perfectly rough footings, [192].

ϕ [deg]	G						
	0.1	0.2	0.4	1	2	4	10
40	90.5	104	127	192	292	484	1020

Chen [49] computed upper bounds of the bearing capacity for any value of interface roughness, based on the governing mechanism between the Hill and the Prandtl type rupture figures. For perfectly rough footings (Table 2.18), the Prandtl type is always governing. The ratio $R_{p_f/c} = \frac{p_f(\delta/\phi)}{c} / \frac{p_f(\delta/\phi=1)}{c}$ is shown in Figure 2.6. Evidently, the effect of footing roughness reduces with reducing G , because interface friction does not have any influence on the bearing capacity of Tresca materials. For $\phi \geq 30^\circ$, $\delta/\phi = 1/2$ is sufficient to mobilise the Prandtl type failure mechanism. The lower limit of $R_{p_f/c}$ is given by a cohesionless soil (cf. Figure 2.5). Based on the results for cohesionless soils, it can be inferred that the results of Chen underestimate $R_{p_f/c}$ for $\phi < 25^\circ$ and

overestimate it for $\phi \geq 30^\circ$. The reason is the relatively constrained geometry of the rupture figures, whereas the exact solution obtained through the method of the stress characteristics allows for a continuous transition between the two extreme mechanisms.

Table 2.18 – Normalised bearing capacity (p_f/c) for perfectly rough footings, [49].

ϕ [deg]	G							
	0.01	0.1	0.2	0.4	1	2	4	10
5	6.49	6.54	6.59	6.68	6.97	7.42	8.29	10.7
10	8.36	8.49	8.63	8.91	9.72	11.0	13.5	20.6
15	11.0	11.3	11.6	12.3	14.1	16.9	22.6	39.1
20	14.9	15.5	16.2	17.5	21.5	27.3	39.2	74.6
25	20.9	22.1	23.5	26.2	34.0	46.6	71.6	146
30	30.4	33.1	36.0	41.7	58.2	85.2	139	299
35	46.8	52.7	59.2	71.7	108	169	290	651
40	76.9	91.2	107	137	226	373	667	1547
45	138	177	218	299	541	942	1743	4146

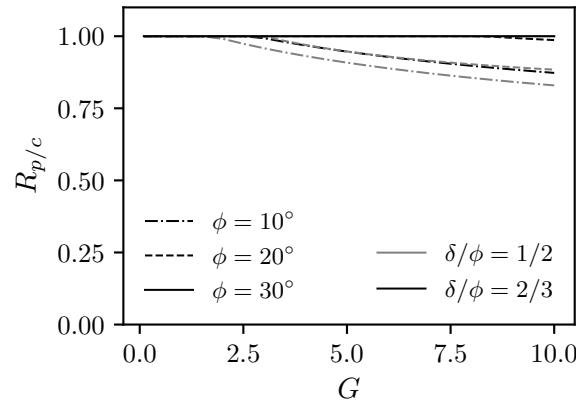


Figure 2.6 – Ratio $R_{p/c} = \frac{p_f(\delta/\phi)}{p_f(\delta/\phi=1)}$ versus G according to the Hill and Prandtl type failure mechanisms computed by Chen [49].

Michalowski [233] gave the bearing capacity according to one consistent multi-block Prandtl type failure mechanism only for $\phi = 15^\circ$ and 35° (Table 2.19). The results of Chen for $G = 0.1$ are nearly the same, and it can be inferred that also for $G = 0.25$ and 0.5 they are in good agreement, even though discrepancies increase. This is obvious because for $G \rightarrow 0$, i.e. weightless soil, the exact solution is given by the geometry of the Prandtl failure mechanism, therefore the multi-block failure mechanism converges toward the continuous rupture figure delimited by a logarithmic spiral with focus at the footing

corner. On the other hand, for increasing G , it is known that the exact deforming region is delimited by curved lines, and therefore the multi-block solution, with higher degree of freedom in its geometry, yields better results.

Table 2.19 – Normalised bearing capacity (p_f/c) for perfectly rough ($\delta = \phi$) footings, [233].

ϕ [deg]	G		
	0.1	0.25	0.5
15	11.3	11.8	12.5
35	52.6	61.4	75.3

Zhu et al. [411] adopted a trapped wedge with $\psi = \pi/4 + \phi/2$ and solved the problem with the so called slip field method, which is within the limit equilibrium method, based on the considerations expressed above concerning N_c and N_q . Han et al. [130] used the same problem formulation (equation (2.31)) but solve it with the stress characteristics for perfectly rough footings. Both gave results as function of ϕ and λ . The assumption of a triangular wedge underneath the whole base is the reason for higher bearing capacities computed by Zhu et al (cf. Table 2.20).

The analytical expression derived by Han et al. takes the same form as (2.32), $N_{\gamma,\min}$ is given by (2.8) with the coefficients β_i for rough footings given in the corresponding section, $N_{\gamma,\max}$ is twice the value given by (2.9), $p = 0.75$, and A_0 is given by (2.33) with coefficients $\beta_i = 0.354, 0.042, 0.648$ and 0.220 .

As shown by Martin [217], the exact bearing capacity is given by the field of stress characteristics constructed according to Lundgren and Mortensen [201], and can be obtained through ABC [215]. This explains why the solutions given by Larkin [192] match the exact solution^{††} (the differences are negligible and can be attributed to numerical reasons).

Figure 2.7 shows the ratio of the normalised bearing capacity p_f/c computed according to the method of superposition with the exact bearing capacity factors and the exact solution based on one consistent failure mechanism. The results show that for the considered range of ϕ and G , this ratio varies between 0.74 and 0.99. For the common domain $15^\circ \leq \phi \leq 30^\circ$ and $0.1 \leq G \leq 1$, the ratio lies between 0.85 and 0.99. An underestimate of around 10 % to 15 % is the usual admitted value.

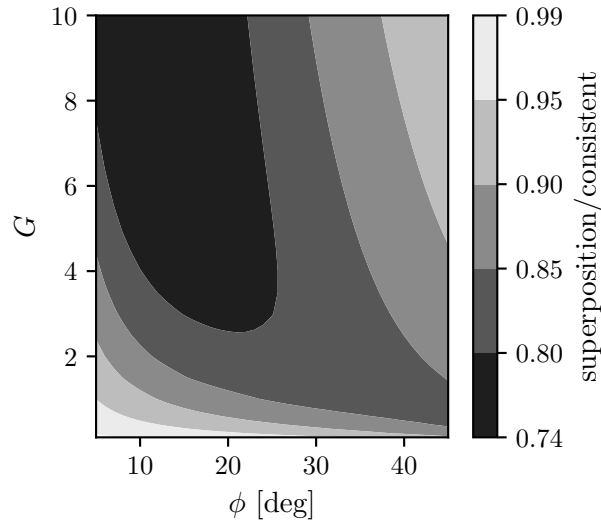
^{††}The results given for $\phi = 40^\circ$ and $G \geq 18.76$, on the other hand, do not match the exact solution, because Larkin adopted the velocity field corresponding to $G = 18.76$ in order to satisfy the condition of no relative slip at the interface.

Table 2.20 – Normalised bearing capacity (p_f/c) for perfectly rough footings, [130, 411].

ϕ [deg]		λ				
		0.01	0.1	1	10	100
5	G	572	57.2	5.72	0.572	0.057
	Zhu	224	29.4	9.00	6.76	6.52
	Han	–	18.78	8.64	6.76	6.52
10	G	284	28.4	2.84	0.284	0.028
	Zhu	326	41.2	12.0	8.74	8.39
	Han	–	28.2	11.5	8.74	8.39
15	G	187	18.7	1.87	0.187	0.019
	Zhu	483	60.1	16.5	11.6	11.0
	Han	–	43.1	15.8	11.6	11.0
20	G	137	13.7	1.37	0.137	0.014
	Zhu	743	90.5	23.3	15.8	14.9
	Han	–	67.6	22.3	15.7	14.9
25	G	107	10.7	1.07	0.107	0.011
	Zhu	1191	142	34.4	22.2	20.9
	Han	–	110	32.9	22.2	20.9
30	G	86.6	8.66	0.866	0.087	0.009
	Zhu	2013	236	53.3	32.7	30.4
	Han	–	186	50.8	32.6	30.4
35	G	71.4	7.14	0.714	0.071	0.007
	Zhu	3637	419	88.0	50.8	46.6
	Han	–	336	83.7	50.7	46.6
40	G	59.6	5.96	0.596	0.060	0.006
	Zhu	7159	810	158.0	84.7	76.3
	Han	–	659	150	84.5	76.3
45	G	50.0	5.00	0.500	0.050	0.005
	Zhu	15 820	1757	317	155	136
	Han	–	1444	298	154	136

Table 2.21 – Exact normalised bearing capacity (p_f/c) for perfectly rough footings, [217].

ϕ [deg]	G							
	0.01	0.1	0.2	0.4	1	2	4	10
5	6.49	6.54	6.59	6.68	6.95	7.36	8.08	9.84
10	8.36	8.49	8.63	8.89	9.62	10.7	12.6	17.1
15	11.0	11.3	11.6	12.2	13.8	16.1	20.1	30.3
20	14.9	15.5	16.1	17.3	20.5	25.2	33.5	55.1
25	20.9	22.1	23.4	25.8	32.1	41.6	58.5	104
30	30.4	33.0	35.7	40.6	53.6	73.1	109	208
35	46.8	52.4	58.2	68.6	96.7	139	218	441
40	77.0	90.2	103	128	193	292	480	1020
45	138	173	207	269	438	699	1199	2649

**Figure 2.7** – Ratio between normalised bearing capacity p_f/c computed with the method of superposition of the exact bearing capacity factors and exact solution based on one consistent failure mechanism.

Derivation of Analytical Expressions for Perfectly Rough Footings

In the previous sections, it was shown that an analytical expression exists for the bearing capacity of purely cohesive soils and that some approximating functions were derived for cohesionless soils. To the author's knowledge, no attempts have been made in the same direction for general soils. In the following, two such expressions are derived, one (model function 1) covering a wide range of the domain $[\phi, G]$, but which is rather complex to manage, and one simpler (model function 2) covering only the most common values of $[\phi, G]$.

Theoretically, weightless soils correspond to $G \rightarrow 0$, whereas cohesionless soils to $G \rightarrow \infty$. Practically, these bounds can be set to 0.1 and 10, respectively. The shear strength angle can reasonably vary from 5° to 45° . These bounds fix the domain for the model function 1. For a number of practical situations involving general soils, G is comprised between 0.1 and 1 [49], and ϕ falls in the range 10° to 40° . Model function 2 is based on these last bounds. A data set of exact solutions of the normalised bearing capacity p_f/c were obtained with ABC. The step interval for ϕ was set to 1° , whereas for G an increment of 0.1 for $0.1 \leq G \leq 1$ and of 0.5 for $1 < G \leq 10$ was selected. This corresponds to 1148 values for model function 1 and to 310 values for model function 2.

Both model functions are obtained through linear least squares minimisation with TableCurve 3D [381]. The objectives of the model functions are to fit well the data points in a general sense, i.e. have high degree of freedom adjusted coefficient of determination ($R_{\text{DOF,adj}}^2$) and low fit standard error (S), and to provide a good local estimate of data points, i.e. low residual errors (ϵ). Moreover, the hypothesis of normally distributed residuals errors assumed by the least squares minimisation method is checked with a quantile-quantile plot (Q-Q plot).

Model function 1

The first model function covers the domain $5^\circ \leq \phi \leq 45^\circ$; $0.1 \leq G \leq 10$. In order to meet the aforementioned goals, a Chebyshev series of order 7 was selected, which may be written as follows

$$\frac{\hat{p}_f}{c} = \sum_{j=0}^7 \sum_{m=j}^0 c_k T_m(\tilde{x}) T_{j-m}(\tilde{y}) \quad (2.34)$$

where $\hat{\cdot}$ is the estimated value, c_k is the k -th estimated coefficient (cf. Table 2.22) with $k = \frac{(j+1)(j+2)}{2} - m - 1$, \tilde{x} is $x = \tan \phi$ scaled to the interval $[-1; 1]$

$$\tilde{x} = \frac{x - 0.5(x_{\min} + x_{\max})}{0.5(x_{\max} - x_{\min})}, \quad (2.35)$$

\tilde{y} is $y = G$ scaled likewise, and $T_m(\alpha)$ is the m -th Chebyshev polynomial of the first kind

$$T_m(\alpha) = \cos(m \cdot \arccos \alpha) \quad (2.36)$$

defined also by the following recursive relation

$$T_0(\alpha) = 1 \quad (2.37)$$

$$T_1(\alpha) = \alpha \quad (2.38)$$

$$T_{m+1} = 2\alpha T_m(\alpha) - T_{m-1}(\alpha) \quad (2.39)$$

Table 2.22 – Chebyshev coefficients c_k for the model function 1.

k	0	1	2	3	4	5
c_k	376.778	586.531	307.895	308.945	495.495	-6.225
k	6	7	8	9	10	11
c_k	119.581	270.744	-8.990	2.471	35.943	107.841
k	12	13	14	15	16	17
c_k	-3.874	3.723	-1.190	8.725	33.135	-1.224
k	18	19	20	21	22	23
c_k	1.718	-1.880	0.649	1.749	8.105	-0.281
k	24	25	26	27	28	29
c_k	0.522	-0.869	0.933	-0.269	0.233	1.633
k	30	31	32	33	34	35
c_k	-0.060	0.133	-0.314	0.525	-0.530	0.134

Model function 1 satisfies the objectives, because $R_{\text{DOF,adj}}^2 = 0.99999921$, $S = 0.310$, $\epsilon_{\max} = 1.5\%$, and $\epsilon_{\min} = -5.82\%$ excluding the outlier $\hat{p}_f/c(\phi = 5^\circ, G = 10)$ for which $\epsilon = -12.33\%$. The graphical representation of the fitted model function 1 is shown in Figure 2.8. To conclude the evaluation of model function 1, the Q-Q plot is shown in Figure 2.9. This plot clearly shows that the point $\phi = 5^\circ, G = 10$ is an outlier, and that the assumption of normally distributed errors is satisfied. Better models can be obtained with series of higher degree. For instance, a Chebyshev polynomial of order 10 ensures a residual $|\epsilon| < 1\%$ over the entire domain.

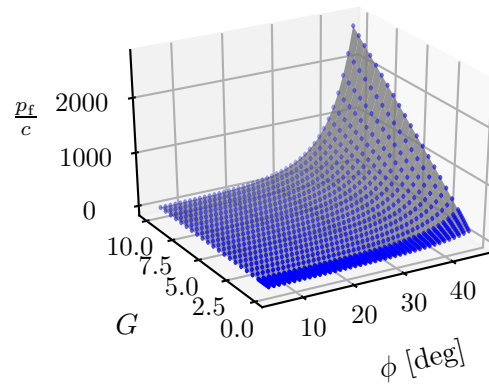


Figure 2.8 – Exact normalised bearing capacity (points) and fitted model function 1 (grey surface).

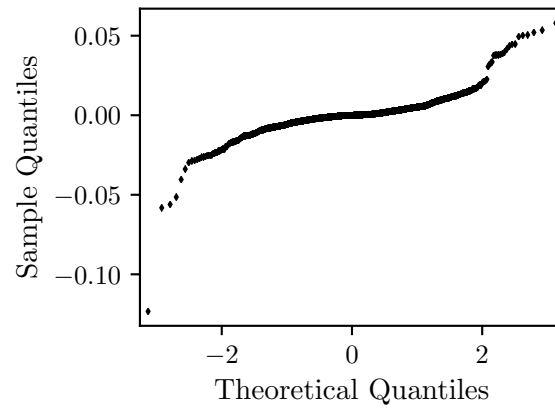


Figure 2.9 – Q-Q plot for model function 1.

Model function 2

The second model function is fitted over the domain $10^\circ \leq \phi \leq 40^\circ$; $0.1 \leq G \leq 1$. As mentioned above, this function should be easily manageable, i.e. it should be easily computed with a hand calculator. For this purpose, a rational polynomial function was chosen, which has the following form

$$\frac{\hat{p}_f}{c} = \frac{a + bx + cx^2 + dx^3 + ey + fy^2}{1 + gx + hy + iy^2 + jy^3} \quad (2.40)$$

where $x = \tan \phi$ and $y = G$ as before, but not scaled. Coefficients a to j are given in Table 2.23. The fitted model function 2 and the Q-Q plot are shown in Figure 2.10 and 2.11, respectively. This model satisfies $R_{\text{DOF,adj}}^2 = 0.99994395$, $S = 0.282$, $\epsilon_{\text{max}} = 3.14\%$ and $\epsilon_{\text{min}} = -2.63\%$.

Table 2.23 – Coefficients for the model function 2.

a	4.241
b	22.816
c	-32.943
d	77.236
e	-5.360
f	3.160
g	-0.510
h	-0.798
i	0.697
j	-0.247

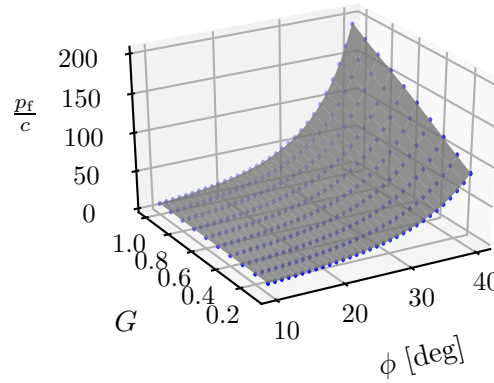


Figure 2.10 – Exact normalised bearing capacity (points) and fitted model function 2 (grey surface).

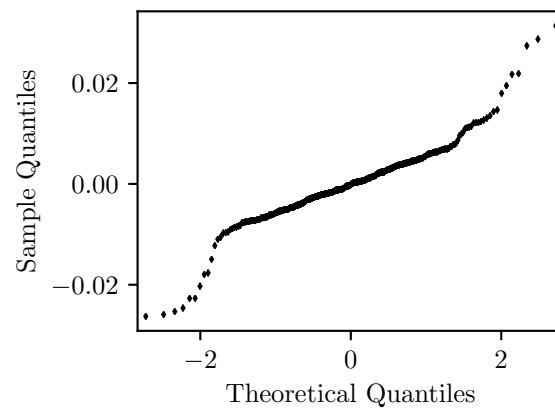


Figure 2.11 – Q-Q plot for model function 2.

2.3 Three-Dimensional Problem

The three-dimensional problem cannot be solved with the method of characteristics because there are more unknown than equations. The axially symmetric plastic field of circular footings, however, becomes statically determinate when the hypothesis proposed by Haar and von Kármán [126] is assumed. This hypothesis stipulates that during plastic deformation, the circumferential principal stress is equal to one of the other two principal stresses acting in the meridional plane. For the problem under consideration, the hoop stress is taken equal to the algebraically smaller of the other two ($\sigma_\theta = \sigma_{II}$). The obtained equations are hyperbolic, and were examined by Hencky [134] for the Tresca yield condition and by Cox et al. [63] for the Mohr-Coulomb yield condition. It is noteworthy that under axial symmetry conditions the Mises yield criterion does not match that of Tresca, and the equations are not hyperbolic.

In the following, results are presented by means of bearing capacity factors as well as shape factors $s = N'/N$, where N' and N are the bearing capacity factors for the finite length and the strip footing, respectively. For reasons of consistency, shape factors are given only when authors have given them explicitly, or when they provided both solutions for strip and finite length footings.

In this section only theoretical results are presented. Shape factors calibrated on experimental results are given in section 2.4.3. It will be seen that the adoption of the Tresca yield criterion for saturated undrained clays is largely supported by experimental evidences. On the other hand, the use of the Mohr-Coulomb criterion for drained soils is much more sensitive to strain conditions (i.e. loading path).

2.3.1 Weightless Mohr-Coulomb Material — $c-\phi$ soil

Shield [343] showed that (2.3) is a lower bound for the average indentation pressure of any convex area. The bound also applies to any uniformly loaded convex area as distinct from an area loaded by a rigid punch. Unlike the plane strain problem, footing roughness increase the bearing capacity of a weightless material [232].

Smooth footing

Circular footing

In case of circular footings B stands for the diameter. Cox et al. [63] extended the partial stress field of stress characteristics in an admissible manner and showed that the coincident velocity characteristics define an admissible velocity field. The results

are shown in Table 2.24. To the author knowledge, this is the first time that for the punch indentation problem, the stress field is extended throughout the body in a non-fully plastic way. It should be said that Cox et al. used a strange substitution for the cohesion where they included the effect of atmospheric pressure, but despite this apparent misunderstanding of the principle of effective stress, the solution is valid [15]. The precision of the numerical solutions is very accurate and matches the values obtained with ABC [215].

Bolton and Lau [15] obtained solutions based on the partial field of stress characteristics (Table 2.24).

Erickson and Drescher [103] computed bearing capacity of circular footings with the finite differences software FLAC, adopting an incremental elasto-plastic constitutive model. The soil was modelled as a homogeneous isotropic linear elastic-perfectly plastic Mohr-Coulomb material. Associated and non-associated flow rules were assumed, but here only results pertaining to the former case are presented. The latter highlights, as it is well-known, that the bearing capacity of non-standard materials is lower. Table 2.24 shows that finite element results are lower than exact ones [215]^{‡‡}. Kumar et al. [182] computed rigorous lower bounds with finite elements and linear programming. It is worth saying that usually incremental elasto-plastic constitutive models use a smooth plastic potential in combination with the Mohr-Coulomb yield condition for numerical reasons. Therefore, the flow rule is not truly associated. However, the difference can in general be considered negligible.

Rough footing

Circular footing

The solutions for circular rough footings are given in Table 2.25. Bolton and Lau [15] wrongly envisaged that roughness has no effect on the bearing capacity of circular footings on weightless soils, as in the case of strip footings. Salençon and Matar [333] provided shape factors in graphical form based on stress characteristics results. These factors apply to the bearing capacity coefficient N_c given by the Prandtl solution (equation (2.1)). The complete solution for perfectly rough bases was obtained by Martin [215].

In order to account for perfectly rough footings, Erickson and Drescher [103] imposed a condition of no relative slip at the interface, except for the outermost node below the footing for numerical reasons. This is probably one reason that explains why they

^{‡‡}Sometimes the theoretical exactness of the axially symmetric solution is questioned due to the heuristic hypothesis of Haar and von Kármán, and because in some situations the solution involves crossing β characteristics.

Table 2.24 – Bearing capacity factor ($N_c = p_f/c$) for circular smooth footings on a weightless Mohr-Coulomb material.

ϕ [deg]	Cox et al. (1961)	Bolt. and Lau (1993) ^a	Eric. and Dr. (2002)	Martin (2004)	Kum. & Kha. (2011)
0	5.69	–	–	5.69	5.61
5	7.44	7.43	–	7.43	7.31
10	9.98	10.2	–	9.99	9.78
15	13.9	13.8	–	13.9	13.5
20	20.1	20.1	19.5	20.1	19.4
25	30.5	30.5	–	30.5	29.1
30	49.3	49.4	–	49.3	47.1
35	85.8	85.7	84	85.9 ^b	81.5
40	164	166	161	165 ^b	154
45	–	358	320	359 ^b	325

^a Computed as $N_c = (N_q - 1) \cot \phi$.^b Involves crossing β characteristics [215].

obtained higher bearing capacity factors compared to the stress characteristics solutions. Kumar et al. [182] computed rigorous lower bounds.

Table 2.25 – Bearing capacity factor ($N'_c = p_f/c$) for perfectly rough circular footings on a weightless Mohr-Coulomb material.

ϕ [deg]	Salen. & Matar (1982) ^a	Erick. and Dr. (2002)	Martin (2004)	Kum. & Kha. (2011)
0	6.17	–	6.05	6.01
5	7.79	–	8.06	8.00
10	10.8	–	11.09	11.0
15	15.4	–	15.8	15.7
20	23.7	22.3	23.7	23.2
25	37.3	–	37.3 ^b	36.2
30	60.2	–	62.7 ^b	61.5
35	115	108	114 ^b	112
40	226	186	228 ^b	224
45	536	380	520 ^b	502

^a Obtained by multiplying s_c from graph times equation (2.1).^b Involves crossing β characteristics [215].

Square and rectangular footings

Michalowski [235] considered an advanced multi-block Prandtl type failure mechanism for perfectly rough rectangular footings. Similarly to [348], the least upper bound for square footings occurs for a mechanism with no symmetry with respect to diagonal

Table 2.26 – Shape factor ($s_c = N'_c/N_c$) for perfectly rough rectangular footings on a weightless Mohr-Coulomb material, [235].

ϕ [deg]	B/L					
	1/10	1/5	1/3	1/2	2/3	1
0	1.01	1.07	1.10	1.18	1.20	1.28
5	1.04	1.08	1.14	1.19	1.25	1.34
10	1.06	1.12	1.09	1.28	1.38	1.52
15	1.09	1.17	1.28	1.42	1.54	1.77
20	1.14	1.25	1.41	1.61	1.77	2.15
25	1.18	1.36	1.57	1.85	2.11	2.67
30	1.27	1.52	1.83	2.23	2.62	3.46
35	1.40	1.78	2.26	2.86	3.47	4.32
40	1.62	2.20	2.97	3.90	4.83	6.65
45	2.03	2.99	4.23	5.80	7.38	10.5

planes. The shape factors, which modify the exact solution given by (2.1), are reported in Table 2.26.

Zhu and Michalowski [412] employed the finite element software ABAQUS and modelled the soil as a linear elastic-perfectly plastic Mohr-Coulomb medium. They imposed a vertical displacement to model the effect of a perfectly rough base. This is equivalent to impose a condition of no relative slip at the interface. The shape factors were obtained with respect to N_c computed by plane strain finite element analysis, and it was shown that it matches very well the Prandtl solution (equation (2.1)). A close-form approximation was given, which writes

$$s_c = 1 + (1.8 \tan^2 \phi + 0.1) \sqrt{\frac{B}{L}} \quad (2.41)$$

The discrepancy between the shape factors obtained by Zhu and Michalowski [412], and by Michalowski [235] increases with increasing values of ϕ and B/L , for which the results of the latter are considerably higher. This is due to the limitation of assuming only plane deformation modes that are perpendicular to the footing edges, and the constraint imposed by the kinematic admissibility on failure mechanisms defined by rigid bodies.

2.3.2 Ponderable Tresca Material — c – γ soil

In a similar fashion to the plane strain problem, the bearing capacity of a Tresca material is invariant with respect to the self-weight also in the general case [115]. Therefore, the solutions for a weightless Mohr-Coulomb material with $\phi = 0$ presented above apply to the present situation.

Table 2.27 – Shape factor ($s_c = N'_c/N_c$) for perfectly rough rectangular footings on a weightless Mohr-Coulomb material, [412].

ϕ [deg]	B/L				
	1/5	1/3	1/2	3/2	1
0	1.02	1.04	1.05	1.06	1.06
5	1.04	1.06	1.08	1.09	1.11
10	1.06	1.09	1.12	1.14	1.16
15	1.08	1.13	1.18	1.21	1.24
20	1.12	1.19	1.25	1.30	1.35
25	1.18	1.27	1.36	1.43	1.51
30	1.25	1.39	1.52	1.63	1.73
35	1.35	1.54	1.73	1.87	2.02
40	1.49	1.76	2.03	2.25	2.46

Shield [348] obtained the value $N'_c = 5$ as a rigorous lower bound for any convex area of indentation by a flat rigid indenter.

Smooth footing

Circular footing

Hencky [134] obtained the solution of the stress characteristics in cylindrical coordinates for a circular smooth footing. He computed the bearing capacity factor $N'_c = 5.64$. Ishlinsky [155] applied a graphical method to obtain the field of stress characteristics and obtained the value 5.68. Shield [344] demonstrated that the partial stress field obtained by Hencky can be extended throughout the body without violating the yield condition and that an admissible velocity field can be associated to it. He obtained $N'_c = 5.69$. The slightly differences with respect to the exact solution are attributable to a slight imprecision in the evaluation of the mean contact pressure, which is not uniform at failure.

Meyerhof [232] obtained the value $3\pi/2 + 1 = 5.71$ with the limit equilibrium method. He explained that the non uniform contact pressure at failure and the increase of strength with respect to strip footings is due to the hoop stresses σ_θ , which act normal to radial planes.

Gourvenec et al. [119] performed finite element simulations using the software ABAQUS and an incremental elasto-plastic formulation. The soil was modelled as a homogeneous isotropic linear elastic-perfectly plastic Tresca solid obeying the normality condition. For a smooth circular footing they computed $N'_c = 5.58$, which is slightly lower than the exact solution.

Square and rectangular footings

For square footings, Shield and Drucker [348] obtained the upper bounds $N'_c = 5.80$ with a simple Hill type velocity field and $N'_c = 5.71$ based on a more sophisticated Hill type failure mechanism (cf. Appendix B). Interestingly, the latter value corresponds to a geometry that is not symmetric with respect to the diagonals of the footing. This aspect has been discussed by Garnier [115], who showed that a symmetric failure mechanism composed of plane strain modes leading to the same result could actually develop. Gourvenec et al. [119] performed finite element analyses and obtained diagonal symmetric displacement fields in which the movements are not planar along each side. In particular it was shown that there are also displacements parallel to the diagonal and that there is a continuous transition between the displacements along each side of the footing. Shield and Drucker suggested the following analytical expressions for rectangular footings

$$N'_c = \begin{cases} 5.24 + 0.47 \frac{B}{L} & \text{if } B/L \geq 0.53 \\ 5.14 + 0.66 \frac{B}{L} & \text{if } B/L < 0.53 \end{cases} \quad (2.42)$$

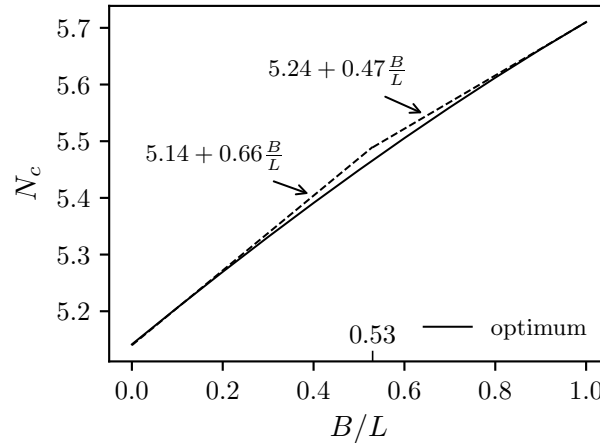


Figure 2.12 – Upper bound of the bearing capacity factor N'_c for smooth rectangular footings resting on a Tresca material, [348].

Michalowski and Dawson [236] proposed a bearing capacity factor for square smooth footings $N'_c = 5.43$, based on finite difference analyses using FLAC and assuming the soil a homogeneous isotropic linear elastic-perfectly plastic associated material obeying to a Tresca yield condition. The finite element computations of Gourvenec et al. [119] provided $N_c = 5.56$. Both displacement fields indicate fourfold symmetry, conversely to the solution obtained by Shield and Drucker [348].

Rough footing

Circular footing

Meyerhof [232] obtained $\pi + 3 = 6.14$ with the limit equilibrium method. Eason and Shield [99] obtained the complete solution $N'_c = 6.05$. Salgado et al. [334] computed rigorous lower and upper bounds with the finite element method and obtained $N'_c = 5.86$ and $N'_c = 6.23$, respectively. The solution of Gourvenec et al. [119] is $N'_c = 5.96$, slightly under-predicting the complete solution.

Square and rectangular footings

Meyerhof [232] considered a footing divided into three zones. A central one of length $L - 2B$ and two square ends. The central portion behaves as a strip footing, and the ends can be computed by assuming that the bearing capacity of a square area is the same as that of a circular one. The shape factor writes

$$s_c = 1 + \left(\frac{N'_{c,\text{circ}}}{N_c} - 1 \right) \frac{B}{L} \quad (2.43)$$

which actually applies to both rough and smooth footings, depending on the value of $N'_{c,\text{circ}}$. This expression can be simplified to

$$s_c = 1 + 0.15 \frac{B}{L} \quad (2.44)$$

According to (2.44), the bearing capacity of a square footing is 15 % higher than that of a strip footing.

The failure solution of Shield and Drucker [348] (upper bound) can be easily adapted to account for base roughness (Appendix B). Given that the Tresca yield criterion is supposed to model saturated undrained clays, a Coulomb law of friction for the interface with adhesion only, i.e $\delta = 0$, is believed to be more representative. The minimum value of N'_c is found by optimisation for given values of relative adhesion $\beta = a/c$ and aspect ratio B/L . For square footings and perfect adherence, i.e. $\beta = 1$, $N_c = 6.70$, value obtained also by Garnier [115], who did not consider intermediate values of roughness.

Chen [49] obtained the upper bound for square footings 6.71 assuming a symmetric Prandtl type failure mechanism. Garnier [115] was able to obtain a better upper bound modifying the Hill type failure mechanism of Shield and Drucker [348] into a Prandtl type failure mechanism. For square footings he obtained $N'_c = 6.4$ (the same solution was obtained independently by Gourvenec et al. [119], 6.41). Michalowski [235] developed an advanced Prandtl type failure mechanism for general soils, which gave for square footings on a Tresca soil $N'_c = 6.56$. Salgado et al. [334] rigorous lower and upper bounds

are shown in Table 2.29. They proposed a closed form of the shape factor based on curve fitting, which is slightly lower than that proposed by Meyerhof [232] and Skempton [359] (cf., equation (2.56)):

$$s_c = 1 + 0.12 \frac{B}{L} \quad (2.45)$$

Table 2.28 – Bearing capacity factor ($N'_c = p_f/c$) for perfectly rough rectangular footings computed with the upper bound limit analysis, [235].

B/L	1/10	1/5	1/3	1/2	2/3	1
N'_c	5.19	5.49	5.64	6.06	6.19	6.56

Table 2.29 – Bearing capacity factor ($N'_c = p_f/c$) for perfectly rough rectangular footings (L:lower, U:upper), [334].

B/L	1/5	1/4	1/3	1/2	1
L	5.17	5.20	5.26	5.36	5.52
U	5.78	5.82	5.89	6.02	6.22

Owing to the independence on the self-weight, the solution of Zhu and Michalowski [412] (Table 2.27) for $\phi = 0$ is applicable to the present situation. For a square footing, they obtained $N'_c = 5.45$. The finite element results of Gourvenec et al. [119] (Table 2.30) gave a bearing capacity factor for a perfectly rough/adherent square footing $N'_c = 5.91$. Given that the finite element result for a strip footing was higher than the exact solution, a correction factor was applied to scale the coefficients for rectangular footings. The shape factors are therefore referred to $N_c = 5.14$. Table 2.30 shows also finite element simulations with a Mises yield criterion based on the plane strain shear strength, and the upper bound solutions based on the Prandtl type failure mechanism derived from that of Shield and Drucker [348]. These solutions are always governing with respect to the Hill type mechanism of Shield and Drucker accounting for perfect adherence (equation (B.2) with $\beta = 1$), as expected. Gourvenec et al. [119] derived a quadratic expression for the shape factor.

$$s_c = 1 + 0.21 \frac{B}{L} - 0.07 \left(\frac{B}{L} \right)^2 \quad (2.46)$$

Equation (2.46) can actually be considered identical to (2.56).

The exact solution for the average indentation pressure of any convex area on a Tresca material can be bracketed between 5 and 6.23 (the upper bound is reduced to 5.71 for

Table 2.30 – Bearing capacity factor ($N'_c = p_f/c$) for perfectly rough rectangular footings (FE: finite element analyses, U: upper bound based on the Prandtl type failure mechanism derived from that of Shield and Drucker [348]), [119].

B/L	1/10	1/5	1/3	1/2	2/3	1
FE	5.26	5.36	5.47	5.61	5.72	5.91
FE ^a	5.38	5.44	5.51	5.60	5.68	5.74
U	5.30	5.44	5.62	5.83	6.03	6.41

^a Mises yield criterion.

smooth footings). Lower bound solutions of Salgado et al. [334] for rough rectangular footings suggest that N'_c is constantly increasing for increasing B/L . Therefore, considering that the effect of roughness disappears for strip footings, $2 + \pi$ may be taken as lower bound for the average indentation pressure of any rigid convex indenter. Interestingly, the exact solution for any uniformly loaded convex area as distinguished from an area loaded by a rigid punch, can be bracketed between 5 and 5.14 [348].

Based on the above results, it can be concluded that early assumptions of the equality between the bearing capacity of square and circular footings, and a linear relation with respect to the aspect ratio B/L , give very accurate results.

2.3.3 Ponderable Cohesionless Mohr-Coulomb Material — ϕ – γ soil

The solution of Shield [343] for weightless materials, equation (2.3), is also a lower bound for the average indentation pressure on ponderable soils. Owing to its validity for smooth interfaces, it is a lower bound for any degree of base roughness.

Smooth footing

Circular footing

Several authors obtained solutions through the method of stress characteristics [15, 40, 75, 191]. Martin [217] demonstrated that such solutions actually correspond to the complete solution and obtained numerical values with the software ABC. The discrepancies among these solutions (Table 2.31) are therefore attributable to numerical precision. The same table shows that the bearing capacity is lower than that of a strip footing for $\phi < 35^\circ$, and higher for $\phi \geq 35^\circ$. The shape factors s_γ attributed to Bolton and Lau [15], and Martin [215] were computed with respect to their solutions for strip footings. Larkin [191] gave them explicitly, but they are unusually low compare to the other solutions based on the method of stress characteristics, which cannot be explained simply by numerical reasons. It was highlighted in the section dedicated to the plane strain

problem, that N_γ given by Larkin was twice the actual computed value. On the other hand, it seems from the graphs for $\phi = 30^\circ$ provided in the same reference, that N'_γ was computed correctly with respect to the average pressure. Therefore, the shape factors given by Larkin are half of the values he actually obtained. This correction is adopted for the values shown in Table 2.31. It can be seen that the corrected solution is similar to the others obtained with the same technique, as expected.

Erickson and Drescher [103] computed the bearing capacity of circular footings as explained previously. Rigorous lower bounds provided Kumar et al. [182] are also given.

Rough footing

Circular footing

Meyerhof [232] used the friction circle method because he estimated that the failure surface on radial planes is approximately circular. He made computations for $\phi = 30^\circ$ and 45° and obtained $s_\gamma \approx 0.5$ with respect to N_γ given in the same reference. Nevertheless, he was not confident about this value and suggested to use an empirical factor instead.

Other researchers employed the method of stress characteristics [15, 40, 75, 333] (Table 2.32). The higher values of Bolton and Lau are due to the imposed trapped wedge below the footing ($\psi = \pi/4 + \phi/2$). The shape factors given in Table 2.32 were computed with respect to the bearing capacity coefficients N_γ given in the same references and can be found in the above section dedicated to the plane strain problem. Table 2.32 shows that the value of ϕ for which $s_\gamma = 1$ decreases from about 34° to about 28° when the base is perfectly rough.

Incremental finite difference and finite element solutions obtained by Erickson and Drescher [103] and Loukidis and Salgado [199], respectively, are also shown in Table 2.32. It is recalled that both imposed a condition of no relative slip at the interface. Loukidis and Salgado calibrated an analytical expression based on their results for $30^\circ \leq \phi \leq 45^\circ$

$$s_\gamma = 1 + (0.26N_\phi - 0.73) \quad (2.47)$$

Lyamin et al. [202] obtained shape factors for perfectly rough circular and rectangular footings with the finite element method and limit analysis. They computed shape factors as a weighted average that accounts for the different convergence rates of the upper bound and the lower bound solutions. These factors, given in Table 2.32, are supposed to multiply the exact solution for strip footings (Table 2.11). Lyamin et al. derived a simple closed form expression for $25^\circ \leq \phi \leq 45^\circ$

Table 2.31 – Bearing capacity factor ($N'_\gamma = 2p_T/(\gamma B)$) for smooth circular footings, and shape factor ($s_\gamma = N'_\gamma/N_\gamma$).

ϕ [deg]	Lar. (1968)		De Sim. (1985) ^a		Bolt. & Lau (1993)		Cas. & Hou. (2002)		Eric. & Dr. (2002)		Mart. (2004)		Kum. & Kha. (2011)	
	N'_γ	s_γ	N'_γ	s_γ	N'_γ	s_γ	N'_γ	s_γ	N'_γ	s_γ	N'_γ	s_γ	N'_γ	s_γ
5	–	–	–	0.667	0.06	0.667	0.062	–	–	0.060	0.714	0.06	–	–
10	–	–	–	0.724	0.21	0.724	0.200	–	–	0.206	0.733	0.20	–	–
15	–	–	–	0.845	0.60	0.845	0.553	–	–	0.535	0.765	0.52	–	–
20	–	–	1.26	0.813	1.30	0.813	1.22	1.7	1.7	1.27	0.804	1.23	–	–
25	–	–	2.83	0.855	3.00	0.855	2.87	–	–	2.97	0.858	2.84	–	–
30	7.34	0.94	6.96	0.917	7.10	0.917	6.94	–	–	7.11	0.929	6.72	–	–
35	–	–	18.0	1.02	18.2	1.02	17.9	21	21	18.0	1.02	16.7	–	–
40	51.3	1.18	50.0	1.16	51	1.16	50.5	58	58	50.2	1.16	45.4	–	–
45	–	–	155	1.33	160	1.33	165	186	186	160	1.36	138	–	–

^a Taken from [182].

$$s_\gamma = (1 + 0.002\phi)s_{\gamma,\text{sq}} \quad (2.48)$$

where ϕ is expressed in degrees, and $s_{\gamma,\text{sq}}$ is the shape factor for square footings, approximated by (2.51) with $B/L = 1$.

The rigorous lower bound obtained by Kumar et al. [182] for perfectly rough footings is also shown in Table 2.32.

Excluding the results of Bolton and Lau with predefined trapped wedge beneath the footing, Table 2.32 shows that the values of the shape factor s_γ obtained with different techniques fall in a narrow range. Therefore, it seems reasonable to apply them to the exact values of N_γ , which can be approximated by one of the expressions presented previously, e.g. (2.15), or read from Table 2.11.

Square and rectangular footings

Meyerhof [231] gave without explanation the following shape factor, which multiplies the bearing capacity coefficient of equation (2.15):

$$s_\gamma = 1 + 0.1N_\phi \frac{B}{L} \quad (\phi > 10^\circ) \quad (2.49)$$

Michalowski [235] considered an advanced multi-block Prandtl type failure mechanism for perfectly rough rectangular footings. Similarly to Shield and Drucker [348], the least upper bound estimate of load on square footings occurs for mechanisms with no symmetry with respect to diagonal planes. However, Zhu and Michalowski [412] demonstrated by means of finite element simulations that the displacement field has actually diagonal symmetry and it is not plane in the regions adjacent to the four sides of the footing. Therefore, enforcing plane deformations in the regions of the failure mechanism in the upper bound limit analysis of three-dimensional systems appears to be a substantial limitation that leads to curious results and could also be a principal source of an overestimation of the collapse load. This mechanism does not approach the optimised multi-block solution for strip footings obtained earlier by the same author [233]. This is due to the fact that in the three-dimensional analysis the kinematic constraints leave a fewer independent parameters with respect to which the mechanism can be optimised. For reasons of consistency, Michalowski calculated shape factors based on the values of N_γ obtained through the three-dimensional rupture figure with $B/L = 0.04$. In this way, they consistently express the effect of moving from a condition of plane strain to a condition for square footings. If it is assumed that the same degree of overestimation applies to any aspect ratio B/L , the actual bearing capacity factors N'_γ of Michalowski

Table 2.32 – Bearing capacity factor ($N'_\gamma = 2pt/(\gamma B)$) for perfectly rough circular footings, and shape factor ($s_\gamma = N'_\gamma/N_\gamma$).

ϕ [deg]	Salen. & Matar		De	Bolt. & Lau		Cass.	Eric.	Mart.	Lya. et al.		Lou. & Sal.		Kum.
			Sim.			& Hou.	& Dr.						&
	(1982)	s_γ	(1985) ^b	(1993)	s_γ	(2002)	(2002)	(2004)	(2007)	(2009)	(2011)		
	N'_γ ^a	s_γ	N'_γ	N'_γ	s_γ	N_γ ^b	N'_γ	s_γ	N'_γ	s_γ	N'_γ	s_γ	N'_γ
5	–	–	–	0.68	1.10	0.067	–	0.081	0.717	–	–	–	0.08
10	0.33	0.760	–	1.37	0.801	0.266	–	0.322	0.744	–	–	–	0.30
15	–	–	–	2.83	0.893	0.796	–	0.932	0.790	–	–	–	0.88
20	2.4	0.845	2.32	6.04	1.01	2.16	2.8	2.42	0.852	–	–	–	2.27
25	6.0	0.924	6.05	13.5	1.16	5.27	–	6.07	0.935	6.22	0.96	–	5.68
30	15.2	1.03	15.7	31.9	1.35	14.1	–	15.5	1.05	15.65	1.06	15.8	14.7
35	41.4	1.2	42.4	82.4	1.62	42.6	45	41.9	1.21	41.33	1.20	42.0	40.0
40	121	1.42	124	238	1.97	129	130	124	1.45	121	1.42	122	116
45	388	1.66	419	803	2.48	505	456	418	1.79	399	1.70	409	380

^a Taken from [215].^b Taken from [182].

for rectangular footings should be obtained by multiplying the shape factors (Table 2.33) times the optimised factors N_γ for plane strain conditions, which can be approximated by (2.25). The results show that $s_\gamma > 1$ for $\phi \geq 20^\circ$. For all values of ϕ , it is found that s_γ is a linear function of B/L .

Table 2.33 – Shape factor ($s_\gamma = N'_\gamma/N_\gamma$) for perfectly rough rectangular footings, [235]. It applies to the bearing capacity coefficient ($N_\gamma = 2p_f/(\gamma B)$) given in [233], approximate by (2.25).

ϕ [deg]	B/L					
	1/10	1/5	1/3	1/2	2/3	1
10	0.998	0.977	0.950	0.888	0.838	0.707
15	0.998	0.996	0.991	0.982	0.970	0.947
20	1.01	1.04	1.07	1.10	1.14	1.19
25	1.03	1.08	1.16	1.24	1.30	1.48
30	1.07	1.17	1.32	1.46	1.55	1.89
35	1.11	1.31	1.52	1.75	1.98	2.48
40	1.14	1.35	1.71	2.02	2.43	3.25
45	1.20	1.64	2.18	2.83	3.24	4.26

Zhu and Michalowski [412] obtained shape factors s_γ with the finite element method as mentioned previously (Table 2.34). The shape factors were computed with respect to N_γ given by equation (2.25). These shape factors are smaller than those computed previously by Michalowski [235] with the upper bound limit analysis. The value of ϕ for which $s_\gamma \geq 1$ is between 30° and 35° , depending on the aspect ratio B/L . The highest value reached by s_γ is 1.17 at $\phi = 40^\circ$ and $B/L \geq 2/3$. They proposed the following analytical expression

$$s_\gamma = \begin{cases} 1 + (0.6 \tan^2 \phi - 0.25) \frac{B}{L} & \text{if } \phi \leq 30^\circ \\ 1 + (1.3 \tan^2 \phi - 0.5) \left(\frac{L}{B}\right)^{\frac{3}{2}} e^{-L/B} & \text{if } \phi > 30^\circ \end{cases} \quad (2.50)$$

To justify $s_\gamma > 1$ for large values of ϕ , they observed the volume of soil, per unit area of the base, displaced by the square and the strip footing. It appears from numerical simulations that for small dilatancy angles, i.e. small shear strength angles for associated soils, the volume displaced by a square footing is smaller than that of a strip footing, whereas for large dilatancy angles is the opposite.

The shape factors obtained by Lyamin et al. [202] (Table 2.35), based upon a weighted average of lower and upper bounds to take into account the different convergence rates, are derived with respect to the exact bearing capacity coefficients N_γ given by Martin [218] (Table 2.11). They found that s_γ is a linear function of B/L , and that the value of ϕ

Table 2.34 – Shape factor ($s_\gamma = N'_\gamma/N_\gamma$) for perfectly rough rectangular footings, [412]. It applies to the bearing capacity coefficient $N_\gamma = 2p_f/(\gamma B)$ given in [233], approximate by (2.25).

ϕ [deg]	B/L				
	1/5	1/3	1/2	2/3	1
10	0.94	0.92	0.89	0.86	0.79
15	0.95	0.93	0.90	0.87	0.80
20	0.97	0.95	0.91	0.88	0.81
25	0.98	0.97	0.94	0.91	0.85
30	1.00	1.01	1.00	0.99	0.93
35	1.01	1.03	1.05	1.06	1.02
40	1.07	1.10	1.16	1.17	1.17

that would lead to $s_\gamma = 1$ for all values of B/L is slightly greater than 30° , in agreement with Zhu and Michalowski [412]. Lyamin et al. derived the following analytical expression for $25^\circ \leq \phi \leq 45^\circ$

$$s_\gamma = 1 + (0.033\phi - 1)\frac{B}{L} \quad (2.51)$$

with ϕ expressed in degrees.

Table 2.35 – Shape factor ($s_\gamma = N'_\gamma/N_\gamma$) for perfectly rough rectangular footings, [202]. It applies to the exact bearing capacity coefficient N_γ given in [218], approximate by (2.15).

ϕ [deg]	B/L				
	1/4	1/3	1/2	5/6	1
25	0.98	0.97	0.95	0.91	0.90
30	1.02	1.02	1.01	0.99	0.98
35	1.04	1.07	1.10	1.12	1.12
40	1.07	1.10	1.17	1.26	1.32
45	1.10	1.18	1.26	1.54	1.56

2.3.4 Ponderable Mohr-Coulomb Material — $c-\phi-\gamma$ soil

A few solutions exist for the bearing capacity factors and shape factors considering a general Mohr-Coulomb soil. The reason is that it is difficult to provide charts or tabulated values owing to the number of parameters involved, and because the conservative superposition approach is preferred in design practice.

Smooth footing

Circular footing

Cox [62] extended the solution obtained previously [63] to the case of ponderable soils (Table 2.36). Cox neither specifically completed the partial stress field, nor derived the velocity field. However, he suggested that there is no apparent reason for which the same techniques employed to derive the complete solution in the case of an imponderable soil should not also be capable of application in the present case. The values obtained with ABC match the results of Cox et al. to the given precision (crossing β characteristics were observed for $\phi = 40^\circ$, $G = 0.01$ and 0.1). It is therefore possible to obtain shape factors based on the exact values of p_f/c for smooth strip footings. It can be seen that for a given value of G , $s_{c\gamma}$ increases with increasing ϕ , which agrees with all theoretical shape factors for cohesionless soils presented previously.

Table 2.36 – Normalised bearing capacity (p_f/c) for smooth circular footings [62], and shape factor ($s_{c\gamma}$) computed with respect to the exact solution.

ϕ [deg]	G							
	0.01		0.1		1		10	
	p_f/c	$s_{c\gamma}$	p_f/c	$s_{c\gamma}$	p_f/c	$s_{c\gamma}$	p_f/c	$s_{c\gamma}$
10	9.99	1.20	10.0	1.19	10.4	1.15	13.8	1.01
20	20.1	1.35	20.3	1.34	22.4	1.25	38.8	1.03
30	49.4	1.63	50.5	1.60	60.6	1.41	141	1.11
40	165	2.17	173	2.08	237	1.71	754	1.32

Rough Footing

Circular footing

Erickson and Drescher [103] obtained a few solutions with the finite difference method for a general soil (Table 2.37). They provided results for a circular footing of 12 m in diameter, and two sets of soil properties: 1) $c = 0.1$ kPa, $\rho = 1500$ kg/m³, and 2) $c = 100$ kPa, $\rho = 2500$ kg/m³, corresponding to $G = 900$ and 1.5 , respectively.

Solutions computed with ABC are summarised in Table 2.38. The evolution of the shape factors is similar to that for smooth footings (Table 2.36), but the values are higher. It is found that for $0.01 \leq G \leq 10$ and $10^\circ \leq \phi \leq 40^\circ$, the shape factor is always greater than 1.

It is known that the sum of the minima (superposition approach) is lower than the consistent minimum for strip footings, and Bolton and Lau [15] demonstrated that this

Table 2.37 – Normalised bearing capacity (p_f/c) for perfectly rough circular footings, [103].

ϕ [deg]	G	
	1.5	900
20	27.6	2710
35	193	43 300
40	366	128 000
45	1281	432 100

Table 2.38 – Normalised bearing capacity (p_f/c) for perfectly rough circular footings, [215], and shape factor ($s_{c\gamma}$) computed with respect to the exact solution for strip footings.

ϕ [deg]	G							
	0.01		0.1		1		10	
	p_f/c	$s_{c\gamma}$	p_f/c	$s_{c\gamma}$	p_f/c	$s_{c\gamma}$	p_f/c	$s_{c\gamma}$
10	11.1	1.33	11.2	1.32	11.9	1.24	17.5	1.02
20	23.7	1.59	24.2	1.56	28.2	1.37	58.4	1.06
30	63.0 ^a	2.07	65.4 ^a	1.98	86.8 ^a	1.62	254	1.22
40	231 ^a	2.99	248 ^a	2.75	400 ^a	2.07	1626	1.59

^a Involves crossing β characteristics [215].

statement holds also for circular footings. If the ratio between the solution obtained by superposition and that obtained by a consistent system is similar for both circular and strip footings, the general shape factors $s_{c\gamma}$ obtained from the superposition approach should be in good agreement with those computed with the consistent approach. For $G = 1$, this ratio (superposition/consistent) for circular and strip footings is respectively, 0.80 and 0.86 for $\phi = 20^\circ$, and 0.75 and 0.84 for $\phi = 30^\circ$. The higher ratio for strip footings means that shape factors obtained from the superposition approach are lower. For the selected shear strength angles, 1.28 and 1.44 are obtained, compared to 1.37 and 1.62 of the consistent solution (Table 2.38). This means an underestimation in the range of 11 %.

Square and rectangular footings

The consistent upper bound solution of Michalowski [235] based on a Prandtl type mechanism for $B/L = 0.5$ is shown in Table 2.39. As explained by Michalowski himself, and already reported previously, owing to the difficulty of building a kinematic admissible failure mechanism in three dimensions, the best upper bound for this mechanism when $B/L \rightarrow 0$ does not converge toward the optimised multi-block solution for strip footings [233] (Table 2.19). Therefore, for consistency reasons the shape factors should

be computed with respect to the three-dimensional failure mechanism with a sufficient low value of B/L (however such results were given by Michalowski only for cohesionless soils).

Table 2.39 – Normalised bearing capacity (p_f/c) for perfectly rough rectangular footings ($B/L = 0.5$), [235].

ϕ [deg]	G		
	0.1	0.25	0.5
15	16.1	17.2	17.9
35	157	177	214

2.4 Real Soils

2.4.1 Presence of Water

The objective of this section is not to give a comprehensive description of the variation of bearing capacity with water conditions, but rather to draw the general guidelines to take into account the presence of water in simple homogeneous steady state conditions. The failure region is supposed to be fully dry, fully saturated or subjected to a homogeneous state of suction.

The dry state does not deserve any comment, given that water is absent. The fully saturated problem is solved by distinguishing between undrained and drained conditions, and by applying the Terzaghi's principle of effective stresses. Details regarding the influence of water table depth by assuming fully dry and fully saturated strata may be found in [6, 178, 229]. An unsaturated soil subjected to a homogenous state of suction is characterised by a homogeneous and isotropic state of stress s , and the analysis must be carried out in terms of effective stresses. Following the procedure proposed by Sokolovskii [366, 367], s must be added to the fictitious uniform state of stress $c \cot \phi$. This leads to the interpretation of suction as an increase of apparent cohesion $s \tan \phi$, which is particularly convenient for the application of the upper bound theorem of the limit analysis:

$$\frac{p_f}{c + s \tan \phi} = N_c + GN_\gamma \quad (2.52)$$

It is noteworthy that heterogeneous soils with a linearly increasing apparent cohesion with depth, can be handled relatively easily [67, 215, 330].

2.4.2 Non-Associated Materials

Real soils usually exhibit non-associated plastic flow. If the critical state defines the ultimate state, plastic distortion takes even place at constant volume and thus the dilatancy angle is $\nu = 0$. However, for soils with internal shear strength angle the plastic strain is not constant along the slip planes, and therefore the mean dilatancy angle at the instant of incipient plastic flow is $0 < \nu < \phi$.

The lower bound theorem of the limit analysis leads to the conclusion that the collapse load of a non-standard material cannot exceed that of a standard material with the same yield condition [299, 300]. Davis [65] showed that in isotropic coaxial perfectly plastic non-associated Mohr-Coulomb materials, shear stresses and normal stresses acting on velocity discontinuity lines, i.e. velocity characteristics, are related by the following relation

$$\tau^* = c^* + \sigma_n^* \tan \phi^* \quad (2.53)$$

where

$$c^* = \eta c \quad (2.54a)$$

$$\tan \phi^* = \eta \tan \phi \quad (2.54b)$$

$$\eta = \frac{\cos \phi \cos \nu}{1 - \sin \phi \sin \nu} \quad (2.54c)$$

Drescher and Detournay [82] demonstrated that for *translational failure mechanisms*, rigorous upper bound solutions can be obtained by adopting the modified yield criterion $\tau^* = c^* + \sigma_n^* \tan \phi^*$ and normality condition. This agrees with the conclusion of Radenkovic, because $\phi^* \leq \phi$. It is noteworthy that the limit equilibrium method provides rigorous upper bounds for statically determined translational failure mechanisms.

It is important to highlight that the modified yield criterion cannot be used to obtain lower bound solutions, because it does not satisfy the normality condition with respect to the direction of the actual plastic strain increment.

The substitution of the non-standard material with an equivalent standard-one seems promising for bearing capacity solutions in plane strain conditions, where multi-block failure mechanisms allow high degree of freedom of the rupture figure. On the other hand, translational failure mechanisms impose considerable constraints to the kinematics of failure mechanisms in the general case [103].

Numerical analysis revealed that the bearing capacity decreases with decreasing dilatancy angle, and that such decrease is higher for higher values of the difference $\phi - \nu$ [103, 110, 122, 199, 233, 395]. This means that for a given relative dilatancy angle $\nu/\phi = \text{cst.}$, the ratio of the bearing capacity of the non-associated material to that of the associated material decreases with increasing ϕ .

Based on elastic-perfectly plastic finite element analyses, Loukidis and Salgado [199] proposed a modified expression for N_q

$$\begin{aligned} N_q &= e^{F(\phi, \nu) \pi \tan \phi} N_\phi \\ F(\phi, \nu) &= 1 - \tan \phi \tan^{2.5}[0.8(\phi - \nu)] \end{aligned} \quad (2.55)$$

which can be used in (2.29) to approximate N_γ .

2.4.3 Experimental Results

The correct determination of the bearing capacity coefficients and the shape factors is a complex task, in particular for N_γ . The estimation of the shearing strength angle is extremely difficult, because it is function of the initial void ratio, the variation of the void ratio upon loading, the actual normal stress acting on the failure planes (non-linear intrinsic line), and the strain conditions (plane strain, axial symmetry, and intermediate situations). These aspects and the non-associated behaviour complicate the comparison between experimental results and theoretical prediction. Moreover, failure takes place for a given settlement, so that in reality there is always the contribution of the overburden pressure and shear strength. Therefore, a direct measure of N_γ for surface footings is not possible.

Model footings are generally worked in order to obtained perfectly rough bases. Therefore, in the following perfectly rough/adherent interfaces are assumed.

Tresca Yield Criterion

Tresca criterion seems appropriate to model dense saturated soils under undrained conditions, such as overconsolidated saturated clays. The key features are the invariance of the average bearing pressure with respect to footing width and soil self-weight, and the increase of it with increasing B/L . The bearing capacity factors N_c obtained with this model are supported by experimental evidences [118, 232, 357, 359]. In particular, the increased bearing capacity of a circular footing with respect to a strip is evident.

Based on the experimental data of Golder and Skempton [118, 357] and unpublished results, Terzaghi [384] suggested to multiply the theoretical bearing capacity factor of strip footings, equation (2.1), by $s_c = 1.3$, both for circular and square footings. Later s_c was modified to 1.2 [385], leading to $N_c = 6.17$. This value is very close to the exact theoretical one 6.05 [99].

Skempton [359] proposed for circular footings $N_c = 6$, and for rectangles the formula

$$s_c = 1 + 0.2 \frac{B}{L} \quad (2.56)$$

which is essentially equal to (2.44).

It is noteworthy that the shear strength under triaxial conditions is lower than that under plane strains [119]. Randolph [301] suggested that the bearing capacity for three-dimensional conditions should be expressed in terms of an average of the shear strengths under triaxial compression $s_{u,TC}$, triaxial extension $s_{u,TE}$, and simple shear $s_{u,SS}$. As remarked by Gourvenec et al. [119], this hypothesis breaks down for gradually more slender footings. A more appropriate value might be

$$\bar{s}_u = s_{u,SS} + (s_{u,TC} + s_{u,TE} - 2s_{u,SS}) \frac{B}{3L} \quad (2.57)$$

which gives $\bar{s}_u = s_{u,SS}$ for strip footings, and $\bar{s}_u = (s_{u,TC} + s_{u,TE} + s_{u,SS})/3$ for square (or circular) footings.

It can be stated that theoretical results qualitatively and quantitatively agree with experimental data. Results obtained by Gourvenec et al. [119] for the Mises yield condition suggest that the intermediate principal stress has little influence on the bearing capacity of homogeneous isotropic soils, definitely negligible for practical applications.

Mohr-Coulomb Yield Criterion

The bearing capacity of strip footings resting on dense sands is well estimated by the general shear failure theory and the Mohr-Coulomb criterion [71, 118, 232].

Measured tip resistance of deep foundations, for which the contribution of the soil self-weight becomes small compared to the confinement, showed that N_q increases with increasing B/L for a given width [70, 232]. Therefore, reasonable inferences can be drawn on the evolution of N_γ with respect to the footing shape.

Based on the results of Golder [118] and other unpublished data, Terzaghi [384, 385] proposed the value $s_\gamma = 0.6$ for circular footings, calibrated on his bearing capacity factor N_γ (Table 2.6). For square shapes, Terzaghi [384] suggested the value $s_\gamma = 0.8$

in combination with his bearing capacity factor. This outcome was based on the most unfavourable test results. It is worth saying that Golder concluded that, despite the scatter of the results and including in his arguments also other data [105, 170, 223], for a given width the bearing capacity is not affected by the ratio B/L . However, it is noteworthy that Golder did not deduce the contribution of N_q that inevitably takes place, so that the invariance could also be attributed to the combination of scatter and balance between the increase of N_q and the reduction of N_γ . Other than the fact that the shape factor proposed by Terzaghi is based on the most unfavourable data, the value of s_γ is directly affected by his theory of bearing capacity for strip footings, and the definition of the shear strength angle used in the experiments.

Later, Terzaghi reduced the shape factor from $s_\gamma = 0.8$ to $s_\gamma = 0.4$, without giving any information about the tests employed in the calibration [385]. This reduction is actually greater than one-half, as it could appear at first glance, because the new shape factor were applied to the values of N_γ derived by Meyerhof [229], and approximated by (2.15), which are lower than those given previously by Terzaghi. This is likely due to the fact that such coefficient was intended to be used in daily design, and more unfavourable data were found.

Other experimental results support the thesis that, for a given width, the bearing capacity of surface footings on sand decreases with increasing B/L [70, 71, 132, 226, 231, 232], and is minimum for a circular area, for which the value $s_\gamma = 0.6$ seems appropriate. For a square footing, Meyerhof [226] found approximatively $s_\gamma = 0.7$.

Hansen [25] gave the expression below, meant to be used along with equation (2.19) or (2.20). He did not furnish any explanation about its derivation.

$$s_\gamma = 1 - \left(0.1 + \frac{\tan^6 \phi}{2}\right) \frac{B}{L} \quad (2.58)$$

According to (2.58), s_γ decreases with increasing ϕ other than B/L .

Alternatively to (2.49), Meyerhof [231] suggested to estimate the shape factor by interpolating between the bearing capacity coefficient for strips and circles in direct proportion to the shape ratio B/L . If the value $s_{\gamma, \text{circ}} = 0.6$ is assumed [132, 384, 385], the formula is as that given by de Beer [71]:

$$s_\gamma = 1 - 0.4 \frac{B}{L} \quad (2.59)$$

Another empirical formula was given by de Beer [71], which assumed $s_\gamma(B/L = 1) = 0.6$ and imposed $s_\gamma(B/L = 1/6) = 1.476s_\gamma(B/L = 1)$ after experimental data:

$$s_\gamma = \frac{1 + 0.2B/L}{1 + B/L} \quad (2.60)$$

Without imposing $s_\gamma(B/L = 1) = 0.6$ and assuming a linear relation, De Beer obtained the following expression

$$s_\gamma = 1 - 0.36 \frac{B}{L} \quad (2.61)$$

which is essentially equal to equation (2.59).

Despite the difficulties highlighted above in the measure of the bearing capacity factor N_γ , it seems evident that for a given cohesionless soil and footing breadth, the bearing capacity decreases with increasing B/L . The physical reason for this is threefold: (1) the intermediate principal stress is higher in plane strain than in nearly triaxial conditions, which increases the confinement [202, 231]; (2) the shear strength angle is higher in plane strain than in nearly triaxial conditions [199, 202, 231]; and (3) for small dilatancy angles the volume displaced by a rectangular footing is lower than that displaced by a strip footing [412].

Reasons (2) and (3) are not taken into account in the derivation of theoretical shape factors, because in the Mohr-Coulomb yield criterion the shear strength angle is not affected by strain conditions, i.e. plane strains or axial symmetry, and they are generally based on the associated flow rule. On the other hand, empirical shape factors consider all these aspects. Therefore, (2) and (3) seem to be fundamental factors which explain the apparent inconsistency between experimental and theoretical results.

Meyerhof [231] proposed to adopt a shear strength angle that considers the transition from a nearly triaxial condition for square footings to a condition of plane strains for strip ones:

$$\phi_r = \left(1.1 - 0.1 \frac{B}{L}\right) \phi_t \quad (2.62)$$

where ϕ_r is the shear strength angle of a rectangular footing, and ϕ_t is the shear strength angle in triaxial condition (axial symmetry). Relation (2.62) implies $\phi_s = 1.1\phi_t$, with ϕ_s denoting the shear strength angle for a strip footing.

Theoretical shape factors that do not take due account for all the processes are ambiguous and may lead to wrong results. Therefore, either empirical shape factors are adopted, which consider all the involved physical phenomena but are subjected to the number and quality of tests, or the bearing capacity factor N'_γ is evaluated by taking due account of the probable value of ϕ and ν .

In the case of a real general cohesive-frictional soils, the increase or decrease of $s_{c\gamma}$ is likely controlled by G .

2.5 Concluding Remarks

A review of the solutions for the bearing capacity of surface footings under vertical load has been presented. It is seen from the above that the problem of bearing capacity has been studying for many years and a number of solutions have been derived. Theoretical bearing capacity factors have been presented in tabulated form and categorised by the type of footing and the soil constitutive model. The theoretical approach and the main assumptions of each solution have also been given. This will help future researchers in the comparison and evaluation of theoretical as well as experimental results. Two new analytical expressions for the normalised bearing capacity of perfectly rough strip footings on general Mohr-Coulomb soils have been derived. The pertinence of theoretical solutions with respect to real soils and experimental data have been discussed. The main conclusions are summarised below:

- The solution obtained through the method of stress characteristics for strip footings correspond to the complete solution according to the theory of plasticity. For circular footings, an hypothesis is needed about the circumferential principal stress and the solution might involve crossing β characteristics. Its rigorousness and completeness might therefore be questionable.
- Imposing a predefined trapped wedge beneath the base leads to higher bearing capacities, in agreement with the limit theorems for frictional interfaces.
- Theoretical and experimental results support the hypothesis that in practice footings can be taken as perfectly rough.
- Experimental and theoretical results are in good agreement for both undrained soils and Tresca yield condition, and drained soils and Mohr-Coulomb yield condition when shear strength parameters are estimated based on realistic loading paths and strain conditions at the instant of collapse. Theoretical shape factors derived from the Tresca yield criterion seem suitable. By contrast, the theoretical derivation of shape factors for Mohr-Coulomb soils that do not take due account for all the physical processes such as the flow rule and the method used to measure ϕ , may lead to wrong results on the unsafe side.

- Despite the theoretical interest in deriving complete solutions for footings of finite length, relevant improvement in the derivation of bearing capacity factors cannot be expected without a proper consideration of the real behaviour of soils. This is true also for shallow footings and general loading conditions.

This research highlighted that theoretical and numerical methods are able to describe qualitatively and quantitatively the bearing capacity of surface footings, and that techniques to take into account the key aspects of real soils are available. Notwithstanding, reliable estimates of the computed bearing capacity can only be achieved through a proper understanding of the involved physical processes and real field conditions. This last conclusion applies to any application of soil mechanics.

Acknowledgements

The support of the Swiss National Science Foundation (project No. 174575, Division InterCo; and No. 200021_175500, Division II) is acknowledged.

If you wish to put up a building you order for it a good foundation, or what one calls a good foundation. After the order has been placed you forget entirely that your structure is going to rest on a foundation.

Karl Terzaghi, The Actual Factor of Safety in Foundations, Lecture delivered in 1934

3

Soil-Structure Interaction of Surface Footings

Preprint version of the article submitted to Computers and Geotechnics for the special issue dedicated to the memory of Prof. Gyan N. Pande.

C Garbellini and L Laloui. “Soil-Structure Interaction of Surface Footings”. In: *Submitted to Computers and Geotechnics* (2020).

Contribution of the candidate: initial idea, theoretical development, analysis of results, writing of manuscript.

LIMIT-STATE ANALYSIS OF soil-structure interacting systems is a classical problem in theoretical and applied soil mechanics. Usually, the capacities of both components are evaluated separately. However, it is well known that soil-structure interaction plays a major role in the actual performance of such systems. Despite the complexity of a rigorous mathematical treatment of the problem, the limit theorems of the theory of plasticity and appropriate consideration of the failure modes of the structural element allow to address soil-structure interaction in a simplified manner. This study shows how the existing solutions for the bearing pressure and footing structural resistance can be coupled to evaluate the impact of the soil-structure interaction. Further, lower and upper bound solutions are developed for foundations that have a slender cross-section.

3.1 Introduction

Soil-structure interacting systems such as foundations, retaining walls, and cut-and-cover tunnels constitute classical limit-state problems [383, 384]. The mutual interaction between these two components is evident. However, they are often treated independently.

Solutions to limit-state problems from the point of view of soil mechanics generally consider the structural component as a rigid or perfectly flexible body, with a focus on the constitutive modelling of the interface and the soil [71, 118, 199, 201, 217, 229, 232, 304, 384, 412]. By contrast, the approach of structural mechanics focuses primarily on the behaviour of structural elements [32, 33, 280, 354, 355].

Evidently, these simplifications are necessary for carrying out laboratory testing to limit the number of parameters and control the governing failure mechanism. However, little effort is made in attempting to combine the respective outcomes within a unified framework.

Recently, rigorous limit-state solutions of soil-structure systems were presented for surface footings and cut-and-cover tunnels [72, 281]. These solutions considered the possibility of simultaneous failure within the structure and the soil, showing the great impact of mutual interactions on the actual performance of such systems.

With the availability of modern commercial software for limit analysis, e.g. [196], similar solutions can be directly obtained in many cases. However, analytical or semi-analytical solutions are fundamental to assess the validity of those results and they greatly simplify parametric analyses, which eventually can be used to obtain closed-form expressions or design charts. Moreover, structural failure modes sometimes fall outside the applicability of the theory of plasticity, e.g. shear failure of concrete members without

transverse reinforcement. These modes cannot be captured by the aforementioned software for limit analysis. Missing one of such failure modes might lead to catastrophic consequences.

In this study, surface footings under centred vertical load were examined as a reference case. An attempt was made to define a unified framework for the analysis of the collapse load considering soil-structure interaction in a simplified manner. For this purpose, sections two to four review the main concepts of soil bearing capacity, contact pressure distribution, and shear capacity of concrete members without transverse reinforcement. The fifth section is dedicated to the soil-structure interaction. It is shown that the knowledge of the three above-mentioned aspects can be combined in a useful way to obtain both quantitative and qualitative outcomes on the overall performance of the foundation. New lower and upper bound solutions for combined failure were derived and extended to the three-dimensional case.

It is believed that, apart from establishing a unified approach toward a more rational limit-state analysis for soil-structure interacting systems, this study might help in soil and structural mechanics education.

3.2 Bearing Capacity of Soils

The maximum load, eventually expressed as average pressure, that a mass of soil can sustain without producing uncontrolled settlements or without causing catastrophic damages to the superstructure is termed *bearing capacity*. This definition follows the interpretation of the *collapse load* given by Hill [146] and Drucker et al. [96] in the framework of the theory of plasticity.

From a theoretical point of view, the bearing capacity of a footing is found by solving the problem of indentation in an elastic-plastic body. The physical properties of the structure in relation to those of the soil define whether the indenter, i.e. the footing, can be considered rigid or not. In many situations it can be considered rigid, and when the soil is dense enough, the type of failure is known as *general shear failure* [384], and the collapse mechanism for strip footings is as depicted in Figure 3.1 [201]. The plastically deformed soil is pushed outward and upward. Depending on the base roughness, footing breadth, and soil properties, a trapped elastic wedge might move downward as an extension of the footing [66, 67, 201].

In the case of surface foundations, the resistance of the soil is due to its apparent cohesion and the weight of displaced soil. In terms of average contact pressure $p_u = Q_u/B$, we can employ the classical Terzaghi's form [384]:

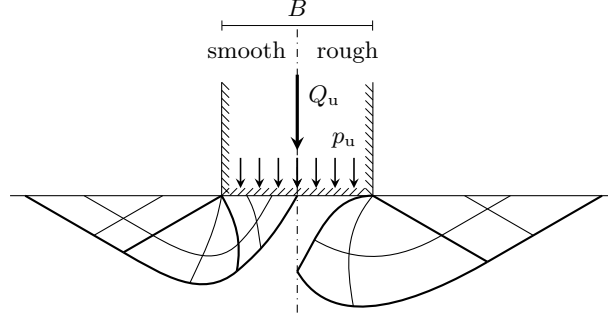


Figure 3.1 – Failure mechanism of smooth and rough strip footings resting on a dense and compact soil.

$$\frac{p_u}{c} = N_c + GN_\gamma \quad (3.1)$$

where c is the apparent cohesion; $G = 0.5\gamma B/c$ is the dimensionless soil weight parameter [62], with γ denoting the soil self-weight and B denoting the footing breadth; and N_c and N_γ are the bearing capacity coefficients, which depend on the geometry of the failure mechanism. If the superposition approach introduced by Terzaghi [384] is adopted, i.e. the contribution of apparent cohesion and soil self-weight are computed independently, these coefficients are a function of the shear strength angle ϕ only.

For rigid strip footings (and circular, if the hypothesis of Haar and Kármán is adopted for the hoop normal principal stress σ_θ [126]) subjected to a centred vertical load and resting on a perfectly rigid plastic isotropic homogeneous (possibly with apparent cohesion linearly increasing with depth) coaxial associated half-space obeying the Tresca or Mohr-Coulomb yield criterion, Martin [215, 217] demonstrated that the solution obtained through the method of stress characteristics [201] corresponds to the complete solution according to the theory of plasticity.

When the bearing capacity factors are computed separately, the exact value of N_c is given by the Prandtl solution [298]:

$$N_c = \cot \phi (e^{\pi \tan \phi} N_\phi - 1) \quad (3.2)$$

where $N_\phi = \tan^2(\pi/4 + \phi/2)$ is the flow value [384]. The exact value of N_γ can be obtained through the free software ABC [215], extracted from [218], or estimated with good accuracy by an older relation proposed by Meyerhof [228]:

$$N_\gamma = (e^{\pi \tan \phi} N_\phi - 1) \tan(1.4\phi) \quad (3.3)$$

The general exact solution p_u/c can be obtained with ABC and estimated with the following analytical expression for $0.1 \leq G \leq 10$ and $5^\circ \leq \phi \leq 45^\circ$:

$$\frac{p_u}{c} = \sum_{j=0}^7 \sum_{m=j}^0 c_k T_m(\tilde{x}) T_{j-m}(\tilde{y}) \quad (3.4)$$

or, for the narrower domain $0.1 \leq G \leq 1$ and $10^\circ \leq \phi \leq 40^\circ$, with the following simpler formula:

$$\frac{p_u}{c} = \frac{a + bx + cx^2 + dx^3 + ey + fy^2}{1 + gx + hy + iy^2 + jy^3} \quad (3.5)$$

Refer to subsection 2.2.4 (Derivation of Analytical Expressions for Perfectly Rough Footings) for a detailed explanation of the 2 equations just mentioned.

Solutions for rectangular footings were obtained empirically [71, 232, 359, 384], with the limit equilibrium or limit analysis method [202, 232, 235, 334, 343, 348], and through incremental elastic-plastic constitutive laws [119, 236, 412]. They are generally expressed through shape factors that multiply the solution for strip footings. Experiments showed that, for a given footing breadth, the bearing capacity p_u increases with an increasing aspect ratio B/L for saturated undrained clays [357, 359], and decreases with an increasing aspect ratio for dry sands [70, 71, 132, 226, 232].

3.3 Contact Pressure

The contact pressure distribution under a surface footing subjected to a centred vertical load is mainly a function of the footing rigidity, soil stiffness, and soil shear strength properties. A qualitative representation of pressure distribution for strip foundations is shown in Figure 4.2. For comparison, the distribution over an elastic half-space is also drawn.

In a purely cohesive soil, the contact pressure at failure is uniform under strip footings and increases slightly toward the footing centre under circular and rectangular footings [134, 232, 344].

In a cohesionless soil, the shear strength at the footing edge is zero (unconfined soil element) and increases toward the footing centre. Therefore, the ultimate contact pressure follows a similar trend. The shape varies between triangular, parabolic, and

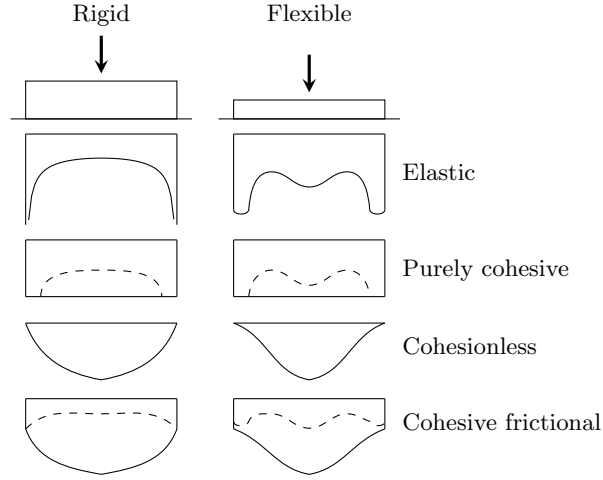


Figure 3.2 – Qualitative contact pressure distribution under isolated surface strip footings. Solid lines represent the distribution at failure, whereas dashed lines correspond to a state prior to collapse.

ellipsoidal depending on the soil characteristics, and footing roughness and breadth [198, 232, 336, 364, 383, 384]. Note that, according to [229], the maximum contact pressure for partly rough footings is not at the footing centre. The same was proposed by [183] for any value of base roughness. However, these conclusions seem less realistic because the confinement increases toward the footing centre.

In a general cohesive frictional soil, the final distribution is a combination of the former. Whether it is closer to that of a purely cohesive or a cohesionless soil, it will depend on the parameters G and ϕ .

3.4 Shear Capacity of Concrete Members without Transverse Reinforcement

One-way shear resistance of concrete members without transverse reinforcement is affected by load distribution and slenderness. This is usually displayed with the help of the so-called Kani's valley [163], where the shear capacity is plotted against the shear span ratio $\alpha = a/d$ (a : shear span, d : effective depth; cf. Figure 3.3). This diagram identifies different regimes of shear carrying actions [107]. The direct strut action governs deep beams ($\alpha < \alpha_1 \approx 1$) and the design can be performed with the strut-and-tie or stress fields methods [212, 337]. In short span beams ($\alpha_1 < \alpha < \alpha_2 \approx 2.5 - 3$), the development of a critical crack within the compressive strut may limit the shear capac-

ity. The modified stress fields theory [394], which accounts for the reduction of concrete compressive strength due to the transverse tensile strain, can be used to analyse these structural elements [107]. The shear resistance of slender beams ($\alpha_2 < \alpha < \alpha_3 \approx 5 - 8$) is affected by both strain and size effects [10, 256]. The critical shear crack theory consistently accounts for both phenomena [42, 107, 252]. For larger values of slenderness ($\alpha > \alpha_3$), the bending resistance is the governing factor, and the classical Euler-Bernoulli beam theory can be employed [280, 337].

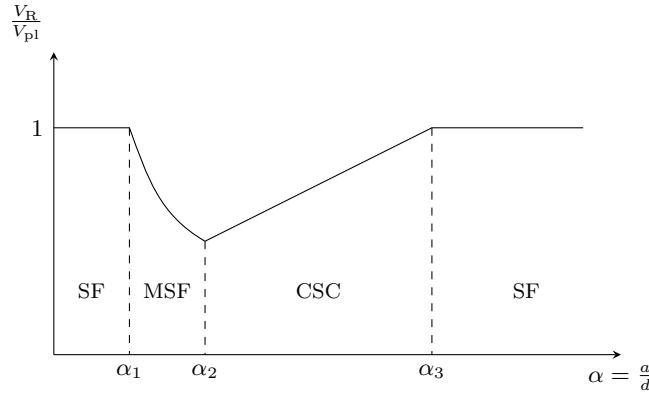


Figure 3.3 – Relative shear capacity versus shear span ratio. V_R is the shear resistance, V_{pl} denotes the shear force that causes the yielding of the flexural reinforcement and crushing of the concrete, a stands for the shear span, and d is the effective depth (maximum effective depth in a variable depth footing). The design method for each regime is indicated: SF stands for stress fields, MSF stands for modified stress fields, and CSC stands for critical shear crack theory.

In Figure 3.4, a generic slender footing subjected to centred vertical load and uniform contact pressure shows the shear transfer mechanisms with the help of a strut-and-tie model [280]. The total shear capacity is given by the following expression:

$$V_R = V_{\text{dir}} + V_{\text{chord}} + V_c \quad (3.6)$$

where V_{dir} is the contribution of the direct strut action, V_{chord} is the vertical component of the inclined compression chord, and V_c is the shear force that can be transferred across the critical shear crack.

It is evident that the contact pressure distribution can have a considerable impact on the shear resistance, and thus on the overall bearing capacity as well. Experiments carried out on slender cantilever beams confirmed this point [280]. Note that for constant depth members, the shear capacity can be as high as 80 % for triangular loading compared to uniformly distributed loading. For the latter, the inclination of the compression chord can lead to an increase of the shear force up to 30 % [280, 371].

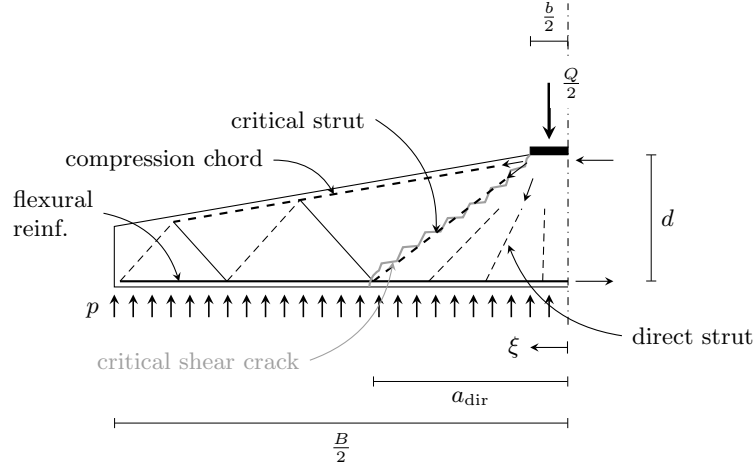


Figure 3.4 – Half of a slender footing with flexural reinforcement subjected to centred vertical load and uniform contact pressure. A strut-and-tie model (strut in dashed line and tie in solid line) shows the load transfer mechanisms. The critical shear crack is represented in grey. Adapted from [280].

3.5 Effects of Soil-Structure Interactions

Based on the previous sections, it is clear that soil-structure interaction plays a major role on the actual performance of foundations. In many practical applications, engineers cannot exempt themselves from adopting simplifying assumptions. In this regard, a series of considerations can be drawn that either allow to take directly into account soil-structure interaction or help make decisions related to a higher level of performance. These considerations are presented in the following subsections.

3.5.1 Deep Beams

Squat footings pertaining to the category of deep beams can generally be considered rigid. Flexural cracking is limited and barely penetrates within the compression field. These types of elements can be analysed without loss of accuracy with a simple strut-and-tie model by replacing the contact pressure with two equivalent concentrated loads acting at a quarter of the footing breadth [173, 337] (uniform contact pressure). A proper consideration of the contact pressure distribution has little influence on the magnitude of the bearing capacity owing to the small value of the ratio B/d .

In this case, the analysis is straightforward. The inclination of the direct strut with respect to the horizontal is expressed as follows:

$$\tan \theta_c = 4 \frac{d - 0.5x_c}{B - b} \approx 4 \frac{d - 0.5x_c}{B} \quad (3.7)$$

where x_c is the depth of the plastically compressed concrete. The force carried by the strut when the soil bearing capacity is fully mobilised is given by the following expression:

$$C = \frac{B}{2 \sin \theta_c} p_u \quad (3.8)$$

3.5.2 Short Span Beams

In footings characterised by a short span beam cross-section, flexural cracks may penetrate within the compression field transversely and reduce the concrete compressive strength. The theory of plasticity can be applied if a strength reduction factor that accounts for the transverse tensile strain is introduced [253, 257, 394]:

$$f_{ce} = k_c f_{cp} \quad (3.9)$$

where f_{ce} is the effective concrete compressive strength, f_{cp} is the concrete equivalent plastic strength, and k_c is the reduction factor.

The influence of the pressure distribution increases with respect to the previous case and replacement with two concentrated loads is a very rough approximation. This is mainly due to the fact that k_c evaluated at the location of the resultant strut is not a representative mean value of the whole compression field.

As an example, the collapse load of a footing subjected to different pressure distributions was computed with the finite element software jconc [106], which is an automatic generator of plane stress elastic-plastic stress fields for reinforced concrete members. The footing had constant depth, breadth $B = 150$ cm, effective depth $d = 45$ cm, flexural reinforcement ratio $\rho = 1.12\%$, concrete compressive strength $f_{cp} = 30$ MPa, null concrete tensile strength $f_{ct} = 0$, concrete Young's modulus $E_c = 30$ GPa, steel yield stress $f_y = 500$ MPa, and steel Young's modulus $E_s = 205$ GPa. Three pressure distributions were considered: (a) uniform, (b) triangular, and (c) external triangular, i.e. the pressure is zero at the footing centre and increases linearly toward the footing edges. Distribution (c) is not realistic, but it is useful to appreciate the influence of the strain effect. The results are shown in Figure 3.5. Taking the collapse load of case (a) as a reference, its value increased by 48.9% for case (b) and decreased by 17.9% for case (c). Considering that the actual contact pressure distribution when the soil bearing capacity is reached is between case (a) and (b), its impact is considerable.

Therefore, the analysis of short span footings by means of strut-and-tie models should be performed with a refinement of the equivalent concentrated load distribution, which replaces the contact pressure. Simplified methods such as those proposed in [69, 336] might be used to redistribute the contact pressure more conveniently. In particular, the technique suggested in [336] allows to consider lower load levels than the soil bearing capacity.

Note that the assumption of uniform pressure is not on the safe side for highly cohesive and stiff soils loaded below their bearing capacity, because the contact pressure is minimum at the footing centre and maximum at the edges.

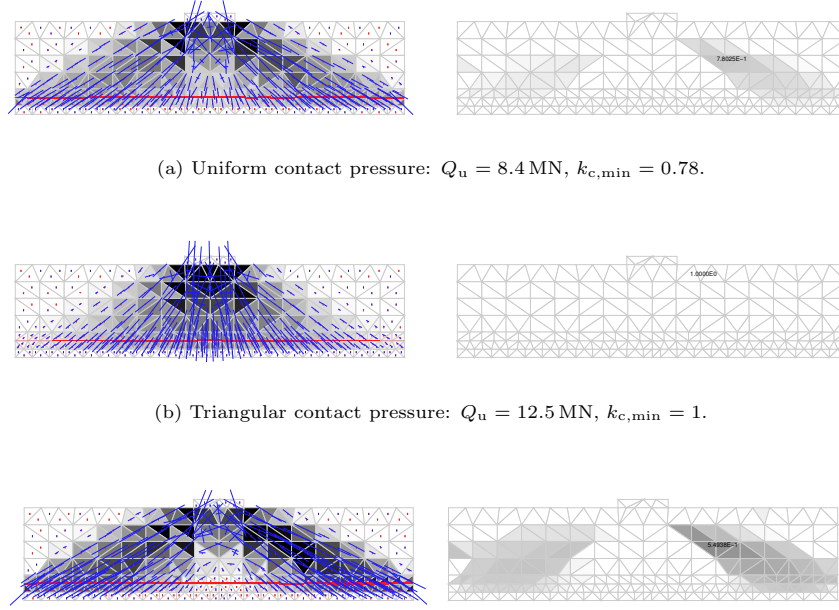


Figure 3.5 – Elastic-plastic stress field (left column) and k_c -value distribution (right column) at collapse for different contact pressure distributions.

3.5.3 Slender Beams

When the shear span ratio of the footing cross-section is between α_1 and α_2 , the foundation fails in shear by development of a critical crack. In this case, the member cannot be analysed by simply considering an equivalent homogeneous material characterised by a reduced compressive strength; the shear carrying mechanisms across the critical crack must be explicitly taken into account.

An experimental study on cantilever beams [280] showed that the load over the region a_{dir} (Figure 3.4), i.e. between the support and the section where the crack intercepts

the flexural reinforcement, is carried by direct strut action. It was suggested that $a_{\text{dir}} \approx 2.75d + b/2$. Another experimental investigation [43] revealed that this distance can fall in the range $d + b/2 \leq a_{\text{dir}} \leq 2.6d + b/2$. Thus, the shear force that must be transmitted through the critical shear crack is expressed as follows (cf. Figure 3.4):

$$V_{\text{E,c}} = \int_{B/2}^{a_{\text{dir}}} p(\xi) d\xi - V_{\text{chord}}(\xi = a_{\text{dir}}) \quad (3.10)$$

According to the critical shear crack theory, the shear capacity across the crack V_c is a function of the crack opening and roughness. The former is then supposed proportional to the strain evaluated at a specific critical section times the effective depth, and the latter can be expressed through the aggregate size. The failure criterion is a hyperbolic law [252]:

$$\frac{V_c}{1[\text{m}]d\sqrt{f_{\text{ck}}}} = \frac{1/3}{1 + 120\varepsilon d/d_{\text{dg}}} \quad (\text{SI units: MPa, mm}) \quad (3.11)$$

where f_{ck} is the characteristic compressive cylinder strength of concrete; ε denotes the strain evaluated in the critical section at $0.6d$ from the outermost compressed fibre, assuming plane-deformed sections and linear elastic behaviour of concrete in compression (the tensile strength is neglected); $d_{\text{dg}} = 16 \text{ mm} + d_g$ with d_g denoting the maximum aggregate size. The critical section is located at $d/2$ from the edge of the wall stressing the footing ($\xi_{\text{cs}} = b/2 + d/2$) and $a_{\text{dir}} = 2.75d + b/2$ [280].

Recently, a power-law failure criterion was proposed to improve the accuracy at low strain [42]:

$$\frac{V_c}{1[\text{m}]d\sqrt{f_{\text{ck}}}} = \frac{k}{\sqrt{\varepsilon_s d/d_{\text{dg}}}} \quad (\text{SI units: MPa, mm}) \quad (3.12)$$

where k is a constant that depends on the main mechanical and geometrical parameters (e.g. $k = 0.019$ for simply supported beams subjected to point load and $k = 0.016$ for simply supported beams subjected to distributed loading, [41]), ε_s is the strain in the flexural reinforcement at the location of the critical section, and $d_{\text{dg}} = \min\{40 \text{ mm}, 16 \text{ mm} + d_g\}$. In the case of cantilever beams, the critical section is located at a distance d from the axis of the support ($\xi_{\text{cs}} = d$) and it is assumed that $a_{\text{dir}} = d$. Owing to the application of the load on the tension face, a_{dir} might be extended [41] (increased dowel action):

$$\begin{aligned}\Delta a_{\text{dir}} &= 0.2 \left(\frac{B}{2} - a_{\text{dir}} \right) = 0.1B - 0.2d \\ a_{\text{dir,tot}} &= 0.1B + 0.8d\end{aligned}\tag{3.13}$$

Equations (3.11) and (3.12), shown graphically in Figure 3.6, are related through the approximate relation $\varepsilon \approx 0.41\varepsilon_s$ [252].

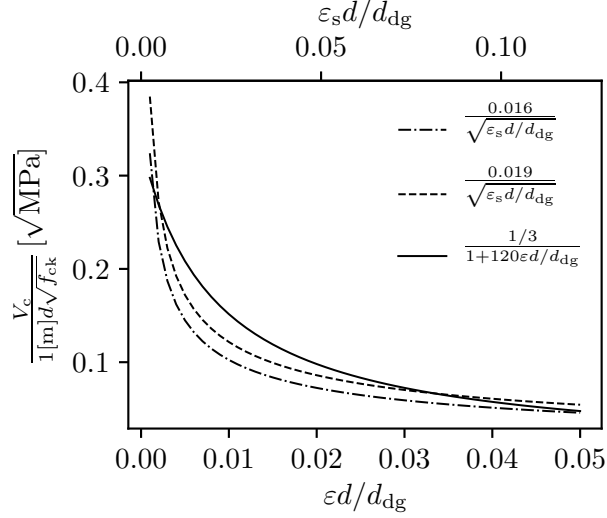


Figure 3.6 – Shear failure criteria based on the critical shear crack theory.

Adopting reasonable assumptions and assuming typical reinforcement and partial safety factors employed in Switzerland [252], the hyperbolic law (3.11) leads to the following design formula:

$$\frac{V_{\text{cd}}}{1[\text{m}]d\sqrt{f_{\text{ck}}}} = \frac{0.2}{1 + 0.0022d \frac{M_{\text{Ed}}}{M_{\text{Rd}}}} \quad (\text{SI units: MPa, mm}) \tag{3.14}$$

where M_{Ed} and M_{Rd} are the design values of the acting bending moment and resisting bending moment, respectively, at the critical section. Similarly, a closed-form expression was obtained from the power law (3.12) [41]:

$$\frac{V_{\text{cd}}}{1[\text{m}]d} = \frac{\kappa}{\gamma_{\text{c}}} \left(\rho f_{\text{ck}} \frac{d_{\text{dg}}}{a_{\text{cs}}} \right)^{1/3} \quad (\text{SI units: MPa, mm}) \tag{3.15}$$

where γ_{c} denotes the partial safety factor for concrete strength (1.5 according to the Swiss code [349]), $a_{\text{cs}} = M_{\text{Ed}}/V_{\text{Ed}}$ is the moment-to-shear ratio at the critical section, and κ is a parameter equivalent to k in (3.12). In the case of cantilever beams, κ takes

the following form:

$$\kappa = \frac{1}{1 - 0.15} (0.5 + 0.2\alpha_{cs}^{1/3}) \quad (3.16)$$

with $\alpha_{cs} = a_{cs}/d$.

Note that in both code-like equations, the location of the critical section was mainly calibrated against beams subjected to point or uniformly distributed loading. However, it was shown that such a location is also representative for triangular loading [280]. Therefore, it is reasonable to assume that it remains representative for general loading conditions, whereas the actual degree of accuracy remains unknown.

Given that the structural resistance is governed by the shear capacity of the critical crack V_c , and that the latter and the acting shear force $V_{E,c}$ are affected by the loading conditions, the actual performance of these foundations is largely influenced by soil-structure interaction. Despite the theoretical exact contact pressure distribution is generally difficult to assess, it can be approximated by simple shapes (rectangular, triangular, parabolic, ellipsoidal, and trapezoidal), as mentioned above. Accordingly, a_{cs} may take the expressions given in Table 3.1.

Table 3.1 – Expressions for the computation of $a_{cs} = M_{Ed}/V_{Ed}$. The value of ξ_{cs} is equal to $b/2 + d/2$ for the hyperbolic criterion and to d for the power law.

Pressure distribution	a_{cs}	$a_{cs}/a_{cs,rect}$
rectangular	$\frac{1}{2}(B/2 - \xi_{cs})$	1
triangular	$\frac{1}{3}(B/2 - \xi_{cs})$	0.67
parabolic	$\frac{3}{8}(B/2 - \xi_{cs})$	0.75
ellipsoidal	$\frac{4}{3\pi}(B/2 - \xi_{cs})$	0.85
trapezoidal	$\frac{1}{3} \frac{2\rho_p + 1}{\rho_p + 1} (B/2 - \xi_{cs})^\dagger$	$0.67 \frac{2\rho_p + 1}{\rho_p + 1}$

$$^\dagger \rho_p = p(\xi = B/2)/p(\xi = \xi_{cs})$$

The shear capacity of the critical shear crack relative to the case of uniform contact pressure $V_c/V_{c,rect}$ is plotted, according to the closed-form equation (3.15), against the moment-to-shear slenderness ratio $\alpha_{cs,rect}$ in Figure 3.7. The increase of V_c is maximum for the triangular distribution, reaching approximately 9 % to 10 %. Note that the actual increase of the structural bearing capacity V_R is enhanced by the reduction of the shear force $V_{E,c}$, which has to be transferred across the critical crack, and the increase of the direct strut action V_{dir} .

Therefore, the influence of soil-structure interaction can be estimated in a simplified manner with the help of Table 3.1. The resulting evaluation procedure is as follows:

- Check the soil average bearing capacity with (3.1)
- Define the pressure distribution
- Check the structural shear capacity V_c :
 - Compute $V_{E,c}$ with (3.10)
 - Compute a_{cs} with Table 3.1
 - Compute V_c either with (3.14) or with (3.15). If the former is used, compute the acting moment at the critical section as $M_{Ed} = a_{cs} \int_{B/2}^{\xi_{cs}} p(\xi) d\xi$
- Check the direct strut capacity V_{dir} :
 - Compute $V_{dir} = \int_{a_{dir}}^0 p(\xi) d\xi$
 - Check the flexural reinforcement and concrete with a strut-and-tie or stress fields model, according to the theory for deep or short span beams

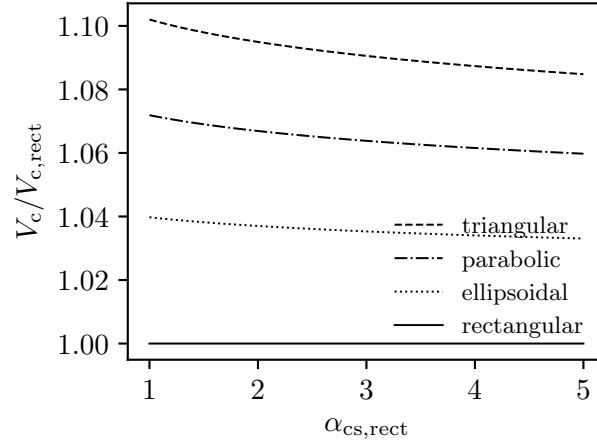


Figure 3.7 – Shear capacity of the critical shear crack V_c over the shear capacity of the critical shear crack for uniform pressure distribution $V_{c,rect}$, according to the closed-form equation (3.15), as a function of the moment-to-shear slenderness ratio $\alpha_{cs,rect} = a_{cs,rect}/d$.

The case of contact pressure distribution increasing toward the footing edge was not considered in this section. This would be the case of a rigid footing, and highly cohesive and stiff soil. By contrast, a slender beam cross-section would show a certain degree of flexibility and the contact pressure would tend to concentrate in the central region. Moreover, the distribution would become closer to uniformity as the soil bearing capacity is approached.

In the case of surface rectangular footings, the above considerations hold only for the central region (in the length direction). Close to the end zones and for footings with high values of the aspect ratio B/L , i.e. close to 1, three-dimensional effects on the contact pressure distribution become more important. In those situations, similar conclusions can be drawn, though they are not detailed here. In fact, there are no physical reasons to reject such conclusions. Actual values can be obtained by extending the suggested contact pressure shapes into three dimensions.

The above conclusions also apply qualitatively to concrete blocks loaded by a column. The governing structural failure is punching shear, which can be similarly investigated through the critical shear crack theory [251, 255].

3.5.4 Very Slender Beams

As the structural element becomes more deformable, the impact of the soil-structure interaction increases. In this section, outcomes obtained through the limit analysis method [96, 98, 146] for footings with a very slender cross-section (cf. Figure 3.3) are presented.

In the following, the soil is idealised as a perfectly rigid plastic isotropic homogeneous coaxial and associated continuum obeying the Tresca or Mohr-Coulomb yield condition. For simplicity, the terms Tresca/Mohr-Coulomb soil or material are used. The footing is a perfectly rigid plastic beam satisfying the normality condition in the space of generalised sectional stresses.

Plane Strain Problem

A combined failure mechanism for strip footings with limited flexural resistance was proposed by Plumey [281, 282]. The geometry of such rupture figure, symmetric with respect to the centre line, is shown in Figure 3.8 for a purely cohesive soil (left-hand side) and for a general cohesive frictional soil (right-hand side). The kinematics is defined by the angular velocity ω and the corresponding centre of rotation, identified by the angle θ_0 and the distance x_0 . The indentation of the footing causes the mass of soil between the ground surface and the failure line to rotate as a rigid body around the centre of rotation. Internal energy dissipation occurs along the lines of soil velocity discontinuity, in the footing plastic hinge, and eventually at the soil-footing interface. For purely cohesive soils, footing roughness is taken into account through an adherent behaviour, i.e. the interface is idealised as an infinitely thin layer of a Tresca material characterised by a shear yield strength βc , where $0 \leq \beta \leq 1$. For other soils, Coulomb interface friction

characterised by the interface friction angle δ is assumed. The external power is due to the collapse load Q_u and the soil self-weight.

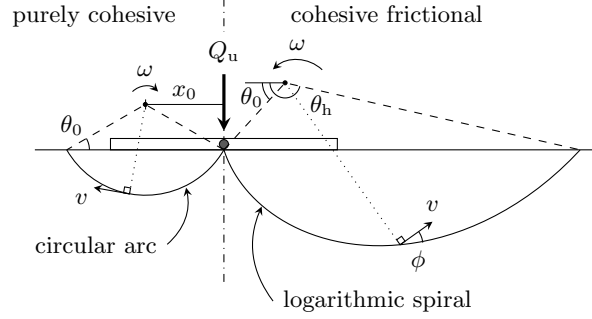


Figure 3.8 – Combined failure mechanism for plane strain conditions [281]. Velocity discontinuity lines within the soil are either a circular arc or a logarithmic spiral. The plastic hinge is shown with a grey circle in the middle of the footing.

Upper bounds were obtained by Plumey for Tresca and cohesionless Mohr-Coulomb soils* [281] (Figure 3.10 and 3.11), and by the authors for a general Mohr-Coulomb soil [111] (Figure 3.12). The curves of the bearing capacity are characterised by an increasing branch, corresponding to the combined failure, and by a plateau, due to the general shear failure (rigid footing). Here, in contrast to [111, 281], the plateau for the Mohr-Coulomb soils (sand and general soils) was taken from the complete solution given by Martin [217].

Note that the considered interface frictional behaviour for the upper bound solutions of the combined failure corresponds to a non-associated behaviour. However, the limit theorems are valid for frictional interfaces if the frictional forces are known, because they can be treated as surface tractions [97]. Given that the relative velocity at the interface is constant, the interface energy dissipation depends only on the resultant interface friction force, which is a function of the resultant contact pressure and independent of its distribution owing to the symmetry of the problem, i.e. the resultant over half-footing is necessarily $Q_u/2$.

A lower bound was also derived by Plumey for the case of a Tresca material (Figure 3.10). The admissible stress field was obtained by applying a contact pressure p , admissible for the soil, over a reduced contact breadth $B_c \leq B$ (Figure 3.9) such that $M(p, B_c) \leq M_R$. For the Tresca soil, such contact pressure is uniform and equal to $p_u = cN_c = c(2 + \pi)$.

*The objective function of the combined failure mechanism for a cohesionless Mohr-Coulomb material was reviewed by the authors in view of a mistake in the derivation of the velocity field for the computation of the rate of energy dissipated at the soil-footing interface [111].

A general formula for the lower bound of any pressure distribution can be obtained by considering half of the footing, the average pressure due to the general shear failure p_u corresponding to a lower bound solution, the relative position of the resultant force of the actual contact pressure distribution $\zeta = a/B_c$ (Figure 3.9), and the contact breadth ratio $\zeta_c = B_c/B$. The solution can be expressed as follows:

$$\zeta_c = \sqrt{\frac{2M_R}{p_u \zeta}} \leq 1 \quad (3.17a)$$

$$Q_u = p_u \zeta_c B \quad (3.17b)$$

The procedure consists in computing p_u with (3.1), redistributing it in an admissible manner, e.g. with one of the simple shapes described in the previous section, and defining ζ (cf. Table 3.1).

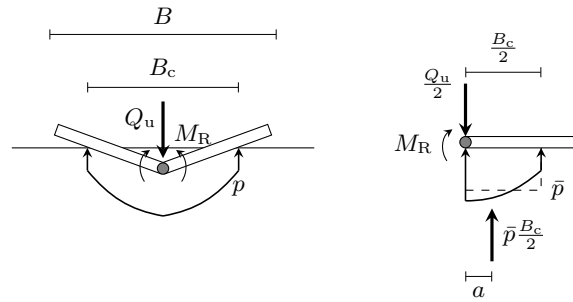


Figure 3.9 – Allowable stress field for combined failure in plane strain conditions [281].

For the Tresca material, considering $p_u = cN_c = c(2 + \pi)$, the dimensionless resisting moment $\mu = M_R/(cB^2)$, and $\zeta = 1/4$, leads to the result obtained by Plumey:

$$\frac{Q_u}{cB} = \sqrt{8(2 + \pi)\mu} \quad (3.18)$$

For a frictional soil, p_u is a function of the contact breadth (size effect). Introducing the dimensionless resisting moment $\eta = M_R/(\gamma B^3)$, (3.17a) becomes, for a cohesionless Mohr-Coulomb material, as follows:

$$\zeta_c = \left(\frac{4\eta}{N_\gamma \zeta} \right)^{1/3} \leq 1 \quad (3.19)$$

and the dimensionless bearing capacity is given by the following expression:

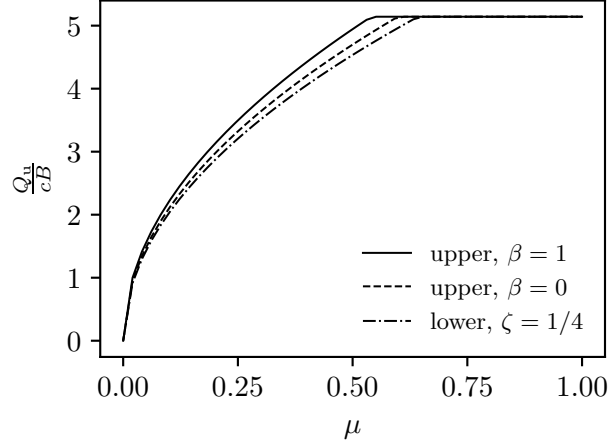


Figure 3.10 – Upper and lower bounds to the collapse load of a strip footing resting on a Tresca material. The normalised bearing capacity is plotted against the dimensionless resisting moment $\mu = M_R/(cB^2)$. The plateau corresponds to the well-known value $2 + \pi$.

$$\frac{2Q_u}{\gamma B^2} = \zeta_c^2 N_\gamma \quad (3.20)$$

The contact pressure distribution for smooth rigid footings is directly obtained with the method of stress characteristics [191]. It increases linearly from the footing edge to the centre. It was shown that the solution obtained in this way is complete [217]. Thus, a triangular distribution is a rigorous lower bound. Moreover, the triangular distribution corresponding to the smooth interface is a rigorous lower bound for any value of footing roughness according to the frictional limit theorems [85]. Improved lower bounds for rough bases can be obtained by considering the appropriate value of the bearing capacity factor N_γ . However, the distribution for rough footings cannot be obtained in the same way, owing to the presence of a non-plastic wedge beneath the base. Several authors suggested that the pressure distribution at collapse is parabolic [198, 364, 383, 384] or can be well approximated by a triangular shape [179, 232, 336]. If a triangular distribution is assumed, the solution for a cohesionless Mohr-Coulomb material is obtained with $\zeta = 1/6$ in (3.19) (Figure 3.11), whereas for a parabolic distribution $\zeta = 3/16$ ($1/6 = 0.167$ and $3/16 = 0.188$).

Shield [343] obtained a rigorous lower bound to the uniform normal strip load for a weightless general Mohr-Coulomb soil. The corresponding solution for the combined failure is shown at the bottom row of Figure 3.12. The solution is obtained as in the case of a Tresca material, but with $N_c = N_c(\phi)$. Such solution is an absolute lower bound because base roughness and soil self-weight increase the soil bearing capacity.

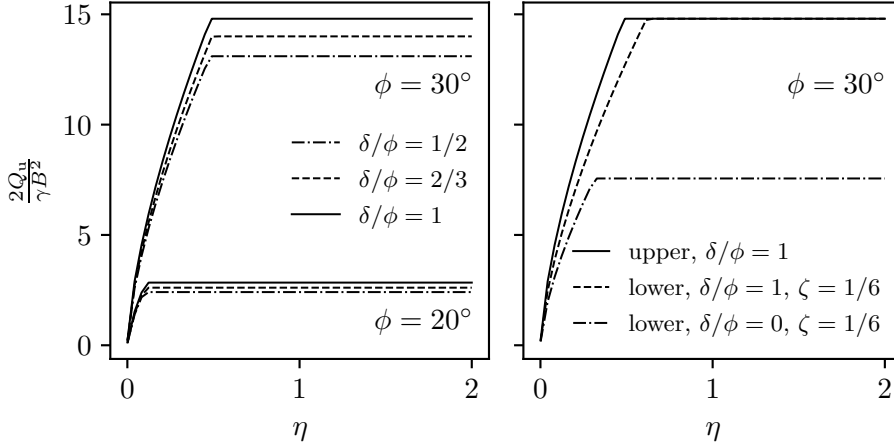


Figure 3.11 – Upper and lower bounds to the collapse load of a strip footing resting on a cohesionless Mohr-Coulomb material. Left-hand side: upper bounds; right-hand side: upper and lower bounds. The normalised bearing capacity is plotted against the dimensionless resisting moment $\eta = M_R/(\gamma B^3)$. The values of the general shear failure (plateau) are taken from [218].

For a ponderable Mohr-Coulomb material, the pressure at the instant of general shear failure is non-zero at the footing edge owing to the apparent cohesion, and then it increases in a linear or parabolic way toward the centre, as explained previously. Therefore, the computation of ζ requires the explicit knowledge of the contribution of the apparent cohesion and the soil self-weight to the bearing capacity, i.e. N_c and N_γ . However, when the principle of superposition is not adopted, such coefficients vary for each combination of ϕ and G , and the solution is generally given as the ratio p_u/c , or similarly, without specifying the individual contributions. Nevertheless, a lower bound solution can be obtained in a simple manner by exploiting the fact that the superposition approach to the soil general shear failure is conservative, i.e. it leads to a lower bound to the collapse load corresponding to a consistent failure mechanism [15, 233, 384]

$$N_c(\phi, c, \gamma = 0) + GN_\gamma(\phi, c = 0, \gamma) \leq N_c(\phi, c, \gamma) + GN_\gamma(\phi, c, \gamma) \quad (3.21)$$

The improved lower bound for the combined failure can be obtained by independently computing ζ_c for a weightless cohesive frictional material (ζ_{cc}) and for a ponderable cohesionless frictional material ($\zeta_{c\gamma}$), and then taking the minimum. However, ζ_{cc} and $\zeta_{c\gamma}$ cannot be simply expressed as a function of the total resisting moment M_R , as before. This would not guarantee an admissible bending moment when the contributions are summed. To ensure an admissible bending moment, it is assumed that the weightless and cohesionless soils respectively contribute to the bending moment by M_c and M_γ as

follows:

$$\begin{aligned} M_c &= \rho_m M_R \\ M_\gamma &= (1 - \rho_m) M_R \end{aligned} \quad (3.22)$$

Considering that $\mu = 2\eta G$ for a general soil, the contact breadth ratio is expressed as follows:

$$\begin{aligned} \zeta_c &= \min\{\zeta_{cc}, \zeta_{c\gamma}\} \\ \zeta_{cc} &= \left(\frac{2\rho_m \mu}{N_c \zeta} \right)^{1/2} \leq 1 \\ \zeta_{c\gamma} &= \left(\frac{2(1 - \rho_m) \mu}{G N_\gamma \zeta} \right)^{1/3} \leq 1 \end{aligned} \quad (3.23)$$

and the dimensionless ultimate load is given by the following expression:

$$\frac{Q_u}{cB} = \zeta_c N_c + \zeta_c^2 G N_\gamma \quad (3.24)$$

The optimum is found by solving the following bounded maximisation problem:

$$\begin{aligned} \max_{\rho_m} \quad & \frac{Q_u}{cB} \\ & 0 \leq \rho_m \leq 1 \end{aligned} \quad (3.25)$$

The problem was transformed in a minimisation problem by multiplying the objective function times -1 . The L-BFGS-B algorithm [31] implemented in SciPy [398] was used for the resolution. A triangular pressure distribution was considered for the soil-weight contribution. Some results are shown in Figure 3.12 with grey lines. Note that the superposition approach, which considers interface friction and soil self-weight, provides a better lower bound, as expected.

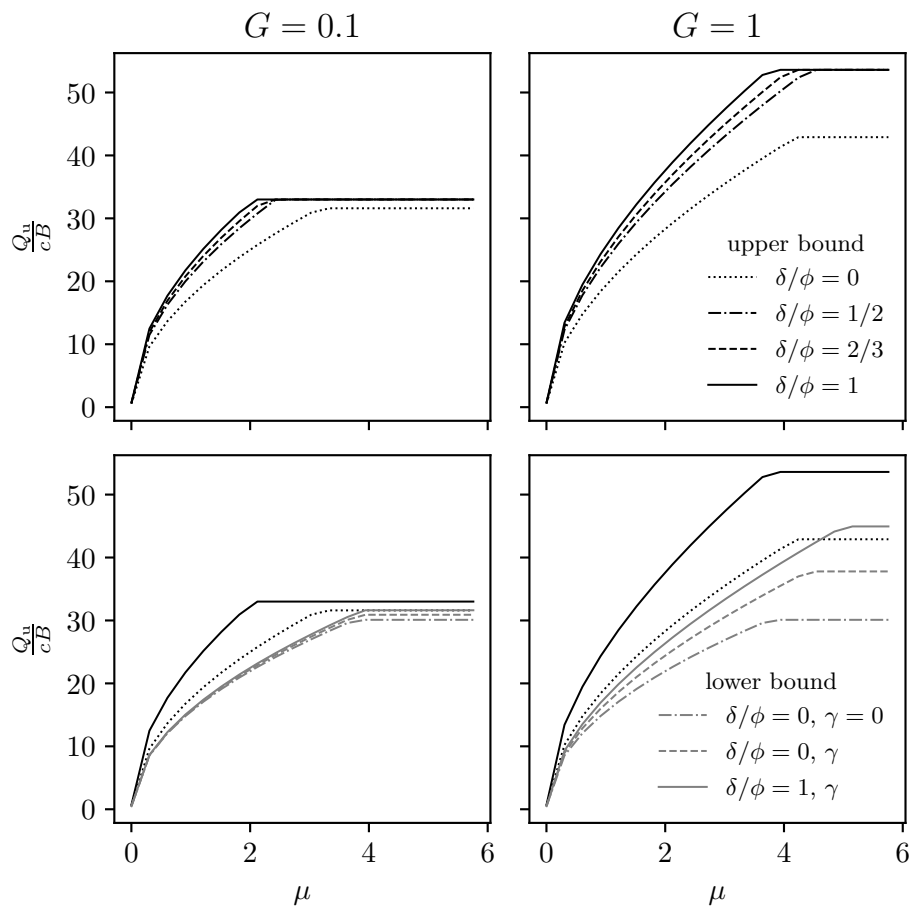


Figure 3.12 – Upper and lower bounds to the collapse load of a strip footing resting on a general Mohr-Coulomb material, $\phi = 30^\circ$. First row: upper bounds; second row: black lines denote upper bounds whereas grey lines denote lower bounds.

Three-Dimensional Problem

A combined failure mechanism for footings with finite length subjected to a centred linear load can be obtained from that of a plane strain situation and considering an admissible velocity field (compatible and satisfying the normality condition) at the end faces.

The velocity field for a Tresca material is simply obtained by extending the bi-dimensional failure mechanism over the footing length L and considering the resulting velocity discontinuity surface at the end faces (Figure 3.13). Hence, internal energy dissipation within the soil occurs on the cylindrical surface and on the end circular segments. The resulting objective function is expressed as follows (cf. C for the mathematical derivation):

$$\begin{aligned} \frac{Q_u}{cB} &= \frac{2}{\zeta_0} \mu + \zeta_0 K_{c1} + \zeta_0^2 K_{c2} \frac{B}{L} \\ K_{c1} &= 2 \left(\frac{\pi - 2\theta_0}{\cos^2 \theta_0} + \beta \tan \theta_0 \right) \\ K_{c2} &= \frac{4}{3} \left\{ \frac{\pi - 2\theta_0}{\cos^3 \theta_0} - \frac{\tan^3 \theta_0}{4} \left[\sin^{-2}(\theta_0/2) - \cos^{-2}(\theta_0/2) + 4 \ln \frac{\cos(\theta_0/2)}{\sin(\theta_0/2)} \right] \right\} \end{aligned} \quad (3.26)$$

where $\zeta_0 = x_0/B$. The solution is found through the following bounded optimisation problem:

$$\begin{aligned} \min_{\zeta_0, \theta_0} \quad & \frac{Q_u}{cB} \\ \zeta_0 &> 0 \\ 0 &< \theta_0 < \pi \end{aligned} \quad (3.27)$$

which was solved numerically as before. The results for perfectly adherent footings ($\beta = 1$) are plotted for $B/L = 0, 0.5$ and 1 in Figure 3.14. To the best of authors' knowledge, the best upper bound for rectangular rigid footings was obtained by Salgado et al. [334] with the limit analysis and finite element method. For the considered rectangular and square shapes, they obtained $N_c = 6.02$ and 6.22 , respectively. For comparison, the complete solution for a perfectly adherent circular punch was obtained by Eason and Shield [99] and is $N_c = 6.05$. The bearing capacity of a Tresca material increases with increasing aspect ratio B/L owing to the presence of hoop stresses [134, 232]. This is also observed in the combined failure. Note that this explanation for enhanced bearing

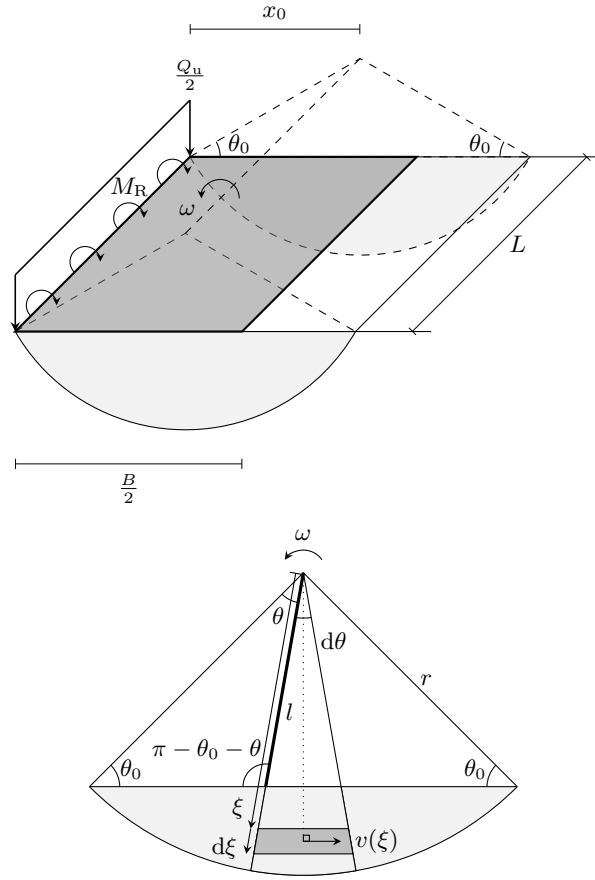


Figure 3.13 – Combined failure mechanism in three dimensions for a Tresca material.

capacity leads to the conclusion that it is maximum for circular footings [231, 359]. Thus, it is likely that $N_c = 6.05$ is an absolute upper bound to the bearing capacity of any rectangular indenter.

Rigorous lower bound solutions can be obtained in the same way as for strip footings. The pressure distribution is not uniform but increases slightly toward the footing centre. However, given that the bearing pressure increases with B/L , an absolute lower bound may be obtained assuming a uniform pressure distribution equal to $c(2 + \pi)$.

The geometry of the end failure surfaces for a Mohr-Coulomb material is more complex because the normality condition imposes an angle ϕ between the velocity vectors and the velocity discontinuity surface. Such a surface for a plane strain motion, i.e. a motion where the velocity vectors are all parallel, was derived by Garnier [115] and is depicted in Figure 3.15. The kinematics is similar to the previous cases, with velocity

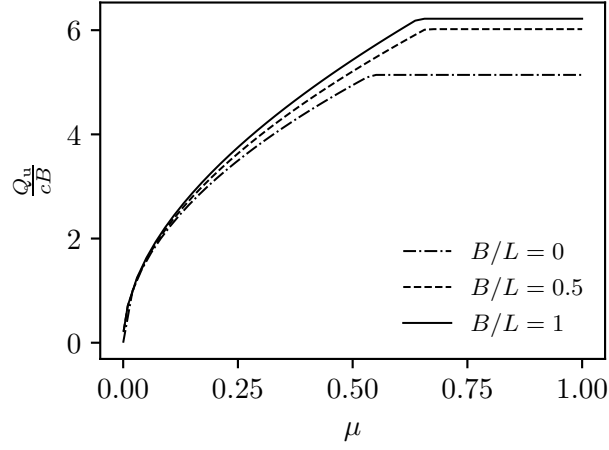


Figure 3.14 – Upper bounds to the collapse load for perfectly adherent rectangular footings with finite flexural resistance resting on a Tresca half-space.

vectors parallel to the xy -plane.

The objective function for a cohesionless Mohr-Coulomb soil is expressed as follows (refer to [D](#) for further details regarding its derivation):

$$\begin{aligned} \frac{2Q_u}{\gamma B^2} &= \frac{2}{1 - \tan \delta \tan \theta_0} \left(\frac{2}{\zeta_0} \eta + 2K_{\gamma 1} \zeta_0^2 + \frac{B}{L} K_{\gamma 2} \zeta_0^3 \right) \\ K_{\gamma 1} &= -\frac{f_1}{\cos^3 \theta_0} + \frac{\tan \theta_0}{6} - \frac{\tan^3 \theta_0}{6 \tan^2 \theta_h} \\ K_{\gamma 2} &= -\frac{1}{\cos^4 \theta_0} \int_{\theta_0}^{\theta_h} \left(e^{4(\theta - \theta_0) \tan \phi} - \frac{\sin^4 \theta_0}{\sin^4 \theta} \right) \sinh[(\theta - \theta_0) \tan \phi] \cos \theta \, d\theta \end{aligned} \quad (3.28)$$

where f_1 was derived by Chen [\[49\]](#):

$$f_1 = \frac{1}{3(1 + 9 \tan^2 \phi)} \left[(3 \tan \phi \cos \theta_h + \sin \theta_h) e^{3(\theta_h - \theta_0) \tan \phi} - 3 \tan \phi \cos \phi - \sin \theta_0 \right] \quad (3.29)$$

Given that θ_h and θ_0 are related through the implicit equation $\sin \theta_h \exp[(\theta_h - \theta_0) \tan \phi] - \sin \theta_0 = 0$ [\[281\]](#), the optimisation problem is expressed as follows:

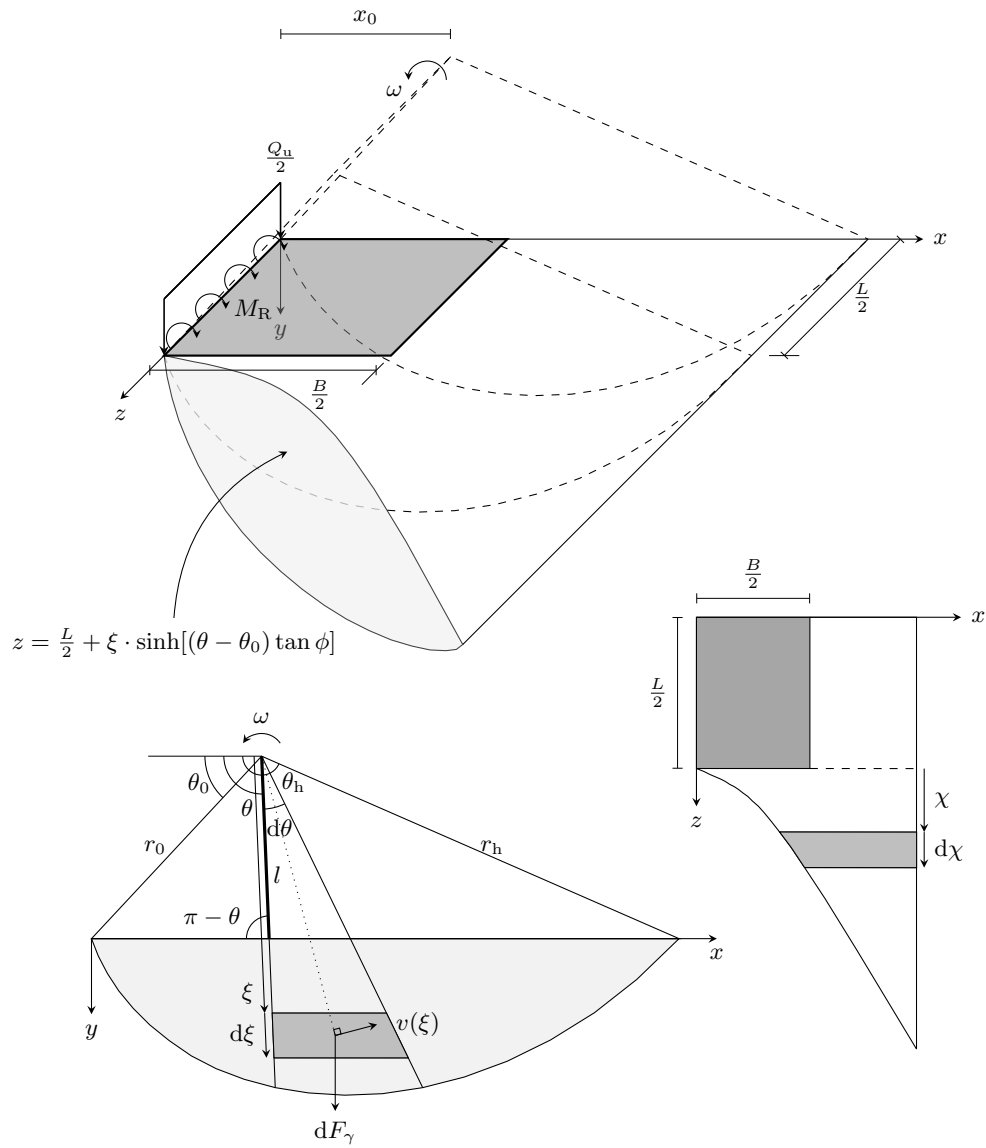


Figure 3.15 – Combined failure mechanism in three dimensions for a Mohr-Coulomb material.

$$\begin{aligned}
& \min_{\zeta_0, \theta_0} \frac{2Q_u}{\gamma B^2} \\
& \zeta_0 > 0 \\
& \begin{cases} 0 < \theta_0 < \pi & \text{if } \delta = 0 \\ 0 < \theta_0 < \tan^{-1}(1/\tan \delta) & \text{otherwise} \end{cases}
\end{aligned} \tag{3.30}$$

In (3.28), the integral was numerically evaluated with the `scipy.integrate.quad` function of SciPy and the optimisation was carried out as in the previous case.

Results for perfectly rough interfaces ($\delta = \phi$), $\phi = 15^\circ$ and 35° are given in Figure 3.16. The bearing capacity for rectangular rigid footings is computed by multiplying the exact solution for strip footings [218] with the analytical expression of the shape factor derived by Lyamin et al. [202], which is based on a weighted average of lower and upper bounds, and thus it is supposed to provide reasonable estimates of the exact solution. Note that the bearing capacity increases with increasing B/L for $\phi = 35^\circ$, whereas the situation is reversed for $\phi = 15^\circ$. This seems inconsistent with respect to the experimental results previously mentioned, according to which the bearing capacity decreases with decreasing L . The reason for this is twofold. First, the shear strength angle for conditions other than plane strains is lower [231]. Second, finite element simulations showed that, for small values of ϕ , the mass of displaced soil reduces with increasing B/L [412]. This causes a reduction of the bearing capacity. The same was observed for higher values of the shear strength angle and dilatancy angles lower than ϕ , which is generally the case for real soils.

To obtain a lower bound, the same approach of the plane strain problem can be adopted but with extension of the shape of the contact pressure distribution to three dimensions. In particular, the pressure must be zero over the entire perimeter of the footing. This actually produces a movement of the resultant pressure closer to the footing centre.

In the case of general Mohr-Coulomb soils, the contribution of the cohesion to the internal energy dissipation must be added to the previous solution. The objective function can be expressed as follows (cf. E):

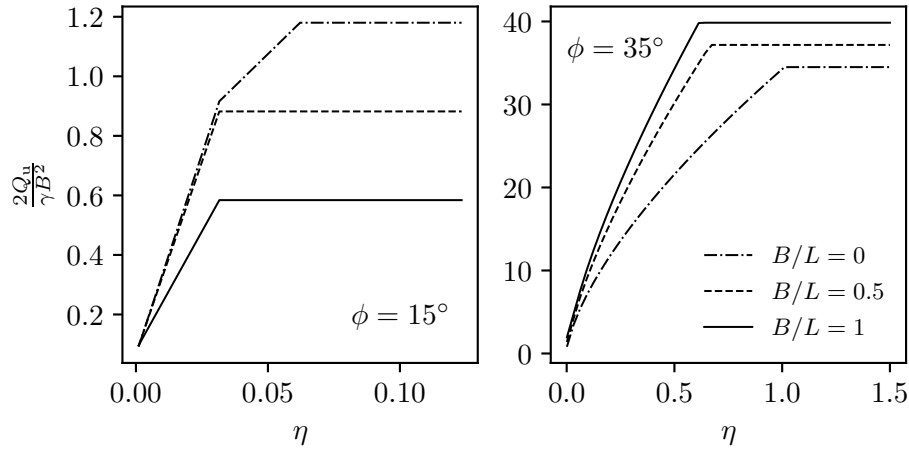


Figure 3.16 – Upper bounds to the collapse load for perfectly rough ($\delta = \phi$) rectangular footings with finite flexural resistance resting on a cohesionless Mohr-Coulomb half-space.

$$\begin{aligned}
 \frac{Q_u}{cB} &= \frac{1}{1 - \tan \delta \tan \theta_0} \left[\frac{2}{\zeta_0} \mu + K_1 \zeta_0 + 4 \left(\frac{B}{L} K_2 - G K_3 \right) \zeta_0^2 - \frac{B}{L} G K_4 \zeta_0^3 \right] \\
 K_1 &= \frac{e^{2(\theta_h - \theta_0) \tan \phi} - 1}{\cos^2 \theta_0 \tan \phi} \\
 K_2 &= \frac{1}{3 \cos^3 \theta_0} \int_{\theta_0}^{\theta_h} \left(e^{3(\theta - \theta_0) \tan \phi} - \frac{\sin^3 \theta_0}{\sin^3 \theta} \right) \cosh[(\theta - \theta_0) \tan \phi] d\theta \\
 K_3 &= -K_{\gamma 1} \\
 K_4 &= -\frac{K_{\gamma 2}}{2}
 \end{aligned} \tag{3.31}$$

with the following optimisation problem:

$$\begin{aligned}
 &\min_{\zeta_0, \theta_0} \frac{Q_u}{cB} \\
 &\zeta_0 > 0 \\
 &\begin{cases} 0 < \theta_0 < \pi & \text{if } \delta = 0 \\ 0 < \theta_0 < \tan^{-1}(1/\tan \delta) & \text{otherwise} \end{cases}
 \end{aligned} \tag{3.32}$$

Results for perfectly rough interfaces, obtained in a similar way to the previous ones

for $G = 0.1$ and 0.5 , $\phi = 15^\circ$ and 35° , and $B/L = 0$ and 0.5 , are plotted in Figure 3.17. A few rigorous upper bound solutions are available for the bearing capacity of finite length footings resting on general soils. The reason for this is that an optimum solution exists for any combination of the parameters G , ϕ , and B/L , which complicates to derive useful and simple analytical expressions or charts. Moreover, practitioners prefer the superposition approach owing to its conservative character. The solutions for rigid footings retained here correspond to the upper bounds obtained by Michalowski [235], who considered an advanced multi-block Prandtl-type failure mechanism. Note that, for the selected values of G , the bearing capacity increases with increasing B/L , similar to the case of a Tresca material. This is due to the fact that, as a rough estimate, a weightless material can be assumed for $G < 0.1$, whereas a cohesionless material can be assumed for $G > 10$ [49]. Therefore, the situation is closer to a weightless material.

An absolute lower bound corresponding to a weightless soil and a smooth footing can be obtained with the admissible uniform contact pressure obtained by Shield [343]. Improved solutions require to take into account the soil self-weight and eventually the base roughness. The superposition approach can be adopted, as in the case of strip footings.

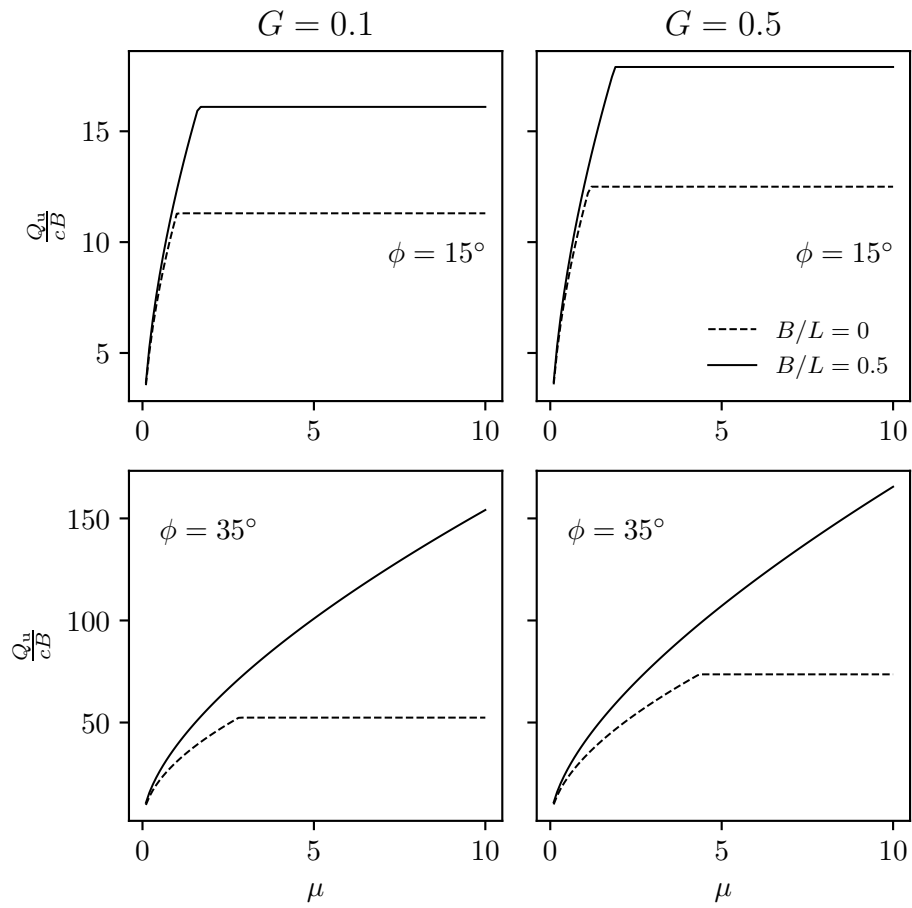


Figure 3.17 – Upper bounds to the collapse load for perfectly rough ($\delta = \phi$) rectangular footings with finite flexural resistance resting on general Mohr-Coulomb half-spaces.

3.6 Concluding Remarks

A general framework for the analysis of the bearing capacity of surface footings under centred vertical load considering soil-structure interaction was presented. The importance of considering both components, i.e. the ground and the structure, for a correct evaluation of the overall foundation performance was emphasised. Two new analytical expressions for the bearing capacity of rigid strip footings resting on a general Mohr-Coulomb soil were given. A simple procedure based on the knowledge of an approximate contact pressure distribution combined with the knowledge of the governing footing failure mode was shown to be a powerful tool for consistent foundation analysis and design.

Detailed analysis of the bearing capacity problem of a surface footing with a very slender cross-section was carried out to show how the limit analysis method can be applied to general three-dimensional soil-structure systems.

Some of the main conclusions that can be drawn from this study are as follows:

- The influence of soil-structure interaction increases with structural slenderness.
- The evaluation of the footing performance assuming a uniform contact pressure distribution, regardless of the soil properties, is only justified for deep beam footings.
- Previous studies coincide on the fact that the contact pressure distribution at the instant of general shear failure is closely approximated by one of the following simple shapes: uniform, triangular, ellipsoidal, and trapezoidal. This can be conveniently exploited to take into account the soil-structure interaction in a simplified manner.

The concepts and techniques presented in this paper can be extended to shallow footings subjected to general loading conditions and to other soil-structure systems, such as retaining walls.

Acknowledgements

This study was supported by the Swiss National Science Foundation (financial support No. 200021_175500, Division II).

Part II

Thermoactive Deep Foundations

“Elastic soils” are those whose response to a given change in effective stress is, for practical purposes, independent of the stress path over the range of stresses encountered. Hence non-linear or irrecoverable behaviour does not necessarily preclude the use of elastic stress-strain formulations.

J. B. Burland, B. B. Broms, V. F. B. De Mello,
Behaviour of Foundations and Structures

4

Three-Dimensional Finite Element Analysis of Piled Rafts with Energy Piles

Postprint version of the article submitted to Computers and Geotechnics.

C Garbellini and L Laloui. “Three-dimensional finite element analysis of piled rafts with energy piles”. In: *Computers and Geotechnics* 114 (2019), p. 103115.

Contribution of the candidate: initial idea, numerical modelling, analysis of results, writing of manuscript.

OVER THE LAST twenty years, the importance of environmentally friendly technologies in the field of construction has grown considerably. In this regard, energy piles are an innovative technology that combines the structural role of piles with that of a ground heat exchanger, through the inclusion of pipes carrying a heat exchanger fluid. Although it is common practice to cast the raft of a piled foundation directly on the ground, most of the available studies on energy piles have not been concerned with the implications that this entails. In this study, attempts have been made to fill this gap through a series of three-dimensional finite element simulations. This paper describes three dimensionless parameters, namely the raft to single isolated pile displacement ratio, the normalised differential displacement and the normalised thermally induced axial stress, which can be used to evaluate the overall performance of the foundation. The influence of the main mechanical parameters on the aforementioned dimensionless parameters is shown in graphical form and comparisons with conventional foundations are made.

4.1 Introduction

Deep foundations can be divided into two main classes: pile groups and piled rafts. In pile groups, the cap is not in contact with the ground and the entire load is transmitted to the piles. In piled rafts, the capping slab is in contact with the soil and part of the load is transferred directly to the ground by contact pressure. Over the last few decades, a new major classification has been introduced with energy piles. This innovative technology combines the mechanical supporting role of piles with that of a ground heat exchanger, leading to unprecedented thermally induced actions on piles and soil behaviour.

During the last century, many researchers focused their efforts on the behaviour of pile groups and piled rafts. This has led to a variety of analytical and numerical methods for the computation of displacements and internal efforts. Among the most recognisable are the method of equivalent sub-grade reaction modules [384], the interaction factor method for pile groups [35, 285] and piled rafts [54, 68], the axisymmetric layer model for pile groups [302], the combined axisymmetric layer and load transfer model for pile groups [258], the equivalent pier method [289, 303], the equivalent capped pile method [152], the boundary element method for pile groups [8, 29] and pile rafts [30], the finite difference method [59] and the finite element method [164, 262, 272]. More recently, the increasing importance of environmentally friendly technologies has led to an extension of the aforementioned methods to energy foundations. This concerns, in particular, the interaction factor method for energy pile groups [321], the equivalent pier

method for energy pile groups [320] and the application of the finite element method [81, 322].

To date, no exhaustive parametric analysis on the influence of the raft stiffness over a group of energy piles has been presented. This lack of knowledge might be a constraint in extrapolating and extending results for energy pile groups to real piled raft foundations, especially during the early design stages. In this study, the finite element method has been employed to solve the three-dimensional (3D) thermo-elastic problem of piled rafts with regular grids of piles activated thermally. The major outcomes of an extensive series of numerical simulations are presented in graphical form through dimensionless parameters. The impact of the main mechanical parameters is discussed in comparison with conventional foundations. Finally, key points are summarised.

4.2 Numerical Modelling

In this section, the parametric analysis is presented and the mathematical model is briefly introduced. Details concerning the finite element model are also given.

4.2.1 Parametric analysis

An extensive parametric analysis (610 simulations) on piled rafts with regular grids of energy piles (Figure 4.1a) was performed. In each simulation, all piles were subjected to a temperature variation $\Delta T = 10^\circ\text{C}$. Neither mechanical load nor gravity field were considered because the aim of this research was to investigate the impact of thermal loads only. This is justified by the fact that linear elasticity was adopted (further details and justification of this assumption are given in sections 4.2.2 and 4.2.3). Thermo-mechanical time-dependent analyses were performed for a period of five months (further details follow in sections 4.2.2 and 4.2.3). The diameter of piles was set equal to $d = 1\text{ m}$. Two main configurations were investigated: semi-floating piles and end-bearing piles. For both, analyses were carried out at a constant spacing to pile diameter ratio $s/d = 5$, constant soil Poisson's coefficient $\nu_s = 0.3$, two pile length to diameter ratios (slenderness) l/d (25 and 50), two pile Young's modulus to soil shear modulus ratios $K = E_p/G_s$ (10^2 and 10^4), three values of soil to pile thermal expansion coefficient ratio $X = \alpha_s/\alpha_p$ (0, 1 and 2), five raft thickness to pile diameter ratios t_r/d (0.25, 0.5, 1, 2 and 4) and five grids of energy piles n_p (1^2 , 2^2 , 3^2 , 4^2 and 5^2 ; in some cases also 6^2). Parametric analyses on s/d , ν_s and l/d were carried out only for the case $K = 3 \times 10^3$, $X = 0$, $t_r/d = 1$ and $n_p = 4^2$. It was assumed that similar tendencies might be extended to all configurations.

The behaviour of pile rafts was analysed in terms of: the raft to pile group displacement ratio $R_r = \bar{w}_r/\bar{w}_g$, where \bar{w}_r is the raft mean displacement and \bar{w}_g is the mean displacement of the pile group in the piled raft configuration; pile group to single pile displacement ratio $R_s = \bar{w}_g/w_s$, where w_s is the head displacement of an isolated free-standing pile equivalent to those in the piled-raft system (i.e. same ΔT , l/d , K , etc.); raft to isolated pile displacement ratio $R = R_r R_s$; raft differential displacements ratios $\Delta w_{1:0}/\bar{w}_r$ and $\Delta w_{1:0.5}/\bar{w}_r$, where $\Delta w_{1:0}$ and $\Delta w_{1:0.5}$ are the differential displacements between normalised coordinate (ξ) 1 and 0, and between 1 and 0.5, respectively (see Figure 4.1b) and normalised thermally induced axial stress within the piles $\varsigma = \sigma/(E_p \alpha_p \Delta T)$, with σ the axial stress in the considered pile due to temperature variation. Values of \bar{w}_r were obtained through the mean of the nodal displacements of the top surface of the raft. Here Δw_ξ was calculated by finding the difference between the corresponding nodal displacements and σ was computed at the integration points along the central line of the piles.

Parameter R summarises all interactions that occur through the soil and the capping slab, Δw_ξ gives a rough estimate of the flatness of the deformed raft and ς is the fraction of the actual stress with respect to the case of a fully blocked pile. Variables K and t_r/d provide information about the bending stiffness of the raft B ($B \propto E_r t_r^3 \propto K(t_r/d)^3$, where E_r designates the Young's modulus of the raft).

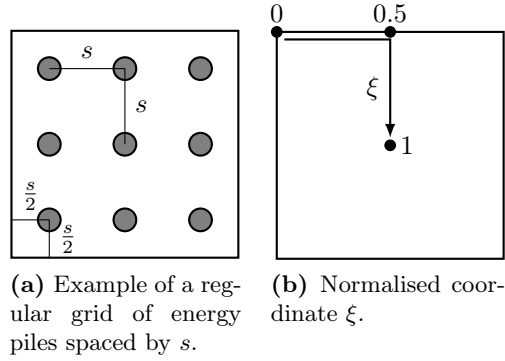


Figure 4.1 – Schematic view of a typical piled raft configuration and definition of the normalised reference system.

4.2.2 Mathematical Formulation

In the following, compressive stresses, contracting strains and downward displacements are considered to be positive.

Weak thermo-mechanical coupling was assumed. This means that the temperature field has an effect on the state of stress, but not the other way around (also known as *one way coupling*). Analyses were performed in transient conditions, i.e. time dependent. This aspect plays a role even in the framework of thermo-elasticity, because it is not guaranteed that at the end of the heating period steady state conditions are reached. Therefore, the extent of the mass of soil affected by piles temperature variation could be lower with respect to that computed with a time independent analysis. As a consequence, a steady state calculation might lead to an overestimate of the impact of thermal loads.

No hydro-mechanical coupling was considered here. The thermal properties of soil (cf., Table 4.1), namely the thermal conductivity and the heat capacity, are typical of saturated sandy or silty soils. In the former case, the behaviour is characterised by a drained response, so that a hydraulic coupling is not necessary. For the latter case, a drained response is in general meaningful only for long term analyses. Nevertheless, field experiments [238, 322] and previous numerical simulations [81] showed that induced excess pore water pressure upon thermal piles activation is negligible.

Table 4.1 – Material properties used in the finite element model. The word *variable* refers to those parameters that were varied to obtain specific values for the parametric analysis (see section 4.2.1).

		Concrete	Soil
Solid skeleton density	ρ [kg m ⁻³]	2778	2650
Porosity	n [-]	0.1	0.42
Young's modulus	E [GPa]	30	variable
Poisson's coefficient	ν [-]	0.2	variable
Thermal expansion coefficient	α [°C ⁻¹]	10 ⁻⁵	variable
Thermal conductivity	λ [W m ⁻¹ K ⁻¹]	1.628	1.628
Heat capacity	c_p [J Kg ⁻¹ K ⁻¹]	837	837

It was assumed that displacements and deformations could be satisfactorily described by linear kinematics under quasi-static conditions. In addition to linear geometry, material linearity was also assumed. These hypotheses may not be completely true, but can be applied successfully to the analysis of pile foundations by choosing appropriate soil and concrete elastic parameters [289] and because, under normal working conditions, thermal loads are not expected to induce plastic deformations at the pile–soil interface [81, 322]. The hypothesis of material linearity, especially in relation to piles interface behaviour, might deserves further considerations. In fact, the interface can be expected to be already in a plastic state after the application of gravity loads. In this case, when the pile is thermally activated, thermally induced stresses modify the shear stress distribution

along the interface and, depending on their sign, they lead to an elastic unloading or to a plastic loading. Therefore, the response of the soil–pile interface would be not linear and, moreover, the symmetry between cooling and heating would be lost. Nevertheless, considering the extent of practical temperature variations, the non symmetric behaviour between heating and cooling happens only during the first thermal cycle (eventually firsts two or three cycles) [22, 78, 189]. After this process of stabilisation, piles head mean displacement remain rather constant, suggesting that the behaviour is reversible. According to that, an appropriate choice of elastic parameters would be sufficient to estimates main thermally induced effects. Certainly there are specific situations where this may not be applicable, as probably would be the case of loose sands, where cyclic compaction might takes longer time. The proposed analysis does not claim to be exhaustive and able to capture all the underlying phenomena, but its purpose is rather to furnish a basic understanding of the response of piled raft foundations with energy piles, to which further analyses might relate. Since the behaviour of piled raft foundations with thermo–active piles was not studied before (at least with an extensive parametric analysis), it is authors opinion that the knowledge of the impact of elastic parameters is fundamental in order to better understand plasticity effects later on.

Finally, it was assumed that all properties are constant with respect to temperature variation.

In the absence of a gravity field, equilibrium under quasi-static conditions can be expressed as

$$\nabla \cdot \sigma_{ij} = 0 \quad (4.1)$$

where $\nabla \cdot$ denotes the divergence operator and σ_{ij} is the Cauchy's total stress tensor. Linear thermo-elasticity implies that

$$\sigma_{ij} = D_{ijkl} (\varepsilon_{kl} + \alpha \Delta T \delta_{ij}) \quad (4.2)$$

where D_{ijkl} is the elasticity tensor and ε_{kl} is the small strain tensors, which in homogeneous and isotropic linear thermo-elasticity can be written as follows:

$$\varepsilon_{ij} = \frac{1}{E} \left[(1 + \nu) \sigma_{ij} - \nu \sigma_{kk} \delta_{ij} \right] - \alpha \Delta T \delta_{ij} \quad (4.3)$$

where E denotes the Young's modulus, ν is the Poisson's coefficient, δ_{ij} indicates the Kronecker delta, α is the linear thermal expansion coefficient and ΔT is the applied temperature variation.

Under transient conditions, the energy conservation principle states that

$$\rho c_p \frac{\partial T}{\partial t} - \nabla \cdot (\lambda \nabla T) = 0 \quad (4.4)$$

where ρ denotes the bulk density, c_p indicates the specific heat, t is the time, λ designates the thermal conductivity and ∇ is the gradient operator. When steady-state conditions are reached, the first term of equation (4.4) vanishes and the problem is governed by the Laplace's equation.

4.2.3 Finite Elements Model

A 3D finite element model was developed with Comsol Multiphysics [60] (cf., Figure 4.3). The dimensions of the soil mass were adjusted for each configuration as follows: the height was $5l$, whereas length and width were computed as $200d + (\sqrt{n_p} - 1)s$. Such dimensions ensure negligible boundary effects.

Piles and raft were made from the same concrete, considered to be a homogeneous and isotropic material and a purely conductive domain. The soil was also modelled with a homogenous and isotropic material and was assumed to be a purely conductive domain with equivalent thermo-physical properties. The values of thermal properties, namely thermal conductivity and heat capacity, agree with those adopted in previous numerical and experimental studies [321, 322, 375]. Material properties are reported in Table 4.1.

Vertical rollers were applied to external sides of the soil mass and pinned supports at its base, whereas zero mechanical load was prescribed at the ground and raft top surfaces. Perfect contact was considered between concrete structural elements and soil. In absence of gravity field and mechanical loads, when the raft is pushed upward upon piles heating, tensile stresses might appear at the soil-raft interface. Such stresses actually reproduce the reduction of contact pressure between the raft and the soil underneath, and the increase of axial load in the piles (cf., Figure 4.2). For practical ranges of temperature variation, as the one considered here, it is unlike that piles heating induce a loss of contact. The temperature was kept constant ($\Delta T = 0^\circ\text{C}$) at the bottom and external soil planes. Adiabatic conditions (no heat flux) were imposed on the top soil plane and on the external boundaries of the raft. A uniform thermal load $\Delta T = 10^\circ\text{C}$ was applied on the lateral surface of each pile. This is justified by the fact that the temperature profile is almost uniform along the length of the pile [21, 80, 238, 322] and axisymmetric over the cross-section, provided that pipes are arranged symmetrically around the reinforcing cage [21]. Finally, two planes of symmetry were imposed to model only one-quarter of the foundation (cf., Figure 4.3).

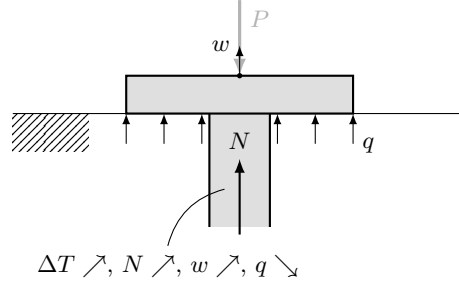


Figure 4.2 – Modification of raft-soil contact pressure (q) upon piles heating.

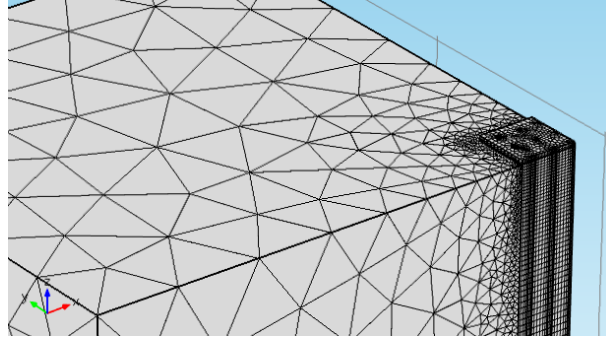


Figure 4.3 – Zoom of the finite element model for the 5^2 configuration. (Source: [60]).

Piles were meshed with triangular prisms, the raft and the soil beneath it with bricks and the surrounding soil with tetrahedrons. The finite element mesh was denser in the region of interest and coarser outside. Depending on the pile configuration n_p , the number of degrees of freedom varied between about 900 000 and 1 600 000.

4.3 Numerical Results

Graphical solutions are summarised in this section. Owing to the huge amount of data, only typical or selected results are presented. In this respect, comments regarding unpublished outcomes are given as well to provide a transparent and comprehensive report. An interpretation of the results is also given here, which should help to clarify the major aspects of the complex interaction phenomena that occur in a piled raft foundation when the piles are thermally activated.

4.3.1 Typical Results of Raft Mean Displacements

Results of raft mean displacement ratio R with respect to the normalised raft thickness t_r/d , dimensionless pile axial stiffness K , number of piles n_p , pile slenderness l/d , soil

Poisson's coefficient ν_s and pile spacing ratio s/d are given in this section.

Effect of Normalised Raft Thickness

The evolution of R_r , R_s and R with respect to the dimensionless raft thickness is presented in Figure 4.4 for the case $n_p = 4^2$.

For $K = 10^4$, all three coefficients are practically constant. Here R_r does not show any influence of X or the pile load bearing behaviour, whereas R_s and R exhibit an increase with X , but only for floating piles. When K is reduced to 10^2 , R_r increases until $t_r/d = 2$ and then remains constant. Such an increase is reduced as X grows and is practically negligible for $X = 2$. R_r grows and approaches the value of one because the bending stiffness of the raft increases. Conversely, R_s shows a decreasing branch in the first portion, until a nearly constant value is reached. This value increases with X and for end-bearing piles. R_s decreases because the connecting cap partially restrains the displacements of central piles, whereas it enhances those of other piles. As the fraction of “retaining” piles (corner, external and some intermediate in big configurations) is dominant, the overall piles' head mean displacement is reduced. Opposite trends of R_r and R_s make R roughly stable also for $K = 10^2$. This means that the stiffness of the raft has a negligible effect on R .

This is in agreement with the behaviour of conventional piled raft foundations. In fact, it is known that the average displacement of a raft foundation is relatively independent of the raft thickness [54, 153] and that up to the yielding point, the overall stiffness of the foundation is mainly given by the pile group [54, 68].

The assumption of a constant R introduces an error, which is more marked for $K = 10^2$ and $X = 2$, but it remains below 10% and it has no effect on further considerations. Therefore, any additional statement can be made with respect to a particular value of R , such as the mean or the maximum. In this study, the latter option has been considered. A similar conclusion can be inferred from all other pile configurations, with higher values of R for slender piles, validating the invariance of R with respect to t_r/d .

Effect of Normalised Pile Axial Stiffness

The effect of K on R for all floating pile configurations is given here (cf., Figure 4.5). For clarity, only results for the case $X = 0$ are presented. Nevertheless, the qualitative impact of end-bearing piles and higher values of X can be inferred from section 4.3.1.

The mean displacement ratio is higher for slender piles. The scatter decreases with increasing K and seems to converge towards 1, regardless of n_p and l/d . It can be

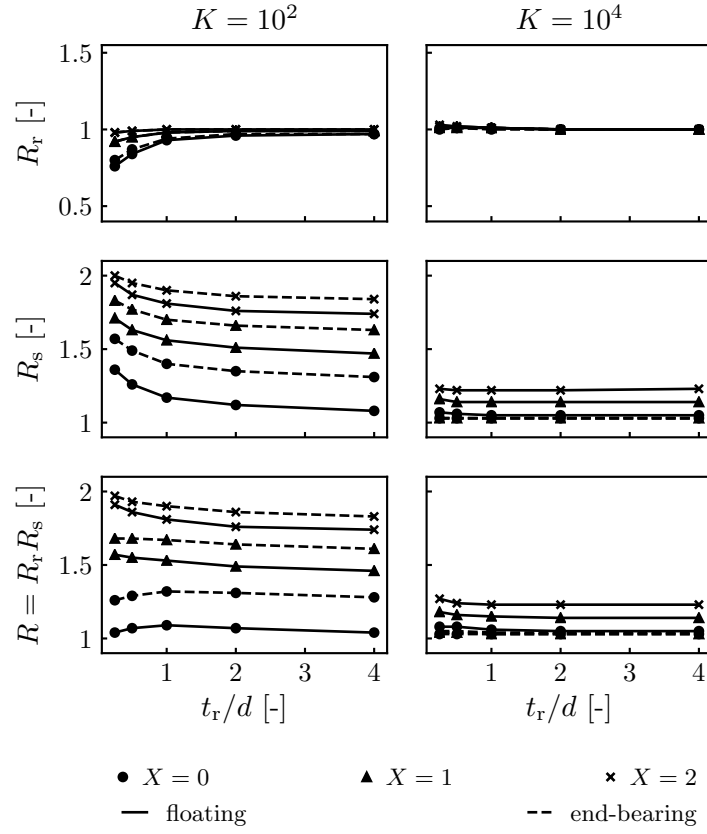


Figure 4.4 – Raft to pile group displacement ratio R_r , pile group to single isolated pile displacement ratio R_s and raft to single isolated pile displacement ratio R with respect to dimensionless raft thickness t_r/d for the $n_p = 4^2$ configuration; both floating and end-bearing piles; $l/d = 25$; $s/d = 5$; $\nu_s = 0.3$; $X = 0, 1$ and 2 ; and $K = 10^2$ and 10^4 .

stated that $\lim_{K \rightarrow \infty} = 1$, which makes sense because a null soil stiffness is equivalent to the absence of soil. Therefore, there would not be any interaction, neither through the soil nor through the slab, because all piles would be subjected to the same imposed deformation $\alpha_p \Delta T$. It is worth mentioning that it cannot be stated whether the trend is linear or not, because only two points for each case are available.

It appears evident that a soil with a thermal expansion coefficient higher than the one of piles can push against the raft and that such an effect is related to the soil stiffness. In agreement with Figure 4.4, 4.5 and 4.6, when $K = 10^2$ the effect of soil thermal expansion properties is greater compared with the case of $K = 10^4$. In fact, for a soft soil and $X > 1$, reinforced concrete structural elements act as “boundary conditions” for the heated soil mass, preventing or restricting its displacements.

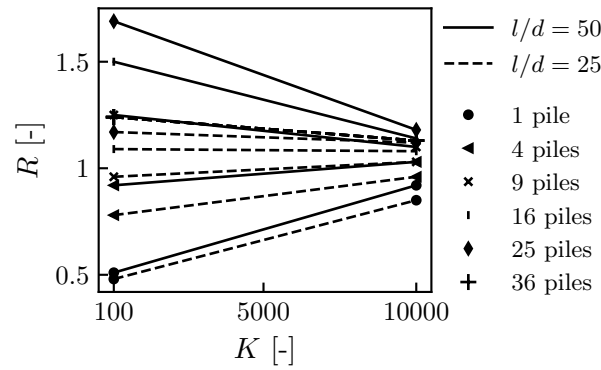


Figure 4.5 – Raft to single isolated pile displacement ratio R with respect to pile normalised stiffness K for all floating pile configurations; $X = 0$; $l/d = 25$ and 50 ; $s/d = 5$; and $\nu_s = 0.3$.

Effect of Number of Piles

The results concerning the influence of n_p on R are given in this section (cf., Figure 4.6). Only $l/d = 25$ is considered (graphs of $l/d = 50$ show analogous trends).

For both values of K , the rate of increase of R is reduced with an increasing number of piles. In the case of stiff soils ($K = 10^2$), at $n_p = 25$ stabilisation is still not reached for all values of X , even though for $X = 0$ the increment between $n_p = 16$ and $n_p = 25$ is very small. R is higher for larger values of X and for end-bearing piles. However, the discrepancy between floating and end-bearing piles decreases with X and is almost negligible when $X = 2$.

When $K = 10^4$, R is nearly constant and equal to 1 for end-bearing piles, for which it does not show any dependence on X . On the other hand, there is an increase for floating

piles with a similar trend to the case of $K = 10^2$, but with a reduction in magnitude. This is probably attributable to two factors: (i) the soil is too soft to push/drag the foundation, but (ii) the soil stiffness is nevertheless sufficient to modify the position of the null point (point along the pile length that does not experience any thermally induced displacement) for floating piles. In end-bearing piles, the null point is necessarily at the base.

It is fair to say that after a certain number of piles, the increase of R is negligible, as happens for free-standing energy pile groups [321] and conventional deep foundations under mechanical load [55, 285].

It is worth noting that R starts from a value lower than 1. This is the main difference with respect to an analysis in which the presence of the slab is neglected. In a free energy pile group, the average pile head displacement ratio (R_s) is always greater than one [321] (also shown in Figure 4.4). Here $R < 1$ indicates that the effect of mechanical interactions among piles is not sufficient to balance the increase of piles load due to the raft unloading. In fact, when piles expand, the contact pressure between the raft and the soil decreases. By equilibrium, the same amount of total load must be introduced in the piles (cf., Figure 4.2). (Note that in the case of active cooling the situation is reversed, i.e. the increase in contact pressure counteracts the settlement due to pile contraction). Here R is lower than one also for $X = 2$, because temperature variation diminishes quickly with radial distance from the piles and the soil pushes the raft only over a small portion, which is not sufficient to reach the displacement of a free isolated energy pile. On the other hand, when the number of piles increases the amount of interactions increases as well and this is enhanced for $X > 1$.

In the presence of a stiff medium with a high thermal expansion coefficient, the overall behaviour of a given piled raft foundation is mainly governed by soil deformation.

Effect of Slenderness, Poisson's Coefficient and Spacing Ratio

As mentioned in section 4.2.1, the influence of slenderness, Poisson's coefficient and spacing ratio is investigated only for the particular case of a piled raft with a square grid of 16 floating piles and a normalised pile stiffness $K = 3 \times 10^3$. Results of this parametric analysis are reported in Figure 4.7. These findings might be extended in a qualitative way to end-bearing piles and other values of K on the basis of previous results.

The coefficient R increases with increasing slenderness, as might also be deduced from Figure 4.5. The same happens to the average displacement ratio of free pile groups under mechanical [285] or thermal [321] loads. Similarly, the ratio between the settlement

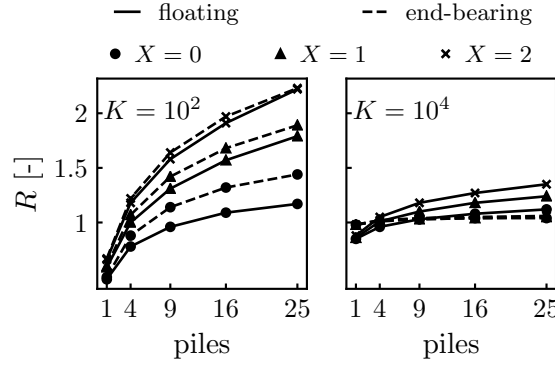


Figure 4.6 – Raft to single isolated pile displacement ratio R as a function of the number of piles n_p for both floating and end-bearing piles; $l/d = 25$; $s/d = 5$; $\nu_s = 0.3$; $X = 0, 1$ and 2 ; and $K = 10^2$ and 10^4 .

of a pile cap unit under uniform vertical load and the settlement of the corresponding free-standing pile increases with increasing slenderness [30, 68, 286]. Low values of l/d can make R lower than 1. It is worth recalling that pile slenderness was varied by changing the length and keeping the diameter constant. Therefore, mechanical interactions among piles through the soil can develop over a greater height. It is worth considering what happens if the slenderness is increased by reducing the diameter. In this case, the interaction height is constant, but it can be shown that the actual strain induced in a receiver pile is higher. Consider a small portion of the pile Δx subjected to a variation of interface shear stress $\Delta\tau$. The induced axial strain $\Delta\varepsilon$ is

$$\Delta\varepsilon = \frac{\Delta\sigma}{E_p} = \frac{1}{E_p} \frac{\Delta\tau \Delta x d \pi}{d^2 \frac{\pi}{4}} \propto \frac{1}{d} \quad (4.5)$$

From equation (4.5) it can be deduced that increasing l/d by reducing d has the same effect and a similar trend of R can be expected.

The raft mean displacement ratio increases with decreasing ν_s . A comparable trend is observed in free energy pile groups [321] and in conventional piled rafts [286], but greater in magnitude. This means that the influence of the raft decreases with decreasing ν_s .

Increasing s/d has the obvious effect of reducing interactions among piles [30, 68, 321], and hence also R .

All three graphs show a nearly linear trend.

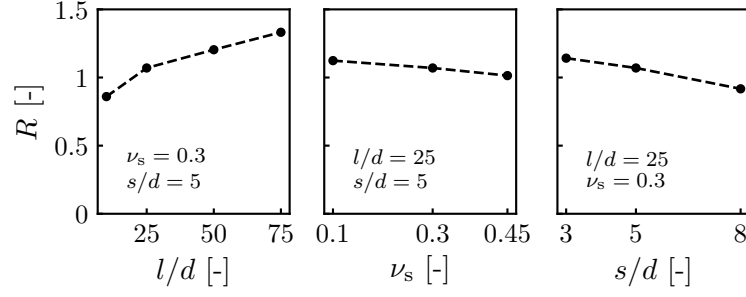


Figure 4.7 – Raft to single isolated pile displacement ratio R for floating piles; $n_p = 4^2$, $K = 3000$; $X = 0$; $t_r/d = 1$; $l/d = 10, 25, 50$ and 75 ; $\nu_s = 0.1, 0.3$ and 0.45 ; and $s/d = 3, 5$ and 8 .

4.3.2 Typical Results of Raft Differential Displacements

Some results of differential displacements between the centre and the edge and between the centre and the corner of the raft are given in this section. Similarly, a few uplift profiles along the normalised coordinate are also presented.

Differential Displacements Between the Centre and the Edge and Between the Centre and the Corner of the Raft

Differential displacements normalised by the mean displacement (\bar{w}_r) are plotted in Figure 4.8 for the 4^2 configuration.

For both values of K , normalised differential displacements between the centre and the corner are higher compared with those between the centre and the edge and there is only a subtle difference between floating and end-bearing piles. In general, normalised differential displacements reduce rather quickly with t_r/d thanks to the fact that the bending stiffness of the raft grows with t_r^3 .

The drop in differential displacements for $K = 10^4$ is extremely fast. The differential displacements are lower than 10% when $t_r/d \geq 1$ and vanish for $t_r/d \geq 2$. Negative values, even if very small, are observed for t_r/d from 1 to 2 when $X = 2$. In those configurations, the situation is such that the external and corner zones of the raft, which can be assimilated to cantilever structural elements, are pushed a little bit higher. As the soil is too soft to be the driving force, the reason has been attributed to the “corrugated” deformed shape of the raft induced by the piles. The restrained piles head radial deformation (a phenomenon explained below) might also play a role.

When $K = 10^2$, the reduction is slower and for $X = 0$ a fraction of differential displacement still persists with $t_r/d = 4$. There is a clear distinction between results for

$X = 0$ and $X = 1$ or 2.

Similar trends but slightly lower values are found for $l/d = 50$. For other pile-grid configurations the same conclusions hold. Configurations with a pile exactly at $\xi = 1$, namely $n_p = 3^2$ and 5^2 , produce higher results. In general, normalised differential displacements tend to reduce as the raft become more compact.

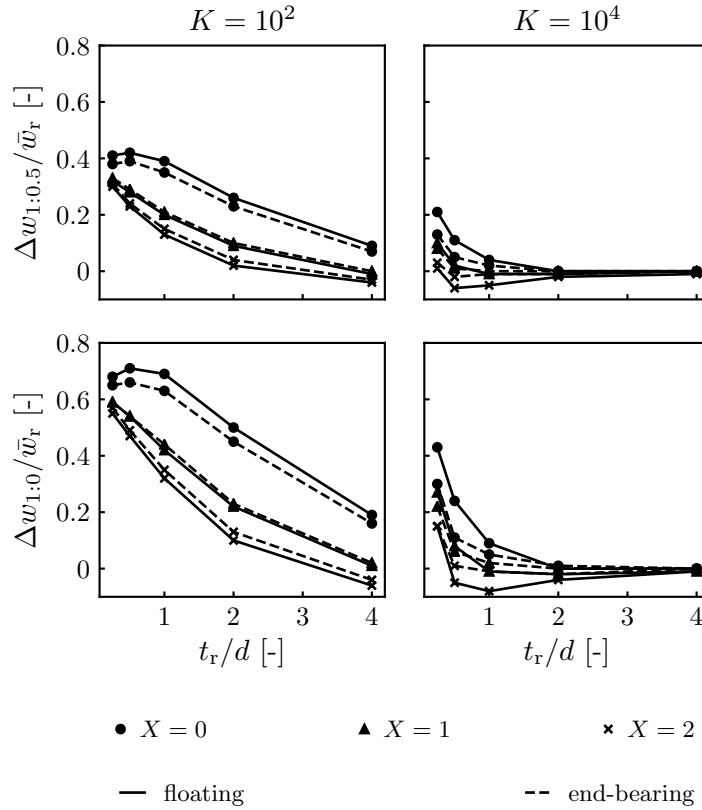


Figure 4.8 – Normalised raft differential displacement $\Delta w_{1:0.5}/\bar{w}_r$ and $\Delta w_{1:0}/\bar{w}_r$ with respect to t_r/d for $n_p = 4^2$; floating and end-bearing piles; $l/d = 25$; $\nu_s = 0.3$; $s/d = 5$; $X = 0, 1$ and 2; and $K = 10^2$ and 10^4 .

Displacement Profile Along the Normalised Coordinate

The discrete normalised differential displacements shown in section 4.3.2 can provide useful information. However, their interpretation in the case of piled-raft foundations is not always straightforward, since the raft does not deform in a simple hollow shape. For this reason, the full profile of raft displacement along the normalised coordinate is shown in Figure 4.9 for a few cases. Displacements increase with growing X and their rate of increase is higher for $K = 10^2$. At $\xi = 0.5$, the change in direction of the normalised

coordinate is reflected by a kink in the uplift profile. Actual values of raft heave do not show a remarkable difference between configurations 4² and 5², for the corresponding values of K . When $t_r/d = 4$, the raft is almost flat and in the case of $X = 2$ it shows a barely visible higher displacement at the corner.

The trend is analogous to piled rafts under uniform mechanical loads [55]. In light of the reasons already explained in section 4.3.1, displacements increase with n_p and X more significantly for stiff soils. A careful reader probably noticed that in the 5² configuration, for which ξ between 0.5 and 1 passes exactly above some piles, the heave profile sometimes has an arched shape between two consecutive piles and not a bowl shape, as might be expected. When $K = 10^2$, this happens only for $X = 2$ and the reason is the pushing of the soil against the raft. When $K = 10^4$, as stated previously, the soil is too soft to raise the raft. The explanation, in this case, is that the soil cannot counter the radial expansion of the piles, whereas it is completely restrained at the head owing to the in-plane stiffness of the raft. Therefore, in the upper part of the heated piles, there is a gradient of radial deformations that induces a curvature over the piles' cross-section. The curvature is then partly transmitted to the raft.

It is worth mentioning that in real applications, the first part of energy piles is insulated and, thus, the phenomenon of induced curvature highlighted above is less important.

4.3.3 Typical Results of Thermal Stresses Induced in the Piles

When piles are heated, their internal stress state is modified. In the following, representative outcomes of such an alteration are described. Results are presented in terms of the normalised stress ς . The effects of the normalised raft thickness t_r/d , dimensionless pile axial stiffness K , number of piles n_p , Poisson's coefficient ν_s and spacing ratio s/d are investigated.

Effect of Position and Normalised Raft Thickness

The normalised stress profile along the pile length for central, external and corner piles for the 5² configuration is shown in Figure 4.10. Highest thermal stresses are experienced by corner piles and lowest by central piles, that is, they decrease with normalised coordinate ξ , in a similar manner to conventional deep foundations [30, 128, 285]. The reason in the case of energy piles is the same, i.e. interactions reduce interface shear stresses in receiver piles. This situation changes close to the pile head in a couple of cases. The case $t_r/d = 4$ maximises thermal efforts in central piles, whereas it minimises them in corner piles. The equalisation of raft displacements with raft stiffness restrains the uplift

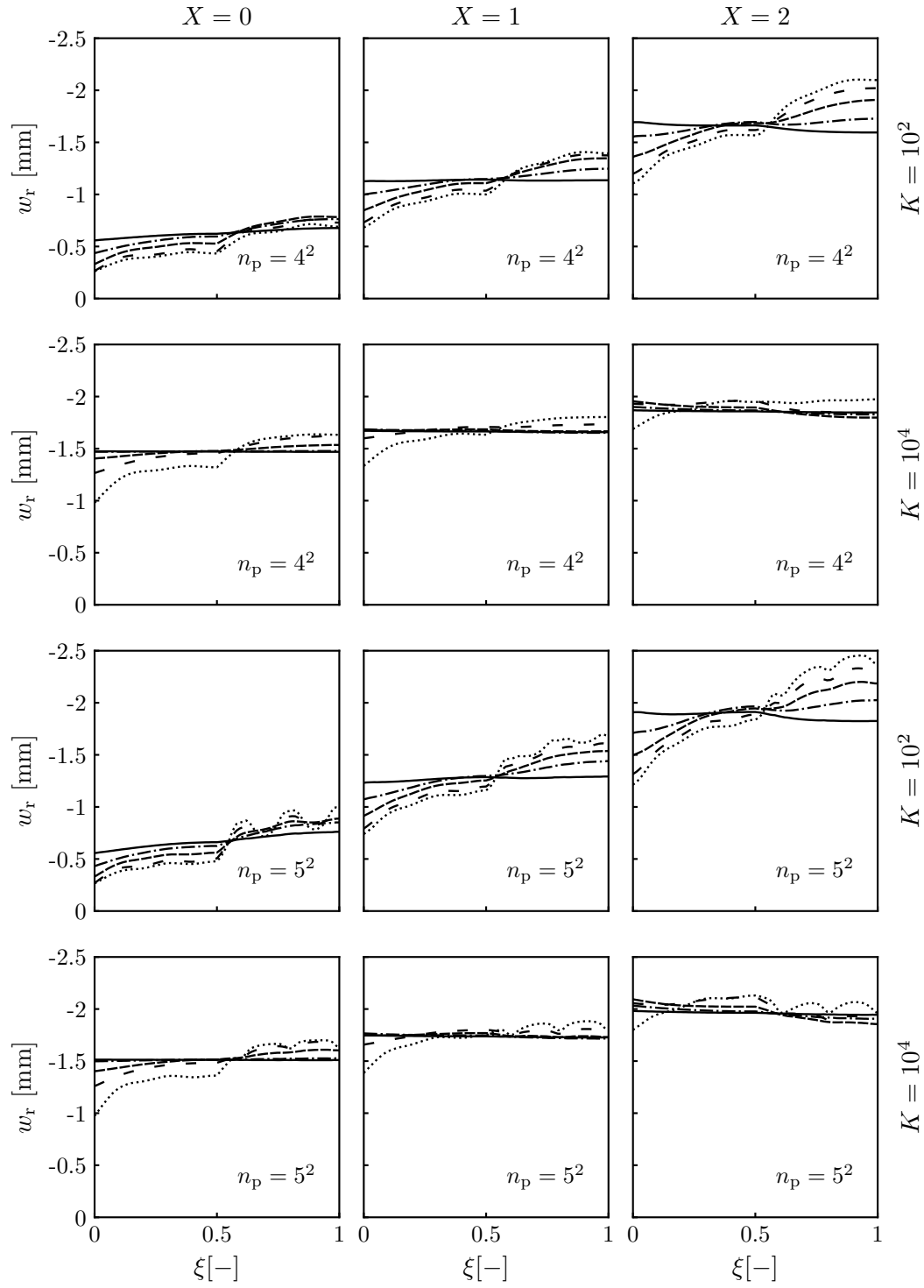


Figure 4.9 – Raft uplift along normalised coordinate ξ for two configurations of floating piles, $n_p = 4^2$ (first two rows) and 5^2 (last two rows); $l/d = 25$; $\nu_s = 0.3$; $s/d = 5$; $X = 0, 1$ and 2 ; $K = 10^2$ and 10^4 ; and t_r/d 0.25, 0.5, 1, 2 and 4.

of central piles and enhances that of corner piles.

Stresses decrease with increasing X . When $X = 2$, central piles might be subjected to tensile thermal stresses. The influence of normalised raft thickness is almost negligible for $X = 0$, whereas it is noticeable for $X = 1$ and 2, especially for central piles. The scatter of stress profile increases with increasing X . As stated previously, when $K = 10^2$ the soil is stiff enough to significantly affect the state of the foundation. Central piles are more susceptible to the variation of X because they receive the highest amount of interactions, both through the soil and the cap. This is reflected in the shape and value of ς , which can even become negative. However, in a real case the global effect of $\varsigma < 0$ is actually only a reduction of the total compression force (the situation might be more sensitive during cooling phases).

Trends of stress profiles shown in Figure 4.10 are similar for other pile-grid configurations.

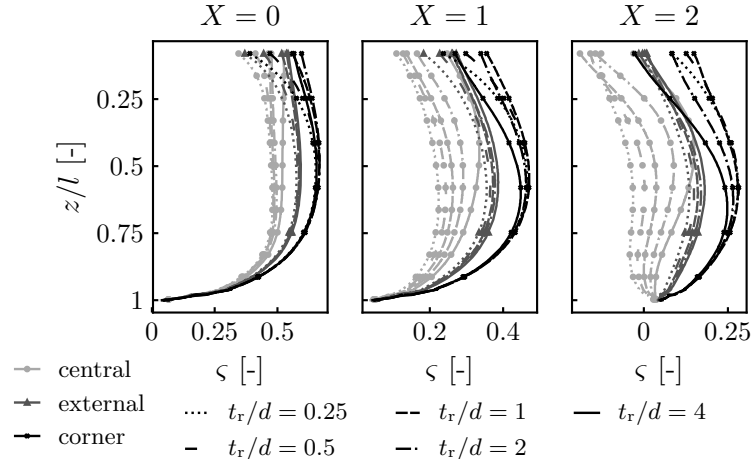


Figure 4.10 – Distribution of normalised thermally induced axial stress in a central, external and corner floating pile in the 5^2 configuration; $l/d = 25$; $K = 10^2$; $\nu_s = 0.3$; $s/d = 5$; $X = 0, 1$ and 2; and $t_r/d = 0.25, 0.5, 1, 2$ and 4.

Effect of Normalised Pile Axial Stiffness

Normalised piles axial stiffness has a significant impact on thermally induced stresses. Figure 4.11 highlights the drop in the maximum axial stress along a central, external and corner pile for the case $n_p = 4^2$. The same order of magnitude is obviously observed for the entire stress profile. When K increases from 10^2 to 3×10^3 , ς_{\max} decreases more than 90 %. For $K > 3 \times 10^3$, the stress decreases very slowly, approaching zero.

The quick drop of thermally induced axial stresses with increasing K shown in Fig-

ure 4.11 reiterates the strong relation between thermally induced effects and soil stiffness. In soft soil, energy piles are freer to deform and therefore only limited efforts appear. Considering that $K = 10^2$ is a very low value, it can be expected that generally $\varsigma_{\max} \leq 0.6$. This value may be higher in a situation where only a fraction of piles is thermally activated or for non square pile-grid configurations. The above statements hold for all piles positions (central, external and corner), as shown by Figure 4.11.

Other pile-grid configurations exhibit the same quick drop of thermally induced axial stresses.

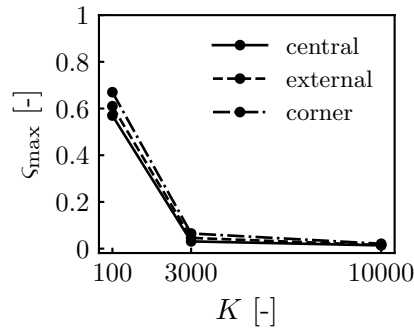


Figure 4.11 – Maximum normalised thermal stress in a central, external and corner floating pile with respect to normalised pile axial stiffness for the 4^2 configuration; $l/d = 25$; $\nu_s = 0.3$; $s/d = 5$; $X = 0$; $t_r/d = 1$; and $K = 10^2$, $3 \cdot 10^3$ and 10^4 .

Effect of the Number of Piles

In this section, a central pile is taken as an example to show how the number of piles affects thermally induced stresses. Results are presented in graphical form in Figure 4.12, where it can be seen that an increase in the number of piles leads to reduced thermal stresses. The decrease of ς_{\max} with increasing number of piles is due to the interactions among piles, which induce interface shear stresses in the opposite direction with respect to those caused by the thermal expansion.

For $K = 10^2$ and $l/d = 50$, the decrease varies between about 30 % when $X = 0$ and 40 % to 60 % when $X = 2$, whereas for $l/d = 25$ it can reach drops of more than 70 % at 25 piles. For a small number of piles, ς_{\max} can reach values close to one and the effect of X is irrelevant. The reduction in stiff soils is significant.

In the case of soft soils ($K = 10^4$), the stress is already low for a single pile, so that the decrease is less pronounced. For both floating and end-bearing piles, the reduction of ς_{\max} for central piles is about 95 % for nine piles, irrespective of slenderness or X .

Figure 4.12 confirms the increase of axial stresses with increasing slenderness, de-

creasing normalised stiffness, decreasing soil to pile thermal expansion coefficient ratio, and for end-bearing piles, as pointed out in Figure 4.10, 4.11 and 4.13.

External and corner piles experience a reduction of ς_{\max} as well, but this is lower in magnitude because they are subjected to fewer interactions. Corner piles show lower rates of reduction and they reach a steady state faster.

Effect of Slenderness, Poisson's Coefficient and Spacing Ratio

A more detailed parametric analysis of pile slenderness, Poisson's coefficient and spacing ratio was conducted for the floating piled raft of the 4^2 configuration with $K = 3 \times 10^3$, $t_r/d = 1$ and $X = 0$. Outcomes regarding maximum normalised stress along the main pile types are shown in Figure 4.13. Stresses within piles increase moving from $\xi = 1$ to 0. The maximum normalised stress increases with increasing l/d , ν_s and s/d . The impact of slenderness is the most pronounced, whereas Poisson's coefficient shows the lowest influence. All other pile-grid configurations confirm the increase of ς_{\max} with slenderness.

The increase of ς_{\max} with slenderness is more pronounced for corner piles, where it can triplicate from $l/d = 10$ to 75. For the same range, a central pile shows an increase of 100 %. However, values of ς_{\max} remain lower than 0.2 because $K = 3 \times 10^3$. The low values of thermally induced stresses for $K \geq 3 \times 10^3$ was already highlighted in section 4.3.3 with reference to Figure 4.11. It is worth recalling that pile slenderness was varied by changing the length and keeping the diameter constant. Nevertheless, the same trend would be observed if the situation was reversed. In fact, suppose a situation in which two bars of the same length, but different diameters ($d_1 > d_2$) are subjected to the same shear stresses over their lateral surface. To make things even more simple, admit a uniform shear stress distribution and no load at one end of the bars. The axial stress ratio between the more and less slender rod at a distance x from the free end is

$$\frac{\sigma_2}{\sigma_1} = \frac{\tau d_2 \pi x}{d_2^2 \frac{\pi}{4}} \frac{d_1^2 \frac{\pi}{4}}{\tau d_1 \pi x} = \frac{d_1}{d_2} > 1 \quad (4.6)$$

Even if the problem of a heat exchanger pile in a piled raft foundation is more complex than the above example, equation (4.6) shows that reference to the slenderness variation, without knowing details, is justified.

The impact of Poisson's coefficient is limited, causing an increase of ς_{\max} less than 4 % for the range 0.1 to 0.45. This is in agreement with the decrease of R with increasing ν_s shown in Figure 4.7. The same happens in a conventional piled raft subjected to uniform vertical load [68].

The reduction of interactions among piles with increasing spacing ratio is well shown in the last row of Figure 4.13. Increasing s/d from 3 to 8 leads to a increase in ς_{\max} of about 8 %.

Trends of R and ς_{\max} are similar for l/d , whereas they are opposite for ν_s and s/d (cf., Figure 4.7 and 4.13).

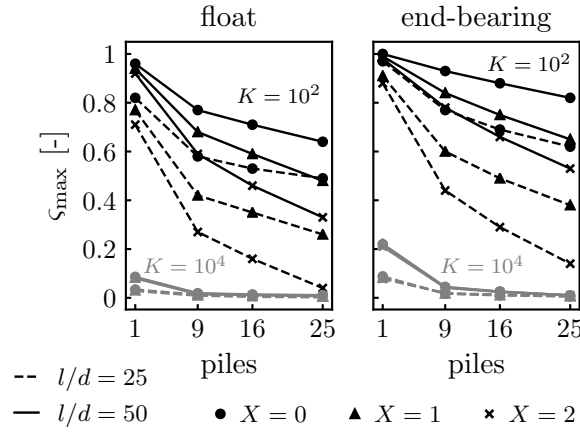


Figure 4.12 – Evolution of the maximum normalised thermal stress with respect to the number of piles for a central pile; $\nu_s = 0.3$; $s/d = 5$; $t_r/d = 1$; $l/d = 25$ and 50 ; $K = 10^2$ and 10^4 ; and $X = 0, 1$ and 2 .

4.4 Concluding Remarks

A thermo-elastic analysis has been presented for the general behaviour of piled raft foundations with regular grids of energy piles. The influence of major parameters involved in the design stages of practical applications have been numerically investigated. Attempts have been made to capture all mechanical interactions that occur among thermally activated piles in a unique general picture. Some of the main conclusions that can be drawn are as follows.

- The ratio between raft mean displacement and equivalent isolated free-standing pile displacement, R , is a convenient parameter to estimate the global effect of all interactions. The results show that it can be assumed constant with respect to the bending stiffness of the raft. The value of R is mainly governed by n_p , K and X , whereas the pile resisting mode, i.e. floating or end-bearing, is of slightly less concern. It has been shown that R can be lower than one in configurations with a few piles. Here R might be roughly bounded between 0.5 and 3.

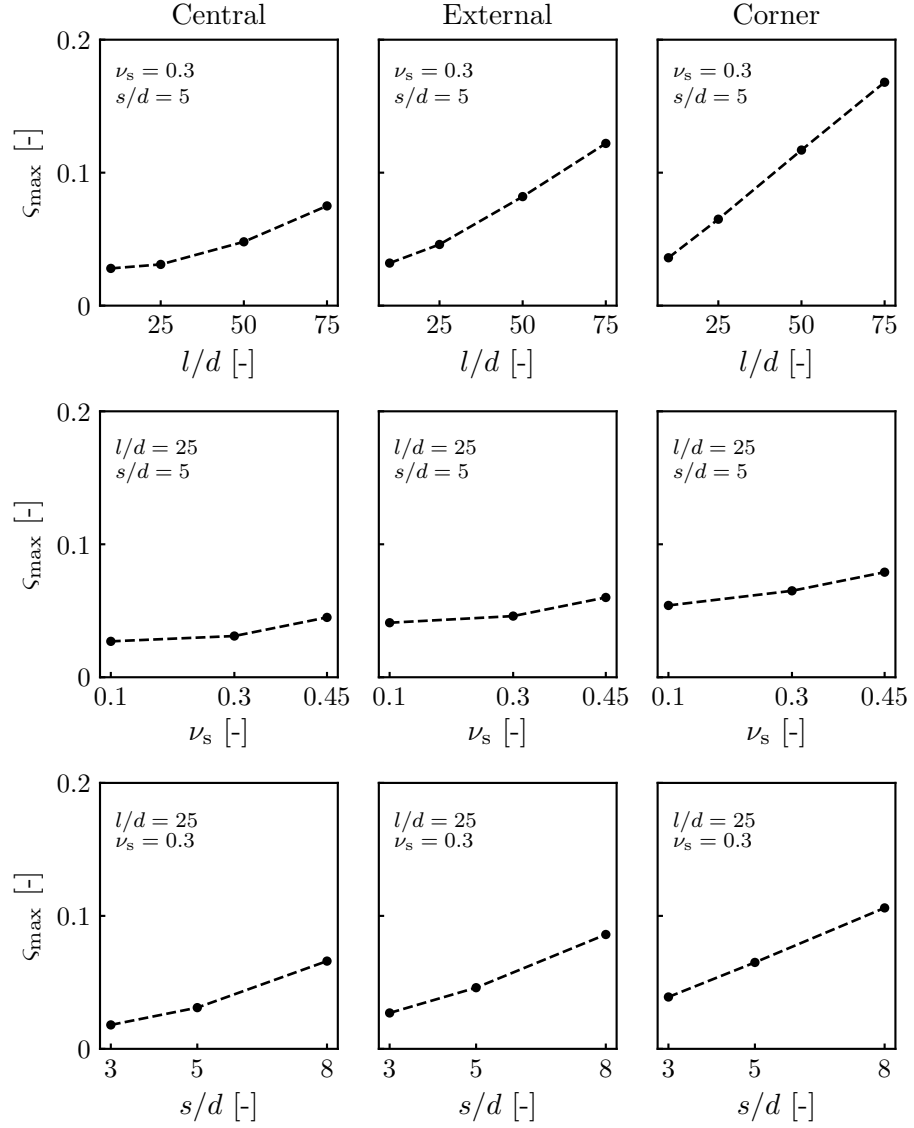


Figure 4.13 – Change in maximum normalised thermal stress with respect to slenderness $l/d = 10, 25, 50$ and 75 ; Poisson's coefficient $\nu_s = 0.1, 0.3$ and 0.45 and spacing ratio $s/d = 3, 5$ and 8 for the 4^2 configuration; $K = 3 \times 10^3$; $t_r/d = 1$; and $X = 0$.

- Thermally induced differential displacements are strongly related to K and the raft bending stiffness. The value of X enhances differential displacements in stiff soils. The results highlight that for $E_c = 30 \text{ GPa}$ and $t_r/d = 4$, differential displacements are negligible.
- The level of stress has been investigated for the piles through the normalised thermally induced axial stress ς . It has been shown that ς_{\max} is mainly affected by K and then by n_p and l/d . The influence of pile position is analogous to conventional foundations, where corner and central piles are the most and less loaded, respectively. From these results, values of ς_{\max} close to one might be expected for compact foundations with slender piles in stiff soils, which might result in concrete cracking under active cooling.
- An important outcome of this research is the analogy between conventional piled rafts subjected to vertical load and piled rafts with energy piles. This suggests that an overall good performance of the foundation can be achieved through a unique design strategy.

The general performance can be assessed through a few parameters, namely R , $\Delta w_\xi/\bar{w}_r$ and ς_{\max} . The outcomes of this research might be used directly for a rough estimate during early design stages, whereas they can be refined afterwards to take into account the mechanical load distribution and the potentially induced plasticity at the soil–pile interface.

Lastly, it seems that in the field a concern remain related to the potential tensile stresses induced in the piles. It appears that a proper consideration of the nature of thermal loads, i.e. imposed displacements, and the consequent response of a reinforced concrete member, could avoid unnecessary additional reinforcement. For this reason, the local (structural) performance of energy piles considering the non-linear behaviour of reinforced concrete is under way. This aspect will be a complement to the already available research that considers the non-linear behaviour of the soil–pile interface and could be a basis for a more rational performance based design approach.

Acknowledgements

The support of the Swiss National Science Foundation (project no. 174575, Division InterCo) is acknowledged.

Yet in reality the structure will still be safe, because the plastic yield of the concrete considerably reduces the intensity of the stresses due to settlement.

Karl Terzaghi, The Actual Factor of Safety in Foundations, Lecture delivered in 1934

5

Thermal Stress Analysis of Energy Piles

Postprint version of the article submitted to Géotechnique.

C Garbellini and L Laloui. “Thermal stress analysis of energy piles”. In: *Géotechnique* (2019), pp. 1–12.

Contribution of the candidate: initial idea, theoretical development, numerical modelling, analysis of results, writing of manuscript.

THIS STUDY IS concerned with the problem of energy piles subjected to constant axial load and temperature variation uniform over the cross-section. In the first part of this article, equations for the analysis of energy piles based on elastic theory and the load-transfer approach are described. Closed form solutions are derived for a few simple cases. It is observed that temperature variation effects can be conveniently expressed by a factor of thermally imposed strain. In the second part of the article, a study on the effect of the non-linearity of reinforced concrete on the performance of energy piles under tension is described. A newly developed finite element model that is within the framework of the load-transfer approach is employed to simulate the response of a pile subjected to thermomechanical loads in isolated as well as in piled raft foundations. The results suggest that the performance of the structure is strongly affected by concrete post-cracking behaviour. Nevertheless, piles can accommodate thermally imposed strains if the ductility capacity is provided. The outcomes of this study may be combined with the knowledge of non-linear behaviour of soil-pile interfaces for a more rational performance-based design approach toward energy piles.

5.1 Introduction

Thermally activated structures, also known as energy geostructures, are reinforced concrete geotechnical structures that incorporate tubes carrying a heat exchanger fluid. They constitute an environmentally friendly technology that exploits the relatively constant temperature of the ground for heating and/or cooling purposes, thereby reducing the environmental footprint of construction [2, 22, 24, 129, 165, 187, 197, 275, 340]. Piled foundations have been demonstrated to be among the most suitable and effective applications of such technology [17].

Over the past twenty years, the research and the necessity of design provisions have increased considerably. Field experiments [5, 21, 81, 188–190, 238, 247–249, 322, 377, 400, 401] and laboratory tests [221, 264, 265, 317, 372, 373, 399] have demonstrated the measurability of thermally induced effects and the occurrence of mechanical and thermal interactions in group configurations. Impelled by the foregoing observations, several methods for estimating thermally induced displacements and stresses have been proposed: (a) techniques based on linear elasticity, such as the interaction factor method [318, 321], equivalent pier method [320], layer model [324], application of Mindlin's equations [324], and finite element method [9, 114, 322]; (b) methods that account for the non-linear behaviour of the soil-pile interface, including the modified interaction factor method [325], load-transfer approach [1, 168, 239, 278, 374, 378], and modelling by the finite differ-

ence [374, 375] and finite element [20, 80, 81, 190, 263, 269, 273, 317] techniques.

All the above-mentioned applications and present design guidelines [46, 124, 350] consider the pile as a linear elastic body. However, it is established that the performance of a reinforced concrete member is strongly affected by the post-cracking behaviour. This limitation compromises the establishment of an exhaustive performance-based design approach toward energy piles [314].

In this study, an attempt has been made to fill this gap. A major source of concern is related to the potential tensile stresses induced in compressed piles upon cooling or the increase in similar stresses in piles subjected to traction forces. The load–transfer approach [64] is adopted for evaluating the performance of energy piles both in isolated and in piled raft foundations. In the following, load–transfer equations are derived step-by-step and original closed form solutions are given for simplified situations. These may be applied as extreme cases. Thereafter, the material models adopted for reinforced concrete, soil–pile interface, and group effects are described. Then, a finite element code, which is specifically developed for this study, is described. Subsequently, the numerical results are discussed, and the impact of the non-linearity of reinforced concrete is highlighted. Finally, concluding remarks are summarised.

In the following discussion, upward displacements, tensile strains, and tensile stresses are considered to be positive.

5.2 General Framework

Piles are slender structural elements ($L/D > 10$) that can be analysed through the Euler–Bernoulli beam theory. Here, it is also assumed that piles are subjected only to vertical loads, temperature variation is uniform over the cross-section, and the magnitude of the temperature variation does not cause any modification of the materials' mechanical and physical properties. Given that instability is prevented by the surrounding soil, the theory of bars can be applied to compute the internal state of piles.

When a body experiences a temperature variation, it contracts or expands according to the sign and magnitude of the temperature change. It is obvious that if the body can deform freely, no stress is induced. Meanwhile, if the body is partially restrained, an internal state of stress develops. This implies that the actual deformation of a linear elastic body subjected to a temperature variation is [386]

$$\frac{\Delta L}{L} = \frac{\sigma}{E} + \alpha \Delta T \quad (5.1)$$

where ΔL is the length variation, L is the initial length of the element, σ is the normal stress in the bar, E represents its Young's modulus, α stands for the linear thermal expansion coefficient and ΔT is the temperature variation. Equation (5.1) may be conveniently expressed as follows

$$\frac{\Delta L_{\text{imp}}}{L} = \frac{\Delta L}{L} - \alpha \Delta T \quad (5.2)$$

where $(\Delta L_{\text{imp}}/L)$ is the strain that is associated with a modification of the state of stress and therefore, with the material model. Because in this form equation (5.2) does not explicitly refer to any type of constitutive law, it can be used to consider material non-linearity.

5.3 Linear Elastic Thermal Stress Analysis of Bar Systems

5.3.1 Single Bar Systems

In this section, solutions for individual bars with various boundary conditions are presented (Figure 5.1).

Free and Clamped Bar

To date, analytical solutions for single piles subjected to thermal loads have been presented only for the two extreme situations of homogeneous free and clamped bar (Figure 5.1a and 5.1b). The solution for the former is

$$\begin{aligned} \Delta L &= \alpha \Delta T L \\ \varepsilon &= \alpha \Delta T \\ \sigma &= 0 \end{aligned} \quad (5.3)$$

whereas the solution for the latter is

$$\begin{aligned} \Delta L &= 0 \\ \varepsilon_{\text{imp}} &= -\alpha \Delta T \\ \sigma &= -E \alpha \Delta T \end{aligned} \quad (5.4)$$

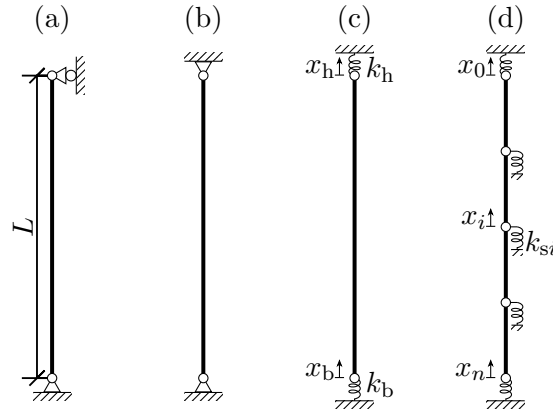


Figure 5.1 – Single bars with different boundary conditions: (a) free bar; (b) clamped bar; (c) bar partially restrained by head and base springs; (d) bar partially restrained by head, base, and shaft springs. Nodal displacements are indicated by x and spring stiffness by k .

Bar Partially Restrained by Head and Base Springs

Figure 5.1c represents a bar partially restrained by head and base springs. The solution is obtained by solving the linear system of equations that expresses the equilibrium of forces at nodes for the two unknown nodal displacements

$$\begin{cases} (k_h + k)x_h - kx_b - EA\alpha\Delta T = 0 \\ -kx_h + (k + k_b)x_b + EA\alpha\Delta T = 0 \end{cases} \quad (5.5)$$

which yields

$$\begin{aligned} x_h &= \frac{EA\alpha\Delta T k_b}{(k + k_h)(k + k_b) - k^2} \\ x_b &= \frac{-EA\alpha\Delta T k_h}{(k + k_h)(k + k_b) - k^2} \end{aligned} \quad (5.6)$$

where x_h and x_b are the head and base nodal displacements; k_h and k_b are the head and base spring stiffness; and k represents the bar axial stiffness (EA/L). Considering that the axial force is constant along the bar, the thermally induced stress may be computed as follows

$$\begin{aligned}
\sigma &= \frac{-k_h x_h}{A} = \frac{k_b x_b}{A} \\
&= -E\alpha\Delta T \frac{k_h k_b}{k^2 - (k + k_h)(k + k_b)} = -E\alpha\Delta T \eta
\end{aligned} \tag{5.7}$$

where the newly introduced parameter η is called *factor of imposed thermal strain*. The position of the null point (the point of the bar that does not experience any displacement) from the base can be computed by imposing the condition of constant strain inside the bar $-x_b/l_{NP} = x_h/(L - l_{NP})$. This yields

$$l_{NP} = \frac{L}{1 + k_b/k_h} \tag{5.8}$$

It is noteworthy that whereas the head and base displacements depend both on the stiffness of the springs and that of the bar, the relative position of the null point is a function of only the relative stiffness of the springs.

Bar Partially Restrained by Head, Base, and Shaft Springs

When the bar is partially restrained also by intermediate springs, the situation is similar to that depicted in Figure 5.1d. The bar is divided into n elements and into $n + 1$ unknown nodal displacements x_i , for $i \in [0; n]$. Note that the subscript 0 designates the head and n the base.

For the general case of a bar subjected to an axial load at its head (F) and to an arbitrary temperature variation along its length, and whose properties may vary with depth, the nodes equilibrium results in the following linear system of equations

$$\begin{pmatrix}
k_0 + k_{s0} & -k_0 & & & \\
-k_0 & k_0 + k_1 + k_{s1} & -k_1 & & \\
& -k_1 & \ddots & \ddots & \\
& & \ddots & \ddots & -k_{n-1} \\
& & & -k_{n-1} & k_{n-1} + k_{sn}
\end{pmatrix}
\begin{pmatrix}
x_0 \\
x_1 \\
\vdots \\
x_n
\end{pmatrix}
+
\begin{pmatrix}
-E_0 A_0 \alpha_0 \Delta T_0 - F \\
E_0 A_0 \alpha_0 \Delta T_0 - E_1 A_1 \alpha_1 \Delta T_1 \\
\vdots \\
E_{n-1} A_{n-1} \alpha_{n-1} \Delta T_{n-1}
\end{pmatrix}
= \mathbf{0} \tag{5.9}$$

where the first term is the stiffness matrix (\mathbf{K}), second term represents the nodal displacement vector (\mathbf{x}), and last term is the force vector (\mathbf{f}). In (5.9), k_i is the axial stiffness of bar element i , and k_{si} is the stiffness of spring at node i (Figure 5.1d).

There is a direct analogy between the problem presented in this section and the load-transfer approach for piles, according to which the mass of soil is replaced by independent and uni-directional springs. Therefore, (5.9) can be used to solve the problem of a single pile subjected to a force and to a thermal load. Moreover, (5.9) is the equation form of the finite element method based on the displacement formulation [413] and can be adapted conveniently in order to include material non-linearity and cyclic loading.

5.3.2 Capped Bars Systems

In this section, solutions for bars partially restrained by a common rigid cap and with various boundary conditions are presented (Figure 5.2). The rigid cap is assumed to move only vertically and without rotation.

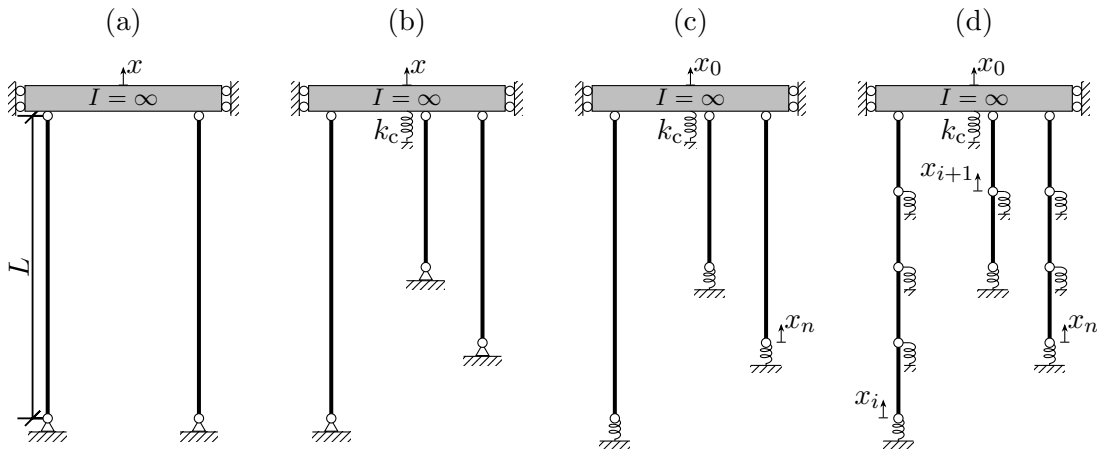


Figure 5.2 – Bars partially restrained by a common rigid cap (second moment of area $I = \infty$) and with different boundary conditions: (a) system of two identical pinned bars; (b) system of n pinned bars; (c) system of n bars resting on base springs; (d) system of n bars partially restrained by base and shaft springs. Nodal displacements are indicated by x and spring stiffness by k .

Pinned Bars Partially Restrained by a Common Rigid Cap

A simple system of two bars of equal length connected by a rigid cap is shown in Figure 5.2a. The total displacement owing to the superposition of the free thermal deformation and the thermal stresses induced through the cap is

$$\begin{cases} \Delta L_1 = \left(\alpha_1 \Delta T_1 + \frac{\sigma_1}{E_1} \right) L \\ \Delta L_2 = \left(\alpha_2 \Delta T_2 + \frac{\sigma_2}{E_2} \right) L \end{cases} \quad (5.10)$$

Kinematic compatibility requires that $\Delta L_1 = \Delta L_2$, and equilibrium implies that $\sigma_1 A_1 + \sigma_2 A_2 = 0$. Therefore, the solution is

$$\sigma_1 = -E_1 \alpha_1 \Delta T_1 \frac{1 - \frac{\alpha_2 \Delta T_2}{\alpha_1 \Delta T_1}}{1 + \frac{A_1 E_1}{A_2 E_2}} = -E_1 \alpha_1 \Delta T_1 \eta_1 \quad (5.11)$$

This solution can be extended to n bars of variable length and a vertical spring with stiffness k_c attached to the cap (Figure 5.2b). Because the cap is assumed to be perfectly rigid, the only unknown is the vertical displacement of the cap. Thus, a unique spring is sufficient to represent the effect of surface springs under the cap. In the absence of mechanical loads, equilibrium yields

$$\begin{aligned} x \left(\sum_{i=0}^{n-1} k_i + k_c \right) - \sum_{i=0}^{n-1} E_i A_i \alpha_i \Delta T_i &= 0 \\ x &= \frac{\sum_{i=0}^{n-1} E_i A_i \alpha_i \Delta T_i}{\sum_{i=0}^{n-1} k_i + k_c} \end{aligned} \quad (5.12)$$

Once the displacement is known, the thermal stress in bar j can be conveniently computed as follows:

$$\begin{aligned} \sigma_j &= E_j (\varepsilon_j - \alpha_j \Delta T_j) \\ &= -E_j \alpha_j \Delta T_j \left(1 - \frac{\sum_{i=0}^{n-1} E_i A_i \alpha_i \Delta T_i}{\alpha_j \Delta T_j L_j (\sum_{i=0}^{n-1} k_i + k_c)} \right) \\ &= -E_j \alpha_j \Delta T_j \eta_j \end{aligned} \quad (5.13)$$

In the above equation, $\varepsilon_j = x/L_j$ is the observed strain of bar j . Equation (5.13) highlights that shorter bars are the most sensitive to mechanical interactions through a rigid cap.

Bars Partially Restrained by a Common Rigid Cap and Base Springs

Following the nomenclature of nodes shown in Figure 5.2c, the resulting stiffness matrix is arrowhead, and the linear system of equations is as follows:

$$\begin{pmatrix} \sum_{i=0}^{n-1} k_i + k_c & -k_0 & \dots & -k_{n-1} \\ -k_0 & k_0 + k_{b1} & & \\ \vdots & & \ddots & \\ -k_{n-1} & & & k_{n-1} + k_{b,n-1} \end{pmatrix} \begin{pmatrix} x_0 \\ x_1 \\ \vdots \\ x_n \end{pmatrix} + \begin{pmatrix} -\sum_{i=0}^{n-1} E_i A_i \alpha_i \Delta T_i \\ E_0 A_0 \alpha_0 \Delta T_0 \\ \vdots \\ E_{n-1} A_{n-1} \alpha_{n-1} \Delta T_{n-1} \end{pmatrix} = \mathbf{0} \quad (5.14)$$

The out-of-diagonal terms of \mathbf{K} represent the interactions through the cap.

Bars Partially Restrained by Common Rigid Cap, Base and Shaft Springs

Figure 5.2d shows a structure composed of bars partially restrained by base springs, shaft springs, and a common rigid cap attached to a spring. The overall linear system of equations is obtained by assembling those of single bars partially restrained by base and shaft springs. Note that here, the head springs of single bars are not considered owing to the connection with the cap. The nodal displacement vector and force vector for a structure with m bars are given as

$$\begin{aligned} \mathbf{x}^T &= (x_o, \bar{\mathbf{x}}^{(0)}, \dots, \bar{\mathbf{x}}^{(j)}, \dots, \bar{\mathbf{x}}^{(m-1)}) \\ \mathbf{f}^T &= \left(\sum_{i=0}^{m-1} f_0^{(i)} - F, \bar{\mathbf{f}}^{(0)}, \dots, \bar{\mathbf{f}}^{(j)}, \dots, \bar{\mathbf{f}}^{(m-1)} \right) \end{aligned} \quad (5.15)$$

where x_0 is the cap displacement, and $\bar{\mathbf{x}}^{(j)}$ is the vector of nodal displacements of bar j ($j \in [0, m-1]$) except the first node, which matches the cap. Similarly, the first term of \mathbf{f} is the sum of forces acting on the cap, $f_0^{(i)}$ is the first component of the force vector of bar i , $\bar{\mathbf{f}}^{(j)}$ is the force vector of bar j except its first term, and F is the external force applied on the cap. The stiffness matrix acquires the form given in (5.16), where $k_{ab}^{(j)}$ is the term of row a and column b of the stiffness matrix of bar j , and n_j is its number of

$$\begin{pmatrix}
 \sum_{i=0}^{n-1} k_{00}^{(i)} + k_c & k_{01}^{(0)} & & & k_{01}^{(j)} & & & \\
 k_{10}^{(0)} & k_{11}^{(0)} & k_{12}^{(0)} & & & & & \\
 & k_{21}^{(0)} & \ddots & \ddots & & & & \\
 & & \ddots & & k_{n_0-1, n_0}^{(0)} & & & \\
 & & & k_{n_0-1, n_0}^{(0)} & k_{n_0 n_0}^{(0)} & & & \\
 k_{10}^{(j)} & & & & & k_{11}^{(j)} & k_{12}^{(j)} & \\
 & & & & & k_{21}^{(j)} & \ddots & \ddots \\
 & & & & & & \ddots & \\
 & & & & & & & k_{n_j-1, n_j}^{(j)} \\
 & & & & & & k_{n_j, n_j-1}^{(j)} & k_{n_j n_j}^{(j)}
 \end{pmatrix} \quad (5.16)$$

degrees of freedom (i.e. number of nodes).

The linear system of equations $\mathbf{K}\mathbf{x} + \mathbf{f} = \mathbf{0}$ obtained from (5.16) and (5.15) can be used to calculate the axial response of a piled raft subjected to a vertical mechanical load and whose piles experience arbitrary temperature variations. This is true provided that group effects are considered. As in the case of single bars, this approach can be adapted for a numerical procedure to handle non-linear behaviour and cyclic loading.

5.4 Material Models

In this study, only foundations subjected to traction forces and cooling are considered as the worst-case scenario. This implies that a monotonic law for the structural component is valid. Meanwhile, after the application of a traction force, cooling induces interface unloading in the upper part of the pile (downward movement). This indicates that cyclic behaviour is fundamental to soil–pile interface response.

5.4.1 Reinforced Concrete Tie Model

The structural response of the pile is modelled with the tension chord model for structural concrete [214]. This model assumes a simplified constitutive behaviour for the tensile response of the concrete, reinforcement, and bond between them (Figure 5.3). The response of the concrete is linear elastic until it attains its effective tensile strength (f_{ct}). Then, the stress decreases to zero owing to the abrupt formation of a crack. The behaviour of the reinforcement follows a bi-linear elastic-plastic model. The yield stress

(f_{sy}) divides the elastic branch from the elastic-plastic one. The ultimate stress (f_{su}) defines the maximum stress that the steel can sustain. The bond shear-slip relationship ($\tau - \delta$) is rigid plastic. The bond stress is τ_{b0} when the reinforcement is in the elastic domain and decreases to $\tau_{b1} = \tau_{b0}/2$ as soon as the reinforcement yields. It is estimated to be equal to $\tau_{b0} \approx 2f_{ct}$ [250]. In this model, cracks are assumed to be equally spaced by s_{rm} .

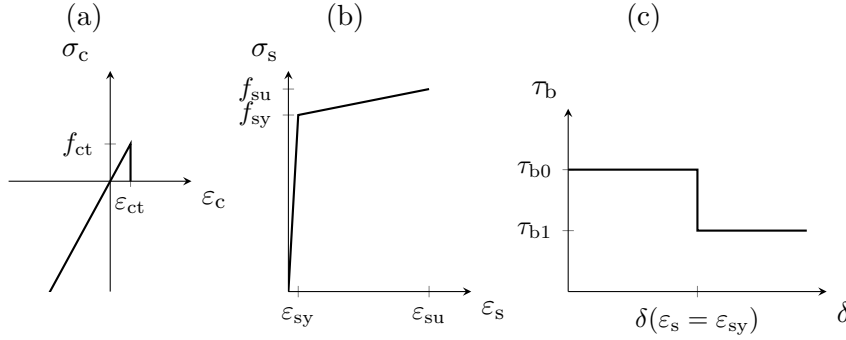


Figure 5.3 – Constitutive models: (a) and (b) stress-strain diagrams for concrete and reinforcement; (c) bond shear-slip relationship.

A typical distribution of stresses and strains based on these assumptions is depicted in Figure 5.4. The speciality of this model is that an analytical relationship that considers structural member effects can be established between the reinforcement mean strain (ϵ_{sm}) and the sectional axial force (N), as shown in Figure 5.5. The response follows a linear reversible path up to the force that causes the concrete to crack (N_r). At that point, the member enters the crack development stage, which here is assumed to be satisfactorily represented by a plateau both for imposed loads and displacements. This is validated by the variability of the concrete tensile strength. This is followed by the stabilised crack stage until the yield strength of reinforcement (N_y) is attained. This phase is characterised by the axial stiffness of the reinforcement. Thereafter, plastic strains develop within the reinforcement until the ultimate stress (N_u) is attained. The overall response is stiffer compared to that of the reinforcement alone, owing to the stiffening effect of the uncracked concrete (tension stiffening). This causes the member response to be shifted toward the left by $\Delta\epsilon_{TS}$ (Figure 5.5). Tension stiffening vanishes for sustained traction loads.

To ensure a ductile behaviour of the member, the reinforcement must be capable of sustaining the cracking force (N_r). This condition is essential also in the case of imposed displacements. This is because concrete tensile strength is not homogeneous, and all the

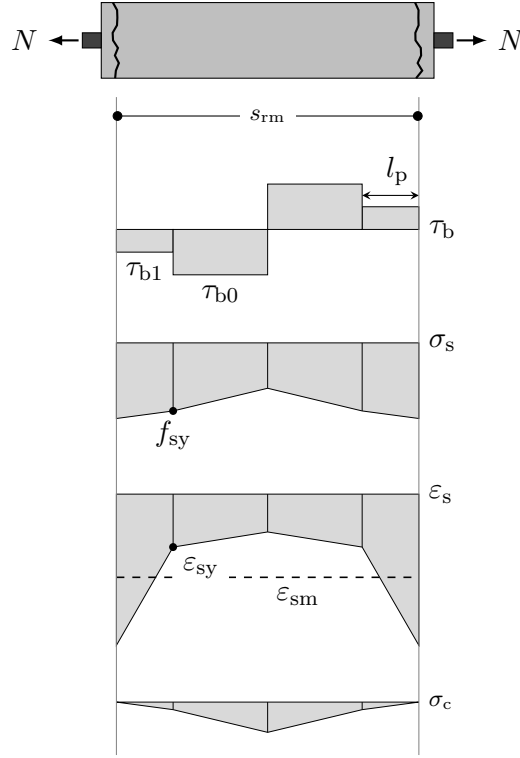


Figure 5.4 – Simple chord element and stress and strain profiles between two cracks. Adapted from [214].

cracks do not form simultaneously. Consequently, if this condition is not satisfied, the member is unable to recover N_r , and strains localise at the crack location after the first crack. The second condition for ductility is that steel plastic strains must penetrate the uncracked concrete ($l_p > 0$). Otherwise, they concentrate at the crack locations. The former condition is achieved by providing a minimum reinforcement ratio, $\rho = A_s/A$ (where A_s is the reinforcement area and A is the gross cross-sectional area) at least equal to

$$\rho_{\min} \approx \frac{f_{ct}}{f_{sy}} \quad (5.17)$$

The second condition requires $f_{su} > f_{sy}$ (this is satisfied by typical reinforcements used in Europe and North America).

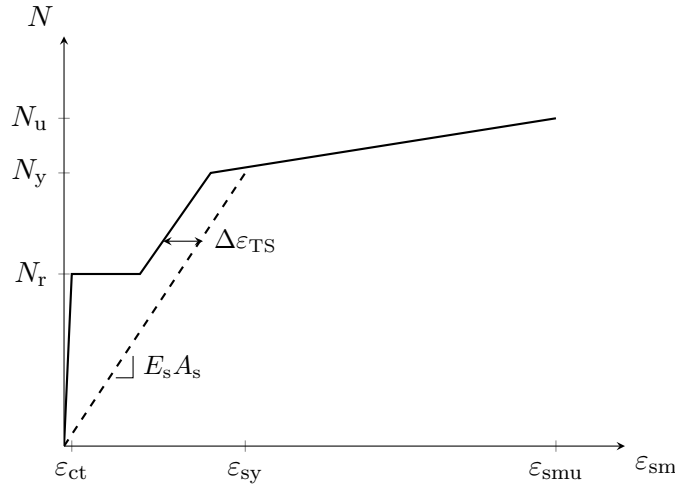


Figure 5.5 – Axial force versus reinforcement mean strain for a reinforced concrete tie according to the tension chord model. (Graph constructed from properties of Table 5.1).

5.4.2 Load–Transfer Model for Soil–Pile Interface

Although this model is a substantial simplification, it has been demonstrated to yield good results for practical applications [168, 176, 378].

For this study, the empirical three-linear constitutive model proposed by [109] and adapted for cyclic loading using the Masing rule [168, 378] is selected (Figure 5.6a). The model is defined by the elastic stiffness (\bar{k}_s), yield shaft friction (t_y), ultimate shaft friction (t_u), and post-yield stiffness ratio (β). The displacement (z) is the soil–pile relative motion. The base reaction model (Figure 5.6b) is analogous, but the stress is the base contact pressure (q) and displacement (z) refers to the tip displacement. Moreover, a tension cut-off is imposed (no tensile stresses allowed between the base and the soil).

Whereas the load–transfer approach is generally used for bearing piles, the lifting-up behaviour is considered in this study. However, because the main difference lies in the ultimate resistance rather than on the mechanical phenomena of load transfer [289], this method can be applied also to pulled piles, provided that the strength parameters are appropriately selected.

5.4.3 Group Effects

Energy piles are typically located in a group configuration with a raft directly cast on the ground. Thus, the response of a pile is also affected by other parameters such as the piles location within the group. A highly noteworthy approach to handling group

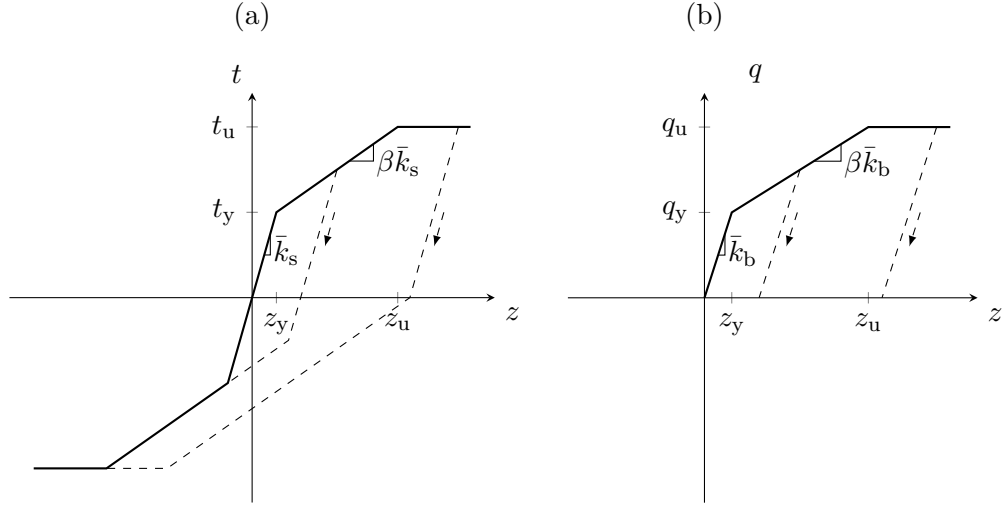


Figure 5.6 – Three-linear cyclic load-transfer constitutive model: (a) shaft reaction and (b) base reaction with tension cut-off.

effects within the load-transfer method for piled rafts was recently presented [59]. The main concept underlying this approach is that when interactions occur, the displacement required to induce a specified relative displacement at the soil-pile interface increases. Therefore, although the formulation of individual piles connected through the cap can be maintained, the stiffness of the springs must be reduced according to the pile spacing and position (corner, external, middle, and inner). The reduction increases from the corner to the inner piles, so that the corner piles will carry a higher load. A stiffness reduction factor applies also to the base and raft reactions. It is noteworthy that similar reduction coefficients were calibrated with respect to mechanical loads rather than temperature variations. Nevertheless, it has been demonstrated [114, 321, 322] that interactions among piles subjected to thermal load follow a similar trend. Therefore, the proposed coefficients are adopted here without any constraint.

The greatest benefit of combining the load-transfer approach with truss (or beam) elements is the ability to compute foundations with many piles in a short time, and to have sectional forces and strains directly available. Therefore, it constitutes a valuable tool for practical applications.

5.5 Finite Elements Model

A finite element code, ThermoBar, is implemented in the framework of the load-transfer approach using the programming language Python [392].

Displacements are described by linear kinematics under quasi-static conditions. The raft is considered as a rigid body, whereas the piles are meshed with constant strain–displacement-based truss elements. Springs are considered based on their contribution to the main diagonal of the stiffness matrix and to the equilibrium of nodes. Because the springs are concentrated at nodes, their properties are obtained from those of the load–transfer curves by integration: over the lateral surface for shaft springs, and over the cross-sectional area for base and head springs. Similarly, the properties of the cap sub-grade reaction are computed by integration over the effective raft–soil contact area. Subsequently, head spring (or cap spring) can be activated to account for the construction stages. Piles can be subjected to any combination and history of axial head load and temperature variations. In the case of piled rafts, the load is applied directly on the raft. The solver uses a modified Newton–Raphson procedure with total secant stiffness for the applied force and a direct integration scheme for the temperature variation. Convergence for the applied force is verified based on the following equilibrium criterion:

$$\|\mathbf{f} + \mathbf{f}_e + \mathbf{f}_s\| \leq tol \quad (5.18)$$

where the operator $\|\cdot\|$ denotes the two-norm, \mathbf{f} stands for the nodal force vector of the applied loads, \mathbf{f}_e is the vector of nodal forces owing to elements reaction, \mathbf{f}_s is the vector of spring reactions on the nodes, and tol is the tolerance, selected equal to 0.1 kN.

5.6 Performance of Single Energy Piles

A pile with diameter $D = 0.5$ m and slenderness $L/D = 20$ is considered. The properties of reinforced concrete are listed in Table 5.1. Two types of soil are defined: Soil 1 is characterised by $\bar{k}_s = 10$ MPa/m, $t_y = 35$ kPa, $t_u = 2t_y$, and $\beta = 0.2$, whereas Soil 2 is assumed to be stiffer and to follow a linear elastic–perfectly plastic relationship for which the strength is higher than the mobilised stress (i.e. the soil–pile interface remains elastic). This soil is defined by $\bar{k}_s = 100$ MPa/m, $t_y = t_u = 120$ kPa, and $\beta = 1$. Because only the traction force and cooling are considered, no base spring is defined. To simplify the interpretation of results, shaft spring properties are considered constant with depth. Although this hypothesis may not be completely realistic, it does not compromise the validity of outcomes with regard to the structural performance of the pile. The latter is first subjected to a traction force (F) applied at its head and then to a severe cooling of $\Delta T = -22^\circ\text{C}$. Two configurations are considered ($F = 0.75N_y$ and $F = 1.1N_y$). The results obtained through linear elastic modelling of the pile are also provided for

comparison. The head spring is activated only for the temperature variation, and its stiffness is $k_h = 390 \text{ MN/m}$. This value is obtained assuming the same stiffness used by [168] for the analysis of an energy pile at the Swiss Federal Institute of Technology, in Lausanne. The pile is meshed with 100 elements.

Table 5.1 – Mechanical properties of concrete and reinforcement.

Concrete	f_{ct}	[MPa]	2.7
	ε_{ct}	[%]	0.009
	E_c	[MPa]	30 000
	τ_{b0}	[MPa]	5.4
	τ_{b1}	[MPa]	2.7
Reinforcement	ρ	[%]	1.04
	f_{sy}	[MPa]	435
	f_{su}	[MPa]	522
	ε_{sy}	[%]	0.212
	ε_{su}	[%]	1.06
	E_s	[MPa]	205 000
Tension chord member	N_r	[kN]	562
	N_y	[kN]	886
	N_u	[kN]	1060
	$\Delta\varepsilon_{TS}$	[%]	0.047
	ε_{smu}	[%]	0.574

The profiles of the mechanical and thermally imposed axial strain, factor of imposed strain, and normalised thermally induced axial force (N_{th}/N_{blc} , where N_{blc} is the thermal axial force in a fully blocked and uncracked equivalent pile) with respect to the relative depth are presented in Figure 5.7 for $F = 0.75N_y$ and in Figure 5.8 for $F = 1.1N_y$.

For $F = 0.75N_y$ and Soil 1, the applied force induces cracking over the top 15 % of the pile length. The interface between the cracked and uncracked parts is clearly marked by a discontinuity in the strain diagram. The temperature variation causes a 5 % increase in the crack length. The factor of imposed strain highlights that the imposed displacement concentrates in the cracked zone close to the cracked–uncracked interface. This is owing to the considerable difference in axial stiffness between these two regions of the pile. The factor η attains a maximum value of four. Nevertheless, the increase in axial force is moderate because of stiffness reduction upon cracking. In particular, the plateau in the crack development stage does not cause any increase in axial stress. When the pile is considered elastic, the factor of imposed strain is considerably marginal. Moreover, the induced thermal force is higher by a factor of up to 1.5. The profile of η considering a complete loss of tension-stiffening is also shown. In this case, the peak value increases

because the “length” of the plateau of the crack development phase increases.

For the same applied load on the stiffer soil (Soil 2), similar qualitative conclusions hold. However, this is not true with regard to the quantitative aspects. The cracked length reduces to 9 % when subjected to mechanical load. Concurrently, upon temperature variation, the cracked length increases to 30 %. The double-step shape of the diagram illustrates that a portion of the pile is still in the crack development stage. This differs from the former case, where there is a direct transition to the stabilised crack stage. This can be associated with the increased capability of the soil to prevent pile displacements. Therefore, the pulling effect of the uncracked zone on the cracked zone is reduced. The maximum value of the factor of imposed thermal strain is practically identical, whereas the thermally induced axial force is considerably higher with respect to the previous scenario. The discrepancy between the forces computed with a linear elastic and a non-linear pile also increases substantially (by up to 7.5 times).

In the case of the higher force ($F = 1.1N_y$), the key aspects highlighted above are observable, namely, the localisation of η in the bottom part of the cracked zone, higher increase in cracked length upon cooling for the stiffer soil, and higher thermally induced axial stress computed with a linear elastic analysis of the pile. The cracked length owing to the applied force is apparently higher compared to the previous case because the force is higher. However, an important difference is the plasticity induced in the reinforcement ($F > N_y = A_s f_{sy}$). In the mechanical strain diagram (ε_{mec}), three regions can be observed along the pile, characterised by as many values of stiffness. This causes two phenomena of localisation of η : one as before close to the uncracked–cracked interface, and one in the steel post yield region. The values of η are higher in the first case because there, the formation of new cracks is followed by a domain of zero stiffness. Meanwhile, in the second situation, the stiffness is reduced but not cancelled. The magnitude of thermally induced axial forces are comparable to those with $F = 0.75N_y$. However, the values computed with a linear elastic pile increases to 2.1 and 10.6 times of those computed with the tension chord model. It is noteworthy that even though the actual intensity of thermally induced axial stresses is relatively low, the impact of considering the tension chord model rather than a linear elastic behaviour is considerable. This difference increases with the applied mechanical load and soil stiffness.

Figures 5.7 and 5.8 highlight that the actual behaviour of reinforced concrete considerably impacts the performance of energy piles and its influence can be comparable to that of the soil–pile interface. This is the point where considering the temperature variation an *imposed displacement*, as it is actually, rather than an imposed force makes the difference. When ductility capacity is ensured, namely when the structure can ac-

commodate the imposed displacement field, the axial force cannot be higher than the structural resistance, because the induced force is simply derived from the constitutive model. Therefore, the member is likely to remain safe under common ranges of temperature variation, no matter the level of the applied mechanical load.

It is of paramount importance to realise that the latter statement concerns only piles subjected to a constant external axial load throughout the period of imposed thermal load. The situation is more sensitive if an additional external axial load is expected, because the thermal load reduces the remaining available resistance. Moreover, it is well known that the bending resistance of a concrete cross-section is strongly affected by the level of axial load. Therefore, thermal load may not be neglected if a variation of axial load or transverse forces are expected.

5.7 Performance of Energy Piled Rafts

In order to understand the implications of group effects on the performance of energy piles in tension, the example depicted in Figure 5.9 is considered. This structure is inspired by the famous *Villa Méditerranée* of Marseilles (FR) [14]. Here, a theoretical variant that uses geothermal energy through thermoactive piles is examined. It is noteworthy that whereas the context is used only to illustrate a feasible application, the values used in the analysis originate from the case of single pile in order to directly compare the outcomes. The building is characterised by a big cantilever, which causes an overturning bending moment at the base. In order to ensure equilibrium, a traction force must be transmitted to the foundation. That force is transferred to the piles by means of a rigid cap. The compact piled rigid raft is a regular grid of equally spaced piles with spacing ratio $s/D = 3$. The piles dimensions and mechanical properties are identical to those of the pile of previous section. Soil 1 is adopted for the shaft springs properties. The computed reduction factors for the corner, external, and inner piles are 0.233, 0.198, and 0.180, respectively. The reduction in stiffness is significant and highlights that strong interactions are likely for such close-spaced piles. A cap spring with stiffness $k_c = 43.1 \text{ MN/m}$ (corresponding to a uniform module of sub-grade reaction of 2.33 MN/m^3) is considered for the cooling phase of the piles. It is assumed that the stiffness of the cap spring is already weighed. The piled raft is subjected to a traction force $F = 0.75N_y n_p$, where n_p is the number of piles. Subsequently, each pile is cooled uniformly by $\Delta T = -22^\circ\text{C}$.

The diagram of the mechanical and thermally imposed strains is illustrated in Figure 5.10. The results of The coefficient of imposed thermal strain (η), normalised internal axial force owing to the applied external load (N_{mec}/\bar{F} ; \bar{F} is the total force divided by

the number of piles), and normalised thermally induced internal axial force (N_{th}/N_{blc}) are provided in Figure 5.11.

The strain induced by the applied external force exhibits a similar trend for each pile and is also analogous to the case of the single pile. As the load distribution is not uniform among the piles, the mechanical strain increases from the internal to the corner piles. The cracked lengths for the internal, external, and corner piles are 13 %, 14 % and 18 %, respectively. The temperature variation increases the cracked length only in the external and corner piles, but not in the internal pile.

The profile of η is similar to that of the single pile for the external and corner piles. However, the inner pile does not exhibit the peak close to the uncracked–cracked interface, although the value of η is significantly higher in the cracked part. This outcome, which need not be generalised, is a result of the fact that the cracked length in the central pile is not increased by the temperature variation. When the pile is considered linear elastic, η is exceptionally low as it generally is. The stepped shape of this diagram is owing only to the precision retained for the computation of strains, which are very low in this case.

The axial force owing to the application of F is presented in the central column of Figure 5.11. As expected for a configuration with a rigid cap, the axial load distribution is such that a corner pile carries a higher load than an external pile, which in turn carries a higher load than the inner pile. The profile of N_{mec}/\bar{F} computed using a linear elastic pile is nearly identical. This is because the mechanism of load distribution is governed by the overall axial stiffness of the interface–pile system. Because the cracked length of the piles differs by a maximum of 5 %, the relative stiffness among the piles is practically unaffected by the structural component, i.e. non-linear or linear elastic pile. This implies that in this case, the load distribution is governed by the interaction effects through the soil mass and that any load redistribution between piles owing to a variation in stiffness (plasticity) is mainly because of the soil–pile interfaces non-linear behaviour.

Meanwhile, the thermally induced axial force is more sensitive to the variation in the structural stiffness. This highlights the *imposed displacement* nature of this type of load. For the linear elastic pile, an increase in the values of N_{th}/N_{blc} from the inner to the corner pile is likely [114]. When the non-linear behaviour of the pile is also considered, over the first 25 %, the thermally induced axial force in the inner pile is higher compared to that of the external pile and attains the value of the corner pile at the head. This is explained by the fact that whereas the cooling does not increase the cracked length of the inner pile, it does so for the corner and external piles. Thereby, no part of an imposed displacement is absorbed by the branch of zero structural stiffness (crack development stage), and the increase in the internal force is larger for the inner pile. Compared to

the isolated pile presented previously, the magnitude of N_{th} decreases by a factor of approximately 10.

It is established that the behaviour of a piled raft with close spaced piles is mainly governed by interactions through the soil and to a lesser extent by interactions through the cap. This is verified in the present analysis. The actual performance of each pile is also affected by the non-linear response of the reinforced concrete non-negligibly. This is highlighted by the strain and factor of imposed thermal strain diagrams. It is important to emphasise that the performance of a structure is defined by the extent of plastic strains and its ductility capacity, rather than by the internal state of stress, which may be similar for a linear and a non-linear analysis. Here, it is demonstrated that the internal state of strain may be significantly different from that obtained through a linear elastic model of the pile. Nevertheless, thermally induced strains are absorbed by the structure because the ductility capacity is ensured. This outcome is however subjected to the same constraint highlighted in the last paragraph of the previous section.

5.8 Concluding Remarks

A general framework for the thermal stress analysis of energy piles subjected to axial load is presented. The linear system of equations and a few closed form solutions are provided for simple bar systems, which can be directly used as limiting cases. This may be effective during early design stages. Thereafter, the derivation of the system of equations for realistic foundations are presented, so that they can be conveniently used by engineers.

This study combines the non-linear behaviour of reinforced concrete with the load-transfer approach to investigate the performance of piles thermally activated under tension. A finite element model capable of handling arbitrary thermomechanical load configurations is developed. It is used to analyse the response of a pile subjected to a traction force and then to a severe cooling, both in isolated and piled rigid raft foundations. The results illustrate that reinforced concrete post-cracking behaviour can significantly impact the response of energy piles, which could be comparable to the soil-pile interface behaviour. Therefore, reinforced concrete non-linearity should be considered for a correct assessment of piles performance. It is highlighted that, for this purpose, temperature variation has to be considered in an *imposed displacement* framework. It is observed that the magnitude of the imposed thermal strain can be higher than $|\alpha\Delta T|$. Nevertheless, if the ductile behaviour of the structural members is ensured, such strains are simply accommodated by the piles. However, imposed thermal loads may have an impact if

variable external loads or transverse forces are expected. Moreover, serviceability limit state may require more attention since the opening of cracks could be an important aspect.

Recommendations pertaining to the design are provided in order to ensure superior energy pile performance at the ultimate limit state. This study is within the recent framework of performance-based design of energy geostructures, which is aimed at a higher resilience.

Acknowledgements

The authors gratefully appreciate Professor A. Muttoni for his valuable comments. Gratitude is also due to R. Cantone. The support of the Swiss National Science Foundation (project No. 174575, Division InterCo) is acknowledged.

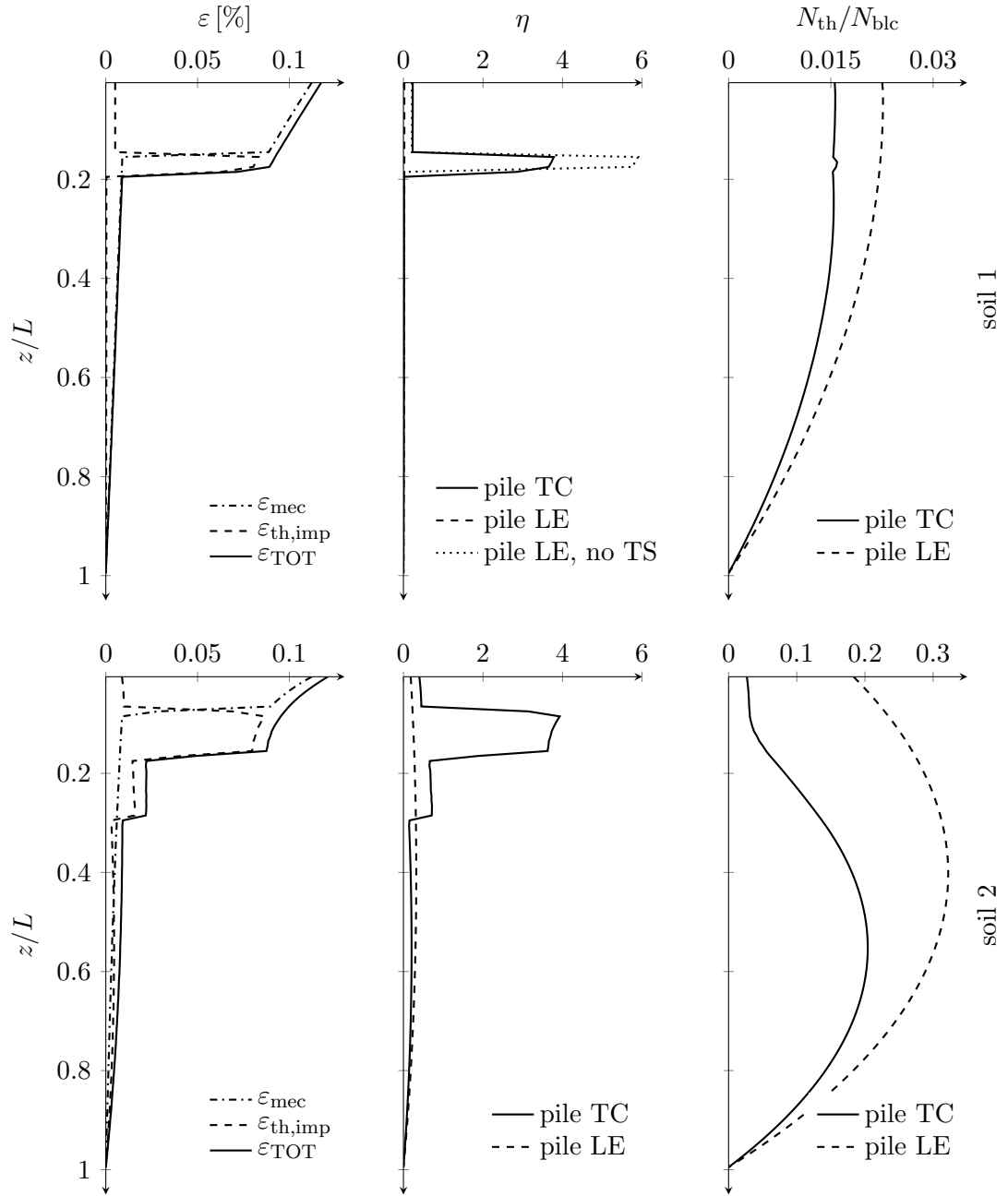


Figure 5.7 – Diagrams of strain induced by head force ε_{mec} , thermal imposed strain $\varepsilon_{th,imp}$, and sum of the two ε_{TOT} ; factor of imposed thermal strain η ; and dimensionless thermal force N_{th}/N_{blc} for isolated pile; tension chord model (TC) and linear elastic pile (LE); traction force $F = 0.75N_y$ and then cooling $\Delta T = -22^\circ\text{C}$; both soil 1 and soil 2.

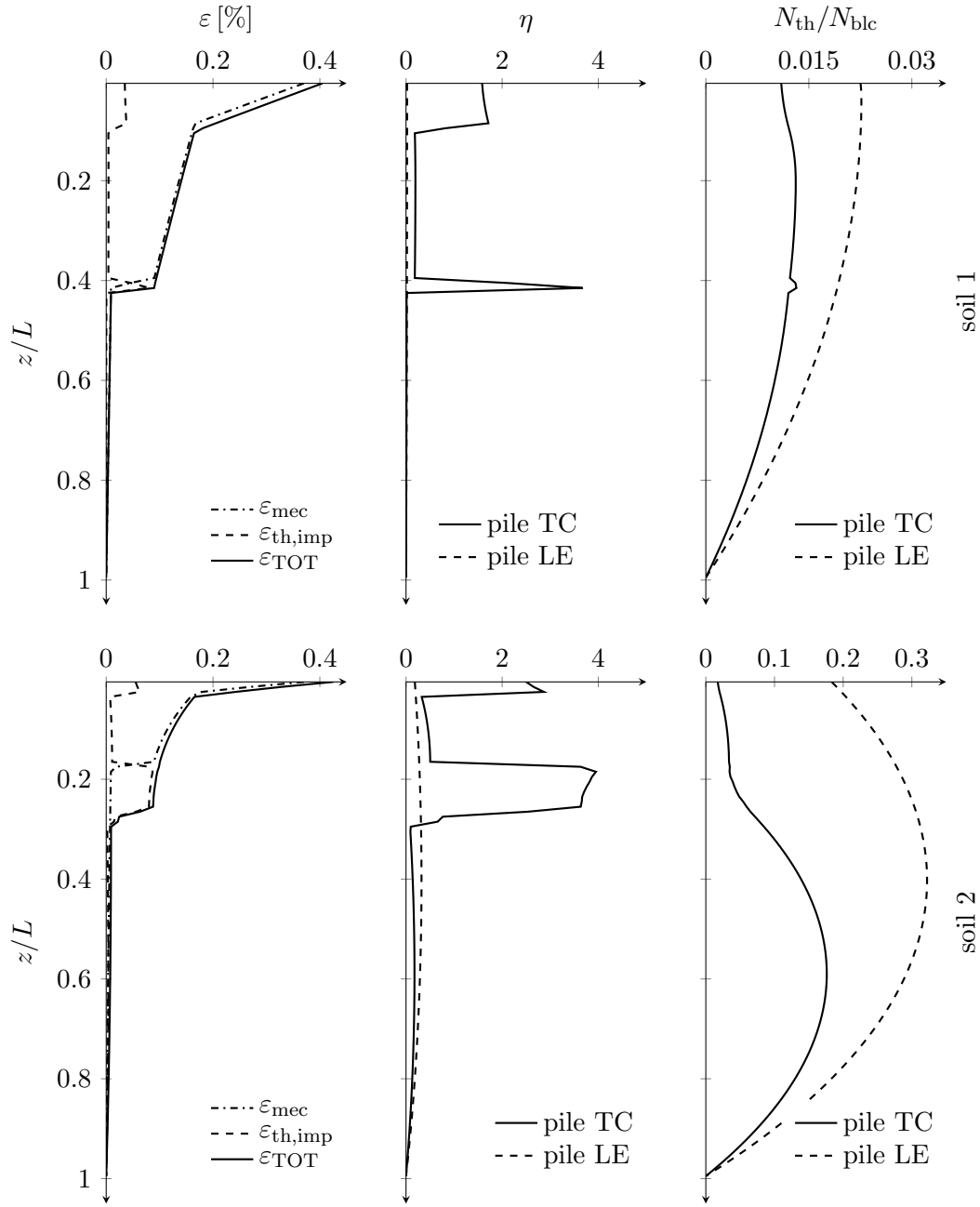


Figure 5.8 – Diagrams of strain induced by head force ε_{mec} , thermal imposed strain $\varepsilon_{th,imp}$, and sum of the two ε_{TOT} ; factor of imposed thermal strain η ; and dimensionless thermal force N_{th}/N_{blc} for isolated pile; tension chord model (TC) and linear elastic pile (LE); traction force $F = 1.1N_y$ and then cooling $\Delta T = -22^\circ\text{C}$; both soil 1 and soil 2.

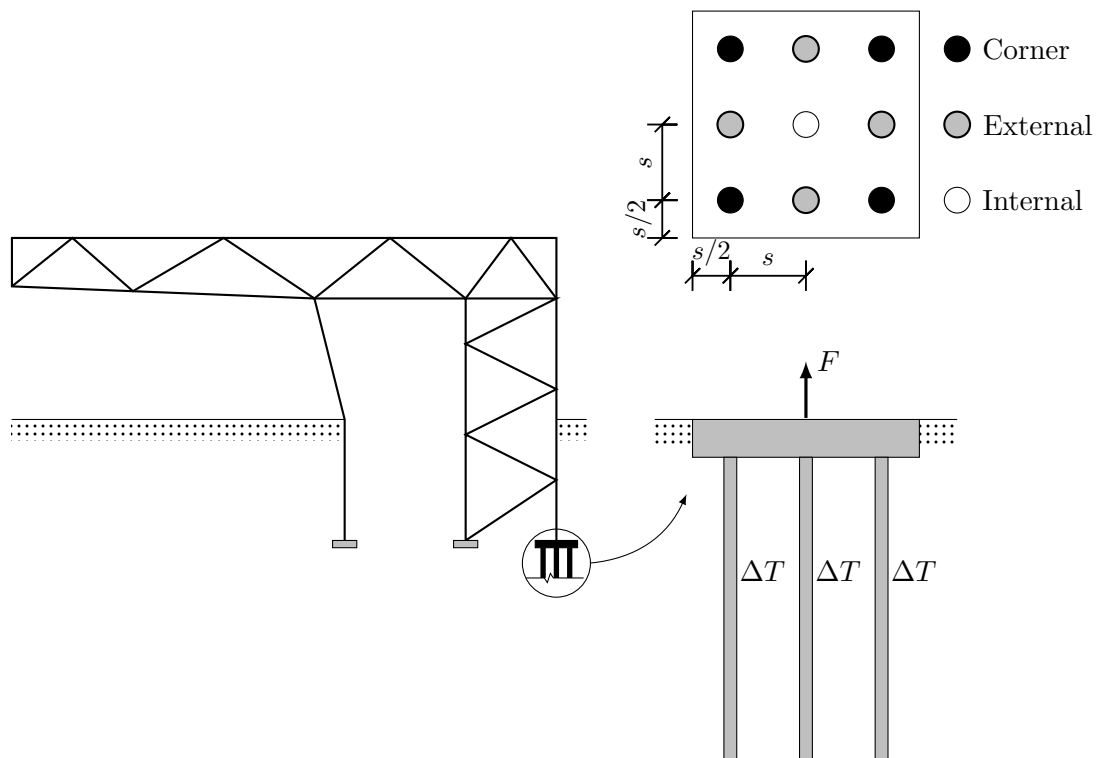


Figure 5.9 – Scheme of a steel frame with piled raft foundation, view of foundation with piles position, and zoom of piled raft with applied loads.

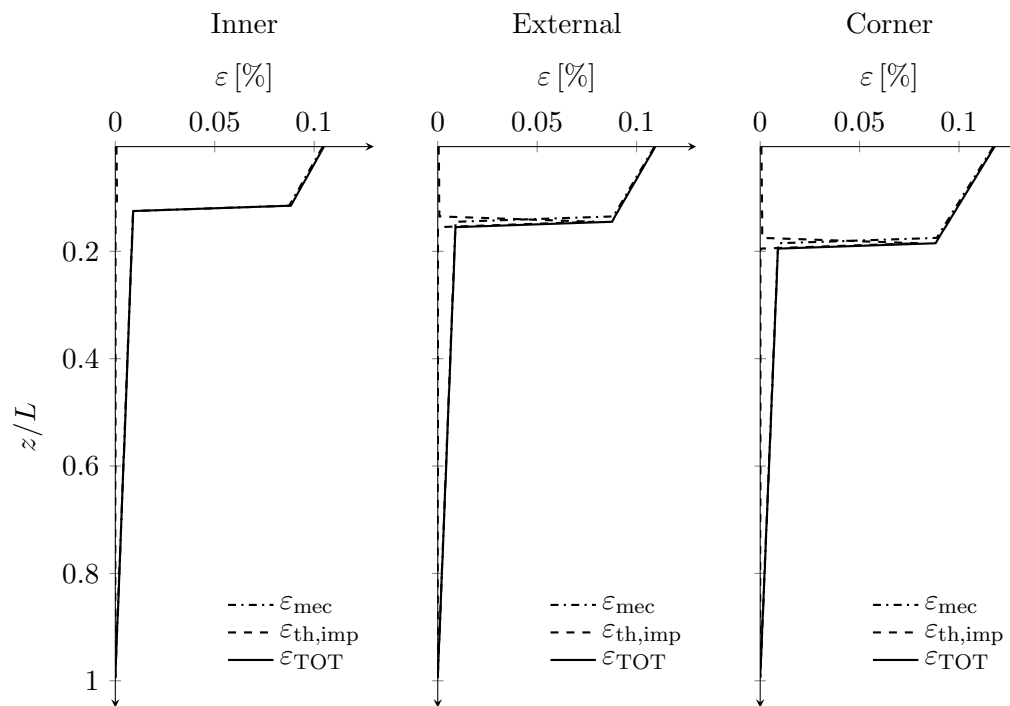


Figure 5.10 – Diagrams of strain induced by cap force ε_{mec} , thermal imposed strain $\varepsilon_{th,imp}$, and sum of the two ε_{TOT} of a corner, an external, and the central pile for the piled raft foundation; traction force $F = 0.75N_{yp}$ and then uniform cooling of each pile $\Delta T = -22^\circ\text{C}$; soil 1.

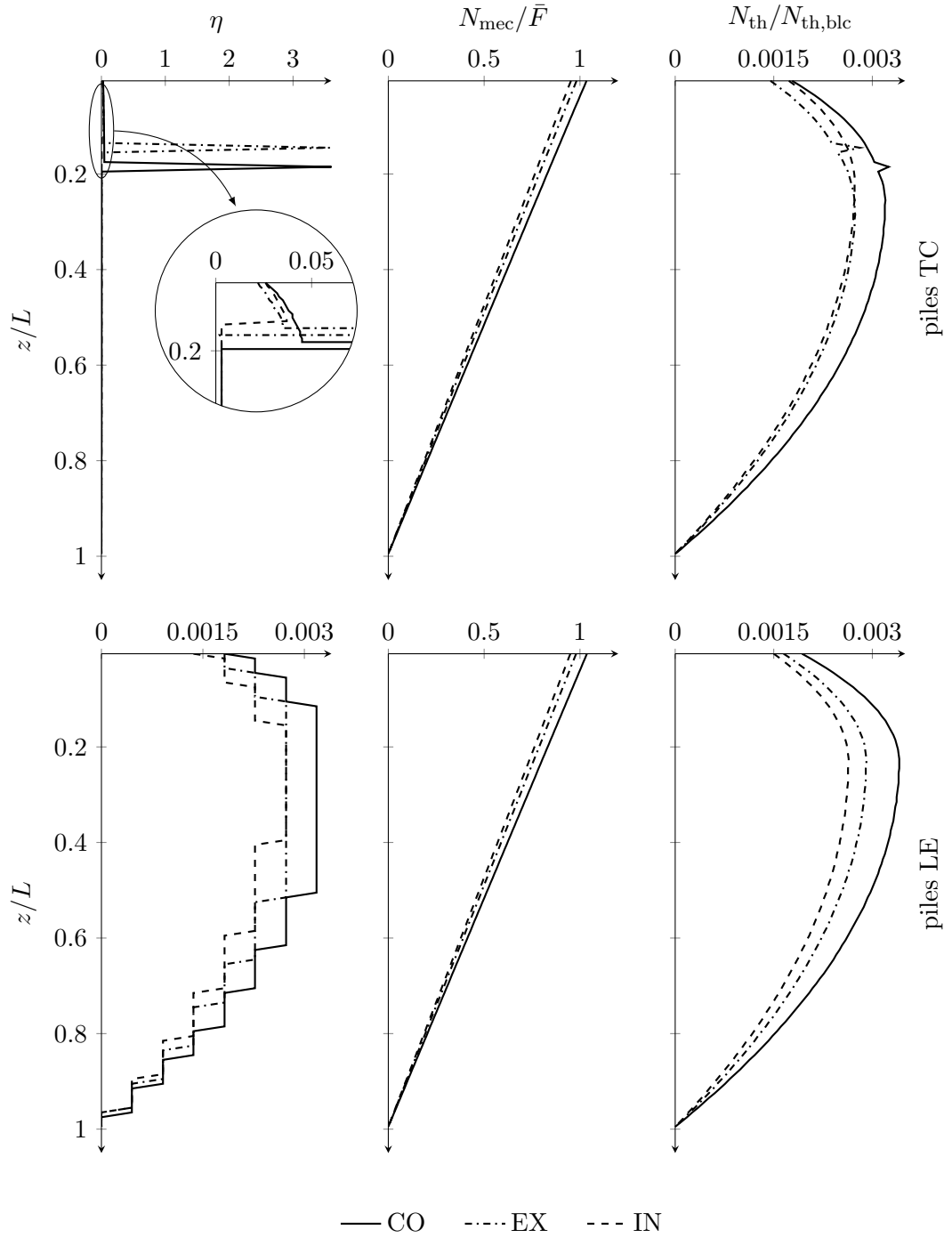


Figure 5.11 – Diagrams of factor of imposed thermal strain η , normalised mechanical force N_{mec}/\bar{F} , and dimensionless thermal force $N_{\text{th}}/N_{\text{th,blc}}$ of a corner (CO), an external (EX), and the central (IN) pile for the piled raft foundation; traction force $F = 0.75N_y n_p$ and then cooling of each pile $\Delta T = -22^\circ\text{C}$; soil 1.

The foundation design for high-rise buildings should therefore be considered as a performance-based soil-structure interaction issue and not limited to traditional empirically based design methods, such as a traditional bearing capacity approach with an applied factor of safety.

Harry G. Poulos, Tall Building Foundation Design

6

The Role of Thermal Loads in the Performance-Based Design of Energy Piles

Postprint version of the article submitted to *Geomechanics for Energy and the Environment*.

A F Rotta Loria, M Bocco, C Garbellini, A Muttoni, and L Laloui. “The role of thermal loads in the performance-based design of energy piles”. In: *Geomechanics for Energy and the Environment* 21 (2020), p. 100153.

Contribution of the candidate: co-investigation of geotechnical and structural limit states, co-development of design strategy, co-writing of text dedicated to the structural performance.

OVER THE PAST two decades, a substantial amount of research has investigated the effects of thermal loads associated with the geothermal operation of energy piles on their mechanical response. Based on this research, consensus about the need for considering the effects of thermal loads on the geotechnical and structural design of energy piles has been achieved. However, the understanding of the influence of thermal loads on the mechanical response of energy piles has prevented the determination of when the effects of these loads should be considered in performance-based design, e.g. only when addressing the deformation (at serviceability limit states) or also the failure (at ultimate limit states) of such foundations. Looking at this challenge, this paper presents an investigation of the role of thermal loads in the mechanical response of energy piles to provide a theoretically based approach for the geotechnical and structural performance-based design of such foundations. The main conclusion that can be drawn from this study and the discussed ductility-based design approach is that thermal loads cause negligible effects at ultimate limit states from both a geotechnical and a structural perspective, while they cause significant effects that should be considered at serviceability limit states.

6.1 Introduction

The utilisation of energy piles has increased considerably over the past twenty years. Consequently, a substantial amount of research has addressed the mechanical response of such foundations subjected to thermal and mechanical loads due to their coupled geothermal and structural support functions, respectively. This research has been motivated by the fundamentally different natures and effects of thermal and mechanical loads on the mechanical response of energy piles.

Thermal loads can be idealised as imposed deformations. These loads cause expansion and contraction of the energy piles and the surrounding ground. Energy piles expand upon heating and contract upon cooling [189, 220]. In contrast, soils can expand or contract upon heating, while they contract upon cooling [34, 45]. In most cases, a portion of the thermally induced deformation of energy piles is restrained by the surroundings and causes thermally induced stress in such foundations [19, 323]. The significance of the observed thermally induced strain and stress depends on the end-restraint conditions [47, 376] and the ratio between the thermal expansion coefficient of the ground and that of the energy piles [20, 322]. Both of these aspects also affect the vertical displacement and stress variations within energy piles [317]. Energy piles subjected to thermal loads generally displace in opposite directions from the so-called null point of the vertical

displacement and mobilise shear stress at the pile shaft to ensure equilibrium from the so-called null point of the shear stress [324]. The locations of the referenced null points are generally different [324] and can change throughout loading [80, 239, 317]. The stress, strain and displacement variations characterising energy piles can markedly vary because of the influence of group effects associated with thermal loads [319, 329]. These effects are responsible for a greater group deformation than that of a single isolated pile under the same average load [318, 321].

Mechanical loads can be idealised as prescribed forces. These loads typically cause stress and strain variations that decrease along the depth of the energy piles and the surrounding ground [3, 21]. In most cases, the evolutions with depth of the variations caused by mechanical loads are more uniform than those caused by thermal loads and are associated with displacement variations in a unique direction [324]. The end-restraint conditions also govern, in this context, the significance of the stress, strain and displacement variations, together with group effects caused by mechanical loads [267, 285].

The phenomena caused by thermal loads involve effects that are coupled with those of mechanical loads and that can be comparable to or even more significant than the effects of mechanical loads. Thus, they should be considered in the geotechnical and structural design of energy piles.

In principle, European Norms, often called the Eurocodes [100] are available to address the performance-based design of structures such as energy piles. In practice, these norms currently lack recognised rules that suitably consider in the design process the effects of thermal loads associated with geothermal operation. One guide in Switzerland [350] one standard in the United Kingdom [124] and one recommendation in France [46] have been proposed to guide the geotechnical and structural design of energy piles. Despite their importance for practitioners, these documents are characterised by drawbacks. The Swiss code [350] neglects aspects whose relevance for design has been noted in recent years (e.g., thermally induced group effects). In addition to suffering from this drawback, the United Kingdom standard [124] is applicable to only a limited number of design situations because it is characterised by prescriptive and not performance-based features. It also involves the excessive oversizing of energy piles because it is based on worst-case scenario considerations. The French recommendations [46] may, in principle, be considered a suitable reference for the design of energy piles because they adopt a performance-based design approach drawing from the Eurocodes. However, they suffer from three main limitations. First, they do not include a comprehensive framework for the design process of energy piles and focus only on the verification of such foundations. Second, they rely on the arguable proposition of establishing ultimate and serviceability

limit state verifications of energy piles by combining the results of analyses while considering the quasi-permanent serviceability limit state load combination. Third, they account for the influence of thermal loads in a way that is not conservative because they employ a partial factor for thermal actions that underestimates the related effect with reference to current experimental evidence.

In addition to the previous references, studies on the performance-based design of energy piles have been reported, for instance, by Xiao et al. [405] Jelušič and Žlender [157] and Habert et al. [127] Despite these studies, a comprehensive performance based design framework for energy piles is not yet available.

Based on the above, vast knowledge is available to address the mechanical response of energy piles, and there is a consensus about the need for considering both thermal and mechanical loads in the design of such foundations. However, two critical questions appear to remain unresolved in this scope:

- Do the effects of thermal loads only govern the deformation of energy piles, or may they also cause the failure of such foundations?
- Should the effects of thermal loads be considered in the design of energy piles only when addressing serviceability limit states or also ultimate limit states, and in what manner should these effects be considered?

This study addresses the previous questions and the associated scientific and engineering challenges by providing a theoretical analysis of (i) the influence of thermal loads on the mechanical response of energy piles and (ii) the role of these loads in the geotechnical and structural design of such foundations. As a result of the analysis presented in this work, a performance-based design approach for energy piles is proposed.

6.2 Performance-Based design of Energy Piles

6.2.1 Rationale

In this study, the performance-based design of single energy piles is carried out in the framework of the Eurocodes. The design is only developed at ultimate limit states. This approach assumes that if no ultimate limit state is exceeded with an appropriate design methodology proposed herein, such a result is unlikely to arise in general as far as such methodology is employed. When design guidance is missing from the Eurocodes, propositions are made to resolve this gap. The influence of both mechanical and thermal actions is considered.

It is worth noting that the design of energy piles should also address the response of the piles in a group and consider both ultimate and serviceability limit states. However, given that these aspects are not essential for the purpose of this work, they are not addressed in the following for sake of brevity.

6.2.2 Design Case Studies and Material Parameters

The design of single non-displacement energy piles of typical slenderness ratios $L/D = 20, 30, 40$ and 50 , where L is the pile length, and pile diameters $D = 0.5$ m, 0.75 m and 1 m, is performed. Energy piles made of reinforced concrete subjected to compressive axial mechanical loads and thermal loads are considered. The energy piles are assumed to be embedded in a sand deposit for which detailed material properties are available [139, 206, 268] (cf., Table 6.1). The reinforced concrete used for the energy piles is assumed to be characterised by (i) uncracked cross-sections, (ii) linear stress–strain relationships and (iii) mean values of the modulus of elasticity, as stated in the Eurocodes [101]

Two conditions are considered for the energy piles: (i) piles free to move at their head and (ii) piles restrained at their head because of the presence of a slab. Conditions (i) and (ii) conservatively analyse the pile vertical displacement and vertical stress, respectively. The slab stiffness K_h is calculated according to Poulos and Davis [288].

In the analyses, it is assumed that (i) the shear strength parameters of the soil are insensitive to temperature variations, (ii) the potential degradation phenomena caused by the cyclic influence of the thermal loads do not affect the pile–soil interface parameters, and (iii) the deformation parameters of the soil are insensitive to temperature variations. Assumptions (i) and (ii) are corroborated by experimental evidence [79, 406] and are also explicated in the French recommendations [46]. Assumption (iii) disregards experimental evidence that may characterise situations in practice [104] based on the argument that these effects are negligible at ultimate limit states.

In all situations, the design mechanical load applied to the energy piles is characterised by a 70 % permanent portion and a 30 % variable portion, as is often done in practice in the absence of more detailed information.

6.2.3 Typical Design Problems

Two typical design problems exist for piles and are considered in this study:

1. *Constant applied mechanical load and varying pile length* – A pile length may be defined for each pile of a foundation to sustain an applied design mechanical load.

Table 6.1 – Material properties used for the analyses in this study.

Pile parameters		Soil parameters		Soil-pile interaction parameters	
Young's modulus, E_{EP} [MPa]	31 000 ^a	Shear modulus, G_{soil} [MPa]	8.46 ^b	Slope of elastic branch of Frank and Zhao's load-displacement relationship [109] for the pile shaft, K_s [MPa/m]	19.48 ^c 15.82 ^d
Poisson's ratio, ν_{EP}	0.25	Poisson's ratio, ν_{soil}	0.30	Slope of elastic branch of Frank and Zhao's load-displacement relationship [109] for the pile base, K_b [MPa/m]	116.87 ^c 94.92 ^d
Bulk density, ρ_{EP} [kg/m ³]	2450	Bulk density, ρ_{soil} [kg/m ³]	2005	Average shaft resistance for a single isolated pile, q_s [kPa]	9.59 ^c 19.19 ^d
Linear thermal expansion coefficient, α_{EP} [1/°C]	10 ⁻⁵	Rheological coefficient, α_r	1/3	Base resistance for a single isolated pile, q_b [kPa]	3409 ^c 6818 ^d

^a This mean Young's modulus refers to the minimum concrete class C25/30 that must be considered for an environmental exposition XC2 following the Eurocodes. Reinforcement steel B500B is employed in all cases.

^b The shear modulus varies with the depth according to the pressure-dependent law proposed by Maehr and Herle [206].

^c Referring to a diameter $D = 0.5$ m and a slenderness $L/D = 20$.

^d Referring to a diameter $D = 1$ m and a slenderness $L/D = 20$.

However, the considered length may be increased to a more meaningful length. As a result, the actual pile design load capacity will be higher than the needed value.

2. *Varying applied mechanical load and constant pile length* – A design mechanical load may be considered for all piles of a foundation based on the maximum load applied to one or more piles. However, not all the piles of the foundation need to effectively sustain this load. As a result, the actual length of the pile will be increased compared to the necessary value.

6.2.4 Design Method

Two aspects must be considered in any case to ensure an adequate structural performance of the energy piles and are proposed in this work:

1. A design compressive strength of the reinforced concrete section (e.g., for no moments applied) at least equal to the design load capacity of the pile must be ensured. When this approach is not employed, the design loads sustained from a geotechnical perspective may induce or exceed an ultimate limit state from a structural perspective. In contrast, the proposed approach guarantees a potential ductile collapse mechanism related to the excess of ultimate limit states from a geotechnical perspective first.
2. A minimum steel reinforcement area of the reinforced concrete section must be chosen. When this approach is not employed, the requirements of durability and deformation (e.g., cracking) of the materials constituting the designed structures may not be satisfied. In contrast, this approach guarantees durability and ductility.

The design of the energy piles should be carried out with reference to the worst-case scenario given by different design approaches proposed by the Eurocodes [102]. Given that this study aims at providing a general approach applicable to common design cases, only “Design approach 1 – Combination 1” is considered in the following. Design approach 1 – Combination 1 often represents the governing design condition in common cases. Moreover, while various approaches can be employed to estimate the design axial load capacity of the piles, the following formulation is considered in this study:

$$Q_{ud} = Q_{sd} + Q_{bd} = \overline{K \sigma'_v \tan \delta A_s + \sigma'_{vb} N_q d_q A_b} \quad (6.1)$$

where Q_{sd} is the design value of the pile shaft capacity, estimated using the frictional expression presented by Coulomb [61]; Q_{bd} is the design value of the pile base capacity,

estimated according to the approach proposed by Hansen [26] by neglecting the terms involving the bearing capacity factors N_c and N_γ and assuming a shape factor $s_q = 1$; \bar{K} is the average value of the relevant coefficient of lateral earth pressure; $\bar{\sigma}'_v$ is the average value of the in situ vertical effective stress; δ' is the pile-soil interface angle of shear strength; A_s is the pile shaft area; σ'_{vb} is the vertical effective stress at the level of the pile base; N_q is a bearing capacity factor; d_q is a factor that accounts for the pile depth; and A_b is the pile base area. When input into the formulations, the angles of shear strength of the soil and the pile-soil interface are assumed to be under constant volume conditions. It is noteworthy that the shaft capacity is strongly affected by the method of pile installation, for example through the variation of the coefficient of lateral earth pressure. The base capacity is also influenced by the construction process and it is well recognised that this term does not increase after a certain depth, typically termed “critical depth”. Therefore, application of Eq. (6.1) to practical cases deserves a careful choice of the parameters.

Eq. (6.1) yields suitable estimates of the load capacity of piles in a soil deposit when fully drained conditions govern the behaviour of the pile [108]. However, Eq. (6.1) may not be applied for situations governed by a (fully or partially) undrained response of the soil or for energy piles in rock.

6.2.5 Analysis Method

Various methods of analysis can be employed to address the mechanical response of energy piles, including the finite element method [116, 190], the load-transfer method [47, 168, 278, 320, 374] and approaches based on charts [244, 318, 321]. In this work, the analysis of energy piles is addressed through the load-transfer method and the use of Thermo-Pile software [168]. Accordingly, a linear thermo-elastic behaviour (weak thermo-mechanical coupling) of the energy pile is assumed, whereas the springs modelling the soil obey to a three-linear model. The three-linear model is described by a linear elastic part until the yield stress is reached, thereafter the stiffness decreases and the stress grows until the soil shear strength is reached. Upon the achievement of the shear strength, the stress remains constant. A symmetric behaviour is considered for the pile-soil interface with respect to the sign of the shear stress and displacement, while this is not done for the pile toe. That is, while the load-transfer relationship employed for describing the pile-soil interface accounts for both loading and unloading, the relationship employed for the pile base only accounts for loading.

6.2.6 Verification Method

Two aspects must be considered to verify the structural and geotechnical performance of energy piles and are accounted for in this work:

1. The vertical stress variations caused by mechanical and thermal loads must be considered with respect to the entire length of the energy piles, and the most stressed section must be verified.
2. The vertical displacement variations caused by mechanical and thermal loads must be considered with respect to the head of the energy piles.

6.2.7 Combination of Actions at Ultimate Limit States

In the context of performance-based design, no limit state must be exceeded in all relevant design situations when the design values for actions or the effects of actions and resistances are introduced in the analysis models [100]. When persistent and transient design situations at ultimate limit states are considered with respect to the influence of only permanent and variable loads, the design effects of actions read as [100]

$$E_d = \sum_{j \geq 1} \gamma_{Gj} G_{kj} + \gamma_{Q1} Q_{k1} + \sum_{i \geq 1} \gamma_{Qi} \psi_{0i} Q_{ki} \leq R_d \quad (6.2)$$

where E_d is the design value of an action or action effect, $\gamma_{j,i}$ are the partial factors of the (j -th and i -th, respectively) actions or action effects, G_{kj} represents the permanent loads, Q_{k1} is the dominant variable load, $\psi_{0i} Q_{ki}$ are the accompanying variable loads, ψ_i are combination factors, and R_d is the design value of the resistance. The symbol “+” may be read as “combined with”, and the symbol “ \sum ” implies “the combined effect of”.

6.2.8 Partial Factors for Thermal Loads Applied to Energy Piles

Thermal loads applied to energy piles can be considered variable, indirect, free and static actions. This classification draws from the one currently considered in the Eurocodes for thermal actions applied to buildings and bridges.

Thermal loads cause significant temperature variations within energy piles, which can be defined with reference to the heat inputs involved in the building energy design, the operation time and the thermal properties of the piles and ground. The resulting characteristic temperature variations are nominal values, ΔT_k .

To account for the burdensome influence of thermal actions applied to energy piles, the following partial factors for the combination, frequent and quasi-permanent values

should be considered, respectively: $\psi_0 = 0.60$, $\psi_1 = 0.50$ and $\psi_2 = 0.50$. The proposed values of ψ_0 and ψ_1 coincide with those reported in the Eurocodes for buildings. They can be considered suitable for energy piles due to the similar probability of occurrence characterising thermal actions applied to buildings and energy piles. The same values have been previously suggested by Burlon et al [28]. The proposed value of ψ_2 differs from that reported in the Eurocodes for buildings (i.e., $\psi_2 = 0$) but coincides with that for bridges. This value has been defined by considering that the average of variables can represent the accompanying values of variable actions [100]. Therefore, factor ψ_2 may be calculated as the ratio between the average temperature variation and the maximum (or minimum) temperature variation observed throughout successive seasonal thermal cycles applied to energy piles. By considering such an approach and referring to the data reported by Loveridge et al. [200], which represent one of the few long-term monitoring examples currently available for energy piles, a value of $\psi_2 = 0.50$ is obtained for heating and cooling. This value approximates the ratio between the average value of a sine wave over half of a cycle and the maximum (or minimum) of this function over the same cycle, i.e., $2/\pi = 0.64$, which may be alternatively employed to describe the influence of thermal loads and estimate ψ_2 . The proposed value of factor ψ_2 differs from the value of $\psi_2 = 0.20$ previously suggested by Burlon et al. [28] and more recently by Habert et al [127].

In the following, a performance-based design is developed by considering, for simplicity, only persistent and transient design situations. One permanent mechanical load and one variable mechanical load applied to the energy piles are considered, in addition to a thermal load (for the heating and cooling seasons). Two design load combinations for energy pile heating and one combination for cooling are derived from the considered loads.

When considering the effects of thermal loads in the combination of actions, the characteristic temperature variation ΔT_k , instead of the effect of this temperature variation $Q_k(\Delta T_k)$, is used. This approach is generally valid, irrespective of whether analyses accounting for a reversible or irreversible mechanical behaviour of the soil are performed (the hypothesis of superposition between the actions and their effects is not made).

6.3 Unlikelihood of Thermal Loads Exceeding Geotechnical Ultimate Limit States

6.3.1 Theoretical Considerations

The design of energy piles against geotechnical ultimate limit states must be addressed with reference to displacement and equilibrium considerations. Displacement considerations involve limiting differential displacements occurring among the piles to ensure that superstructures (e.g., redundant) are not affected by unacceptable stress variations that may be associated with failure or collapse mechanisms. Equilibrium considerations involve comparing the design values of the load acting on the pile and the load supported by the pile (i.e., load capacity) to ensure that no failure or collapse mechanisms in the ground are achieved.

In this context, the worst foreseeable condition for the geotechnical performance of energy piles involves foundations with fully mobilised shaft and base capacities caused by a cooling thermal load and a (compressive) mechanical load. In this theoretical condition where the shaft and base capacities are fully mobilised and soil behaviour can be assumed as perfectly plastic, the null point of an energy pile subjected to cooling thermal loading is located at or towards the toe depending on whether a slab is present at the head, respectively. Therefore, the maximum possible head settlements of energy piles caused by thermal loading, in addition to those caused by mechanical loading, occur. This phenomenon has the potential to exceed a geotechnical ultimate limit state. A possible criterion to identify that a geotechnical ultimate limit state is exceeded corresponds to a pile toe settlement of 10 % of the pile diameter [102].

Piles with fully mobilised capacities subjected to a heating thermal load are of no concern because such a load causes no head settlement. In this theoretical condition where the shaft and base capacities are fully mobilised and soil behaviour can be assumed as perfectly plastic, the null point of an energy pile subjected to heating thermal loading is necessarily located at the head irrespective of whether a slab is present or not at the head. This is the only way to ensure equilibrium. Otherwise, any other location of the null point would cause an increase of the compression force within the pile in the zone above the null point (upward movement), which could not be balanced because a downward movement of the part below the null point would be produced freely (perfect plasticity). The application of a heating thermal load in all other cases induces an upward head displacement of the energy piles. However, the considered phenomenon represents a serviceability limit state problem and is not considered in the following design at ultimate

limit states.

Typical characteristic values of temperature variation associated with cooling thermal loads applied to energy piles can be considered to range between $\Delta T_k = -5^\circ$ and -10° . At worst, a value of $\Delta T_k = -15^\circ$ may be considered in warm climates. The design temperature variations resulting from the previous characteristic values are $\Delta T_d = \gamma_Q \Delta T_k = -7.5^\circ$, -15° and -22° ($\gamma_Q = 1.5$, considering the partial factor proposed by the Eurocodes for variable actions).

The results reported in the following expand on the effects of cooling thermal loads and mechanical loads on the geotechnical performance of energy piles.

6.3.2 Energy Pile Response for a Constant Applied Mechanical Load and Varying Pile Length

Tables 6.2 and 6.3 summarise, for energy piles subjected to combined mechanical and cooling thermal loads, the proportions of vertical head displacement induced by mechanical loading w_d^m and cooling thermal loading w_d^{th} , as well as the total displacement $w_d^m + w_d^{th}$ caused by these loadings. Piles free to move at their head with $L/D = 20$ and 50 are considered for $D = 0.5$ m (cf., Table 6.2) and $D = 1$ m (cf., Table 6.3). In all cases, a design mechanical load P_d corresponding to the design load capacity for $L/D = 20$, i.e., $Q_{ud}(L/D = 20)$, and design temperature variations $\Delta T_d = \gamma_Q \Delta T_k = -7.5^\circ$ and -22° are considered.

The design settlement induced by the combined action of mechanical loading and cooling can be considered small in all cases and incapable of causing excessive differential displacements. Therefore, no geotechnical ultimate limit states are involved.

For the same applied mechanical load and pile diameter, increasing the pile slenderness ratio results in lower head settlements of the energy piles. The reason for this phenomenon is because, for an increase in the pile slenderness, the bearing load that the piles can sustain (and are subjected to) is greater. This result corroborates the rationale of designs considering longer piles to ensure greater safety against the actions of mechanical loads.

For the same applied thermal load and pile diameter, increasing the pile slenderness ratio results in greater head settlements of the energy piles. The reason for this phenomenon is because, although equal thermal loads cause the same thermally induced strains under free expansion conditions, irrespective of the pile length, these loads cause greater vertical displacements for longer piles. This result is in contrast with the belief that longer piles ensure greater safety against the action of thermal loads.

For the same pile slenderness ratio and a greater pile diameter, more significant head settlements of the energy piles are caused by mechanical loads, while lower head settlements are caused by thermal loads. The reason for these phenomena is because, for greater values of the pile diameter, the loads that the piles can sustain are greater. Therefore, if the aim is to limit the vertical displacement of the energy piles caused by thermal loads, longer pile lengths should be avoided, while greater pile diameters should be employed.

Table 6.2 – Normalised vertical head displacements for energy piles of $D = 0.5$ m that are free at their head and subjected to cooling, with a constant applied mechanical load and varying pile length.

D [m]	L/D	P_d/Q_{ud}	ΔT [°C]	w_d^m/D [%]	w_d^{th}/D [%]	w_d^{m+th}/D [%]
0.5	20	1	-7.5	1.28	0.15	1.43
			-22.5	1.28	0.45	1.73
	50	$P_u/Q_{ud}(L/D = 20)$	-7.5	0.09	0.21	0.30
			-22.5	0.09	0.69	0.78

Table 6.3 – Normalised vertical head displacements for energy piles of $D = 1$ m that are free at their head and subjected to cooling, with a constant applied mechanical load and varying pile length.

D [m]	L/D	P_d/Q_{ud}	ΔT [°C]	w_d^m/D [%]	w_d^{th}/D [%]	w_d^{m+th}/D [%]
1	20	1	-7.5	1.60	0.15	1.75
			-22.5	1.60	0.45	2.05
	50	$P_u/Q_{ud}(L/D = 20)$	-7.5	0.15	0.19	0.34
			-22.5	0.15	0.65	0.80

6.3.3 Energy Pile Response for Varying Applied Mechanical Loads and Constant Pile Length

Tables 6.4 and 6.5 summarise the vertical head displacements w_d^m , w_d^{th} and w_d^{m+th} for energy piles free to move at their head with $D = 0.5$ m and 1 m, respectively, $L/D = 20$ and 50. The combined action of $P_d = Q_{ud}$ and $0.2Q_{ud}$, $\Delta T_d = -7.5^\circ$ and -22.5° is considered.

The settlement induced by the combined action of mechanical loading and cooling can again be considered small. Hence, no geotechnical ultimate limit states are involved.

For the same pile diameter and pile slenderness ratio, decreasing the applied mechanical load results in lower head settlements of the energy piles. At the same time,

decreasing the applied mechanical load results in lower energy pile head settlements for the same subsequently applied temperature variation. The reason for these phenomena is because, for lower values of the applied mechanical load, the load range for which the soil behaviour remains elastic widens. Therefore, as the stiffness of the materials associated with elastic conditions is greater compared to that associated with plastic conditions, lower vertical displacements occur for less notable loads, while higher stresses are to be expected.

Table 6.4 – Normalised vertical head displacements for energy piles of $D = 0.5$ m that are free at their head and subjected to cooling, with a varying applied mechanical load and constant pile length.

D [m]	L/D	P_d/Q_{ud}	ΔT [°C]	w_d^m/D [%]	w_d^{th}/D [%]	w_d^{m+th}/D [%]
0.5	20	1	-7.5	1.28	0.15	1.43
			-22.5	1.28	0.45	1.73
		0.2	-7.5	0.04	0.10	0.14
			-22.5	0.04	0.30	0.34
	50	1	-7.5	0.09	0.21	0.30
			-22.5	0.09	0.69	0.78
		0.2	-7.5	0.02	0.16	0.18
			-22.5	0.02	0.53	0.55

Table 6.5 – Normalised vertical head displacements for energy piles of $D = 1$ m that are free at their head and subjected to cooling, with a varying applied mechanical load and constant pile length.

D [m]	L/D	P_d/Q_{ud}	ΔT [°C]	w_d^m/D [%]	w_d^{th}/D [%]	w_d^{m+th}/D [%]
1	20	1	-7.5	1.60	0.15	1.75
			-22.5	1.60	0.45	2.05
		0.2	-7.5	0.05	0.10	0.15
			-22.5	0.05	0.30	0.35
	50	1	-7.5	0.15	0.19	0.34
			-22.5	0.15	0.65	0.80
		0.2	-7.5	0.03	0.14	0.16
			-22.5	0.03	0.49	0.51

6.3.4 Summary

Based on the previous results, cooling thermal loads are unlikely to involve energy pile settlements capable of generating a collapse mechanism. Therefore, from the perspective

of displacement considerations, the effects of thermal loads can be considered negligible for the sake of geotechnical verifications at ultimate limit states. Group effects caused by the interactions among piles may increase these displacements. However, these effects should only be considered at serviceability limit states due to the magnitude of the phenomena involved.

From the perspective of equilibrium considerations, the following remark about the possibility of dealing with effects caused by thermal loads that exceed geotechnical ultimate limit states must be considered. In principle, full mobilisation of the capacity of energy piles may be caused by thermal loads and mechanical loads. In practice, the null point of the shear stress always ensures equilibrium with respect to the influence of thermal loads. In fact, for any magnitude of thermal load applied to energy piles, the reactions provided by the soil below and above the null point of the shear stress compensate for each other and prevent the formation of a collapse mechanism. Energy pile equilibrium will thus always be ensured, with zero thermally induced displacements occurring in correspondence with the null point of the vertical displacement that will prevent the formation of a collapse mechanism.

Based on the above, thermal loads cannot cause a geotechnical collapse mechanism for energy piles; i.e., they cannot involve geotechnical ultimate limit states. Therefore, the effects of thermal loads can be neglected in the design of energy piles at ultimate limit states from a geotechnical perspective.

6.4 Unlikelihood of Thermal Loads Involving Structural Ultimate Limit State

6.4.1 Theoretical Considerations

The design of energy piles against structural ultimate limit states must be addressed with reference to equilibrium considerations. Equilibrium considerations involve comparing the design values of the acting load on the pile and the load supported by the considered pile cross-section (or portion) to ensure that no failure mechanisms in the structure are achieved. In this context, the worst foreseeable conditions for the structural performance of energy piles involves foundations with partially mobilised shaft and base capacities caused by either a significant cooling thermal load and a low (compressive) mechanical load or by a significant heating thermal load and a high (compressive) mechanical load. In these conditions, stresses are generated by the applied loads (with an increasing magnitude for the greater restraint characterising energy piles), with the

potential to exceed a structural ultimate limit state. Typical characteristic values of the temperature variation associated with the heating thermal loads applied to energy piles range between $\Delta T_k = 10^\circ$ and 20° . At worst, a value of $\Delta T_k = 30^\circ$ may occur in cool climates. The design temperature variations resulting from these characteristic values are $\Delta T_d = \gamma_Q \Delta T_k = 15^\circ, 30^\circ$ and 45° . The results reported in the following expand on the effects of heating and cooling thermal loads as well as mechanical loads on the structural performance of energy piles.

6.4.2 Energy Pile Response for a Constant Applied Mechanical Load and Varying Pile Length

Energy Pile Heating

Figure 6.1 presents the normalised axial load N_{Ed}/N_{Rd} characterising the most stressed section of energy piles free to move at their head for varying values of L/D . Piles with $D = 0.5$ m, 0.75 m and 1 m are considered under the combined action of $P_d \equiv Q_{ud}(L/D = 20)$ and $\Delta T_d = \gamma_Q \Delta T_k = 15^\circ, 30^\circ$ and 45° or $\Delta T_d = \gamma_Q \psi_{01} \Delta T_k = 13.5^\circ, 27^\circ$ and 40.5° , depending on the load combination. The design acting load N_{Ed} is generally caused by both mechanical and thermal loads. The design resisting load N_{Rd} corresponds to the compression axial resisting load when no moments are applied.

The combined action of the mechanical and heating thermal loads involves normalised axial loads of up to $N_{Ed}/N_{Rd} = 0.4$. In other words, no structural ultimate limit states are involved due to the combined action of mechanical and heating thermal loads.

The effect of thermal loads increases as the pile slenderness and pile diameter increase. Increasing the concrete class for values of L/D that may be associated with applied design mechanical loads greater than the axial resisting compressive load ensures greater safety against structural ultimate limit states.

Fig. 2 shows the normalised axial load, N_{Ed}/N_{Rd} , experienced by energy piles restrained at their head for a varying slab stiffness relative to the soil, $K_h D/G_{soil}(z = 0)$, where G_{soil} is the soil shear modulus. Piles of $L/D = 50$ with $D = 0.5$ m, 0.75 m and 1 m are considered under the previous mechanical and heating thermal loads.

The combined action of mechanical and heating thermal loads does not involve structural ultimate limit states. However, a more burdensome effect of thermal loads compared to situations where the energy piles are free to move at their head is caused when a restraint is provided by a slab (i.e., $N_{Ed}/N_{Rd} = 0.5$ instead of 0.4 at worst). This effect becomes significant for relative stiffness values of approximately $K_h D/G_{soil}(z = 0) = 10$ as well as for increasing values of the pile diameter.

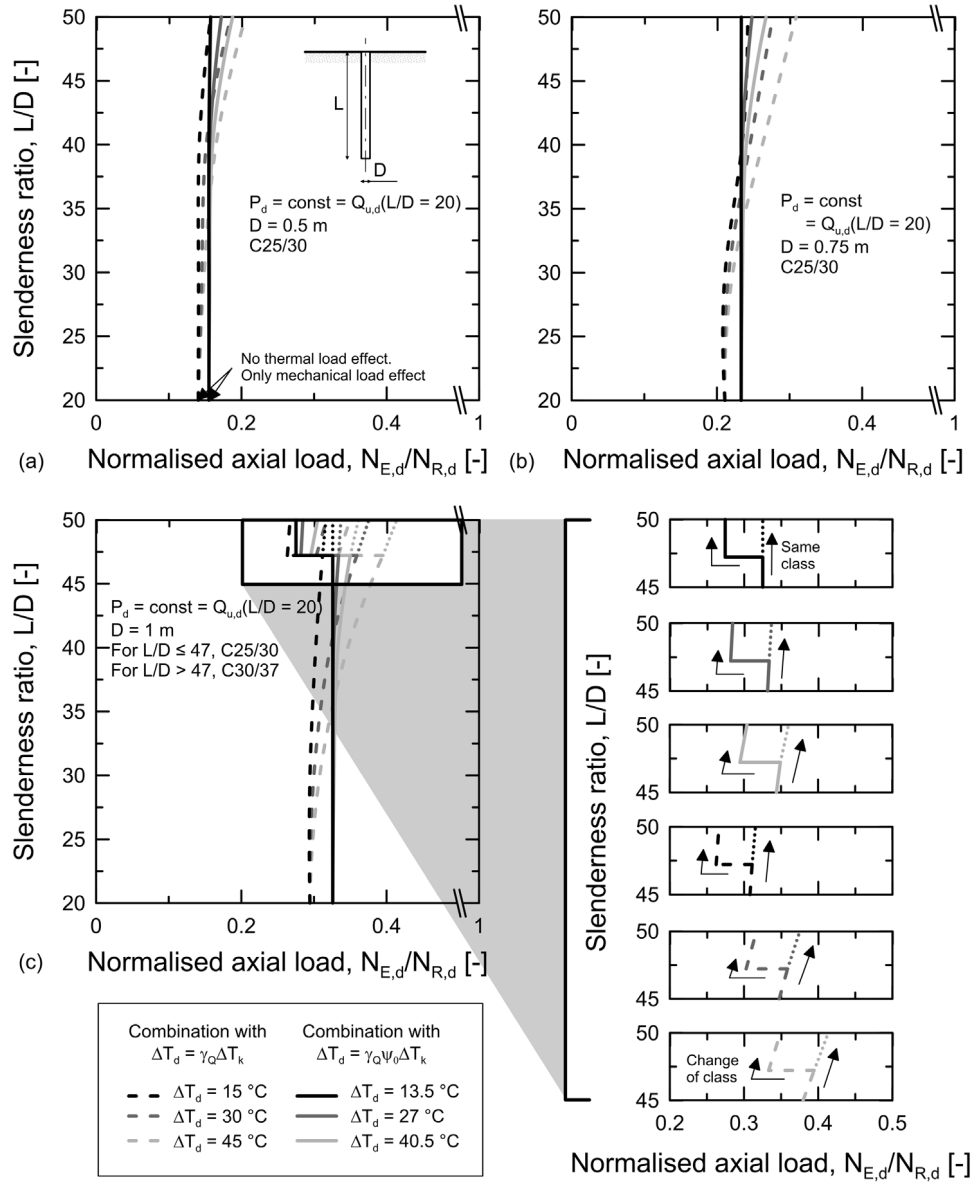


Figure 6.1 – Normalised axial loads for energy piles that are free at their head and subjected to heating, with a constant applied mechanical load and varying pile length.

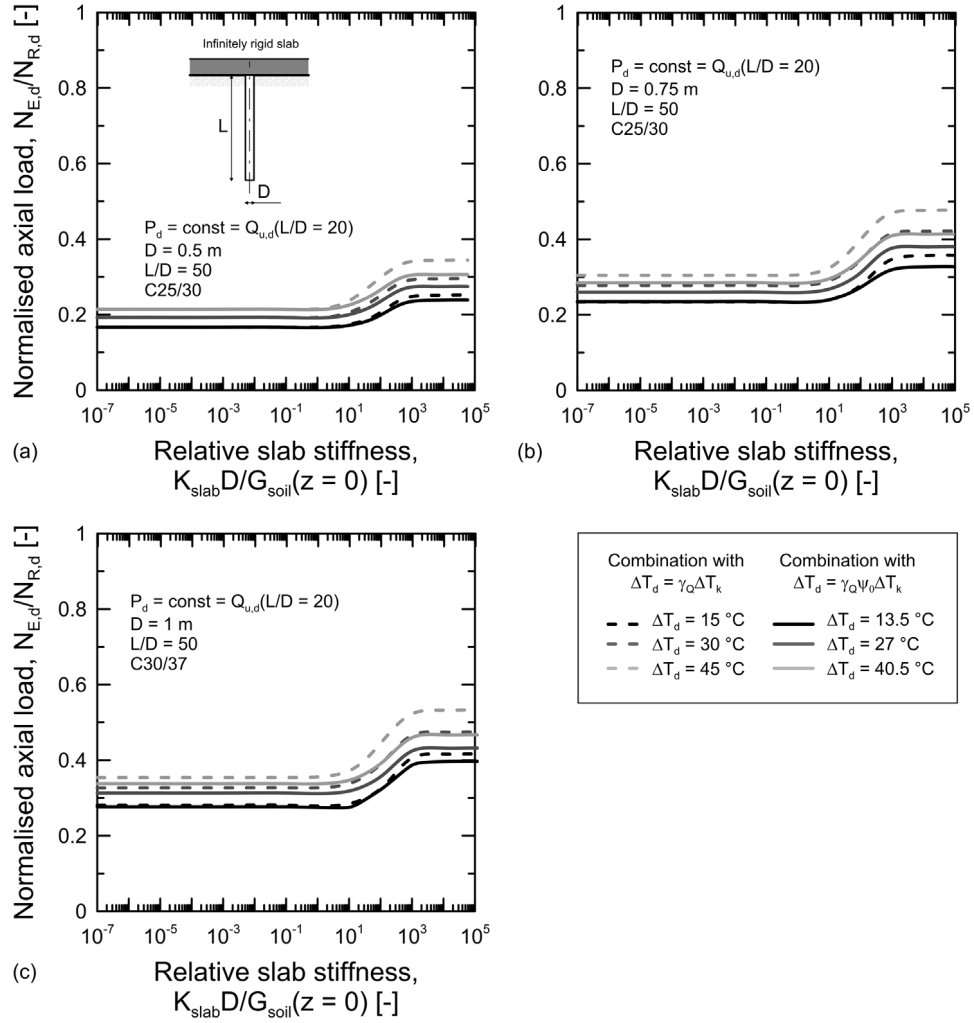


Figure 6.2 – Normalised axial loads for energy piles restrained at their head and subjected to heating, with a constant applied mechanical load and varying pile length.

Energy Pile Cooling

Figure 6.3 presents the normalised axial load $N_{\text{Ed}}^*/N_{\text{Rd}}^*$ characterising the most stressed section of energy piles free to move at their head for varying values of L/D . Piles with $D = 0.5$ m, 0.75 m and 1 m are considered under the combined action of $P_{\text{d}} \equiv Q_{\text{ud}}(L/D = 20)$ and $\Delta T_{\text{d}} = \gamma_{\text{Q}}\Delta T_{\text{k}} = -7.5^\circ$, -15° and -22.5° . The design acting load N_{Ed}^* is generally caused by both mechanical and thermal loads. The design resisting load N_{Rd}^* corresponds to the distance between the actual design load caused by the thermal load (applied after the mechanical load) and the traction resisting load of the reinforced concrete cross-section when no moments are applied.

Cooling thermal loads cause a more pronounced variation of the axial load compared to heating thermal loads. The combined action of mechanical and cooling thermal loads involves variations of N_{Ed}^* that can exceed N_{Rd}^* . In other words, structural ultimate limit states can be exceeded due to mechanical and cooling thermal loads. This situation requires the design of a proper minimum reinforcement based on mechanical considerations.

Figure 6.4 shows the normalised axial load $N_{\text{Ed}}^*/N_{\text{Rd}}^*$ experienced by energy piles restrained at their head for a varying slab stiffness relative to the soil $K_{\text{slab}}D/G_{\text{soil}}(z = 0)$. Piles of $L/D = 50$ with $D = 0.5$ m, 0.75 m and 1 m under the previous mechanical and cooling thermal loads are considered.

For the case of extremely rigid slabs, normalised axial loads of up to $N_{\text{Ed}}^*/N_{\text{Rd}}^* = 2$ can be observed. Therefore, structural ultimate limit states can again be exceeded.

It is noteworthy that relying on the concrete tensile strength is questionable. Therefore, one can safely neglect the concrete tensile strength and design the reinforcement to sustain the entire design traction load.

6.4.3 Energy Pile Response for Varying Mechanical Loads and a Constant Pile Length

Energy Pile Heating

Figure 6.5 presents the normalised axial load $N_{\text{Ed}}/N_{\text{Rd}}$ characterising the most stressed section of energy piles free to move at their head for varying values of $P_{\text{d}}/Q_{\text{ud}}$. Piles of $L/D = 20$ and 50 with $D = 0.5$ m, 0.75 m and 1 m are considered under the combined action of varying values of $P_{\text{d}}/Q_{\text{ud}}$ and $\Delta T_{\text{d}} = \gamma_{\text{Q}}\Delta T_{\text{k}} = 15^\circ$, 30° and 45° or $\Delta T_{\text{d}} = \gamma_{\text{Q}}\psi_{01}\Delta T_{\text{k}} = 13.5^\circ$, 27° and 40.5° , depending on the load combination.

In all cases, no structural ultimate limit states are caused by mechanical and heating

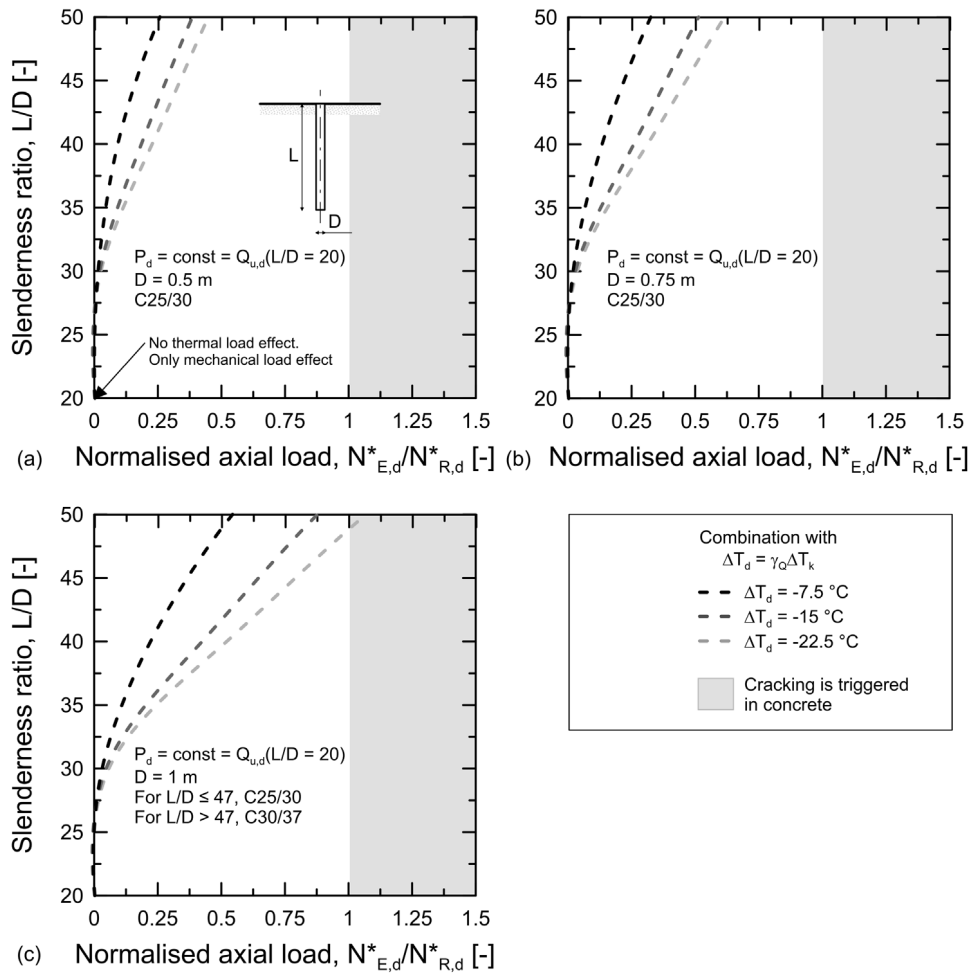


Figure 6.3 – Normalised axial loads for energy piles that are free at their head and subjected to cooling, with a constant applied mechanical load and varying pile length.

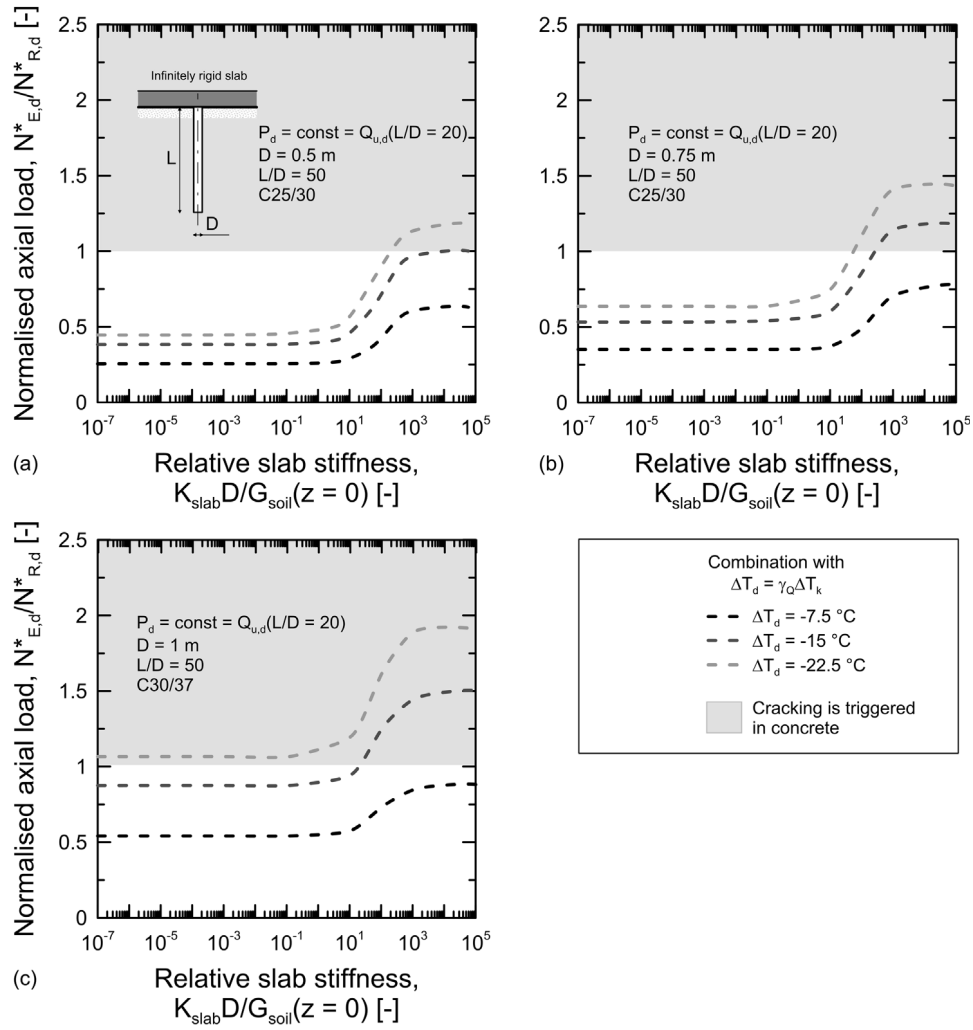


Figure 6.4 – Normalised axial loads for energy piles restrained at their head and subjected to cooling, with a constant applied mechanical load and varying pile length.

thermal loads. Lower design mechanical loads ensure greater safety against the occurrence of a structural ultimate limit state potentially caused by thermal loads. However, there is a greater impact of the design thermal loads on the variation of the axial load within the energy piles.

Figure 6.6 shows the normalised axial load N_{Ed}/N_{Rd} experienced by energy piles restrained at their head for a varying slab stiffness relative to the soil, $K_{slab}D/G_{soil}(z = 0)$. Piles of $L/D = 50$ with $D = 0.5$ m, 0.75 m and 1 m are considered under the previous mechanical and heating thermal loads. The combined action of the mechanical and heating thermal loads does not involve structural ultimate limit states.

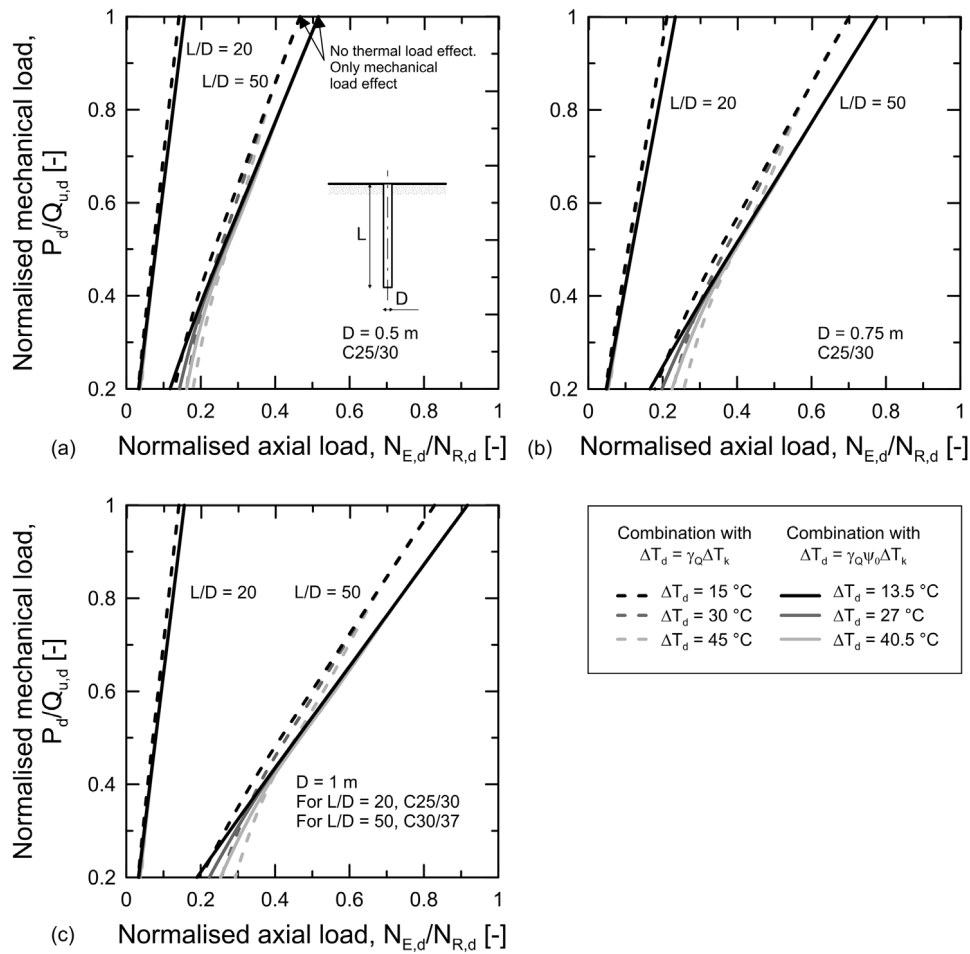


Figure 6.5 – Normalised axial loads for energy piles that are free at their head and subjected to heating, with a varying applied mechanical load and constant pile length.

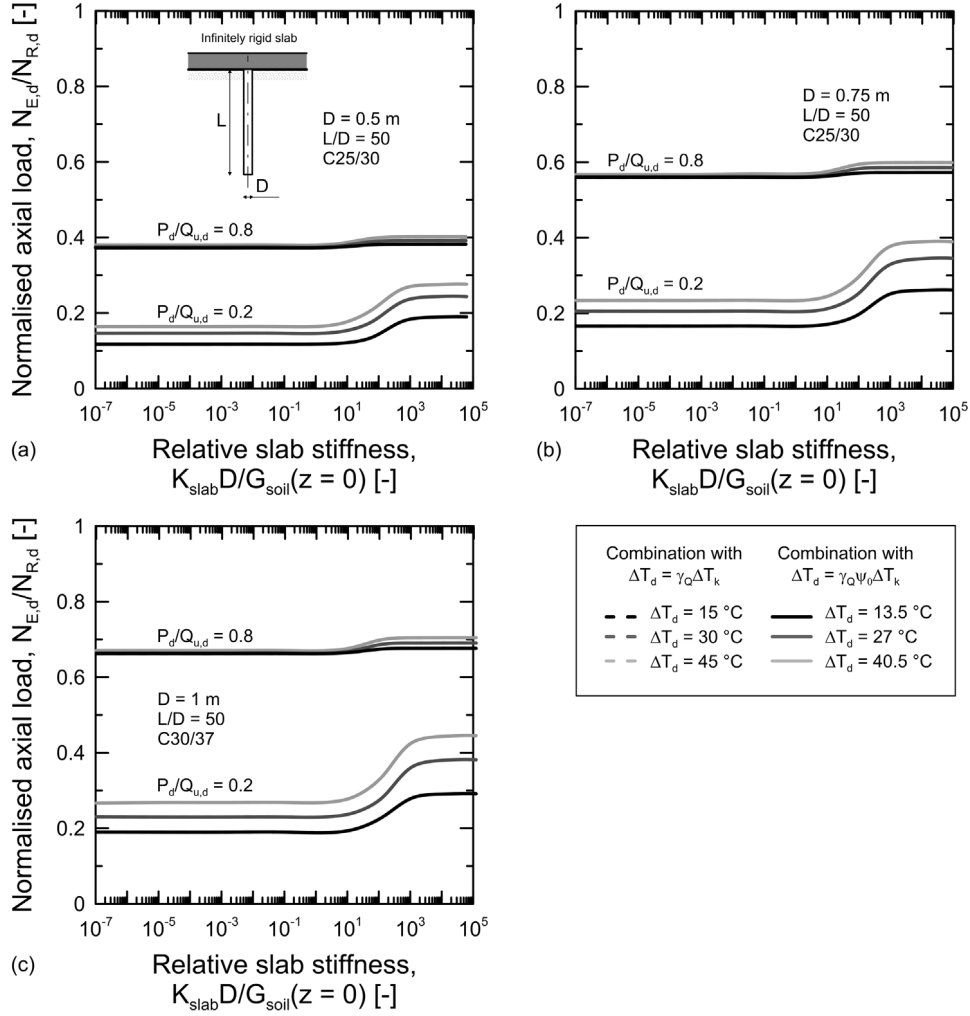


Figure 6.6 – Normalised axial loads for energy piles of $L/D = 50$ that are restrained at their head and subjected to heating, with a varying applied mechanical load and constant pile length.

Energy Pile Cooling

Figure 6.7 presents the normalised axial load, N_{Ed}^*/N_{Rd}^* , characterising the most stressed section of energy piles free to move at their head for varying values of P_d/Q_{ud} . Piles of $L/D = 20$ and 50 with $D = 0.5$ m, 0.75 m and 1 m are considered under the combined action of $P_d \equiv Q_{ud}(L/D = 20)$ and $\Delta T_d = \gamma_Q \Delta T_k = -7.5^\circ$, -15° and -22.5° . Figure 6.8 shows the evolution of N_{Ed}^*/N_{Rd}^* for energy piles restrained at their head for varying $K_{slab}D/G_{soil}(z = 0)$. Piles of $L/D = 50$ with $D = 0.5$ m, 0.75 m and 1 m are considered under the combined action of the previous mechanical and cooling thermal loads.

The effect of mechanical and cooling thermal loads can involve normalised axial loads of up to $N_{Ed}^*/N_{Rd}^* = 2.3$. In other words, structural ultimate limit states can be exceeded due to mechanical and cooling thermal loads.

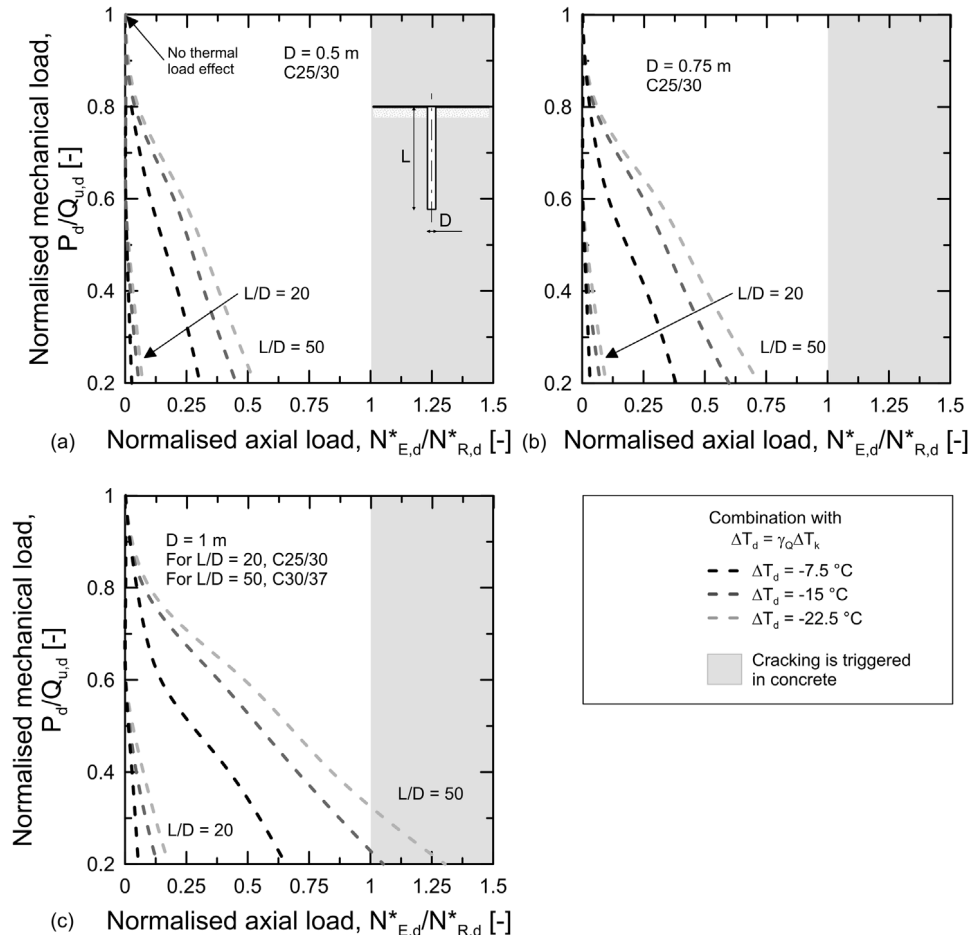


Figure 6.7 – Normalised axial loads for energy piles that are free at their head and subjected to cooling, with a varying applied mechanical load and constant pile length.

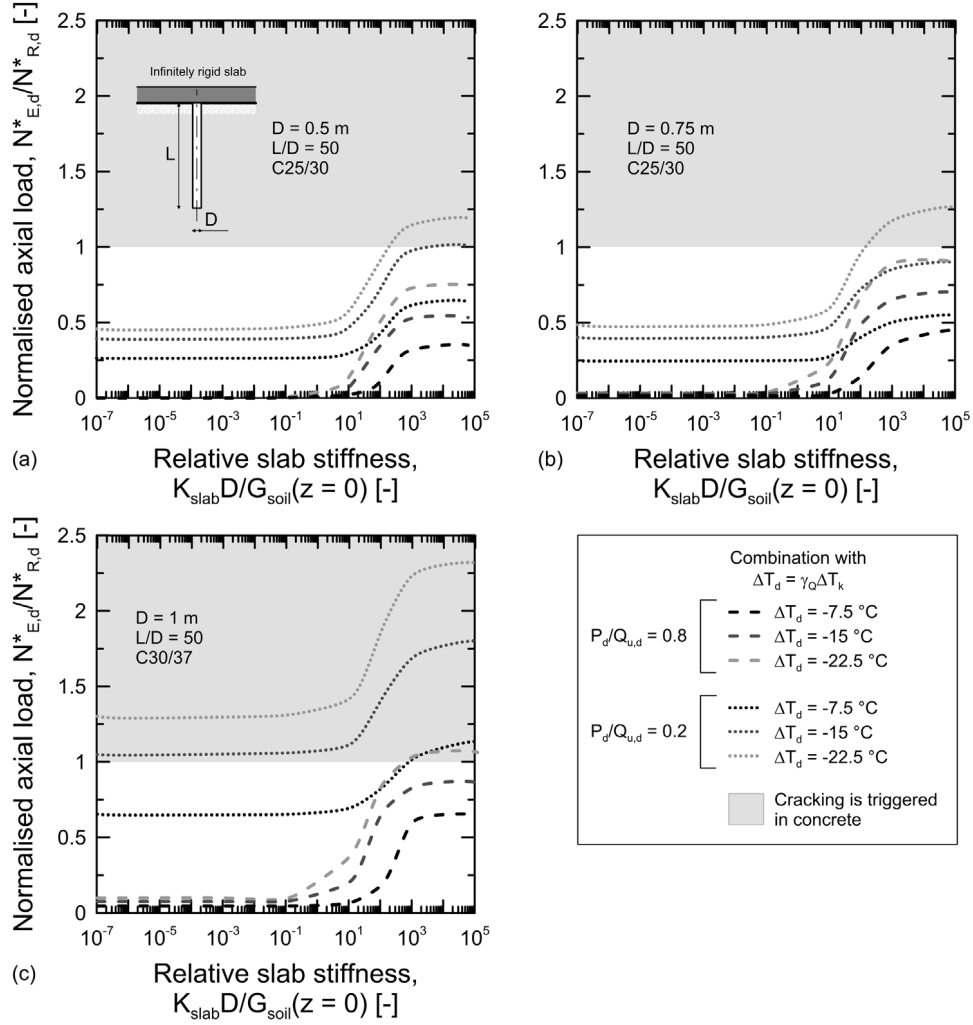


Figure 6.8 – Normalised axial loads for energy piles of $L/D = 50$ that are restrained at their head and subjected to cooling, with a varying applied mechanical load and constant pile length.

6.4.4 Summary

Based on the previous results, heating thermal loads applied in conjunction with mechanical loads are unlikely to overcome the design compressive strength characterising the cross-sections of energy piles; i.e., they are unlikely to exceed structural ultimate limit states. This result is achieved through the consideration of the design approach related to the design compressive strength characterising the cross-sections of energy piles that has been proposed in this work. In contrast, at least in principle, cooling thermal loads applied in conjunction with mechanical loads may overcome the design tensile strength characterising the cross-sections of energy piles; i.e., they may exceed structural ultimate limit states. In practice, the following considerations prove that the above can be avoided if appropriate design rules are adopted.

The actual behaviour of reinforced concrete is non-linear and characterised by the appearance of cracks beyond specific strain levels. If the minimum reinforcement is able to sustain the cracking force, the member does not fail upon the formation of the first crack (brittle behaviour) and the appearance of cracks leads to stress redistribution and a decrease in the stiffness of the structure. The considered stiffness involves lower values of stress compared to those associated with a stiffness related to uncracked cross-sections and linear stress–strain relationships. Therefore, although the Eurocodes [101] state to consider linear stress–strain relationships and uncracked cross-sections in performance-based design, lower stresses can be expected after the strain levels associated with cracking are achieved.

As soon as a due account of the non-linear stress-strain relationship characterising reinforced concrete is made, a ductility oriented design approach becomes essential. The reason for this is that, when a displacement is imposed to a redundant structural member, equilibrium is ensured as far as ductility capacity is sufficient. Therefore, thermally imposed tensile strains can be accommodated by the structure and the induced stress is simply derived from the constitutive model. To ensure an adequate ductility capacity of the reinforced concrete members, (i) the resisting axial force of the cross-sections needs to be greater than the axial force needed to crack them due to potential strain localisation effects, (ii) the reinforcement has to be characterised by a large deformation capacity, and (iii) the ratio f_t/f_y has to respect a lower bound (where f_t and f_y are the tensile strength and yield strength of the reinforcement steel). Condition (i) is achieved by ensuring a minimum reinforcement ratio that can be expressed as

$$\rho_r = \rho_{r,\min} > \frac{f_{ct}}{f_y} \quad (6.3)$$

where f_{ct} and f_y are appropriate values of the tensile strength of concrete and steel yield strength (a conservative value of f_{ct} is the mean value of the axial tensile strength of concrete, f_{ctm}). Condition (ii) is related to the magnitude of the action effects. Condition (iii) is generally met because standards prescribe minimum values of the ratio f_t/f_y .

Once a ductility-oriented design approach is ensured, the key aspect eventually relies on understanding the level of deformation associated with a given load. This final aspect allows considering unsatisfactory verifications, such as those previously encountered, to be satisfactory.

Based on the above, the following aspects can be highlighted for energy piles:

1. The current predictions of the Eurocodes for the minimum reinforcement areas of bored piles do not always satisfy inequality (3). Therefore, the quoted predictions should be avoided, and the proposed formulation for the minimum area of longitudinal reinforcement should be employed for energy piles.
2. The proposed minimum reinforcement area ensures sufficient ductility. Although concrete cracking causes a variation of axial stiffness along the piles that might involve phenomena of strain localisation, the strain caused by thermal loads remains within the cracked development stage for practical temperature variations. This result is qualitatively shown in Figure 6.9 with reference to the relationship between the design traction axial load N_d and the normalised axial displacement $\Delta w/L$ characterising a reinforced concrete energy pile member that has minimum reinforcement. This relationship is compared with that of the same member characterised by the simultaneous occurrence of cracks (i.e., coinciding with the response of a single mean cross-section), as well as with the relationship of the reinforcement steel alone.
3. By comparing the imposed strain levels caused by thermal loads with the deformation capacity of an appropriately designed cross-section, it can be realised that structural ultimate limit states will never be exceeded by the influence of these loads, irrespective of whether strain localisation is developed or not. Cracking may occur in concrete because of the action of cooling thermal loads. However, a sufficient ductility capacity is ensured by the proposed design approach, and structural ultimate limit states cannot occur. Concrete cracking is an ordinary phenomenon that needs to be controlled.

Based on the above, thermal loads cannot involve the structural failure of energy piles; i.e., they cannot exceed structural ultimate limit states. Therefore, the effects of

thermal loads can be neglected in the design of energy piles at ultimate limit states from a structural perspective. This statement agrees with the Eurocodes [101], in which it is specified that “thermal effects should be considered for ultimate limit states only where they are significant (e.g., fatigue conditions and second order effects). In other cases, they need not be considered, provided that the ductility and rotation capacity of the elements are sufficient”.

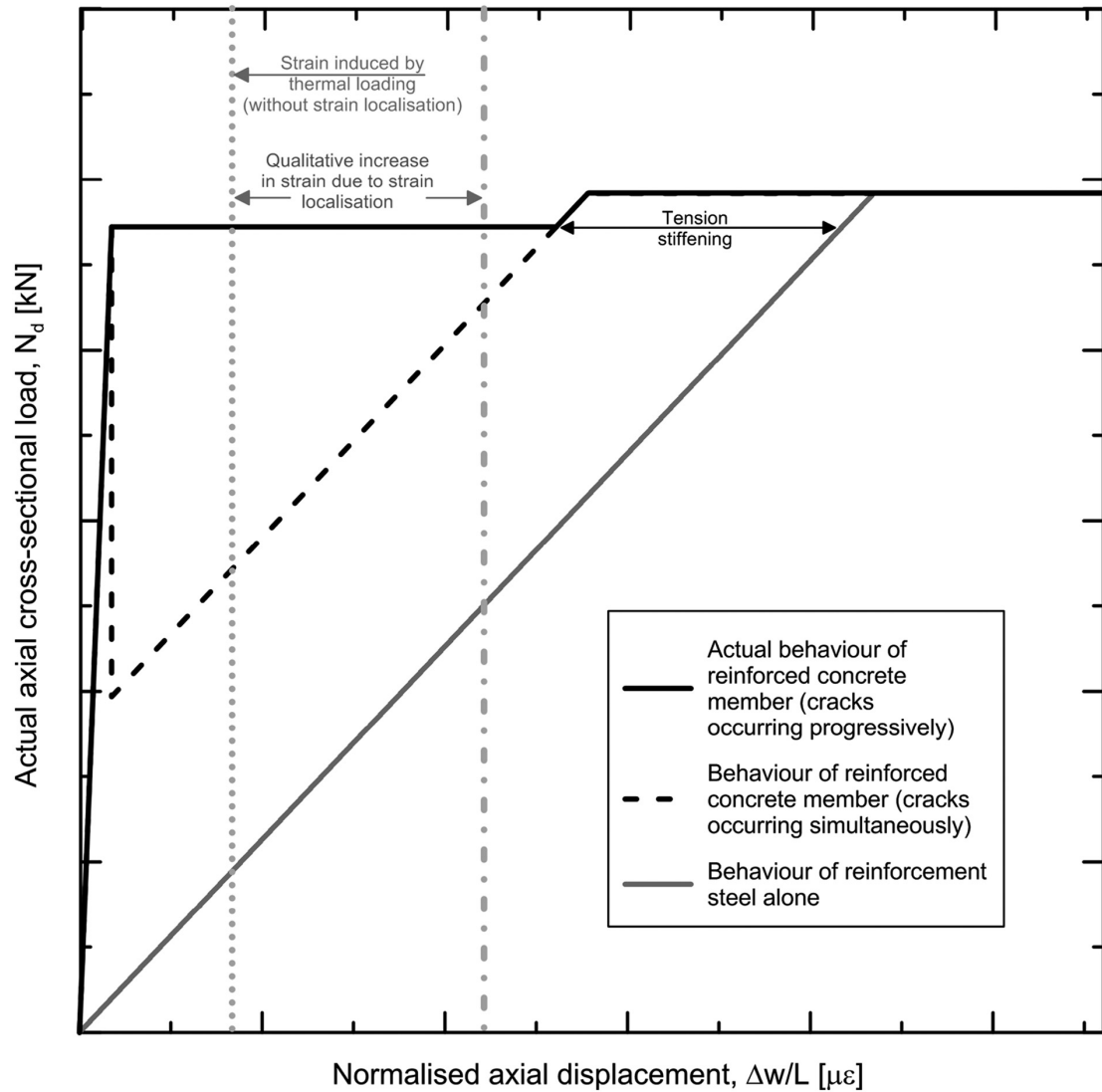


Figure 6.9 – Relationships between axial cross-sectional load and normalised axial displacement for energy piles made of reinforced concrete.

6.5 Concluding Remarks

This paper presents an investigation on the role of thermal loads in the mechanical response of energy piles and the related geotechnical and structural performance-based design, and proposes a performance-based design approach for such foundations. The following conclusions can be drawn from the results of this work:

- Thermal loads involve effects that are unlikely to cause the failure of energy piles and only characterise in a significant way the deformation of such foundations.
- The above holds as long as the design approach proposed for energy piles in this paper is considered. This approach requires the provision of (i) a design compressive strength of the cross-sections of energy piles at least equal to the pile design load capacity and (ii) a minimum longitudinal reinforcement ensuring ductility.
- Accordingly, the effects of thermal loads can be neglected in the performance-based design of energy piles at ultimate limit states, while they should be considered at serviceability limit states.
- At serviceability limit states, the following aspects should be addressed: (i) single and group vertical displacement (e.g., differential and average) limitation; (ii) deflection and angular distortion control; (iii) compressive stress limitation; (iv) tensile stress limitation; and (v) crack control.

Acknowledgements

The willingness of Dr Fleur Loveridge to share monitored temperature data of the full-scale energy piles discussed in this paper is highly appreciated. The financial support N. 160117 (Division I–III) provided by the Swiss National Science Foundation is gratefully acknowledged. The financial support N. 174575 provided by the Swiss National Science Foundation, Switzerland in the context of the COST Action TU1405 is also acknowledged.

Conclusions and Perspectives

This thesis provides a theoretical contribution to the understanding of soil-structure interactions in the field of surface footings and thermoactive deep foundations. It consists of two main parts: (i) the analysis of the bearing capacity of surface footings subjected to centred and vertical load in the framework of the theory of plasticity; (ii) the evaluation of the performance of thermoactive deep foundations considering soil-pile-raft interactions and material non-linearity.

Before this work, a significant amount of research was available to address the bearing capacity of soils loaded by rigid footings, the shear capacity of foundations, and the thermo-mechanical performance of single energy piles and energy pile groups. However, some aspects worthy of further study were identified:

1. Little effort was made to combine the soil mechanics and structural mechanics outcomes on the bearing capacity of surface footings.
2. Little knowledge was present to address the effect of a raft cast directly on the ground on the overall behaviour of thermoactive deep foundations. Therefore, it was not sure whether a unique optimal design strategy could be adopted for both mechanical and thermal loads, and at what extent the outcomes for energy pile groups with a free head or with a rigid cap were meaningful.
3. The structural performance of energy piles was not properly addressed in a displacement based framework, and the ductility capacity of reinforced concrete was not taken into account, leading to inappropriate provisions for the ultimate limit state design of such foundations.

Surface Footings

In an attempt to consistently catalogue the large amount of available research on the bearing capacity of soils, a comprehensive review of the limit analysis theorems was

carried out in chapter 1. Attention was given to the assumption of perfect plasticity, and to the extended limit theorems for non-associated materials and frictional interfaces. The relevance of such theorems for real soils and structures was also discussed.

Most of the available knowledge on the bearing capacity of surface footings subjected to centred vertical load was summarised in chapter 2 and critically judged within the framework of the limit analysis. Interface roughness, three-dimensional conditions, and comparison with experimental results were carefully considered. In addition, two new analytical expressions for the bearing capacity of perfectly rough surface strip footings resting on a general Mohr-Coulomb material were derived.

In the third chapter, corresponding to a journal article submitted for a special issue of *Computers and Geotechnics*, an attempt was made to provide insights on the relevance of soil-structure interactions on the collapse load of surface footings. A simplified procedure for the estimation of such effects was proposed and new upper and lower bound solutions were established for the combined failure of footings with a very slender cross-section.

The main conclusions for the first part are:

- Owing to the path dependency of common yield criteria employed in soil mechanics limit analysis, the definition of the strength parameters might be dependent on the application under investigation.
- Extended limit theorems and translational failure mechanisms can be conveniently used to assess the collapse load of soil-structure interacting systems.
- Theoretical and experimental results support the hypothesis that in practice footings can be taken as perfectly rough.
- Theoretically estimated and experimentally measured bearing capacities are in good agreement both for undrained soils and Tresca yield criterion, and drained soils and Mohr-Coulomb yield criterion when shear strength parameters are estimated based on realistic loading paths and strain conditions at the instant of collapse. Theoretical shape factors derived from the Tresca load function seem suitable. By contrast, theoretical shape factors based on the Mohr-Coulomb criterion that do not account properly for all the physical processes such as the flow rule and the strain conditions in the measure of ϕ , may lead to over-estimated bearing capacities.
- The classification of surface footings by means of the Kani's diagram highlighted that the effect of soil-structure interaction increases with increasing footing cross-section slenderness.

- The evaluation of footings collapse load assuming a uniform contact pressure distribution, regardless of the soil properties, is only justified for deep beams. Generally, such a hypothesis leads to a conservative structural design.
- Previous studies agree on the fact that the contact pressure distribution at the instant of general shear failure is closely approximated by one of the following simple shapes: rectangular, triangular, ellipsoidal, and trapezoidal. This can be conveniently exploited to take into account soil-structure interaction in a simplified yet rational manner.

Thermoactive Deep Foundations

The fourth chapter, corresponding to the published journal paper [114], presented an extensive three-dimensional thermo-elastic parametric analysis of piled rafts with energy piles. The investigated variables included normalised raft thickness (and thus indirectly raft bending stiffness), normalised piles axial stiffness, soil-to-pile thermal expansion coefficient ratio, piles spacing ratio, piles slenderness, piles bearing mode, normalised thermally induced piles axial stress, and normalised thermally induced average and differential raft displacements.

Chapter 5, corresponding to the published journal paper [113], presented an analysis of thermally induced stresses and strains in energy piles. The first part focused on the derivation of simple mathematical expressions for the computation of axial thermal stresses in conditions other than the free or clamped bar. A few closed form expressions that account for head and base partial restraint, and interactions through a rigid cap were presented. The second part was dedicated to the assessment of the reinforced concrete post-cracking behaviour on the performance of thermoactive piles subjected to traction forces. For this purpose, a finite element code that is within the framework of the load-transfer approach and which includes the tension-chord model for structural concrete was developed. An extension of the tension-chord model for members subjected to uniformly distributed axial load, that was not published in the journal paper, was added as appendix to this chapter.

Finally, the sixth chapter, corresponding to the published journal article [316], presented an investigation on the role of thermal loads in the mechanical response of energy piles and the related geotechnical and structural performance-based design, and proposed a performance-based design approach for such foundations.

The main conclusions are listed below:

- The ratio between raft mean displacement and equivalent isolated free-standing pile displacement R , due to piles thermal activation, is a convenient parameter to estimate the global effect of all interactions. The results showed that it can be assumed constant with respect to the bending stiffness of the raft. The value of R is mainly governed by the number of piles n_p , pile-soil relative stiffness K and soil-to-pile thermal expansion coefficient ratio X , whereas the pile resisting mode, i.e. floating or end-bearing, is of slightly less concern. It was shown that R can be lower than one in configurations with a few piles. Here R might be roughly bounded between 0.5 and 3.
- Thermally induced differential displacements are strongly related to K and the raft bending stiffness. The value of X enhances differential displacements in stiff soils. The results highlighted that for $E_c = 30 \text{ GPa}$ and $t_r/d = 4$, differential displacements are negligible.
- The level of stress within energy piles in piled raft foundations was investigated through the normalised thermally induced axial stress ς . It was shown that ς_{\max} is mainly affected by K , and at a less extent by the pile configuration n_p and slenderness L/D . The influence of pile position is analogous to conventional foundations, where corner and central piles are the most and less loaded, respectively. From these results, values of ς_{\max} close to one might be expected for compact foundations with slender piles in stiff soils, which might result in concrete cracking under active cooling.
- An important outcome of this research is the analogy between conventional piled rafts subjected to vertical load and piled rafts with energy piles. This suggests that an overall good performance of the foundation can be achieved through a unique design strategy.
- Reinforced concrete post-cracking behaviour can significantly impact the response of energy piles, which could be comparable to the effect soil-pile interface behaviour.
- It was observed that the magnitude of the imposed tensile thermal strain can be higher than $|\alpha\Delta T|$. Nevertheless, if the ductile behaviour of the structural member is ensured, such strains are accommodated by the pile. However, thermal loads may have an impact if variable axial loads, bending moments or transverse forces are expected. Moreover, the serviceability limit state may require additional considerations owing to the cracks opening.

- Thermal loads involve effects that are unlikely to cause the geotechnical or structural failure of energy piles and only characterise in a moderate way the deformation of such foundations. This holds as long as the proposed approach is considered, which requires the provision of (i) a design compressive strength of the cross-section of energy piles at least equal to the geotechnical pile design load capacity, and (ii) a minimum longitudinal reinforcement ensuring ductility.
- Accordingly, the effects of thermal loads can be neglected in the performance-based design of energy piles at ultimate limit states, whereas they should be considered at serviceability limit states.
- At serviceability limit states, the following aspects should be addressed: (i) single and group vertical displacement (e.g. differential and average) limitation; (ii) deflection and angular distortion control; (iii) compressive stress limitation; and (iv) tensile stress limitation (crack control).

Perspectives

This doctoral thesis aimed at providing some insights in the soil-structure interaction analysis of foundations through a theoretical approach. This purpose was motivated by the belief that the large amount of available knowledge coming from soil and structural mechanics is suffering from a lack of integration within a unified framework. For this reason, the considerable advances achieved in the last decades in these two fields seem hard to implement in applied soil mechanics. Some possible ideas for future research are listed hereafter:

- Theoretical work
 - Advanced constitutive and mechanical models are available for both the soil and the structural element behaviour. Their coupling constitutes an opportunity to better understand the complex interaction mechanisms between the soil and the structure, both under working and collapse conditions. Refined finite elements models would enable a better understanding of the influence of strain conditions and other phenomena on these failures.
 - The use of finite elements in the limit analysis offers an unprecedented capability of bracketing the theoretical collapse load of a number of interesting

problems. Their use allows a simpler and more general investigation of potential failure mechanisms and the consideration of particular conditions, such as tension cut-off and non-linear yield criteria.

- Simplified procedures and code-like formulations would facilitate the tech-transfer between academia and practice.
- Experimental work
 - Laboratory testing on structural members are usually performed at real scale, whereas this is not the case for soils. Failure mechanisms in soil masses are often investigated at reduced scale, e.g. centrifuge tests, or by replacing the soil with another material, e.g. Schneebeli cylinders. This introduces a number of differences between the real and the tested materials and makes very hard to study combined failure mechanisms. This is especially the case if structural failure is characterised by size effects, such as the shear failure of slender concrete members without shear reinforcement. The knowledge of soil-structure interacting systems at failure would benefit from tests executed at real scale.
 - Additional experimental programs with detailed measurements that account for soil-structure interaction are needed to better understand the actual behaviour and to validate theoretical results. Newly available measuring techniques could play a fundamental role in the definition of the actual kinematics of the failure mechanisms. In this regard, the use of optical fibres and digital image correlation would allow to obtain valuable informations concerning the development of the structural and soil collapse.
 - Equip the reinforcement of energy piles with optical fibres would enable to estimate the actual crack development and the steel strain. This would allow to validate the theory of thermoactive piles presented in this research.



Hill Type Failure for a General Mohr-Coulomb Material

The Hill type failure mechanism adopted by Chen [49] is shown in Figure A.1. The bearing capacity factor N_c he obtained for smooth footings writes as in equation (A.1). For the same rupture figure and rough interfaces, this coefficient is simply multiplied by an amplification factor, which does not modify the subsequent considerations because it approaches 1 as ϕ goes to 0 ($\delta \leq \phi$ and it was also shown previously that the bearing capacity of a strip footing on a Tresca material is not affected by interface friction).

$$\begin{aligned}
 N_c = & \frac{\sin \xi \cos \phi + \sin \zeta |\cos(\xi - \zeta - \phi)|}{\sin(\zeta + \xi) \sin(\zeta - \phi)} \\
 & + \frac{\alpha \sin \zeta (e^{2(\pi - \eta - \xi) \tan \phi} - 1)}{\sin(\zeta + \xi) \sin \phi \sin(\zeta - \phi)} \\
 & + \frac{\alpha \sin \zeta \sin \eta e^{2(\pi - \eta - \xi) \tan \phi}}{\cos(\eta + \phi) \sin(\zeta + \xi) \sin(\zeta - \phi)}
 \end{aligned} \tag{A.1}$$

where

$$\alpha = \begin{cases} \sin(\zeta + \xi - 2\phi) & \text{if } \zeta + \xi - \frac{\pi}{2} - \phi > 0 \\ \sin(\zeta + \xi) & \text{otherwise} \end{cases} \quad (\text{A.2})$$

Knowing that the optimum angles for $\lim_{\phi \rightarrow 0^+} N_c$ are $\zeta_{\text{opt}} = \xi_{\text{opt}} = \eta_{\text{opt}} = \pi/4$, one may substitute these values in (A.1) and compute the limit:

$$\begin{aligned} \lim_{\phi \rightarrow 0^+} \left(\frac{2 \sin(\frac{\pi}{4})}{\sin(\frac{\pi}{2}) \sin(\frac{\pi}{4} - \phi)} + \frac{\sin(\frac{\pi}{4})(e^{\pi \tan \phi} - 1)}{\sin \phi \sin(\frac{\pi}{4} - \phi)} + \frac{2 \sin(\frac{\pi}{4})e^{\pi \tan \phi}}{\cos(\frac{\pi}{4} + \phi) \sin(\frac{\pi}{4} - \phi)} \right) \\ = 2 + \pi + 2\sqrt{2} \end{aligned} \quad (\text{A.3})$$

The solution of (A.3) is clearly not the one expected. The incorrectness of (A.1) may also be proved by computing the optimum angles for $\phi \rightarrow 0$. In this case it is found that such values are not equal to $\pi/4$, other than $N_c \neq 2 + \pi$, which is not possible.

Chen showed that the optimum angles satisfy

$$\begin{aligned} \eta_{\text{opt}} &= \frac{\pi}{4} - \frac{\phi}{2} \\ \zeta_{\text{opt}} &= \frac{\pi}{2} + \phi - \xi_{\text{opt}} \end{aligned} \quad (\text{A.4})$$

Therefore, the optimal geometry of the failure mechanism implies that $\pi/2 - \xi = \zeta - \phi$, which means that $v_0 = v_1$ (cf. Figure A.1), and therefore the relative velocity v_{01} between the wedge abc and the log-spiral sector bcd is 0. Energy dissipation occurs along failure lines ac , cd , de (and eventually the interface ab), and within the radial shear region bcd . Considering only half of the mechanism due to symmetry:

$$\begin{aligned} \dot{D}_{c, ac} &= cv_1 \frac{B}{2} \sin \xi \\ \dot{D}_{c, de} &= cv_1 e^{2\theta \tan \phi} \frac{B}{2} \sin \zeta \\ \dot{D}_{c, cd} + \dot{D}_{c, bcd} &= 2\dot{D}_{c, cd} = cv_1 \frac{B \sin \zeta}{2 \sin \phi} (e^{2\theta \tan \phi} - 1) \end{aligned} \quad (\text{A.5})$$

where $\theta = \pi - \xi - \eta = 3\pi/4 - \phi/2 - \xi$ is the angle of the logarithmic spiral sector. The total dissipation is

$$\dot{D}_c = cv_1 \frac{B}{2} \left[\sin \xi + \sin \zeta \left(e^{2\theta \tan \phi} + \frac{e^{2\theta \tan \phi} - 1}{\sin \phi} \right) \right] \quad (\text{A.6})$$

The external power due to footing pressure is given by

$$P_p = p_f \frac{B}{2} v_1 \sin(\zeta - \phi) \quad (\text{A.7})$$

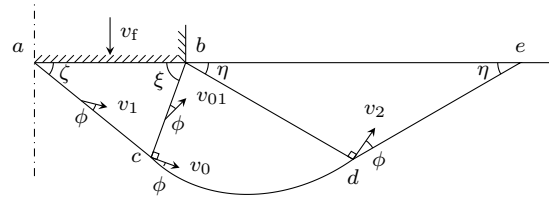
Finally, the bearing capacity factor writes

$$N_c = \frac{2}{c B v_1 \sin(\zeta - \phi)} \dot{D}_c = \frac{\sin \xi}{\sin(\zeta - \phi)} + \frac{\sin \zeta}{\sin(\zeta - \phi)} \left(e^{2\theta \tan \phi} + \frac{e^{2\theta \tan \phi} - 1}{\sin \phi} \right) \quad (\text{A.8})$$

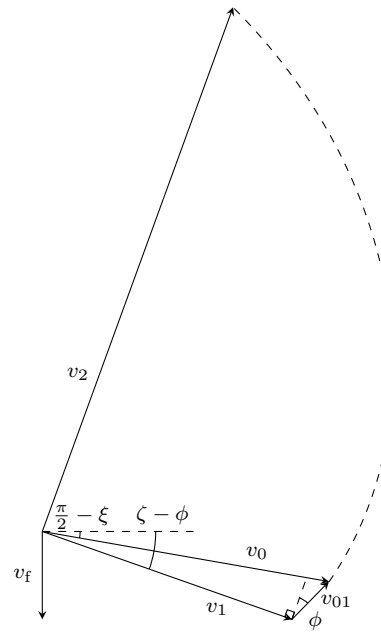
Once again, one may substitute the known optimum values and compute the limit to show that (A.8) is correct

$$\lim_{\phi \rightarrow 0^+} N_c \Big|_{\zeta = \xi = \pi/4} = 1 + 1(1 + \pi) = 2 + \pi \quad (\text{A.9})$$

A numerical optimisation performed with the simplex algorithm available in Python [392] and imposing $\phi = 0.001$, showed that $2 + \pi$ is actually a global minimum for (A.8) over the domain $0 < \zeta, \xi < \pi/2$, and that $\zeta_{\text{opt}} = \xi_{\text{opt}} = \pi/4$.



(a) Half of the Hill type failure mechanism.



(b) Odograph.

Figure A.1 – Kinematics of the Hill type failure mechanism.



Shield and Drucker Failure Considering Adhesion

The geometry of the Hill type failure mechanism developed by Shield and Drucker [348] for rectangular footings on a (isotropic homogeneous associated perfectly plastic) Tresca material is shown in Figure B.1. The kinematics is defined by regions of plane strain motion.

The contributions to the internal energy dissipation are additive, thus the rate of energy dissipated at the interface by adherence \dot{D}_a can be added to the solution for smooth footings. By introducing the normalised adhesion as a fraction of the apparent cohesion $\beta = a/c$, \dot{D}_a writes

$$\begin{aligned}\dot{D}_a &= cv\beta(S_{\text{xmp}} \cot \theta_1 + S_{\text{cbmp}} \cot \theta_2) \\ &= cv\beta\left(\frac{1}{2}\frac{B}{2}d \cot \theta_1 + \frac{1}{2}\left[\frac{L}{2} + \left(\frac{L}{2} - d\right)\right]\frac{B}{2} \cot \theta_2\right)\end{aligned}\tag{B.1}$$

where S stands for surface area. Considering the double symmetry, the principle of virtual velocities implies

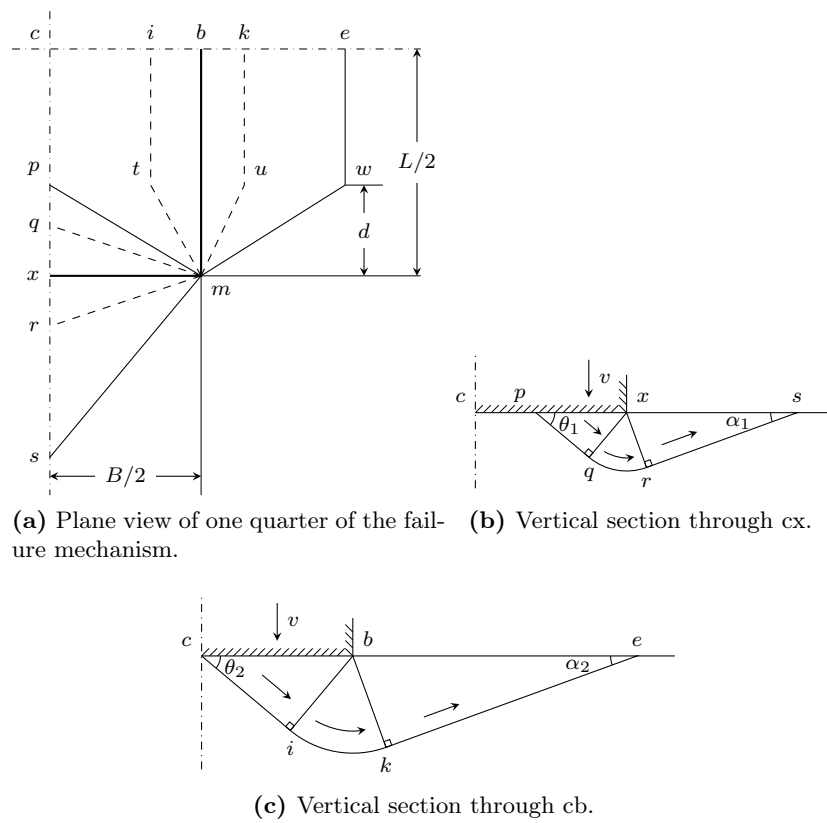
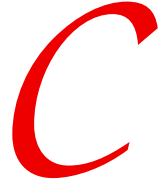


Figure B.1 – Geometry and velocity field of the failure mechanism.

$$\begin{aligned}
N'_c &= N'_{c,\text{smooth}} + \frac{4\dot{D}_a}{cvBL} \\
&= 2(\alpha_2 + \theta_2) + \cot \alpha_2 + \cot \theta_2(1 + \beta) \\
&\quad + \xi \frac{B}{L} \left(\sqrt{1 + 4\xi^2 \sin^2 \theta_1} (\alpha_1 + \theta_1 + \cot \alpha_1 + \cot \theta_1) \right. \\
&\quad \left. + \sqrt{1 + \frac{\sin^2 \theta_2}{4\xi^2}} (\alpha_2 + \theta_2 + \cot \alpha_2 + \cot \theta_2) \right. \\
&\quad \left. + \alpha_1 + \theta_1 - 3(\alpha_2 + \theta_2) - 2(\cot \alpha_2 + \cot \theta_2) + \beta(\cot \theta_1 - \cot \theta_2) \right)
\end{aligned} \tag{B.2}$$

with $\xi = d/B$. The minimum value of N'_c is found by optimisation of the parameters α_1 , θ_1 , α_2 , θ_2 and ξ for given values of β and B/L .



3D Combined Failure for a Tresca Material

The external power resulting from the applied load, the rate of internal energy dissipation due to the plastic hinge, the interface adherence, and the lateral cylindrical surfaces are simply obtained by multiplying the expressions for the plane strain problem [281] times the footing length L . The expression of interface dissipation is based on the assumption, verified a posteriori, that $\min\{r \cos \theta_0; B/2\} = r \cos \theta_0$.

The rate of energy dissipation within the soil due to plastic shearing at the end faces is given by the following expression (cf. Figure 3.13):

$$D_{c2} = 4 \int_{\theta=0}^{\theta=\pi-2\theta_0} \int_{\xi=l}^{\xi=r} dD_{c2} \quad (C.1)$$

where $l = r \sin \theta_0 / \sin(\theta_0 + \theta)$ (thick black line in Figure 3.13) and $dD_{c2} = cvdA = c\omega\xi^2 d\xi d\theta$ with dA denoting the differential of the lateral end surface area (dark grey rectangle in Figure 3.13). Dissipation D_{c2} is expressed as follows:

$$D_{c2} = \frac{4}{3} c\omega r^3 \left(\pi - 2\theta_0 - \sin^3 \theta_0 \int_{\theta=0}^{\theta=\pi-2\theta_0} \sin^{-3}(\theta_0 + \theta) d\theta \right) \quad (C.2)$$

introducing $M_R = \mu c B^2$, $r = \zeta_0 B / \cos \theta_0$, and knowing that the following expression is fulfilled

$$\int_{\theta=0}^{\theta=\pi-2\theta_0} \sin^{-3}(\theta_0 + \theta) \, d\theta = \frac{1}{4} \left[\sin^{-2}(\theta_0/2) - \cos^{-2}(\theta_0/2) \right] + \ln \frac{\cos(\theta_0/2)}{\sin \theta_0/2} \quad (\text{C.3})$$

the objective function (3.26) is obtained.



3D Combined Failure for a Cohesionless Mohr-Coulomb Material

As in the case of a Tresca soil, the solution is obtained by multiplying the expressions for the plane strain problem [281] times L , and by adding the contribution of the end regions. For a cohesionless Mohr-Coulomb material, the latter participates in the external power of the gravity field P_γ . Considering only one quarter of the failure mechanism, the exercise consists in computing the rate of work done by the gravity force in the region $z \geq L/2$ (cf. Figure 3.15). Considering the bounds of the integration variables:

$$\begin{aligned}\theta_0 &\leq \theta \leq \theta_h \\ l(\theta) &\leq \xi \leq r(\theta) \\ 0 &\leq \chi \leq z(\xi, \theta)\end{aligned}\tag{D.1}$$

where

$$\begin{aligned}l(\theta) &= r_0 \sin \theta_0 / \sin \theta \\ r(\theta) &= r_0 e^{(\theta - \theta_0) \tan \phi} \\ z(\xi, \theta) &= \xi \sinh[(\theta - \theta_0) \tan \phi]\end{aligned}\tag{D.2}$$

P_γ is expressed as follows:

$$\begin{aligned} \frac{P_\gamma}{4} &= \int_{\theta=\theta_0}^{\theta=\theta_h} \int_{\xi=l}^{\xi=r} \int_{\chi=0}^{\chi=z} dP_\gamma \\ &= \frac{1}{4} \omega \gamma r_0^4 \int_{\theta_0}^{\theta_h} \left(e^{4(\theta-\theta_0) \tan \phi} - \frac{\sin^4 \theta_0}{\sin^4 \theta} \right) \sinh[(\theta - \theta_0) \tan \phi] \cos \theta d\theta \end{aligned} \quad (\text{D.3})$$

where the differential of the rate of gravitational work is $dP_\gamma = \gamma \omega \xi^2 \cos \theta d\chi d\xi d\theta$. Finally, the objective function (3.28) is obtained by considering that $r_0 = \zeta_0 B / \cos \theta_0$ and $M_R = \eta \gamma B^3$.



3D Combined Failure for a General Mohr-Coulomb Material

The upper bound solution for the combined three-dimensional failure mechanism and a general Mohr-Coulomb soil is obtained from the plane strain solution [111] and the three-dimensional solution for the cohesionless soil (Appendix D). The former is extended over the entire footing length, the formulation of the gravitational power for the end regions of the latter remains the same, and the contribution of the apparent cohesion to the internal energy dissipation D_c on the end faces is added.

Given that velocity vectors make an angle ϕ with the discontinuity surface, the differential of energy dissipation is $dD_c = c\omega r \cos \phi dA$, where the differential of surface area in cylindrical coordinates is expressed as follows:

$$\begin{aligned}
dA &= \sqrt{1 + \left(\frac{\partial z}{\partial \xi}\right)^2 + \frac{1}{\xi^2} \left(\frac{\partial z}{\partial \theta}\right)^2} \xi d\xi d\theta \\
\frac{\partial z}{\partial \xi} &= \sinh[(\theta - \theta_0) \tan \phi] \\
\frac{\partial z}{\partial \theta} &= \xi \cosh[(\theta - \theta_0) \tan \phi] \tan \phi
\end{aligned} \tag{E.1}$$

Considering the integration variables θ and ξ as in equation (D.1), the contribution of the cohesion is given by the following expression:

$$\begin{aligned}
\frac{D_c}{4} &= c\omega \cos \phi \int_{\theta=\theta_0}^{\theta=\theta_h} \int_{\xi=l}^{\xi=r} \sqrt{\cosh^2[(\theta - \theta_0) \tan \phi] (1 + \tan^2 \phi)} \xi^2 d\xi d\theta \\
&= c\omega \frac{r_0^3}{3} \int_{\theta=\theta_0}^{\theta=\theta_h} \left(e^{3(\theta-\theta_0) \tan \phi} - \frac{\sin^3 \theta_0}{\sin^3 \theta} \right) \cosh[(\theta - \theta_0) \tan \phi] d\theta
\end{aligned} \tag{E.2}$$

Finally, by applying the principle of virtual velocities, rearranging the terms, and considering that $r_0 = \zeta_0 B / \cos \theta_0$, $M_R = \mu c B^2$, and $G = 0.5 \gamma B / c$, equation (3.31) is recovered.



Tension-Chord Model for Structural Concrete Subjected to Distributed Axial Load

A modified tension-chord model is proposed for reinforced concrete members in the stabilised crack stage and subjected to uniformly distributed axial load q (Figure F.1). The assumptions of the original tension-chord model remain unchanged, but here it is assumed that the steel is in the elastic domain. The extension into the plastic range is straightforward.

The axial force profile N is linear owing to the constant axial load q . Following the sign convention defined in Figure F.1, the difference in axial load between two cracks spaced by s_{rm} is $\Delta N = -qs_{rm}$. Contrary to the original model, the reverse of bond stress does not happen at mid-distance between the two cracks. The position of this section, necessary for the computation of the mean steel strain ε_s , can be obtained by expressing the equilibrium at this location:

$$\sigma_{sr}A_s - \tau_{b0}\phi\pi l^* = (\sigma_{sr} + \Delta\sigma_{sr})A_s - \tau_{b0}\phi\pi(s_{rm} - l^*) \quad (F.1)$$

Considering that $\Delta\sigma_{sr} = \Delta N/A_s$, one obtains

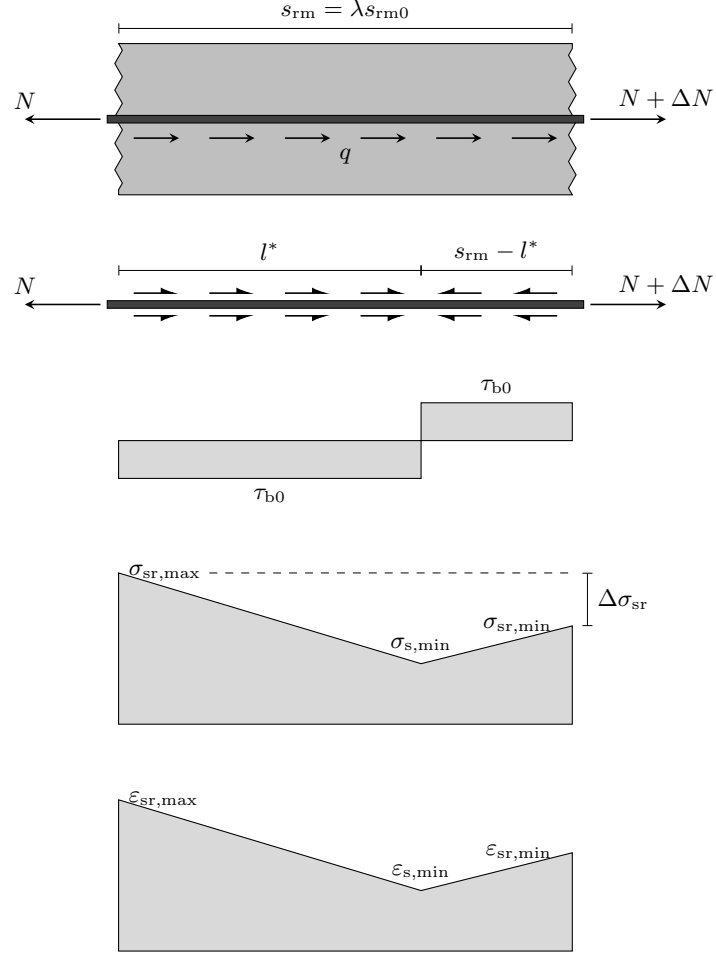


Figure F.1 – Simple chord element subjected to uniform axial load distribution, bond stress, steel axial stress, and steel axial strain distributions.

$$l^* = \frac{\lambda s_{rm0}}{2} \left(1 + \frac{q}{\tau_{b0} \phi \pi} \right) \quad (F.2)$$

The chord element elongation is given by

$$\begin{aligned}
\Delta l &= \int_{-l^*}^{s_{\text{rm}}-l^*} \varepsilon_s(x) \, dx \\
&= (\varepsilon_{\text{sr,max}} + \varepsilon_{\text{s,min}}) \frac{l^*}{2} + (\varepsilon_{\text{s,min}} + \varepsilon_{\text{sr,min}}) \frac{s_{\text{rm}} - l^*}{2} \\
&= \frac{\Delta \sigma_{\text{sr}}}{2E_s} l^* + \left(\sigma_{\text{sr,max}} - \Delta \sigma_{\text{sr}} + \sigma_{\text{sr,max}} - \frac{4\tau_{\text{b0}} l^*}{\phi} \right) \frac{s_{\text{rm}}}{2E_s} \\
&= \frac{\sigma_{\text{sr,max}}}{E_s} s_{\text{rm}} - \frac{2\tau_{\text{b0}}}{\phi E_s} l^* s_{\text{rm}} - \frac{\Delta \sigma_{\text{sr}}}{2E_s} (s_{\text{rm}} - l^*)
\end{aligned} \tag{F.3}$$

Finally, the mean steel axial strain writes

$$\varepsilon_{\text{sm}} = \frac{\Delta l}{s_{\text{rm}}} = \frac{\sigma_{\text{sr,max}}}{E_s} - \underbrace{\left[\frac{2\tau_{\text{b0}}}{\phi E_s} l^* + \frac{\Delta \sigma_{\text{sr}}}{2E_s} \left(1 - \frac{l^*}{s_{\text{rm}}} \right) \right]}_{\Delta \varepsilon_s} \tag{F.4}$$

Introducing (F.2) into (F.4), and assuming $\tau_{\text{b0}} = 2f_{\text{ct}}$, the following expression is obtained

$$\Delta \varepsilon_s = \underbrace{\frac{\lambda(1-\rho)f_{\text{ct}}}{2\rho E_s}}_{\Delta \varepsilon_{\text{TS}}} + \underbrace{\frac{\lambda(1-\rho)q}{2\rho\phi\pi E_s} \left(1 - \frac{q}{4f_{\text{ct}}\phi\pi} \right)}_{\Delta \varepsilon_{\text{q}}} \tag{F.5}$$

It is noteworthy that expression (F.5) is not obtained if the original tension-chord model and a variable axial load are considered. Indeed, the chord element elongation would be

$$\begin{aligned}
\Delta l &= \int_{-s_{\text{rm}}/2}^{s_{\text{rm}}/2} \varepsilon_s(x) \, dx \\
&= \int_{-s_{\text{rm}}/2}^{s_{\text{rm}}/2} \left(\frac{N(x)}{E_s A_s} - \Delta \varepsilon_{\text{TS}} \right) \, dx \\
&= \frac{s_{\text{rm}}}{2E_s} (2\sigma_{\text{sr,max}} - \Delta \sigma_{\text{sr}}) - \Delta \varepsilon_{\text{TS}} s_{\text{rm}}
\end{aligned} \tag{F.6}$$

and the mean steel strain

$$\varepsilon_{\text{sm}} = \frac{\sigma_{\text{sr,max}}}{E_s} - \Delta \varepsilon_{\text{TS}} - \frac{\lambda(1-\rho)q}{2\rho\phi\pi E_s} \tag{F.7}$$

By comparing equation (F.7) to equations (F.4) and (F.5), it can be seen that the original tension-chord model yields a stiffer response, i.e. a smaller mean steel axial strain owing to a higher value of $\Delta\varepsilon_q$. The reason for this is that in the original model the mean steel strain ε_s was not expressed for a differential length dx , but for the finite length s_{rm} . This implies that the integral form in the second equality of equation (F.6) is not correct, because the integrand is not a local quantity.

List of Symbols

Chapter 1

$[S]$	Discontinuity surface
$[v]_i$	Velocity jump vector
α	Material parameter of the Drcuker-Prager yield criterion
δ	Interface friction angle
δ_{ij}	Kronecker delta
$\dot{\varepsilon}_{ij}$	Strain rate tensor
$\dot{\lambda}$	Plastic multiplier
$\dot{\sigma}_{ij}$	Cauchy's stress rate tensor
η	ratio $\tan \phi^* / \tan \phi$, or c^* / c
ν	Poisson's coefficient
ϕ	Shear strength angle
ϕ^*	Shear strength angle on velocity discontinuity lines
ψ	Dilatancy angle
σ_n^*	Normal stress on velocity discontinuity lines
σ_n	Normal stress
σ_{ij}	Cauchy's stress tensor
τ	Shear stress

τ^*	Shear stress on velocity discontinuity lines
θ	Angle between $[v]_i$ and T_i
c	Apparent cohesion
c^*	Apparent cohesion on velocity discontinuity lines
E	Young's modulus
f	Yield function
k	Material parameter of the Drucker-Prager yield criterion
Q	Applied forces
q	Load multiplier
Q_c	Collapse load
Q_{fix}	Fixed applied forces
Q_l	Lower bound to the collapse load
Q_u	Upper bound to the collapse load
Q_{var}	Forces that are increased until collapse
S	Boundary of domain V
s_{ij}	Deviator of Cauchy's stress tensor
T_i	Surface tractions resultant vector
t_i	Surface tractions vector
V	Region
v_i	Velocity vector

Chapter 2

\bar{p}_f	Normalised average contact pressure at failure
β	Parameter
δ	Interface friction angle

η	ratio $\tan \phi^* / \tan \phi$, or c^* / c
γ	Soil self-weight
λ	Surcharge ratio
ϵ	Residual error
ν	Dilatancy angle
ϕ	Shear strength angle for rectangular footings
ϕ	Shear strength angle
ϕ^*	Shear strength angle on velocity discontinuity lines
ϕ_s	Shear strength angle for strip footings
ϕ_t	Shear strength angle in triaxial conditions
ψ	Angle defining the elastic trapped wedge beneath the footing
σ_n^*	Normal stress on velocity discontinuity lines
τ^*	Shear stress on velocity discontinuity lines
a	Parameter
B	Footing breadth
c	Apparent cohesion
c^*	Apparent cohesion on velocity discontinuity lines
c_k	Estimated coefficient k
G	Dimensionless soil weight parameter $0.5\gamma B/c$
$K_{p\gamma}$	Coefficient of passive earth pressure
L	Footing length
N'	Bearing capacity factor for finite length footings
N_γ	Bearing capacity factor due to soil self-weight
N_ϕ	Flow value

N_c	Bearing capacity factor due to cohesion
N_q	Bearing capacity factor due to overburden pressure
p_f	Average contact pressure at failure
q	Overburden pressure
$R_{\text{DOF,adj}}^2$	Degree of freedom adjusted coefficient of determination
R_i	Ratio of parameter i
S	Fit standard error
s	Suction
s_γ	Shape factor N'_γ/N_γ
s_c	Shape factor N'_c/N_c
s_u	Undrained shear strength
T_m	m -th Chebyshev polynomial of the first kind

Chapter 3

α	Shear span ratio a/d
α_{cs}	Shear span ratio at the control section
β	Relative interface adhesion adh/c
χ	Coordinate
δ	Interface friction angle
ε	Strain at control depth
η	Dimensionless resisting moment $M_R/(\gamma B^3)$
γ	Soil self-weight
γ_c	Partial safety factor for concrete strength
κ	Coefficient of the power-law failure criterion
μ	Dimensionless resisting moment $M_R/(cB^2)$

ω	Angular velocity
ϕ	Shear strength angle
ρ	Reinforcement ratio
ρ_m	M_c/M_R
θ_0, θ_h	Angles defining the geometry of the failure mechanism
θ_c	Strut inclination
ξ	Coordinate
ζ	Relative distance of half contact pressure resultant a/B_c
ζ_{cc}	ζ_c for weightless soil
ζ_c	Contact breadth ratio B_c/B
$\zeta_{c\gamma}$	ζ_c for cohesionless soil
a	Shear span (for specimens subjected to point loads is the distance between the axis of the load and the axis of the support)
a_{cs}	M/V at the control section
a_{dir}	Distance of direct support region
B	Footing breadth
B_c	Contact breadth
c	Apparent cohesion
d	Effective depth
d_{dg}	$d_g + 16 \text{ mm}$
d_g	Maximum aggregate size
E_c	Concrete Young's modulus
E_s	Reinforcement Young's modulus
f_{ce}	Effective concrete compressive strength

f_{ck}	Characteristic compressive cylinder strength of concrete
f_{cp}	Concrete equivalent plastic compressive strength
f_{ct}	Concrete tensile strength
f_y	Reinforcement yield stress
G	Dimensionless soil weight parameter $0.5\gamma B/c$
k_c	Concrete compressive strength reduction factor
K_i	i -th coefficient describing the geometry and kinematics of the failure mechanism
L	Footing length
M	Bending moment
M_γ	Bending moment caused by cohesionless soil
M_c	Bending moment caused by weightless soil
M_R	Resisting moment
N_γ	Bearing capacity factor due to soil self-weight
N_c	Bearing capacity factor due to cohesion
p	Contact pressure
p_u	Average collapse contact pressure Q_u/B
Q_u	Collapse load
r, r_0, r_h	Radii defining the geometry of the failure mechanism
V	Shear force
v	Velocity
V_{chord}	Shear force carried by inclination of compression chord
V_c	Shear force carried by concrete
V_{dir}	Shear force carried by direct strut action
$V_{E,c}$	Shear force acting at the tip of the critical shear crack

V_R	Shear resistance
x	Coordinate
x_0	Distance of the centre of rotation
x_c	Depth of plastically compressed concrete
y	Coordinate
z	Coordinate

Chapter 4

α_p	Pile linear thermal expansion coefficient
α_s	Soil linear thermal expansion coefficient
ΔT	Temperature variation
$\Delta w_{a:b}$	Displacement difference between $\xi = a$ and $\xi = b$
δ_{ij}	Kronecker delta
ε_{ij}	Small strain tensor
λ	Thermal conductivity
$\nabla \cdot$	Divergence operator
∇	Gradient operator
ν_s	Soil Poisson's coefficient
ρ	Bulk density
σ	Pile axial stress
σ_{ij}	Cauchy's stress tensor
ς	$\sigma/(E_p \alpha_p \Delta T)$, normalised pile axial stress
ξ	raft normalised coordinate
B	Raft bending stiffness
c_p	Heat capacity

d	Pile diameter
D_{ijkl}	Tensor of elastic constants
E_p	Pile Young's modulus
E_r	Raft Young's modulus
G_s	Soil shear modulus
K	E_p/G_s , pile to soil relative stiffness
l	Pile length
l/d	Pile slenderness coefficient
n	Porosity
n_p	Number of piles
R	$R_r R_s$, raft to single pile displacement ratio
R_r	\bar{w}_r/\bar{w}_g , raft to pile group displacement ratio
R_s	\bar{w}_g/w_s , pile group to single pile displacement ratio
s	Pile spacing
s/d	Pile spacing ratio
t_r	Raft thickness
\bar{w}_g	Mean displacement of pile group in the piled raft foundation
\bar{w}_r	Raft mean displacement
w_s	Head displacement of isolated pile
X	α_s/α_p , soil to pile thermal expansion coefficient ratio

Chapter 5

α	Coefficient of linear thermal expansion
ΔL	Pile length variation
ΔL_{imp}	Imposed pile length variation

ΔT	Temperature variation
η	Coefficient of thermal imposed strain ($-\varepsilon_{\text{th, imp}}/\alpha\Delta T$)
σ	Axial stress
ε	Axial strain
$\varepsilon_{\text{th, imp}}$	Thermal imposed axial strain
A	Cross-sectional area
E	Young's modulus
f	Applied nodal forces
f_e	Nodal forces due to elements deformation
f_s	Nodal forces due to springs reaction
k	Truss element axial stiffness
k_b	Base spring stiffness
k_c	Cap spring stiffness
k_h	Head spring stiffness
k_s	Spring stiffness
L	Pile length
l_{NP}	Distance of the null point from the pile base
x	nodal displacement
x_b	Base node displacement
x_h	Head node displacement

Chapter 6

α_{EP}	Energy pile linear thermal expansion coefficient
α_{r}	Rheological coefficient
$\bar{\sigma}'_{\text{v}}$	Average value of vertical effective stress

\bar{K}	Average lateral earth pressure coefficient
ΔT_d	Design value of temperature variation
ΔT_k	Characteristic value of temperature variation
δ'	Pile-soil interface effective friction angle
ε	Axial strain
γ_G	Partial load factor for permanent loads
γ_Q	Partial load factor for variable loads
ν_{EP}	Energy pile Poisson's coefficient
ν_{soil}	Soil Poisson's coefficient
ψ_i	Combination factors. 0: rare action; 1: frequent action; 2: quasi-permanent action
ρ_{EP}	Energy pile bulk density
ρ_{min}	Minimum reinforcement ratio to avoid axial brittle failure
ρ_r	Reinforcement ratio
ρ_{soil}	Soil bulk density
σ'_{vb}	Vertical effective stress at the pile base level
A_b	Pile base area
D	Pile diameter
d_q	Depth factor for bearing capacity factor N_q
E_d	Design value of actions effect
E_{EP}	Energy pile Young's modulus
f_{ctm}	Average concrete tensile strength
f_{ct}	Concrete tensile strength
f_t	Reinforcement tensile strength

f_y	Reinforcement yield stress
G_k	Characteristic value of permanent load
G_{soil}	Soil shear modulus
K_b	Stiffness of the elastic branch of Frank and Zhao load-transfer curve for pile base
K_h	Spring stiffness simulating pile head restraint due to slab
K_s	Stiffness of the elastic branch of Frank and Zhao load-transfer curve for pile shaft
L	Pile length
N_{Ed}^*	Design internal axial force due to compressive mechanical load and cooling
N_{Rd}^*	Design tensile axial resistance
N_c	Bearing capacity factor due to cohesion
N_{Ed}	Design internal axial force due to compressive mechanical load and heating
N_q	Bearing capacity factor due to overburden pressure
N_{Rd}	Design compressive axial resistance
P_d	Applied load
Q_{bd}	Design value of pile base capacity
q_b	Base resistance for an isolated pile
Q_{k1}	Characteristic value of dominant variable load
Q_k	Characteristic value of variable load
Q_{sd}	Design value of pile shaft capacity
q_s	Average shaft resistance for an isolated pile
Q_{ud}	Load capacity $Q_{\text{sd}} + Q_{\text{bd}}$
R_d	Design value of resistance
s_q	Shape factor for bearing capacity factor N_q
w_d^m	Design head displacement due to mechanical load

w_d^{th} Design head displacement due to thermal load

z Coordinate

References

- [1] S Abdelaziz and T Y Ozudogru. “Non-uniform thermal strains and stresses in energy piles”. In: *Environmental Geotechnics* 3.4 (2016), pp. 237–252.
- [2] D Adam and R Markiewicz. “Energy from earth-coupled structures, foundations, tunnels and sewers”. In: *Géotechnique* 59.3 (2009), pp. 229–236.
- [3] G A Akrouch, M Sánchez, and J-L Briaud. “Thermo-mechanical behavior of energy piles in high plasticity clays”. In: *Acta Geotechnica* 9.3 (2014), pp. 399–412.
- [4] D E Allen. “Limit states design—a probabilistic study”. In: *Canadian Journal of Civil Engineering* 2.1 (1975), pp. 36–49.
- [5] BL Amatya, K Soga, PJ Bourne-Webb, T Amis, and L Laloui. “Thermo-mechanical behaviour of energy piles”. In: *Géotechnique* 62.6 (2012), pp. 503–519.
- [6] E Ausilio and E Conte. “Influence of groundwater on the bearing capacity of shallow foundations”. In: *Canadian geotechnical journal* 42.2 (2005), pp. 663–672.
- [7] L D Baikie. “Comparison of limits states design methods for bearing capacity of shallow foundations”. In: *Canadian geotechnical journal* 35.1 (1998), pp. 175–182.
- [8] P K Banerjee and T G Davies. “Analysis of pile groups embedded in Gibson soil”. In: *Proc. of 9th Int. Conf. of Soil Mech. and Found. Eng., Tokyo*. Vol. 1. 1977, pp. 381–386.
- [9] N Batini et al. “Energy and geotechnical behaviour of energy piles for different design solutions”. In: *Applied Thermal Engineering* 86 (2015), pp. 199–213.
- [10] Z P Bazant and J-K Kim. “Size effect in shear failure of longitudinally reinforced beams”. In: American Concrete Institute. 1984.
- [11] B F Bélidor. *La science des ingénieurs dans la conduite des travaux de fortifications et d’architecture civile*. Paris, Jombert, 1729.

- [12] J F W Bishop. “On the complete solution to problems of deformation of a plastic-rigid material”. In: *Journal of the Mechanics and Physics of Solids* 2.1 (1953), pp. 43–53.
- [13] J F W Bishop, A P Green, and R Hill. “A note on the deformable region in a rigid-plastic body”. In: *Journal of the Mechanics and Physics of Solids* 4.4 (1956), pp. 256–258.
- [14] Boeri Architetti. *Villa Méditerranée*. <https://www.stefanoberiarchitetti.net/project/villa-mediterranee-2/>. Accessed: 2019-09-04. 2019.
- [15] M D Bolton and C K Lau. “Vertical bearing capacity factors for circular and strip footings on Mohr–Coulomb soil”. In: *Canadian Geotechnical Journal* 30.6 (1993), pp. 1024–1033.
- [16] A Bottero, R Negre, J Pastor, and S Turgeman. “Finite element method and limit analysis theory for soil mechanics problems”. In: *Computer Methods in Applied Mechanics and Engineering* 22.1 (1980), pp. 131–149.
- [17] P Bourne-Webb. “Observed response of energy geostructures”. In: *Energy geostructures: Innovation in underground engineering* (2013), pp. 45–77.
- [18] P J Bourne-Webb. “An overview of observed thermal and thermo-mechanical response of piled energy foundations”. In: *European Geothermal Congress. Pisa, Italy*. 2013, pp. 1–8.
- [19] P J Bourne-Webb, B Amatya, and K Soga. “A framework for understanding energy pile behaviour”. In: *Proceedings of the Institution of Civil Engineers-Geotechnical Engineering* 166.2 (2013), pp. 170–177.
- [20] P J Bourne-Webb, T M Bodas Freitas, and R M Freitas Assunção. “Soil–pile thermal interactions in energy foundations”. In: *Géotechnique* 66.2 (2015), pp. 167–171.
- [21] P J Bourne-Webb et al. “Energy pile test at Lambeth College, London: geotechnical and thermodynamic aspects of pile response to heat cycles”. In: *Géotechnique* 59.3 (2009), pp. 237–248.
- [22] P Bourne-Webb, S Burlon, S Javed, S Kürten, and F Loveridge. “Analysis and design methods for energy geostructures”. In: *Renewable and Sustainable Energy Reviews* 65 (2016), pp. 402–419.
- [23] L E Bowles. *Foundation analysis and design*. 5th ed. McGraw-hill, New York, 1996.

- [24] H Brandl. “Energy foundations and other thermo-active ground structures”. In: *Géotechnique* 56.2 (2006), pp. 81–122.
- [25] J Brinch Hansen. “A general formula for bearing capacity”. In: *Danish Geotechnical Institute, Bulletin* 11 (1961), pp. 38–46.
- [26] J Brinch Hansen. “A revised and extended formula for bearing capacity”. In: *Bulletin of the Danish Geotechnical Institute* 28 (1970), pp. 5–11.
- [27] O T Bruhns. “Some remarks on the history of plasticity–Heinrich Hencky, a pioneer of the early years”. In: *The History of Theoretical, Material and Computational Mechanics-Mathematics Meets Mechanics and Engineering*. Springer, 2014, pp. 133–152.
- [28] S Burlon, J Habert, F Szymkiewicz, M Suryatriyastuti, and H Mroueh. “Towards a design approach of bearing capacity of thermo-active piles”. In: *European geothermal congress*. 2013, pp. 1–6.
- [29] R Butterfield and P K Banerjee. “The elastic analysis of compressible piles and pile groups”. In: *Géotechnique* 21.1 (1971), pp. 43–60.
- [30] R Butterfield and P K Banerjee. “The problem of pile group–pile cap interaction”. In: *Géotechnique* 21.2 (1971), pp. 135–142.
- [31] R H Byrd, P Lu, J Nocedal, and C Zhu. “A limited memory algorithm for bound constrained optimization”. In: *SIAM Journal on scientific computing* 16.5 (1995), pp. 1190–1208.
- [32] S Campana, M Fernández Ruiz, and A Muttoni. “Strength of arch-shaped members in bending and shear”. In: *4th fib Congress, Mumbai*. CONF. 4th fib Congress, Mumbai. 2014, p. 9.
- [33] S Campana and A Muttoni. “Analysis and design of an innovative solution for tunnels using elastic-plastic stress fields”. In: *Proceeding of the 8th fib-PhD Symposium*. CONF. Proceeding of the 8th fib-PhD Symposium. 2010, pp. 75–80.
- [34] R G Campanella and J K Mitchell. “Influence of temperature variations on soil behavior”. In: *Journal of Soil Mechanics & Foundations Div* (1968).
- [35] V Caputo and C Viggiani. “Pile foundation analysis: a simple approach to non-linearity effects”. In: *Rivista Italiana di Geotecnica* 18.1 (1984), pp. 32–51.
- [36] A Caquot. *Équilibre des massifs à frottement interne: stabilité des terres, pulvérulentes ou cohérentes*. Gauthier-Villars, 1934.

- [37] A Caquot and J Keérisel. *Traité de mécanique des sols*. 3rd ed. Paris: Gauthier-Villars, 1956.
- [38] A Caquot and J Kerisel. “Sur le terme de surface dans le calcul des fondations en milieu pulvérulent”. In: *Proc. 3rd Int. Conf. on Soil Mechanics and Foundation Engineering*. Vol. 1. 1953, pp. 336–337.
- [39] A Caquot and J Kérisel. “Traité de mécanique des sols”. In: (1949).
- [40] M J Cassidy and G T Houlsby. “Vertical bearing capacity factors for conical footings on sand”. In: *Géotechnique* 52.9 (2002), pp. 687–692.
- [41] F Cavagnis. “Shear in reinforced concrete without transverse reinforcement”. EPFL, 2017.
- [42] F Cavagnis, M Fernández Ruiz, and A Muttoni. “A mechanical model for failures in shear of members without transverse reinforcement based on development of a critical shear crack”. In: *Engineering Structures* 157 (2018), pp. 300–315.
- [43] F Cavagnis, M Fernández Ruiz, and A Muttoni. “Shear failures in reinforced concrete members without transverse reinforcement: An analysis of the critical shear crack development on the basis of test results”. In: *Engineering Structures* 103 (2015), pp. 157–173.
- [44] CEB. *Ultimate limit state design models: a state-of-the-art report*. Comité euro-international du béton, Lausanne, Switzerland, 1995. 1995.
- [45] C Cekerevac and L Laloui. “Experimental study of thermal effects on the mechanical behaviour of a clay”. In: *International journal for numerical and analytical methods in geomechanics* 28.3 (2004), pp. 209–228.
- [46] CFMS-SYNTec-SOFFONS-FNTP. *Recommandations pour la conception, le dimensionnement et la mise en oeuvre des géostructures thermiques*. Comité français de mécanique des sols, France. 2017, p. 120.
- [47] D Chen and J S McCartney. “Parameters for load transfer analysis of energy piles in uniform nonplastic soils”. In: *International Journal of Geomechanics* 17.7 (2017), p. 04016159.
- [48] W-F Chen. *Extensibility of concrete on rock and the theorem of limit analysis, November 1968 (70-11)*. Tech. rep. Lehigh Univ Dep Civ Eng, 1968.
- [49] W-F Chen. *Limit analysis and soil plasticity*. 1st ed. Amsterdam, Oxford, New York: Elsevier, 1975.
- [50] W-F Chen. *Plasticity in reinforced concrete*. J. Ross Publishing, 2007.

- [51] W-F Chen and D J Han. *Plasticity for structural engineers*. Elsevier, 1988.
- [52] W-F Chen and X L Liu. *Limit analysis in soil mechanics*. Elsevier, 1990.
- [53] W Chen and G Y Baladi. *Soil plasticity: theory and implementation*. Elsevier, 1985.
- [54] P Clancy and M F Randolph. “An approximate analysis procedure for piled raft foundations”. In: *International Journal for Numerical and Analytical Methods in Geomechanics* 17.12 (1993), pp. 849–869.
- [55] P Clancy and M F Randolph. “Simple design tools for piled raft foundations”. In: *Géotechnique* 46.2 (1996), pp. 313–328.
- [56] I F Collins. “A note on the interpretation of Coulomb’s analysis of the thrust on a rough retaining wall in terms of the limit theorems of plasticity theory”. In: *Géotechnique* 23.3 (1973), pp. 442–447.
- [57] I F Collins. “Discussion: A note on the interpretation of Coulomb’s analysis of the thrust on a rough retaining wall in terms of the limit theorems of plasticity theory”. In: *Géotechnique* 24.1 (1974), pp. 106–108.
- [58] I F Collins. “The upper bound theorem for rigid/plastic solids generalized to include Coulomb friction”. In: *Journal of the Mechanics and Physics of Solids* 17.5 (1969), pp. 323–338.
- [59] E M Comodromos, M C Papadopoulou, and L Laloui. “Contribution to the design methodologies of piled raft foundations under combined loadings”. In: *Canadian Geotechnical Journal* 53.4 (2015), pp. 559–577.
- [60] COMSOL Inc. *COMSOL Multiphysics: Reference manual, version 5.3*. 2017. URL: <https://www.comsol.com/>.
- [61] C A Coulomb. “Essai sur une application des règles des maximis et minimis à quelques problèmes de statique”. In: *Memoires Acad. Royale des Sciences* 7 (1776).
- [62] A D Cox. “Axially-symmetric plastic deformation in soils—II. Indentation of ponderable soils”. In: *International Journal of Mechanical Sciences* 4.5 (1962), pp. 371–380.
- [63] A D Cox, G Eason, and H G Hopkins. “Axially symmetric plastic deformations in soils”. In: *Philosophical Transactions of the Royal Society of London. Series A, Mathematical and Physical Sciences* 254.1036 (1961), pp. 1–45.
- [64] H M Coyle and L C Reese. “Load transfer for axially loaded piles in clay”. In: *Journal of the Soil Mechanics and Foundations Division* 92.2 (1966), pp. 1–26.

- [65] E H Davis. “Theories of plasticity and the failure of soil masses”. In: *Soil mechanics: selected topics* (ed. I. K. Lee), London: Butterworth. 1968, pp. 341–380.
- [66] E H Davis and J R Booker. “The bearing capacity of strip footings from the standpoint of plasticity theory”. In: *Proc. 1st Australia-New Zeland Conf. on Geomechanics, Melbourne, Australia*. 1971, pp. 276–282.
- [67] E H Davis and J R Booker. “The effect of increasing strength with depth on the bearing capacity of clays”. In: *Geotechnique* 23.4 (1973), pp. 551–563.
- [68] E H Davis and H G Poulos. “The analysis of piled raft systems”. In: *Australia Geotechnique Journal* 2.1 (1972), pp. 21–27.
- [69] R O Davis and A P S Selvadurai. *Elasticity and Geomechanics, 201 pages*. University Press, Cambridge, 1996.
- [70] E E de Beer. “Etude expérimentale de la capacité portante du sable sous des fondations circulaires établies en surface”. In: *Proc. 5th Int. Conf. on SMFE*. Vol. 1. 1961, pp. 577–581.
- [71] E E de Beer. “Experimental determination of the shape factors and the bearing capacity factors of sand”. In: *Geotechnique* 20.4 (1970), pp. 387–411.
- [72] P de Buhan. *Plasticité et calcul à la rupture*. Presses des Ponts, 2007.
- [73] G de Josselin de Jong. “Lower bound collapse theorem and lack of normality of strainrate to yield surface for soils”. In: *Rheology and Soil Mechanics/Rhéologie et Mécanique des Sols*. Springer, 1966, pp. 69–78.
- [74] L de Sanctis and A Mandolini. “Bearing capacity of piled rafts on soft clay soils”. In: *Journal of Geotechnical and Geoenvironmental Engineering* 132.12 (2006), pp. 1600–1610.
- [75] P de Simone. “Bearing capacity of a circular footing on a Coulomb medium”. In: *International conference on numerical methods in geomechanics*. 1985, pp. 829–836.
- [76] C S Desai and H J Siriwardane. *Constitutive laws for engineering materials with emphasis on geologic materials*. BOOK. Prentice-Hall, 1984.
- [77] D M Dewaikar and B G Mohapatro. “Computation of bearing capacity factor N_γ —Terzaghi’s mechanism”. In: *International Journal of Geomechanics* 3.1 (2003), pp. 123–128.

- [78] A Di Donna, F Dupray, and L Laloui. “Effect of thermo-plasticity of soils on the design of energy piles”. In: *Proceedings of European Geothermal Conf.(EGC 2013), Pisa, Italy, European Geothermal Energy Council, Paper SG4-03*. 2013, p. 10.
- [79] A Di Donna, A Ferrari, and L Laloui. “Experimental investigations of the soil–concrete interface: physical mechanisms, cyclic mobilization, and behaviour at different temperatures”. In: *Canadian Geotechnical Journal* 53.4 (2016), pp. 659–672.
- [80] A Di Donna and L Laloui. “Numerical analysis of the geotechnical behaviour of energy piles”. In: *International journal for numerical and analytical methods in geomechanics* 39.8 (2015), pp. 861–888.
- [81] A Di Donna, A F Rotta Loria, and L Laloui. “Numerical study of the response of a group of energy piles under different combinations of thermo-mechanical loads”. In: *Computers and Geotechnics* 72.1 (2016), pp. 126–142.
- [82] A Drescher and E Detournay. “Limit load in translational failure mechanisms for associative and non-associative materials”. In: *Géotechnique* 43.3 (1993), pp. 443–456.
- [83] D C Drucker. “A more fundamental approach to plastic stress-strain relations”. In: *Proc. of 1st US National Congress of Applied Mechanics, 1951*. 1951, pp. 487–491.
- [84] D C Drucker. “Concept of path independence and material stability for soils”. In: *Rheology and Soil Mechanics/Rhéologie et Mécanique des Sols*. Springer, 1966, pp. 23–46.
- [85] D C Drucker. *Coulomb friction, plasticity, and limit loads*. Tech. rep. Brown Univ Providence Ri Div of Applied Mathematics, 1953.
- [86] D C Drucker. “Limit analysis of two and three dimensional soil mechanics problems”. In: *Journal of the Mechanics and Physics of Solids* 1.4 (1953), pp. 217–226.
- [87] D C Drucker. “On stress-strain relations for soils and load carrying capacity”. In: *Proceedings of the First International Conference on the Mechanics of Soil-Vehicle Systems, Turin, Italy*. 1961, pp. 15–23.
- [88] D C Drucker. “On structural concrete and the theorems of limit analysis”. In: *IABSE-Reports* 21 (1961), pp. 45–59.
- [89] D C Drucker. “On uniqueness in the theory of plasticity”. In: *Quarterly of Applied Mathematics* 14.1 (1956), pp. 35–42.

- [90] D C Drucker. *Plastic design methods, Advantages and limitations*. Tech. rep. Brown Univ Providence Ri, 1957.
- [91] D C Drucker. “Plasticity of metals-mathematical theory and structural applications”. In: *Transactions of the American Society of Civil Engineers* 116.1 (1950), pp. 1059–1072.
- [92] D C Drucker. “Some implications of work hardening and ideal plasticity”. In: *Quarterly of Applied Mathematics* 7.4 (1950), pp. 411–418.
- [93] D C Drucker. *Stress-strain relations in the plastic range. A survey of theory and experiment*. Tech. rep. Brown Univ Providence Ri Div of Applied Mathematics, 1950.
- [94] D C Drucker. “Yield Conditions in Beams, Plates, and Shells”. In: *Handbook of Materials Behavior Models*. Elsevier, 2001, pp. 187–194.
- [95] D C Drucker, R E Gibson, and D J Henkel. “Soil mechanics and work-hardening theories of plasticity”. In: *Trans. ASCE* 122 (1957), pp. 338–346.
- [96] D C Drucker, H J Greenberg, and W Prager. “The safety factor of an elastic-plastic body in plane strain”. In: *Journal of Applied Mechanics* 18.1951 (1951), pp. 371–378.
- [97] D C Drucker and W Prager. “Soil mechanics and plastic analysis or limit design”. In: *Quarterly of applied mathematics* 10.2 (1952), pp. 157–165.
- [98] D C Drucker, W Prager, and H J Greenberg. “Extended limit design theorems for continuous media”. In: *Quarterly of applied mathematics* 9.4 (1952), pp. 381–389.
- [99] G Eason and R T Shield. “The plastic indentation of a semi-infinite solid by a perfectly rough circular punch”. In: *Zeitschrift für angewandte Mathematik und Physik ZAMP* 11.1 (1960), pp. 33–43.
- [100] EN. *Code 1990. Basis of Structural Design*. London, United Kingdom, 2004. 2002, p. 90.
- [101] EN. *Code 1992. Design of Concrete Structures – Part 1-1: General Rules and Rules for Buildings*. London, United Kingdom, 2004. 2004, p. 225.
- [102] EN. *Code 1997. Geotechnical Design*. London, United Kingdom, 2004. 2004.
- [103] H L Erickson and A Drescher. “Bearing capacity of circular footings”. In: *Journal of geotechnical and geoenvironmental engineering* 128.1 (2002), pp. 38–43.

- [104] H Eslami, S Rosin-Paumier, A Abdallah, and F Masrouri. “Pressuremeter test parameters of a compacted illitic soil under thermal cycling”. In: *Acta Geotechnica* 12.5 (2017), pp. 1105–1118.
- [105] W Fellenius. “Jordstatiska beräkningar för vertikal belastning på horisontal markyta under antagande av cirkulär cylindriska glidytor (Stability calculations for vertical loads on horizontal ground surface assuming cylindrical failure surfaces)”. In: *Teknisk Tidskrift* 59 (1929), pp. 57–63.
- [106] M Fernández Ruiz and A Muttoni. “On development of suitable stress fields for structural concrete”. In: *ACI, Structural Journal* 104 (2007), pp. 495–502.
- [107] M Fernández Ruiz, A Muttoni, and J Sagaseta. “Shear strength of concrete members without transverse reinforcement: A mechanical approach to consistently account for size and strain effects”. In: *Engineering Structures* 99 (2015), pp. 360–372.
- [108] K Fleming, A Weltman, M Randolph, and K Elson. *Piling engineering*. CRC press, 2008.
- [109] R Frank and S R Zhao. “Estimation par les paramètres pressiométriques de l’enfoncement sous charge axiale de pieux forés dans des sols fins”. In: *BULL LIAISON LAB PONTS CHAUSS* 119 (1982).
- [110] S Frydman and Harvey J Burd. “Numerical studies of bearing-capacity factor N_γ ”. In: *Journal of geotechnical and geoenvironmental engineering* 123.1 (1997), pp. 20–29.
- [111] C Garbellini and L Laloui. “On the Soil-Structure Interaction of Surface Strip Footings at Ultimate Limit State”. In: *26th European Young Geotechnical Engineers Conference*. Vol. 1. CONF. ISSMGE. 2018.
- [112] C Garbellini and L Laloui. “Soil-Structure Interaction of Surface Footings”. In: *Submitted to Computers and Geotechnics* (2020).
- [113] C Garbellini and L Laloui. “Thermal stress analysis of energy piles”. In: *Géotechnique* (2019), pp. 1–12.
- [114] C Garbellini and L Laloui. “Three-dimensional finite element analysis of piled rafts with energy piles”. In: *Computers and Geotechnics* 114 (2019), p. 103115.
- [115] D Garnier. “Analyse par la théorie du calcul à la rupture des facteurs de réduction de la capacité portante de fondations superficielles”. PhD thesis. 1995.

- [116] K A Gawecka et al. “Numerical modelling of thermo-active piles in London Clay”. In: *Proceedings of the Institution of Civil Engineers-Geotechnical Engineering* 170.3 (2017), pp. 201–219.
- [117] H Geiringer. *Fondements mathématiques de la théorie des corps plastiques isotropes*. Gauthier-Villars, 1937.
- [118] H Q Golder. “The ultimate bearing pressure of rectangular footings.” In: *Journal of the Institution of Civil Engineers* 18.5274 (1942), pp. 161–174.
- [119] S Gourvenec, M F Randolph, and O Kingsnorth. “Undrained bearing capacity of square and rectangular footings”. In: *International Journal of Geomechanics* 6.3 (2006), pp. 147–157.
- [120] J Graham and J G Stuart. “Scale and boundary effects in foundation analysis”. In: *Journal of the Soil Mechanics and Foundations Division* 97.11 (1971), pp. 1533–1548.
- [121] H J Greenberg. “Complementary minimum principles for an elastic-plastic material”. In: *Quarterly of Applied Mathematics* 7.1 (1949), pp. 85–95.
- [122] D V Griffiths. “Computation of bearing capacity factors using finite elements”. In: *Geotechnique* 32.3 (1982), pp. 195–202.
- [123] D V Griffiths. “Computation of bearing capacity on layered soils”. In: *Proceedings of the 4th international conference on numerical methods in geomechanics, Edmonton, Alberta, Canada, May. Balkema, Rotterdam, The Netherlands*. Vol. 1. 1982, pp. 163–170.
- [124] GSHPA. *Thermal pile design, installation & materials standards*. Ground Source Heat Pump Association, National Energy Center, Davy Avenue, Knowlhill, Milton Keynes. 2012, p. 82.
- [125] A A Gvozdev. “The determination of the value of the collapse load for statically indeterminate systems undergoing plastic deformation”. In: *International Journal of Mechanical Sciences* 1.4 (1960), pp. 322–335.
- [126] A Haar and T von Kármán. “Zur Theorie der Spannungszustände in plastischen und sandartigen Medien”. In: *Nachrichten von der Gesellschaft der Wissenschaften zu Göttingen, Mathematisch-Physikalische Klasse* 1909 (1909), pp. 204–218.
- [127] J Habert et al. “Synthesis of a benchmark exercise for geotechnical analysis of a thermoactive pile”. In: *Environmental Geotechnics* (2019), pp. 1–12.

- [128] S J Hain and I K Lee. “The analysis of flexible raft-pile systems”. In: *Géotechnique* 28.1 (1978), pp. 65–83.
- [129] Y Hamada, H Saitoh, M Nakamura, H Kubota, and K Ochifuji. “Field performance of an energy pile system for space heating”. In: *Energy and Buildings* 39.5 (2007), pp. 517–524.
- [130] D Han, X Xie, L Zheng, and L Huang. “The bearing capacity factor N_γ of strip footings on $c - \phi - \gamma$ soil using the method of characteristics”. In: *SpringerPlus* 5.1 (2016), p. 1482.
- [131] G H Handelman, C C Lin, and W Prager. “On the mechanical behaviour of metals in the strain-hardening range”. In: *Quarterly of Applied Mathematics* 4.4 (1947), pp. 397–407.
- [132] B Hansen. “The bearing capacity of sand, tested by loading circular plates”. In: *5th International Conference on Soil Mechanic Foundation. England*. Vol. 1. 1961, pp. 659–664.
- [133] B Hansen and N H Christensen. “Discussion of theoretical bearing capacity of very shallow footings”. In: *Journal of Soil Mechanics & Foundations Div* (1969).
- [134] H Hencky. “Über einige statisch bestimmte Fälle des Gleichgewichts in plastischen Körpern”. In: *ZAMM-Journal of Applied Mathematics and Mechanics/Zeitschrift für Angewandte Mathematik und Mechanik* 3.4 (1923), pp. 241–251.
- [135] H Hencky. “Zur Theorie plastischer Deformationen und der hierdurch im Material hervorgerufenen Nachspannungen”. In: *ZAMM-Journal of Applied Mathematics and Mechanics/Zeitschrift für Angewandte Mathematik und Mechanik* 4.4 (1924), pp. 323–334.
- [136] D J Henkel. “The effect of overconsolidation on the behaviour of clays during shear”. In: *Géotechnique* 6.4 (1956), pp. 139–150.
- [137] D J Henkel. “The relationships between the effective stresses and water content in saturated clays”. In: *Géotechnique* 10.2 (1960), pp. 41–54.
- [138] D J Henkel. “The relationships between the strength, pore-water pressure, and volume-change characteristics of saturated clays”. In: *Géotechnique* 9.3 (1959), pp. 119–135.

- [139] I Herle and G Gudehus. “Determination of parameters of a hypoplastic constitutive model from properties of grain assemblies”. In: *Mechanics of Cohesive-frictional Materials: An International Journal on Experiments, Modelling and Computation of Materials and Structures* 4.5 (1999), pp. 461–486.
- [140] R Hill. “A general theory of uniqueness and stability in elastic-plastic solids”. In: *Journal of the Mechanics and Physics of Solids* 6.3 (1958), pp. 236–249.
- [141] R Hill. “A variational principle of maximum plastic work in classical plasticity”. In: *The Quarterly Journal of Mechanics and Applied Mathematics* 1.1 (1948), pp. 18–28.
- [142] R Hill. “On the problem of uniqueness in the theory of a rigid-plastic solid—I”. In: *Journal of the Mechanics and Physics of Solids* 4.4 (1956), pp. 247–255.
- [143] R Hill. “On the problem of uniqueness in the theory of a rigid-plastic solid—II”. In: *Journal of the Mechanics and Physics of Solids* 5.1 (1956), pp. 1–8.
- [144] R Hill. “On the problem of uniqueness in the theory of a rigid-plastic solid—III”. In: *Journal of the Mechanics and Physics of Solids* 5.3 (1957), pp. 153–161.
- [145] R Hill. “On the problem of uniqueness in the theory of a rigid-plastic solid—IV”. In: *Journal of the Mechanics and Physics of Solids* 5.4 (1957), pp. 302–307.
- [146] R Hill. “On the state of stress in a plastic-rigid body at the yield point”. In: *The London, Edinburgh, and Dublin Philosophical Magazine and Journal of Science* 42.331 (1951), pp. 868–875.
- [147] R Hill. *The mathematical theory of plasticity*. Oxford: Clarendon Press, 1950.
- [148] R Hill. “The plastic yielding of notched bars under tension”. In: *The Quarterly Journal of Mechanics and Applied Mathematics* 2.1 (1949), pp. 40–52.
- [149] M Hjiiaj, A V Lyamin, and S W Sloan. “Numerical limit analysis solutions for the bearing capacity factor $N\gamma$ ”. In: *International Journal of Solids and Structures* 42.5-6 (2005), pp. 1681–1704.
- [150] P Hodge and W Prager. “A Variational Principle for Plastic Materials with Strain-Hardening”. In: *Journal of Mathematics and Physics* 27.1-4 (1948), pp. 1–10.
- [151] C A Hogentogler and K Terzaghi. “Interrelationship of load, road and subgrade”. In: *Public Roads* 10.3 (1929), pp. 37–64.
- [152] K Horikoshi and M F Randolph. “Estimation of overall settlement of piled rafts”. In: *Soils and Foundations* 39.2 (1999), pp. 59–68.

- [153] K Horikoshi and M F Randolph. “On the definition of raft-soil stiffness ratio for rectangular rafts”. In: *Géotechnique* 47.5 (1997).
- [154] C Iodice, R Di Laora, and A Mandolini. “Analytical Solutions for Ultimate Limit State Design of Thermal Piles”. In: *Journal of Geotechnical and Geoenvironmental Engineering* 146.5 (2020), p. 04020016.
- [155] A J Ishlinsky. “The axial-symmetrical problem in plasticity and the Brinell test”. In: *Theoretical Research Translation* 2 (1944), p. 47.
- [156] N Janbu. “Earth pressure and bearing capacity calculations by generalized procedure of slices”. In: *Proc. 4th ICSMFE, London, 1957* (1957).
- [157] P Jelušič and B Žlender. “Determining optimal designs for conventional and geothermal energy piles”. In: *Renewable Energy* 147 (2020), pp. 2633–2642.
- [158] A W Jenike. “Steady gravity flow of frictional-cohesive solids in converging channels”. In: *Journal of Applied Mechanics* 31 (1964), pp. 5–11.
- [159] A W Jenike and R T Shield. “On the plastic flow of Coulomb solids beyond original failure”. In: *Appl. Mech.* 81 (1959), pp. 599–602.
- [160] G de Josselin de Jong. *Statics and kinematics in the failable zone of a granular material*. Delft: Waltman, 1959.
- [161] J L Justo. “Discussion: A note on the interpretation of Coulomb’s analysis of the thrust on a rough retaining wall in terms of the limit theorems of plasticity theory”. In: *Géotechnique* 24.1 (1974), pp. 106–108.
- [162] L M Kachanov. *Fundamentals of the Theory of Plasticity*. Courier Corporation, 2004.
- [163] G N J Kani. “The riddle of shear failure and its solution”. In: *Journal Proceedings*. Vol. 61. 4. 1964, pp. 441–468.
- [164] R Katzenbach, U Arslan, and J Gutwald. “A numerical study on pile foundation of the 300 m high Commerzbank-tower in Frankfurt am Main”. In: *Proc. 3 European Conf. on Numerical Methods in Geomechanics, Manchester*. 1994, pp. 271–277.
- [165] R Katzenbach, K Knoblich, E Mands, A Rückert, and B Sanner. “Energiepfähle–Verbindung von Geotechnik und Geothermie”. In: *IZW-Bericht* 2.97 (1997), pp. 91–98.
- [166] G Kazinczy. “Kiserletek befalazott tartokkal (Experiments with fixed-end beams)”. In: *Betonszemle* 2 (1914), pp. 101–104.

- [167] N C Kist. “Does a stress analysis based on Hooke’s law lead to a satisfactory design of steel bridges and buildings”. In: *Inaugural lecture, Delft* (1917).
- [168] C Knellwolf, H Peron, and L Laloui. “Geotechnical analysis of heat exchanger piles”. In: *Journal of Geotechnical and Geoenvironmental Engineering* 137.10 (2011), pp. 890–902.
- [169] H Ko and R F Scott. “Bearing capacities by plasticity theory”. In: *Journal of Soil Mechanics & Foundations Div* 99.sm1 (1973).
- [170] F Kögler and A Scheidig. *Baugrund und Bauwerk*. Ernst, 1938.
- [171] W T Koiter. “General theorems for elastic plastic solids”. In: *Progress of Solid Mechanics* (1960), pp. 167–221.
- [172] W T Koiter. “Stress-strain relations, uniqueness and variational theorems for elastic-plastic materials with a singular yield surface”. In: *Quarterly of applied mathematics* 11.3 (1953), pp. 350–354.
- [173] N Kostic. “Topologie des champs de contraintes pour le dimensionnement des structures en béton armé”. Lausanne: IS, 2009, p. 235.
- [174] F Kötter. “Die Bestimmung des Drucks an gekrümmten Gleitflächen, eine Aufgabe aus der Lehre vom Erddruck”. In: *Sitzungsberichte der Akademie der Wissenschaften* (1903), pp. 229–233.
- [175] F Kötter. “Über das problem der erddruckbestimmung”. In: *Physikalische gesellschaft zu berlin* 7 (1888), pp. 1–8.
- [176] L M Kraft Jr, R P Ray, and T Kagawa. “Theoretical τ - z curves”. In: *Journal of Geotechnical and Geoenvironmental Engineering* 107.ASCE 16653 (1981).
- [177] H Krey. *Erddruck, Erdwiderstand und Tragfähigkeit des Baugrundes: Gesichtspunkte für Berechnung*. Ernst & Sohn, 1932.
- [178] S Krishnamurthy and N S V K Rao. “Effect of submergence on bearing capacity”. In: *Soils and Foundations* 15.3 (1975), pp. 61–66.
- [179] J Kumar. “ N_γ for rough strip footing using the method of characteristics”. In: *Canadian Geotechnical Journal* 40.3 (2003), pp. 669–674.
- [180] J Kumar. “Effect of footing—soil interface friction on bearing capacity factor N_γ ”. In: *Géotechnique* 54.10 (2004), pp. 677–680.
- [181] J Kumar. “The variation of N_γ with footing roughness using the method of characteristics”. In: *International Journal for Numerical and Analytical Methods in Geomechanics* 33.2 (2009), pp. 275–284.

- [182] J Kumar and Vishwas N Khatri. “Bearing capacity factors of circular foundations for a general c - ϕ soil using lower bound finite elements limit analysis”. In: *International Journal for Numerical and Analytical Methods in Geomechanics* 35.3 (2011), pp. 393–405.
- [183] J Kumar and Vishwas N Khatri. “Effect of footing roughness on lower bound N_γ values”. In: *International Journal of Geomechanics* 8.3 (2008), pp. 176–187.
- [184] J Kumar and K M Kouzer. “Effect of footing roughness on bearing capacity factor N_γ ”. In: *Journal of Geotechnical and Geoenvironmental Engineering* 133.5 (2007), pp. 502–511.
- [185] A S Kumbhojkar. “Numerical evaluation of Terzaghi’s N_γ ”. In: *Journal of Geotechnical Engineering* 119.3 (1993), pp. 598–607.
- [186] F Kuwabara. “An elastic analysis for piled raft foundations in a homogeneous soil”. In: *Soils and foundations* 29.1 (1989), pp. 82–92.
- [187] L Laloui and A Di Donna. *Energy geostructures: innovation in underground engineering*. John Wiley & Sons, 2013.
- [188] L Laloui, M Moreni, A Fromentin, D Pahud, and L Vuillet. “In-situ thermo-mechanical load test on a heat exchanger pile”. In: (1999).
- [189] L Laloui, M Moreni, and L Vulliet. “Comportement d’un pieu bi-fonction, fondation et échangeur de chaleur”. In: *Canadian Geotechnical Journal* 40.2 (2003), pp. 388–402.
- [190] L Laloui, M Nuth, and L Vulliet. “Experimental and numerical investigations of the behaviour of a heat exchanger pile”. In: *International Journal for Numerical and Analytical Methods in Geomechanics* 30.8 (2006), pp. 763–781.
- [191] L A Larkin. “Theoretical bearing capacity of very shallow footings”. In: *Journal of the Soil Mechanics and Foundations Division* 94.6 (1968), pp. 1347–1360.
- [192] L A Larkin. “Upper Bound Analysis of Rough Footing Indentation”. In: *Journal of the Engineering Mechanics Division* 98.2 (1972), pp. 493–496.
- [193] J Lee, Y Kim, and S Jeong. “Three-dimensional analysis of bearing behavior of piled raft on soft clay”. In: *Computers and Geotechnics* 37.1-2 (2010), pp. 103–114.
- [194] J Lemaitre. *Handbook of Materials Behavior Models*. Elsevier, 2001.
- [195] M Lévy. “Mémoire sur les équations générales des mouvements intérieurs des corps solides ductiles au delà des limites où l’élasticité pourrait les ramener à leur premier état”. In: *CR Acad. Sci. Paris* 70 (1870), pp. 1323–1325.

- [196] Limit State Ltd. *Limit State*. 2019. URL: <http://limitstate.com/>.
- [197] U Lindblom. “Utilization of Underground for Solar and Waste Heat Storage”. In: *Subsurface Space*. Elsevier, 1981, pp. 509–514.
- [198] D Loukidis, T Chakraborty, and R Salgado. “Bearing capacity of strip footings on purely frictional soil under eccentric and inclined loads”. In: *Canadian Geotechnical Journal* 45.6 (2008), pp. 768–787.
- [199] D Loukidis and R Salgado. “Bearing capacity of strip and circular footings in sand using finite elements”. In: *Computers and Geotechnics* 36.5 (2009), pp. 871–879.
- [200] F A Loveridge, W Powrie, T Amis, M Wischy, and J Kiauk. “Long term monitoring of CFA energy pile schemes in the UK”. In: *Energy Geotechnics*. CRC Press. 2016, pp. 585–592.
- [201] H Lundgren and K Mortensen. “Determination by the theory of plasticity of the bearing capacity of continuous footings on sand”. In: *Proc., 3th Int. Conf. Soil Mech. Found. Eng.* Vol. 1. 1953, pp. 409–412.
- [202] A V Lyamin, R Salgado, S W Sloan, and M Prezzi. “Two-and three-dimensional bearing capacity of footings in sand”. In: *Géotechnique* 57.8 (2007), pp. 647–662.
- [203] A V Lyamin and S W Sloan. “Lower bound limit analysis using non-linear programming”. In: *International Journal for Numerical Methods in Engineering* 55.5 (2002), pp. 573–611.
- [204] A V Lyamin and S W Sloan. “Upper bound limit analysis using linear finite elements and non-linear programming”. In: *International Journal for Numerical and Analytical Methods in Geomechanics* 26.2 (2002), pp. 181–216.
- [205] J Lysmer. “Limit analysis of plane problems in soil mechanics”. In: *Journal of Soil Mechanics & Foundations Div* (1970).
- [206] M Maehr and I Herle. “Volume loss and soil dilatancy”. In: *Rivista italiana di geotecnica* 38.4 (2004), pp. 32–41.
- [207] A Makrodimopoulos and C M Martin. “Lower bound limit analysis of cohesive-frictional materials using second-order cone programming”. In: *International Journal for Numerical Methods in Engineering* 66.4 (2006), pp. 604–634.
- [208] A Makrodimopoulos and C M Martin. “Upper bound limit analysis using simplex strain elements and second-order cone programming”. In: *International journal for numerical and analytical methods in geomechanics* 31.6 (2007), pp. 835–865.

- [209] J Mandel. “Bases physiques et équations fondamentales de la théorie de la plasticité”. In: *Proceedings, Séminaire de plasticité, Paris*. 1961, pp. 13–36.
- [210] A Mandolini and C Viggiani. “Settlement of piled foundations”. In: *Géotechnique* 47.4 (1997), pp. 791–816.
- [211] N Manoharan and S P Dasgupta. “Bearing capacity of surface footings by finite elements”. In: *Computers & Structures* 54.4 (1995), pp. 563–586.
- [212] P Marti. “Basic tools of reinforced concrete beam design”. In: *Journal Proceedings*. Vol. 82. 1. 1985, pp. 46–56.
- [213] P Marti. “Plastic analysis of reinforced concrete shear walls”. In: *IABSE* (1979), pp. 51–69.
- [214] P Marti, M Alvarez, W Kaufmann, and V Sigrist. “Tension chord model for structural concrete”. In: *Structural Engineering International* 8.4 (1998), pp. 287–298.
- [215] C M Martin. “ABC—Analysis of bearing capacity”. In: *Available online from <http://www2.eng.ox.ac.uk/civil/people/cmm/software>* (2004).
- [216] C M Martin. “Discussion of “Calculations of Bearing Capacity Factor N_γ Using Numerical Limit Analyses” by B Ukritchon, A J Whittle, and C Klangvithit”. In: *Journal of Geotechnical and Geoenvironmental Engineering* 130.10 (2004), pp. 1106–1107.
- [217] C M Martin. “Exact bearing capacity calculations using the method of characteristics”. In: *Proc. IACMAG. Turin* (2005), pp. 441–450.
- [218] C M Martin. “Exact bearing capacity factors for strip footings—notes”. In: *Available online from <http://www2.eng.ox.ac.uk/civil/people/cmm>* (2005).
- [219] J B Martin. *Plasticity: fundamentals and general results*. MIT press, 1975.
- [220] J S McCartney and K D Murphy. “Strain distributions in full-scale energy foundations (DFI Young Professor Paper Competition 2012)”. In: *DFI Journal-The Journal of the Deep Foundations Institute* 6.2 (2012), pp. 26–38.
- [221] J S McCartney and J E Rosenberg. “Impact of heat exchange on side shear in thermo-active foundations”. In: *Geo-Frontiers 2011: Advances in Geotechnical Engineering*. 2011, pp. 488–498.
- [222] John S McCartney. “Engineering performance of energy foundations”. In: *Pan-Am CGS Geotechnical Conf.* 2011.
- [223] H Meischeder. “Über den Einfluß der Flächenform auf die Tragfähigkeit von Fundamentplatten”. In: *Der Bauingenieur* 21 (1940), pp. 83–92.

- [224] E Melan. “Der Spannungszustand eines Mises-Henckys chen Kontinuums bei veraderlicher Belastung”. In: *Sitzber Akad. Wiss. Wien Iia* 147 (1938), pp. 73–87.
- [225] E Melan. “Zur plastizität des räumlichen kontinuums”. In: *Archive of Applied Mechanics* 9.2 (1938), pp. 116–126.
- [226] G G Meyerhof. “An investigation of the bearing capacity of shallow footings on dry sand”. In: *Proc. 2nd ICSMFE*. Vol. 1. 1948, pp. 238–243.
- [227] G G Meyerhof. “Development of geotechnical limit state design”. In: *Canadian Geotechnical Journal* 32.1 (1995), pp. 128–136.
- [228] G G Meyerhof. “Discussion on Foundations other than piled foundations”. In: *Proceedings, 5th International Conference on Soil Mechanics and Foundation Engineering, Paris*. 1961, pp. 193–195.
- [229] G G Meyerhof. “Influence of roughness of base and ground-water conditions on the ultimate bearing capacity of foundations”. In: *Geotechnique* 5.3 (1955), pp. 227–242.
- [230] G G Meyerhof. “Some recent foundation research and its application to design”. In: *The Structural Engineer* 31.6 (1953), pp. 151–167.
- [231] G G Meyerhof. “Some recent foundation research and its application to design”. In: *The Structural Engineer* 31.6 (1963), pp. 151–167.
- [232] G G Meyerhof. “The ultimate bearing capacity of foudations”. In: *Geotechnique* 2.4 (1951), pp. 301–332.
- [233] R L Michalowski. “An estimate of the influence of soil weight on bearing capacity using limit analysis”. In: *Soils and foundations* 37.4 (1997), pp. 57–64.
- [234] R L Michalowski. “The rule of equivalent states in limit-state analysis of soils”. In: *Journal of geotechnical and geoenvironmental engineering* 127.1 (2001), pp. 76–83.
- [235] R L Michalowski. “Upper-bound load estimates on square and rectangular footings”. In: *Géotechnique* 51.9 (2001), pp. 787–798.
- [236] R L Michalowski and E M Dawson. “Three-dimensional analysis of limit loads on Mohr-Coulomb soil”. In: *Foundations of civil and environmental engineering* 1.1 (2002), pp. 137–147.
- [237] R L Michalowski and L Shi. “Bearing capacity of footings over two-layer foundation soils”. In: *Journal of Geotechnical Engineering* 121.5 (1995), pp. 421–428.
- [238] T Mimouni and L Laloui. “Behaviour of a group of energy piles”. In: *Canadian Geotechnical Journal* 52.12 (2015), pp. 1913–1929.

- [239] T Mimouni and L Laloui. “Towards a secure basis for the design of geothermal piles”. In: *Acta Geotechnica* 9.3 (2014), pp. 355–366.
- [240] R von Mises. “Mechanik der festen Körper im plastisch-deformablen Zustand”. In: *Nachrichten von der Gesellschaft der Wissenschaften zu Göttingen, Mathematisch-Physikalische Klasse* (1913), pp. 582–592.
- [241] R von Mises. “Mechanik der plastischen Formänderung von Kristallen”. In: *ZAMM-Journal of Applied Mathematics and Mechanics/Zeitschrift für Angewandte Mathematik und Mechanik* 8.3 (1928), pp. 161–185.
- [242] O Mohr. “Ueber die Darstellung des Spannungszustandes eines Korperelements: Civilingenieure, v. 28”. In: (1882).
- [243] E Mörsch. “Reinforced concrete construction, theory and application”. In: *Wittwer, Stuttgart* 1.Part 1 (1908).
- [244] H Mroueh, J Habert, and D Rammal. “Design charts for geothermal piles under various thermo-mechanical conditions”. In: *ce/papers* 2.2-3 (2018), pp. 181–190.
- [245] Z Mroz. “Non-associated flow laws in plasticity”. In: *Jour. De Mechanique* 2.1 (1963), pp. 21–42.
- [246] Z Mróz and A Drescher. “Limit Plasticity Approach to Some Cases of Flow of Bulk Solids”. In: *Journal of Engineering for Industry* 91.2 (1969), pp. 357–364.
- [247] K D Murphy and J S McCartney. “Seasonal response of energy foundations during building operation”. In: *Geotechnical and Geological Engineering* 33.2 (2015), pp. 343–356.
- [248] K D Murphy, J S McCartney, and K S Henry. “Evaluation of thermo-mechanical and thermal behavior of full-scale energy foundations”. In: *Acta Geotechnica* 10.2 (2015), pp. 179–195.
- [249] K D Murphy, J S McCartney, and K S Henry. “Thermo-mechanical characterization of a full-scale energy foundation”. In: *From Soil Behavior Fundamentals to Innovations in Geotechnical Engineering: Honoring Roy E. Olson*. 2014, pp. 617–628.
- [250] A Muttoni and M Fernández Ruiz. “Concrete cracking in tension members and application to deck slabs of bridges”. In: *Journal of Bridge Engineering* 12.5 (2007), pp. 646–653.

- [251] A Muttoni and M Fernández Ruiz. “Shear strength in one-and two-way slabs according to the Critical Shear Crack Theory”. In: *fib Symposium, Amsterdam 2008*. CONF. fib Symposium, Amsterdam 2008. 2008.
- [252] A Muttoni and M Fernández Ruiz. “Shear strength of members without transverse reinforcement as function of critical shear crack width”. In: *ACI Structural Journal* 2 (2008), pp. 163–172.
- [253] A Muttoni, M Fernández Ruiz, and N Kostic. *Champs de contraintes et méthode des bielles-et-tirants–Applications dans la conception et le dimensionnement des structures en béton armé*. Tech. rep. EPFL-IBETON, 2011.
- [254] A Muttoni, M Fernández Ruiz, F Niketic, and M-R Backes. *Assessment of existing structures based on elastic-plastic stress fields-Modelling of critical details and investigation of the in-plane shear transverse bending interaction*. Tech. rep. Rapport OFROU, 2016.
- [255] A Muttoni, M Fernández Ruiz, and J T Simões. “The theoretical principles of the critical shear crack theory for punching shear failures and derivation of consistent closed-form design expressions”. In: *Structural Concrete* 19.1 (2018), pp. 174–190.
- [256] A Muttoni and J Schwartz. “Behavior of beams and punching in slabs without shear reinforcement”. In: *IABSE colloquium*. Vol. 62. CONF. IABSE Colloquium. 1991, pp. 703–708.
- [257] A Muttoni, J Schwartz, and B Thürlimann. *Design of concrete structures with stress fields*. Springer Science & Business Media, 1996.
- [258] G Mylonakis and G Gazetas. “Settlement and additional internal forces of grouped piles in layered soil”. In: *Géotechnique* 48.1 (1998), pp. 55–72.
- [259] A Nadai. “Der Beginn des Fließvorganges in einem tordierten Stab”. In: *ZAMM-Journal of Applied Mathematics and Mechanics/Zeitschrift für Angewandte Mathematik und Mechanik* 3.6 (1923), pp. 442–454.
- [260] P M Naghdi. “Stress-strain relations in plasticity and thermoplasticity”. In: *Plasticity: Proceedings of the Second Symposium on Naval Structural Mechanics*. Pergamon. 1960, pp. 121–169.
- [261] M Navier. *Leçons sur l'application de la mécanique aux constructions*. 1833.

- [262] D J Naylor and J A Hooper. “An Effective Stress Finite Element Analysis to Predict the Short and Long Term Behaviour of a Piled–Raft Foundation on London Clay”. In: *Proceedings of Conference on Settlement of Structure, Cambridge, England*. 1975, pp. 394–402.
- [263] C W W Ng, Q J Ma, and A Gunawan. “Horizontal stress change of energy piles subjected to thermal cycles in sand”. In: *Computers and Geotechnics* 78 (2016), pp. 54–61.
- [264] C W W Ng, C Shi, A Gunawan, and L Laloui. “Centrifuge modelling of energy piles subjected to heating and cooling cycles in clay”. In: *Geotechnique letters* 4.4 (2014), pp. 310–316.
- [265] C W W Ng, C Shi, A Gunawan, L Laloui, and H L Liu. “Centrifuge modelling of heating effects on energy pile performance in saturated sand”. In: *Canadian Geotechnical Journal* 52.8 (2014), pp. 1045–1057.
- [266] M P Nielsen and L C Hoang. *Limit analysis and concrete plasticity*. 3rd ed. CRC press, 2016.
- [267] M W O’Neill, R A Hawkins, and L J Mahar. “Field study of pile group action”. In: (1981).
- [268] J Ohde. *Zur theorie der druckverteilung im baugrund*. 1939.
- [269] C G Olgun, T Y Ozudogru, S L Abdelaziz, and A Senol. “Long-term performance of heat exchanger piles”. In: *Acta Geotechnica* 10.5 (2015), pp. 553–569.
- [270] E T Onat and R M Haythornthwaite. *The load carrying capacity of circular plates at large deflection*. Tech. rep. Brown Univ Providence Ri Div of Engineering, 1954.
- [271] Optum Computational Engineering. *OptumCE*. 2019. URL: <https://optumce.com/>.
- [272] M Ottaviani. “Three-dimensional finite element analysis of vertically loaded pile groups”. In: *Géotechnique* 25.2 (1975), pp. 159–174.
- [273] T Y Ozudogru, C G Olgun, and C F Arson. “Analysis of friction induced thermo-mechanical stresses on a heat exchanger pile in isothermal soil”. In: *Geotechnical and Geological Engineering* 33.2 (2015), pp. 357–371.
- [274] D Padmini. “Review of Methods to Predict the Bearing Capacity of Shallow Foundations”. In: *International Research Journal of Engineering and Technology* 5.11 (2018), pp. 217–226.

- [275] D Pahud, A Fromentin, and M Hubbuch. “Heat exchanger pile system for heating and cooling at Zürich airport.” In: *IEA Heat Pump Centre Newsletter* 17.1 (1999), pp. 15–16.
- [276] A C Palmer. “A limit theorem for materials with non-associated flow laws”. In: *Journal de mécanique* 5 (1966), pp. 217–222.
- [277] L A Palmer, E S Barber, and D P Krynine. “Principles of soil mechanics involved in fill construction”. In: *Highway Research Board Proceedings*. Vol. 17. 1938.
- [278] C Pasten and J C Santamarina. “Thermally induced long-term displacement of thermoactive piles”. In: *Journal of Geotechnical and Geoenvironmental Engineering* 140.5 (2014), p. 06014003.
- [279] W H Pell and W Prager. “Limit design of plates”. In: *Journal of Applied Mechanics-Transactions of the ASME*. Vol. 18. 3. ASME-Amer Soc Mechanical Eng 345 E 47TH ST, New York, NY 10017. 1951, pp. 325–325.
- [280] A Pérez Caldentey, P Padilla, A Muttoni, and M Fernández Ruiz. “Effect of load distribution and variable depth on shear resistance of slender beams without stirrups”. In: *ACI Structural Journal* 109.ARTICLE (2012), pp. 595–603.
- [281] S Plumey. “Interaction sol-structure dans le domaine des tranchées couvertes”. PhD thesis. École polytechnique fédérale de Lausanne, 2007.
- [282] S Plumey, A Muttoni, L Vulliet, and V Labieuse. “Plasticity in soil-structure interaction applied to cut-and-cover tunnels”. In: *5th International PhD Symposium in civil engineering*. Vol. 2. CONF. 5th International PhD Symposium in civil engineering. 2004, pp. 989–995.
- [283] J-V Poncelet. *Mémoire sur la stabilité des revêtements et de leurs fondations*. Bachelier, 1840.
- [284] H G Poulos. “An approximate numerical analysis of pile–raft interaction”. In: *International Journal for Numerical and Analytical Methods in Geomechanics* 18.2 (1994), pp. 73–92.
- [285] H G Poulos. “Analysis of the settlement of pile groups”. In: *Géotechnique* 18.4 (1968), pp. 449–471.
- [286] H G Poulos. “The influence of a rigid pile cap on the settlement behaviour of an axially-loaded pile”. In: *CE Trans. Inst. Engrs., Australia* CE10.2 (1968), pp. 206–208.

- [287] H G Poulos, J P Carter, and J C Small. “Foundations and retaining structures-Research and practice”. In: *Proceedings of the international conference on soil mechanics and geotechnical engineering*. Vol. 4. AA Balkema Publishers. 2002, pp. 2527–2606.
- [288] H G Poulos and E H Davis. *Elastic solutions for soil and rock mechanics*. BOOK. John Wiley, 1974.
- [289] H G Poulos and E H Davis. *Pile foundation analysis and design*. New York: Wiley, 1980.
- [290] W Prager. “An introduction to the mathematical theory of plasticity”. In: *Journal of Applied Physics* 18.4 (1947), pp. 375–383.
- [291] W Prager. *Limit analysis and design*. Tech. rep. Brown Univ Providence Ri Div of Applied Mathematics, 1952.
- [292] W Prager. *On the use of singular yield conditions and associated flow rules*. Tech. rep. Brown Univ Providence Ri Div of Applied Mathematics, 1953.
- [293] W Prager. “Recent developments in the mathematical theory of plasticity”. In: *Journal of applied physics* 20.3 (1949), pp. 235–241.
- [294] W Prager. “The general theory of limit design”. In: *Proc. 8th Int. Congress Theoretical and Applied Mechanics, Istanbul 1952*. 1955, pp. 65–72.
- [295] W Prager. “The theory of plasticity: a survey of recent achievements”. In: *Proceedings of the Institution of Mechanical Engineers* 169.1 (1955), pp. 41–57.
- [296] W Prager and P G Hodge. *Theory of perfectly plastic solids*. New York: Wiley, 1951.
- [297] L Prandtl. “Spannungsverteilung in plastischen Körpern”. In: *Proceedings of the 1st international congress on applied mechanics*. 1924, pp. 43–54.
- [298] L Prandtl. “Über die härte plastischer körper”. In: *Nachrichten von der Gesellschaft der Wissenschaften zu Göttingen, Mathematisch-Physikalische Klasse* 1920 (1920), pp. 74–85.
- [299] D Radenkovic. “Théorèmes limites pour un matériau de Coulomb à dilation non standardisée”. In: *Comptes rendus hebdomadaires des seances de l'academie des sciences* 252.26 (1961), pp. 4103–4104.
- [300] D Radenkovic. “Théorie des charges limites extension a la mécanique des sols”. In: *Publ. Sci. Tech. Minist. Air (Fr.)* 116 (1961).

- [301] M F Randolph. “Effect of strength anisotropy on capacity of foundations”. In: *Proc., Booker Memorial Symp., Sydney, Australia*. CRC Press/Balkema. 2000, pp. 313–327.
- [302] M F Randolph and C P Wroth. “An analysis of the vertical deformation of pile groups”. In: *Géotechnique* 29.4 (1979), pp. 423–439.
- [303] M F Randolph and C P Wroth. “Analysis of deformation of vertically loaded piles”. In: *Journal of Geotechnical and Geoenvironmental Engineering* 104.ASCE 14262 (1978).
- [304] W J M Rankine. “On the stability of loose earth”. In: *Philosophical transactions of the Royal Society of London* 147 (1857), pp. 9–27.
- [305] H Reissner. “Zum erddruckproblem”. In: *Proc. 1st Int. Congress for Applied Mechanics*. Delft. 1924, pp. 295–311.
- [306] J Résal. *Poussées des terres: Vol. I, Stabilité des murs de soutènement*. Paris: Béranger, 1910.
- [307] J Résal. *Poussées des terres: Vol. II, Théorie des terres cohérentes*. Paris: Béranger, 1910.
- [308] O Reul. “Numerical study of the bearing behavior of piled rafts”. In: *International Journal of Geomechanics* 4.2 (2004), pp. 59–68.
- [309] A Reuss. “Berücksichtigung der elastischen Formänderung in der Plastizitätstheorie”. In: *ZAMM-Journal of Applied Mathematics and Mechanics/Zeitschrift für Angewandte Mathematik und Mechanik* 10.3 (1930), pp. 266–274.
- [310] F Rioagl. “Yield Limits and Characteristic of Deflection Lines”. In: *Preliminary Publication of 2nd Congress of International Association for Bridges and Structural Engineering, Berlin-Munich*. 1936.
- [311] M Ritter. “Limits of Equilibrium of Earths and Loose Materials”. In: *Int. Assoc. for Bridge and Struct. Eng., Second Congress*. 1936.
- [312] W Ritter. “Die Bauweise Hennebique”. In: (1899).
- [313] K H Roscoe, A N Schofield, and C P Wroth. “On the yielding of soils”. In: *Géotechnique* 8.1 (1958), pp. 22–53.
- [314] A F Rotta Loria. “Performance-based Design of Energy Pile Foundations”. In: *DFI Journal-The Journal of the Deep Foundations Institute* 12.2 (2018), pp. 94–107.
- [315] A F Rotta Loria. “Thermo-mechanical performance of energy pile groups”. PhD thesis. École polytechnique fédérale de Lausanne, 2018.

- [316] A F Rotta Loria, M Bocco, C Garbellini, A Muttoni, and L Laloui. “The role of thermal loads in the performance-based design of energy piles”. In: *Geomechanics for Energy and the Environment* 21 (2020), p. 100153.
- [317] A F Rotta Loria, A Gunawan, C Shi, L Laloui, and C W W Ng. “Numerical modelling of energy piles in saturated sand subjected to thermo-mechanical loads”. In: *Geomechanics for Energy and the Environment* 1 (2015), pp. 1–15.
- [318] A F Rotta Loria and L Laloui. “Displacement interaction among energy piles bearing on stiff soil strata”. In: *Computers and Geotechnics* 90 (2017), pp. 144–154.
- [319] A F Rotta Loria and L Laloui. “Group action effects caused by various operating energy piles”. In: *Géotechnique* 68.9 (2018), pp. 834–841.
- [320] A F Rotta Loria and L Laloui. “The equivalent pier method for energy pile groups”. In: *Géotechnique* 67.8 (2017), pp. 691–702.
- [321] A F Rotta Loria and L Laloui. “The interaction factor method for energy pile groups”. In: *Computers and Geotechnics* 80 (2016), pp. 121–137.
- [322] A F Rotta Loria and L Laloui. “Thermally induced group effects among energy piles”. In: *Géotechnique* 67.5 (2016), pp. 374–393.
- [323] A F Rotta Loria and L Laloui. “Thermo-mechanical schemes for energy piles”. In: *International Symposium on Energy Geotechnics*. Springer. 2018, pp. 218–225.
- [324] A F Rotta Loria, A Vadrot, and Laloui. “Analysis of the vertical displacement of energy pile groups”. In: *Geomechanics for Energy and the Environment* 16 (2018), pp. 1–14.
- [325] A F Rotta Loria, A Vadrot, and L Laloui. “Effect of non-linear soil deformation on the interaction among energy piles”. In: *Computers and Geotechnics* 86 (2017), pp. 9–20.
- [326] G Russo. “Numerical analysis of piled rafts”. In: *International Journal for Numerical and Analytical Methods in Geomechanics* 22.6 (1998), pp. 477–493.
- [327] G Sacchi and M Save. “A note on the limit loads of non-standard materials”. In: *Meccanica* 3.1 (1968), pp. 43–45.
- [328] B de Saint-Venant. “Mémoire sur l’établissement des équations différentielles des mouvements intérieurs opérés dans les corps solides ductiles au delà des limites où l’élasticité pourrait les ramener à leur premier état”. In: *Compt. Rend* 70 (1870), pp. 473–480.

- [329] D Salciarini, F Ronchi, E Cattoni, and C Tamagnini. “Thermomechanical effects induced by energy piles operation in a small piled raft”. In: *International journal of Geomechanics* 15.2 (2015), p. 04014042.
- [330] J Salençon. “Discussion: The effect of increasing strength with depth on the bearing capacity of clays”. In: *Geotechnique* 24.3 (1974), pp. 449–451.
- [331] J Salençon. *Calcul à la rupture et analyse limite*. Presses de l’ E.N.P.C., Paris, 1983.
- [332] J Salençon. “Théorie de la plasticité pour les applications à la mécanique des sols, Eyrolles, Paris”. In: (1974).
- [333] J Salençon and M Matar. “Capacité portante des fondations superficielles circulaires.” In: *Journal de Mécanique théorique et appliquée* 1.2 (1982), pp. 237–267.
- [334] R Salgado, A V Lyamin, S W Sloan, and H S Yu. “Two-and three-dimensional bearing capacity of foundations in clay”. In: *Géotechnique* 54.5 (2004), pp. 297–306.
- [335] A K Sani, R M Singh, T Amis, and I Cavarretta. “A review on the performance of geothermal energy pile foundation, its design process and applications”. In: *Renewable and Sustainable Energy Reviews* 106 (2019), pp. 54–78.
- [336] S Saran. *Shallow Foundations and Soil Constitutive Laws*. CRC Press, 2017.
- [337] J Schlaich, K Schäfer, and M Jennewein. “Toward a consistent design of structural concrete”. In: *PCI journal* 32.3 (1987), pp. 74–150.
- [338] A Schofield and P Wroth. *Critical state soil mechanics*. McGraw-Hill London, 1968.
- [339] R F Scott. “Plasticity and constitutive relations in soil mechanics”. In: *Journal of Geotechnical Engineering* 111.5 (1985), pp. 559–605.
- [340] K Sekine, R Ooka, M Yokoi, Y Shiba, and S Hwang. “Development of a Ground-Source Heat Pump System with Ground Heat Exchanger Utilizing the Cast-in-Place Concrete Pile Foundations of Buildings.” In: *Ashrae Transactions* 113.1 (2007).
- [341] M Shafique and T Qayyum. “Comparison of bearing capacity equations for vertical central loading”. In: *Proceedings of the 1st international conference on geotechnique, construction materials and environment*. 2011, pp. 583–588.
- [342] R T Shield. “Mixed boundary value problems in soil mechanics”. In: *Quarterly of Applied Mathematics* 11.1 (1953), pp. 61–75.

- [343] R T Shield. “On Coulomb’s law of failure in soils”. In: *Journal of the Mechanics and Physics of Solids* 4.1 (1955), pp. 10–16.
- [344] R T Shield. “On the plastic flow of metals under conditions of axial symmetry”. In: *Proceedings of the Royal Society of London. Series A. Mathematical and Physical Sciences* 233.1193 (1955), pp. 267–287.
- [345] R T Shield. “Plastic potential theory and Prandtl bearing capacity”. In: *Trans. ASME, J. Appl. Mechanics* 21 (1954), pp. 193–194.
- [346] R T Shield. “Stress and velocity fields in soil mechanics”. In: *Journal of Mathematics and Physics* 33.1-4 (1954), pp. 144–156.
- [347] R T Shield. *The Bearing Capacity of a Footing on a Soil (plane-strain)*. Tech. rep. Brown Univ Providence RI Div of Applied Mathematics, 1953.
- [348] R T Shield and D C Drucker. “The application of limit analysis to punch-indentation problems”. In: *Journal of Applied Mechanics* (1953), pp. 453–460.
- [349] SIA. *Code 262 for Concrete Structures*. Swiss Society of Engineers and Architects, Zurich, Switzerland, 2013. 2013, p. 102.
- [350] SIA D0190. *Utilisation de la chaleur du sol par des ouvrages de fondation et de soutènement en béton. Guide pour la conception, la réalisation et la maintenance*. Société suisse des ingénieurs et des architectes, Zurich, Switzerland. 2005.
- [351] J-G Sieffert and C Bay-Gress. “Comparison of European bearing capacity calculation methods for shallow foundations”. In: *Proceedings of the Institution of Civil Engineers-Geotechnical Engineering* 143.2 (2000), pp. 65–74.
- [352] V Silvestri. “A limit equilibrium solution for bearing capacity of strip foundations on sand”. In: *Canadian geotechnical journal* 40.2 (2003), pp. 351–361.
- [353] J T Simões. “The mechanics of punching in reinforced concrete slabs and footings without shear reinforcement”. PhD thesis. École polytechnique fédérale de Lausanne, 2018, p. 223.
- [354] J T Simões, J Bujnak, M Fernández Ruiz, and A Muttoni. “Punching shear tests on compact footings with uniform soil pressure”. In: *Structural Concrete* 17.4 (2016), pp. 603–617.
- [355] J T Simões, D M V Faria, M Fernández Ruiz, and A Muttoni. “Strength of reinforced concrete footings without transverse reinforcement according to limit analysis”. In: *Engineering structures* 112 (2016), pp. 146–161.

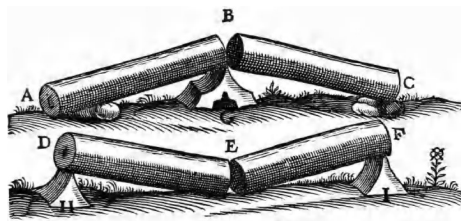
- [356] J T Simões, M Fernández Ruiz, and A Muttoni. “Validation of the Critical Shear Crack Theory for punching of slabs without transverse reinforcement by means of a refined mechanical model”. In: *Structural Concrete* 19.1 (2018), pp. 191–216.
- [357] A W Skempton. “An investigation of the bearing capacity of a soft clay soil”. In: *J. Inst. Civil Eng* 18.1305 (1942), pp. 307–321.
- [358] A W Skempton. “Landmarks in early soil mechanics”. In: *Proceedings of the 7th European Conference on Soil Mechanics and Foundation Engineering, Brighton*. Vol. 5. 1979, pp. 1–26.
- [359] A W Skempton. “The bearing capacity of clays”. In: *Proceedings Building Research Congress*. Vol. 1. 1951, pp. 180–189.
- [360] S W Sloan. “Lower bound limit analysis using finite elements and linear programming”. In: *International Journal for Numerical and Analytical Methods in Geomechanics* 12.1 (1988), pp. 61–77.
- [361] S W Sloan. “Upper bound limit analysis using finite elements and linear programming”. In: *International Journal for Numerical and Analytical Methods in Geomechanics* 13.3 (1989), pp. 263–282.
- [362] S W Sloan and P W Kleeman. “Upper bound limit analysis using discontinuous velocity fields”. In: *Computer Methods in Applied Mechanics and Engineering* 127.1-4 (1995), pp. 293–314.
- [363] S W Sloan and H S Yu. “Rigorous Plasticity Solutions for the Bearing Capacity Factor N_γ ”. In: *7th Australia New Zealand Conference on Geomechanics: Geomechanics in a Changing World: Conference Proceedings*. Institution of Engineers, Australia. 1996, p. 544.
- [364] C C Smith. “Complete limiting stress solutions for the bearing capacity of strip footings on a Mohr-Coulomb soil”. In: *Géotechnique* 55.8 (2005), pp. 607–612.
- [365] C Smith and M Gilbert. “Application of discontinuity layout optimization to plane plasticity problems”. In: *Proceedings of the Royal Society A: Mathematical, Physical and Engineering Sciences* 463.2086 (2007), pp. 2461–2484.
- [366] V V Sokolovskii. *Statics of granular media*. Pergamon Press, 1965.
- [367] V V Sokolovskii. *Statics of soil media*. Butterworths Scientific Publications, 1960.
- [368] A-H Soubra. “Upper-bound solutions for bearing capacity of foundations”. In: *Journal of Geotechnical and Geoenvironmental Engineering* 125.1 (1999), pp. 59–68.

- [369] M G Spangler and R L Handy. *Soil engineering*. 4th ed. Harper and Row, New York, 1982.
- [370] A J M Spencer. “Perturbation methods in plasticity—III plane strain of ideal soils and plastic solids with body forces”. In: *Journal of the Mechanics and Physics of Solids* 10.2 (1962), pp. 165–177.
- [371] G D Stefanou. “Shear resistance of reinforced concrete beams with non-prismatic sections”. In: *Engineering Fracture Mechanics* 18.3 (1983), pp. 643–666.
- [372] M A Stewart and J S McCartney. “Centrifuge modeling of soil-structure interaction in energy foundations”. In: *Journal of Geotechnical and Geoenvironmental Engineering* 140.4 (2013), p. 04013044.
- [373] M A Stewart and J S McCartney. “Strain distributions in centrifuge model energy foundations”. In: *GeoCongress 2012: State of the Art and Practice in Geotechnical Engineering*. 2012, pp. 4376–4385.
- [374] M E Suryatriyastuti, H Mroueh, and S Burlon. “A load transfer approach for studying the cyclic behavior of thermo-active piles”. In: *Computers and Geotechnics* 55 (2014), pp. 378–391.
- [375] M Suryatriyastuti, H Mroueh, and S Burlon. “Thermo-mechanics behaviour of energy pile subjected by monotonic thermal loading”. In: *Congrès français de mécanique*. Vol. 1. 1. 2011.
- [376] M Sutman, T Brettmann, and C G Olgun. “Full-scale in-situ tests on energy piles: Head and base-restraining effects on the structural behaviour of three energy piles”. In: *Geomechanics for Energy and the Environment* 18 (2019), pp. 56–68.
- [377] M Sutman, C G Olgun, and T Brettmann. “Full-scale field testing of energy piles”. In: *Proceedings of IFCEE, San Antonio, TX, USA*. American Society of Civil Engineers (ASCE), 2015, pp. 1638–1647.
- [378] M Sutman, C G Olgun, and L Laloui. “Cyclic Load–Transfer Approach for the Analysis of Energy Piles”. In: *Journal of Geotechnical and Geoenvironmental Engineering* 145.1 (2018), p. 04018101.
- [379] M Sutman, C G Olgun, and L Laloui. “Cyclic load–transfer approach for the analysis of energy piles”. In: *Journal of Geotechnical and Geoenvironmental Engineering* 145.1 (2019), p. 04018101.
- [380] P S Symonds and B G Neal. “Recent progress in the plastic methods of structural analysis”. In: *Journal of the Franklin Institute* 252.5 (1951), pp. 383–407.

- [381] Systat Software Inc. *TableCurve 3D user's manual, version 4.0*. 2017. URL: <https://systatsoftware.com/products/tablecurve-3d/>.
- [382] L D Ta and J C Small. "Analysis of piled raft systems in layered soil". In: *International Journal for Numerical and Analytical Methods in Geomechanics* 20.1 (1996), pp. 57–72.
- [383] D W Taylor. *Fundamentals of soil mechanics*. Vol. 66. 2. LWW, 1948.
- [384] K Terzaghi. *Theoretical soil mechanics*. New York: Wiley, 1943.
- [385] K Terzaghi, R B Peck, and G Mesri. *Soil mechanics in engineering practice*. John Wiley & Sons, 1996.
- [386] S Timoshenko and J N Goodier. *Theory of elasticity*. 2nd ed. New York: McGraw-Hill, 1951.
- [387] H E Tresca. *Sur l'écoulement des corps solides soumis a de fortes pressions*. Imprimerie de Gauthier-Villars, successeur de Mallet-Bachelier, rue de Seine ..., 1864.
- [388] C Truesdell. "Review: W. Prager and P. G. Hodge, Theory of perfectly plastic solids". In: *Bulletin of the American Mathematical Society* 58.6 (1952), pp. 674–677.
- [389] B Ukritchon, A J Whittle, and C Klangvijit. "Calculations of bearing capacity factor N_γ using numerical limit analyses". In: *Journal of Geotechnical and Geoenvironmental Engineering* 129.5 (2003), pp. 468–474.
- [390] J A Van den Broek. *Theory of Limit Design*. John Wily and Sons Inc., New York, 1948.
- [391] J A Van den Broek. "Theory of limit design". In: *Proceedings of the American Society of Civil Engineers*. Vol. 65. 2. ASCE. 1940, pp. 193–216.
- [392] G Van Rossum and F L Drake. *Python 3 Reference Manual*. Scotts Valley, CA: CreateSpace, 2009. ISBN: 1441412697.
- [393] R Vaz Rodrigues, O Burdet, and A Muttoni. "Experimental investigation of the shear capacity of plastic hinges". In: *fib Symposium, Budapest 2005*. Vol. 2. CONF. fib Symposium, Budapest 2005. 2005, pp. 651–656.
- [394] F J Vecchio and M P Collins. "The modified compression-field theory for reinforced concrete elements subjected to shear." In: *ACI J*. 83.2 (1986), pp. 219–231.

- [395] M Veiskarami, J Kumar, and F Valikhah. “Effect of the flow rule on the bearing capacity of strip foundations on sand by the upper-bound limit analysis and slip lines”. In: *International Journal of Geomechanics* 14.3 (2014), p. 04014008.
- [396] A Vesić. “Bearing capacity of shallow foundations”. In: *Winterkorn, H., Fang, H. (Eds.), Foundation engineering handbook. Van Nostrand Reinhold, New York.* 1975, pp. 121–147.
- [397] A S Vesic. “Analysis of ultimate loads of shallow foundations”. In: *Journal of Soil Mechanics & Foundations Div* 99.sm1 (1973), pp. 45–71.
- [398] P Virtanen et al. “SciPy 1.0: Fundamental Algorithms for Scientific Computing in Python”. In: *Nature Methods* 17 (2020), pp. 261–272. DOI: <https://doi.org/10.1038/s41592-019-0686-2>.
- [399] B Wang, A Bouazza, and C Haberfield. “Preliminary observations from laboratory scale model geothermal pile subjected to thermal-mechanical loading”. In: *Geo-Frontiers 2011: Advances in Geotechnical Engineering*. 2011, pp. 430–439.
- [400] B Wang et al. “Field and laboratory investigation of a heat exchanger pile”. In: *GeoCongress 2012: State of the Art and Practice in Geotechnical Engineering*. 2012, pp. 4396–4405.
- [401] B Wang et al. “Posttemperature effects on shaft capacity of a full-scale geothermal energy pile”. In: *Journal of Geotechnical and Geoenvironmental Engineering* 141.4 (2014), p. 04014125.
- [402] B Wang et al. “Posttemperature effects on shaft capacity of a full-scale geothermal energy pile”. In: *Journal of Geotechnical and Geoenvironmental Engineering* 141.4 (2015), p. 04014125.
- [403] Y-J Wang, J-H Yin, and Z-Y Chen. “Calculation of bearing capacity of a strip footing using an upper bound method”. In: *International Journal for Numerical and Analytical Methods in Geomechanics* 25.8 (2001), pp. 841–851.
- [404] G Wilson. “The calculation of the bearing capacity of footings on clay”. In: *Journal of the Institution of Civil Engineers* 17.1 (1941), pp. 87–96.
- [405] J Xiao, Z Luo, J R Martin, W Gong, and L Wang. “Probabilistic geotechnical analysis of energy piles in granular soils”. In: *Engineering Geology* 209 (2016), pp. 119–127.

- [406] N Yavari, A M Tang, J-M Pereira, and G Hassen. “Effect of temperature on the shear strength of soils and the soil–structure interface”. In: *Canadian Geotechnical Journal* 53.7 (2016), pp. 1186–1194.
- [407] H-S Yu. *Plasticity and geotechnics*. Vol. 13. Springer Science & Business Media, 2007.
- [408] B Zadroga. “Bearing capacity of shallow foundations on noncohesive soils”. In: *Journal of geotechnical engineering* 120.11 (1994), pp. 1991–2008.
- [409] P D Zararis and I P Zararis. “Shear strength of reinforced concrete beams under uniformly distributed loads”. In: *ACI Structural Journal* 105.6 (2008), p. 711.
- [410] D Y Zhu, C F Lee, and H D Jiang. “A numerical study of the bearing capacity factor $N \gamma$ ”. In: *Canadian Geotechnical Journal* 38.5 (2001), pp. 1090–1096.
- [411] D Y Zhu, C F Lee, and K T Law. “Determination of bearing capacity of shallow foundations without using superposition approximation”. In: *Canadian geotechnical journal* 40.2 (2003), pp. 450–459.
- [412] M Zhu and R L Michalowski. “Shape factors for limit loads on square and rectangular footings”. In: *Journal of geotechnical and Geoenvironmental Engineering* 131.2 (2005), pp. 223–231.
- [413] O C Zienkiewicz, R L Tylor, and J Z Zhu. *The finite element method: its basis and fundamentals*. 7th ed. Elsevier, 2013.

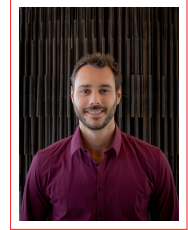


THIS THESIS WAS typeset using L^AT_EX, originally developed by Leslie Lamport and based on Donald Knuth's T_EX. The body text is set in 11 point Computer Modern, developed by Donald Knuth. The above illustration shows the cylindrical beam studied by Galileo Galilei [G Galilei. *Discorsi e dimostrazioni matematiche intorno a due nuove scienze*. Leyden, 1638].

Cristiano Garbellini

Curriculum Vitæ

Chemin de l'Ochettaz 16
1025, Saint-Sulpice
☎ +41 79 481 00 87
✉ cristiano.garbellini@gmail.com



PERSONAL DETAILS

Place and birth Lugano, 3 January 1991
Nationality Swiss

EDUCATION

- 2016–Present **Ph.D. in Soil Mechanics**, *Laboratory of Soil Mechanics–Swiss Federal Institute of Technology in Lausanne*, Lausanne, Switzerland.
Focused on soil-structure interaction.
- 2014–2016 **M.Sc. in Civil Engineering**, *Swiss Federal Institute of Technology in Lausanne*, Lausanne, Switzerland.
Specialisation in structural engineering.
- 2011–2014 **B.Sc. in Civil Engineering**, *Swiss Federal Institute of Technology in Lausanne*, Lausanne, Switzerland.

PROFESSIONAL EXPERIENCE

Practice

- 2014 **Civil engineering internship**, *AR&PA Engineering Sagl*, Lugano, Switzerland.
Structures, geotechnics.

Teaching Assistantship

- 2016–Present **Master's theses in geotechnics**, *Laboratory of Soil Mechanics–Swiss Federal Institute of Technology in Lausanne*, Lausanne, Switzerland.
- 2018–2020 **Soil Mechanics and Subsurface Flows**, *Laboratory of Soil Mechanics–Swiss Federal Institute of Technology in Lausanne*, Lausanne, Switzerland.
3d semester class at EPFL in civil engineering.
- 2017–2018 **Geomechanics**, *Laboratory of Soil Mechanics–Swiss Federal Institute of Technology in Lausanne*, Lausanne, Switzerland.
Master class at EPFL in civil engineering.
- 2016 **Timber Constructions**, *Laboratory of Timber Constructions–Swiss Federal Institute of Technology in Lausanne*, Lausanne, Switzerland.
Master class at EPFL in civil engineering.

2015 **Steel Structures**, *Steel Structures Laboratory–Swiss Federal Institute of Technology in Lausanne*, Lausanne, Switzerland.
4th semester class at EPFL in civil engineering.

LANGUAGES

Italian	Mothertongue
French	Fluent
English	Intermediate

COMPUTER SKILLS

Software	ZSoil, GeoSlope, Cubus, \LaTeX	Languages	Python, Matlab, C++
----------	---	-----------	---------------------

PROFESSIONAL ASSOCIATIONS

2018–Present	CFMS , <i>Comité français de mécanique des sols et de géotechnique</i> , France.
2019–Present	GI , <i>Geo-Institute (ASCE)</i> , USA.

PUBLICATIONS

- [1] Garbellini, C. “Efficient analysis methods for reinforced concrete sections under variable bending and axial load”. Master thesis. Lausanne: Swiss federal institute of technology, 2016.
- [2] Garbellini, C., Laloui, L. “On the Soil-Structure Interaction of Surface Strip Footings at Ultimate Limit State”. In: *Proceedings of the 26th European Young Geotechnical Engineers Conference*. Vol. 1. CONF. ISSMGE. 2018.
- [3] Garbellini, C., Laloui, L. “Performance of Energy Piles Considering Reinforced Concrete Non-Linearity”. In: *Proceedings of the Geo-Congress 2020*. ASCE. 2020, pp. 45–54.
- [4] Garbellini, C., Laloui, L. “Thermal stress analysis of energy piles”. In: *Géotechnique* (2019), pp. 1–12.
- [5] Garbellini, C., Laloui, L. “Three-dimensional finite element analysis of piled rafts with energy piles”. In: *Computers and Geotechnics* 114 (2019), p. 103115.
- [6] Rotta Loria, A. F., Bocco, M., Garbellini, C., Muttoni, A., Laloui, L. “The role of thermal loads in the performance-based design of energy piles”. In: *Geomechanics for Energy and the Environment* 21 (2020), p. 100153.